JAERI-M
90-087

EXPERIMENTAL STUDY OF RADIATION LOSSES ON THE JT-60 TOKAMAK

June 1990

Takeo NISHITANI

日本原子力研究所
Japan Atomic Energy Research Institute

JAERI-Mレポートは，日本原子力研究所が不定期に公刊している研究報告書です。
入手の問合わせは，日本原子力研究所技術情報部情報資料課（〒319-11茨城県那珂郡東海村）あて，お申しこしください。なお，このほかに財団法人原子力弘済会資料センター（〒319-11茨城県那珂郡東海村日本原子力研究所内）で複写による実費頒布をおこなっております。

JAERI-M reports are issued irregularly.
Inquiries about availability of the reports should be addressed to Information Division Department of Technical Information, Japan Atomic Energy Research Institute, Tokai-mura, Naka-gun, Ibaraki-ken 319-11, Japan.

編集兼発行　日本原子力研究所
印　　刷　いばらき印刷㈱

JAERI-M 90-087

Experimental Study of Radiation Losses on the JT-60 Tokamak

Takeo NISHITANI

Department of Large Tokamak Research
Naka Fusion Research Establishment
Japan Atomic Energy Research Institute
Naka-machi, Naka-gun, Ibaraki-ken

(Received May 11, 1990)

The accumulation of impurities and the accompanying radiation losses in a core plasma are serious problem to achieve a reactor grade plasma not only because the radiation losses degrade the energy confinement of the core plasma but also because the impurities dilute the reacting plasma to reduce reaction rate. Whereas, appropriate radiation loss localized in the peripheral plasma is sometimes favorable to reduce the heat load onto the first wall and influx of impurities from the wall by cooling edge plasma namely remote radiative cooling.

Bolometric measurement system and associated diagnostics, soft x-ray pulse-height-analyzer, soft x-ray intensity and Balmer α line measurement systems, were developed to investigate the radiation losses of the JT-60 plasmas. The bolometric measurement is the most important diagnostics in the radiation loss study. The soft x-ray pulse-height-analyzer is useful to estimate the metallic impurity concentration, and the soft x-ray intensity and Balmer α line measurements are monitors of radiation in x-ray region and particle recycling in the plasma edge, respectively.

Very low radiation loss of the main plasma (10% of the absorbed power) was realized in NB heated outer X-point discharges with TiC coated molybdenum wall. Whereas, the limiter plasma with TiC coated molybdenum limiters was very radiative where the radiated power was more than 60% of the absorbed power in ohmically and NB heated discharges. In the discharges with graphite wall, radiated power from the main plasma was 20 - 25% for both limiter and lower X-point configurations. The radiated

power from the divertor region increased from several percent to 40% of the absorbed power with the increase of $\bar{n}_e$. The improved divertor confinement (IDC) regime was obtained in NB heated lower X-point discharges with graphite wall. In IDC discharges the radiation loss from the divertor region increased to be up to 40% (typically 10 MW) of the absorbed power. Whereas, that from the main plasma and the heat load onto divertor plates decreased.

In JT-60, the marfe has been observed frequently in high-Ip and high density limited discharges with NB heating after the replacement of the first wall from TiC coated molybdenum tiles to graphite ones. The threshold electron density of the marfe onset increased with the NB power. The empirical scaling of the marfe onset taking account of the NB power was obtained. This scaling was useful to predict the marfe onset condition in NB heated discharges on JT-60. The marfe was modelled based on the radiative thermal instability. The simple model can explain the marfe onset condition. The radiated power from the plasma with marfe was about 90% of the absorbed power. Both stored energy and central electron temperatures did not change by the marfe onset in spite of the such intense radiation loss.

Finally, this study revealed that the most clean plasma was obtained in the metallic first wall with the divertor on JT-60. This fact is suggesting the capability of the metallic material for the first wall of next devices. Enhance radiation localized in the peripheral plasma such as marfe and IDC does not degrade the core plasma confinement or somewhat improves it, so that marfe and IDC are suitable operational regime in the high density region for future devices because they have strong remote-radiative-cooling-effect.

Keywords: Radiation Loss, Global Power Balance, JT-60, Impurity, Divertor, Bolometer, First Wall, Heat Load, Marfe

JAERI－M 90－087

JT－60トカマクにおける放射損失の実験的研究

日本原子力研究所那珂研究所臨界プラズマ研究部
西谷　健夫

（1990年5月11日受理）

プラズマの磁場閉じ込めにおいて，中心プラズマにおける不純物の蓄積はそれに伴う放射損失がエネルギー閉じ込めを劣化させるばかりでなく，燃料粒子を希釈するので，核融合炉級のプラズマを得る上で最も重要な問題の一つである。一方，周辺プラズマにおける適度な放射損失は，周辺プラズマの温度を低下させることによって，壁からの不純物流入を減少させる効果が期待できる。JT－60プラズマの放射損失を調べるためにボロメータ測定装置と関連する計測装置（軟X線波高分析測定，軟X線強度分布測定およびバルマーα線測定）の研究開発を行った。

TiC被覆モリブデン壁の場合，リミター放電では，放射損失の全吸収パワーに対する割合は60％以上であるが，外側ダイバータ放電では，約20 MWの中性粒子加熱時にも，主プラズマの放射損失は全吸収パワーの僅か5～10％であった。一方炭素壁の場合は，主プラズマの放射損失が，磁場配位にかかわらず全吸収パワーの20～25％であることが特徴的である。また，下側ダイバータ放電では，電子密度の増加とともにダイバータ部の放射損失が，全吸収パワーの数％から40％まで増大するが，ダイバータ板への熱負荷と主プラズマの放射損失は減少することがわかった。

JT－60では第一壁を炭素に交換してから高電子密度，高プラズマ電流の中性粒子加熱プラズマで頻繁にMARFEが観測されるようになった。MARFEは密度限界近くで発生する。その電子密度の閾値はプラズマ電流にほぼ比例して上昇するが，中性粒子加熱パワーの増加によっても大きくなることを明らかにし，線平均電子密度の閾値のプラズマ電流と中性粒子加熱パワーに対する経験則を得た。MARFEが発生するとプラズマ全体の放射損失は全吸収パワーの90％程度になる。このような高放射損失にもかかわらずプラズマの蓄積エネルギーは減少せず，MARFEが周辺部のみの放射冷却に寄与し，中心プラズマの閉じ込めを劣化させないことを示している。

以上述べたように，JT－60では，TiC被覆モリブデン第一壁によるダイバータ放電により，放射損失が極めて少ないプラズマを達成した。このことは次期装置の第一壁の候補として金属材の可能性を示している。また，MARFEやIDCはダイバータ部を含めた周辺プラズマに局在した放射損失であり，遠隔放射冷却の効果により，中心プラズマの閉じ込め改善が期待できる。これらのモードは定常運転が可能であり，核融合炉の運転モードとして有望であると考えられる。

那珂研究所：〒311－01　茨城県那珂郡那珂町大字向山801－1

Contents

目　　次

1. Introduction

1.1 STATUS OF TOKAMAK FUSION RESEARCH

Thermonuclear fusion has been studied to obtain the ultimate energy resource for the human being. The condition for the achievement of fusion reactor is given as values of $n\tau_e$ and T_i, where n in the plasma density, τ_e is the energy confinement time and T_i is the ion temperature. The condition presented by Lawson is called Lawson criterion [1]. The Lawson criterion shows $n\tau_e$ of ~10^{20} m^{-3} s for DT plasma with T_i of 10 keV.

The studies of the plasma confinement have been carried out by various magnetic confinement systems such as tokamak, stellalator, and mirror, and inertial confinement systems. The excellent characteristics of tokamak was presented by T-3 tokamak at the third International Conference held on Novosibirsk in 1968 [2]. After the conference, the tokamak became the main current of the study in the magnetic confinement. The tokamak experiments with ohmically heated plasma had been performed on ST [3], JFT-2 [4], etc. in the first half of the 1970's. The minimum temperature of 7.5 keV to make fusion work was first obtained in PLT with the neutral beam (NB) heating in 1978, while the requisite minimum confinement quality $n\tau_e > 10^{20}$ m^{-3} s was first reached in Alcator in 1975. The next step was to achieve both high temperature and high confinement quality simultaneously in the same tokamak. The three large tokamaks in the world, TFTR (Tokamak Fusion Test

Reactor) [5] of United States, JET (Joint European Torus) [6] of EC, and JT-60 (JAERI Tokamak-60) [7] of Japan started experiments in the middle of the 1980's aiming to demonstrate the marginal fusion energy breakeven.

The impurity accumulation in the core plasma is a severe problem to obtain the reactor grade plasma not only because the energy confinement degrades by the radiation losses but also because impurities dilute the reacting hydrogen plasma resulting in the reduction of the fusion power density. The major source of the impurity is the first wall which consists of limiter, armor plate, liner and divertor plate. The metallic first wall was popular among the small and medium size tokamaks in early stage. As the additional heating power increased, the radiation loss due to metallic impurities became severe problem. The plasma of 7.5 keV was obtained in PLT with 2.1 MW of NB heating by the replacement of the first wall from tungsten to carbon. Thus almost medium and large tokamaks employed carbon for the first wall. Recently, some tokamaks with high power NB injection are bothered with the burst of carbon named carbon bloom. So the beryllium limiter is tested in JET.

In order to define the plasma boundary, a limiter has been used in many tokamaks. Limiters are classified geometrically into three types, rail limiter, poloidal limiter and toroidal limiter. The rail or poloidal limiters were popular in the early tokamaks. As the additional heating power increased, the toroidal limiter has been employed in order to receive high-power heat load. The limiter touches to the plasma directly, so that it is the major source of the impurity influx into the plasma. Many studies of the material and structure of the limiter have been performed for the impurity control.

A divertor was proposed as the most effective technique for impurity control. The effectiveness of the divertor was indicated experimentally by the pioneer work of DIVA [8] and confirmed by following tokamaks such as D-III [9], ASDEX [10] and PDX [11]. Divertors are classified geometrically into three types, bundle divertor, poloidal divertor and toroidal divertor. Almost divertor used in tokamaks is a poloidal divertor.

The types of the limiter and divertor, and the materials of the limiter and divertor plates of the tokamaks are summarized in Table 1.1. Here a bumper limiter, which is popular in recent large tokamaks, is a large area toroidal limiter which covers inner side of the vacuum vessel.

In 1982, an H-mode discharge, which had no degradation of the energy confinement by NB heating, was found in NB heated divertor discharges on ASDEX [12]. D-III [13] and PDX [14] obtained similar discharges and indicated that the reduction of particle recycling between the first wall and plasma was

very important in creating good H-mode discharges. In TFTR, a high-ion-temperature mode, they called super shot, where the ion temperature reached up to 30 keV, was obtained by degassing of the first wall using helium discharge cleaning [15]. Thus the importance of edge plasma physics has been recognized as an improving effect on core plasma confinement.

Table 1.1 The major parameters and first wall of the tokamaks.

Device	Completion (year)	Major radius (m)	Minor radius (m)	Limiter type	Divertor type	Materials Limiter	Divertor
T-3	1967	1.0	0.15				
ST	1970	1.09	0.14	Poloi./Rail		W(P),Mo(R)	
ORMAK	1971	0.8	0.23	Poloidal		W(P)	
TFR	1973	0.98	0.2	Rail		Inco./C	
JFT-2	1973	0.9	0.25	Poloi./Rail		Mo/SUS/C	
DIVA	1974	0.6	0.1×0.14	Movable	Inner side	Au	Ti
PLT	1975	1.32	0.4	Rail		W/SUS/C	
ISX-B	1978	0.93	0.27	Mushroom		TiC/C	
PDX	1979	1.38	0.38	Rail	4-node pol.	C	
D-III	1979	1.43	0.43×0.65	Blade	Inner side	C	Inco.
ASDEX	1980	1.65	0.4	Poloidal	Upper/Lower	Ti	Ti
TEXTOR	1982	1.75	0.5	Rail		Inco./C	
JFT-2M	1985	1.35	0.35×0.53	Rail	Upper/Lower	C	C
TFTR	1982	2.55	0.83	Bumper		C	
JET	1984	2.96	1.25×2.1	Bumper	Upper/Lower	C	C
JT-60	1985	3.04	1.93	Toroi./Bump.	Out/Lower	TiC Mo/C	TiC Mo/C
DIII-D	1986	2.2	0.67×1.41	Blade	Upper/Lower	C	C

1.2 THEORETICAL BACKGROUND

1.2.1 Radiation Losses

A pure hydrogen plasma emits electromagnetic radiation. Microscopically this is due to the acceleration of the charged particles. Because the electron is much lighter than the ion, electrons radiate much more strongly and only the radiation by electrons need be considered. The electrons are

accelerated in two ways. Firstly they are accelerated by collisions resulting in the radiation called bremsstrahlung. Secondly they subjected to the acceleration of the cyclotron motion and the associated radiation is called cyclotron radiation. In the presence of impurity ions, the bremsstrahlung is enhanced.

The power radiated by an electron undergoing an acceleration is

$$P = \frac{e^2}{6\pi\varepsilon_0 c^3} a^2 . \tag{1.1}$$

The acceleration of an electron during a collision with an ion is caused by the Coulomb force $Ze^2/4\pi\varepsilon_0 r^2$, where r is their separation and Ze is the charge of the ion. Because of the resulting r^{-4} dependence of P, close collisions dominate. There is a cut-off for r at the quantum mechanical distance $d \approx \pi d^2$, and duration of the collision is typically $2d/\bar{v}$, where $\bar{v}$ is an averaged electron velocity. Thus the energy lost per collision, $\Delta E = 2Pd/\bar{v}$, is

$$\Delta E \approx \frac{Z^2 e^6}{6(2\pi\varepsilon_0 cd)^3 / m_e^3 \bar{v}} . \tag{1.2}$$

Since the effective collision frequency is $n_z\sigma\bar{v}$, where n_z is the density of charge Z ions, the bremsstrahlung power for an electron density n_e is $P_{br} \sim n_e n_z \sigma \Delta E$. Taking $(1/2)m_e\bar{v}^2 = (3/2)T_e$ and substituting the numerical factor obtained from a full calculation gives the bremsstrahlung radiation due to ions of charge Z as

$$P_{br} = g \frac{e^6}{6(3/2)^{1/2} \pi^{3/2} \varepsilon_0^3 c^3 h m_e^{3/2}} Z^2 n_e n_z T_e^{1/2} , \tag{1.3}$$

where g is the Gaunt factor [13].

The power radiated from a single non-relativistic electron in the cyclotron motion is given by Eq. (1.1) with the acceleration $a = \omega_{ce}^2 \rho_e$. By putting $\rho_e = (2T_e/m_e)^{1/2}/\omega_{ce}$ and $\omega_{ce} = eB/m_e$, the power density of cyclotron radiation is obtained as

$$P_c = (e^4/3\pi\varepsilon_0 m_e^3 c^3) B^2 n_e T_e . \tag{1.4}$$

This power is very large and estimated to be ~1MWm^{-3} in the reactor class plasma. However, this is not the power loss from the plasma because the plasma is optically thick to the radiation at the fundamental frequency. The power in each harmonics falls rapidly with increasing harmonic number, so that the cyclotron radiation is not significant in the power balance of the plasma [16].

The presence of impurity ions in the plasma produces energy losses through two types of radiation. The first is the enhancement of bremsstrahlung because of the higher value of the ionic charge for impurities. The second is the radiation through the atomic processes of line radiation and recombination. The power radiated from a given impurity species is proportional to the electron density n_e and the impurity density, and the radiated power density is given by

$$P_{rad} = n_e n_I L , \tag{1.5}$$

where L is the radiative cooling rate which is a function of electron temperature [17]. The L for light impurities has a maximum value around 10 eV and above the temperature the radiation is substantially reduced. As the temperature is increased, electrons are successively removed from the impurity ions. The ions of the light impurities such as carbon and oxygen are fully stripped at a temperature higher than 1 keV, so that these radiation losses are negligible in the hot core plasma. However, these are important in the edge plasma where the light impurities are stripped incompletely. For temperatures above 100 eV the radiation per ion of high Z impurities is much greater than for low Z impurities. The high Z impurities are not fully stripped in the core plasma, even in the reactor class plasma, so that these radiation losses are dominant in the core plasma.

1.2.2 Global Power Balance

A schematic of the energy flow for the tokamak plasma is shown in Fig. 1.1 [18]. The ohmic input power goes mainly to the electrons in the hot plasma core. The electron energy is lost from the core by collisional equilibration with the ions, by line radiation of high Z impurity, bremsstrahlung and cyclotron radiation, and by transport to the plasma edge in the form of particle outflow and heat conduction. At the plasma edge, particle outflow along field lines carries part of input power to the limiter or divertor plates.

The portion of the ohmic input power that flows from the electrons to the ions in the plasma core is lost again by direct charge exchange and by transport in the form of particle flow and heat conduction to the plasma edge. In the outer plasma region, the heat flow from the electrons to the ions may reverse, depending on the relative temperature profiles of the electrons and ions. When auxiliary heating such as NB is added, overall pattern is similar, except that ion temperature T_i may rise above T_e, so that the heat flow from electrons to ions is reversed there.

1.3 PURPOSE OF THIS THESIS

JT-60 is a unique device having a closed divertor chamber among the three large tokamaks, JET, TFTR and JT-60. JT-60 has three magnetic configurations (outer X-point divertor, lower X-point divert and limiter), two types first wall (TiC coated molybdenum and carbon graphite), and high power auxiliary heating and long discharge duration. Therefore, JT-60 is suitable to investigate the radiation losses and impurity control. This thesis work is focused on the following subjects:

(1) Developments of radiation-loss-measurement systems for JT-60

In order to investigate the radiation losses of the JT-60 plasmas, bolometric measurement system and associated diagnostics, soft x-ray pulse-height-analyzer, soft x-ray intensity and Balmer line measurement systems, were developed. The bolometric measurement is the most important diagnostics in the radiation loss study. The soft x-ray pulse-height-analyzer is useful to estimate the metal impurity concentration, and the soft x-ray intensity and Balmer line measurements are monitors of radiation in x-ray region and particle recycling in the plasma edge, respectively.

(2) Investigation of the radiation losses and global power balance

From the view point of the impurity control, the radiation losses and global power balance of the plasma with three types of magnetic configurations and two types of first wall were investigated consistently in one device aiming to provide the database for the design of the next device such as ITER.

(3) Investigation of the enhanced radiation in the peripheral plasma

Appropriate radiation losses localized in the peripheral plasma are sometimes favorable to reduce the heat load onto the first wall and influx of impurities from the wall by cooling edge plasma namely remote radiative cooling. As the the enhanced radiation in the peripheral plasma, the marfe (multifaceted radiation from the edge) and the IDC (improved divertor confinement) which was found in JT-60 for the first time and their effects on the core plasma confinements were investigated. And the usefulness of the enhanced radiation in the peripheral plasma for the operation of the reactor class tokamak is discussed.

Chapter 2 presents the overviews of JT-60 machine and the diagnostics. Development of the bolometric measurement system which is a major diagnostic in radiation loss study is described in Chapter 3. Chapter 4 presents the soft x-ray pulse-height-analyzer and its experimental results about the electron temperature, the metal impurity concentration, and the effective ionic charge Z_{eff}. Chapter 5 presents the soft x-ray intensity and Balmer α line measurement systems and their principal experimental-results. The global power balance of ohmic and NB heated plasmas are discussed in Chapter 6. Characteristics of marfe and IDC phenomena are described in Chapter 7. Summary and conclusion are presented in the final Chapter 8.

REFERENCES TO CHAPTER 1

[1] J.D. Lawson, Proc. Phys. Soc., London, **B70** (1957) 6.

[2] L.A. Artimovich, G.A. Bobrovsky, E.P. Gorbunov, D.P. Ivanov, V.D. Kirilov, et al., in Plasma Physics and Controlled Nuclear Fusion Research (*Proc. 3rd Int. Conf. Novosibirsk, 1968*). Nucl. Fusion Special Suppl. 1969, p17.

[3] D.J. Grove, D.L. Dimock, E. Hinnov, J.C. Hosea, L.C. Johnson, et al., in European Conf. on Controlled Fusion and plasma Physics, Rome (1970). Princeton Plasma Physics Larolatory MATT-813 (1970).

[4] S. Itoh, et al., in Toroidal Plasma Confinement (*Proc. 3rd Int. Symp. Garching, March 1973*) B-4.

[5] K.M. Young et al., Plasma Phys. Controll. Fusion **26** (1984) 11.

[6] P.H. Rebut et al., Plasma Phys. Controll. Fusion **26** (1984) 1.

[7] JT-60 Team (presented by M. Yoshikawa), Plasma Phys. Controll. Fusion **28** (1986) 165.

[8] DIVA Group, Nucl. Fusion **18** (1978) 1619.

[9] M. Nagami, N. Fujisawa, K. Itoki, A. Kitsunezaki, et al., in Plasma Physics and Controlled Nuclear Fusion Research (*Proc. 8th Int. Conf. Brussel, 1980*) Vol. 2, IAEA, Vienna (1981) 367.

[10] M. Keilhacker, et al., in Plasma Physics and Controlled Nuclear Fusion Research (*Proc. 8th Int. Conf. Brussel, 1980*) Vol. 2, IAEA, Vienna (1981) 351.

[11] R.J. Fonk, M. Bell, K. Bol, K. Brau, R. Budny, et al., J. Nucl. Mater. **111&112** (1982) 343.

[12] F. Wagner, G. Becker, K. Behringer, D. Campbell, A. Eberhargen, et al, Phys. Rev. Lett. **42** (1982) 1408.

[13] M. Nagami, M. Kasai, A. Kitsunezaki, T. Kobayashi, S. Konoshima, et al., Nucl. Fusion **24** (1984) 415.

[14] S.M. Kaye, M.H. Bell, D. Boyd, K. Brau, D. Buchenauer, et al., J. Nucl. Mater. **121** (1984) 115.

[15] R.J. Goldston, V. Arunasalam, M.G. Bell, M. Bitter, W.R. Blanchard, et al., in Plasma Physics and Controlled Nuclear Fusion Research (*Proc. 11th Int. Conf. Kyoto, 1986*) Vol. 1, IAEA, Vienna (1987) 75.

[16] J. Wesson, *Tokamak* (Clendon Press, Oxford, 1987) p100.

[17] P.E. Post, R.V. Jensen, C.B. Tarter, W.H. Grasbarger and W.A. Lokke, Atomic Data and Nucl. Data Tables **20** (1977) 397.

[18] E. Teller, *Fusion* (Academinc Press, New York, 1981) Vol.1, p185.

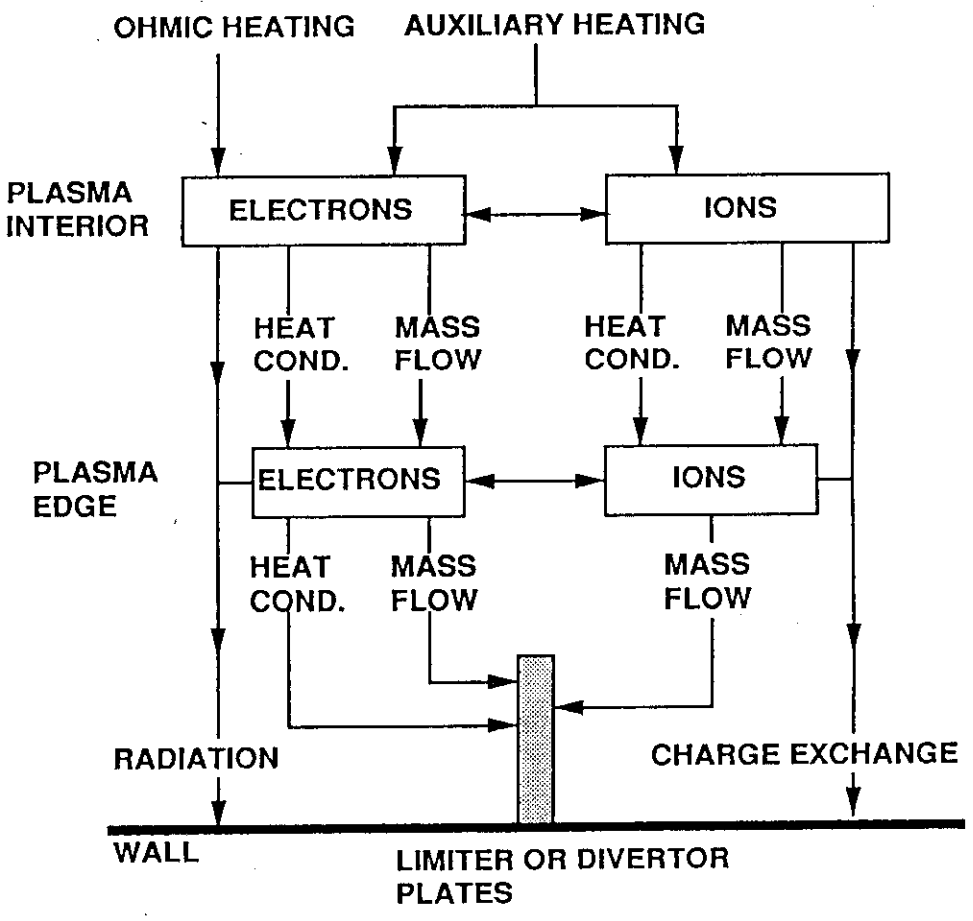

Fig. 1.1 Schematic power-flow diagram for the tokamak plasma.

2. Overviews of JT-60 and its Diagnostics

2.1 JT-60 MACHINE

JT-60 is a large tokamak fusion experimental device aiming at achieving a break-even plasma condition. JT-60 has various features to study physical and technological aspects of reactor-grade plasma. JT-60 has a long discharge duration of 10 seconds, a poloidal divertor for impurity control and confinement improvement, NB and RF heating with high power and long pulse duration, RF current drive and real time plasma control. JT-60 started experiments in April 1985. Figure 2.1 shows a bird's-eye view of JT-60, which is composed of a vacuum vessel, toroidal field coils, poloidal field coils, mechanical support structures, NB injectors, RF heating systems, many diagnostics and other components. Major parameters of JT-60 are listed in Table 2.1. Detailed technical descriptions of JT-60 are provided in Refs. [1-3].

Original feature of JT-60 is a large tokamak device with a plasma of circular cross-section and a poloidal divertor outside the torus. The poloidal cross-section of the original JT-60 are shown in Fig. 2.2. The vacuum vessel is composed of eight rigid sectors and eight parallel bellows welded together. Those materials are Inconel 625 alloy. The toroidal limiters, divertor plates, inboard armour plates, and the protective plates of the divertor coils were made of molybdenum coated with TiC of 20 μm thickness originally. Protective plates elsewhere are made of Inconel 625 coated with TiC of the same thickness.

Table 2.1 Major parameters of JT-60.

Major radius	3.0 mm
Minor radius	0.95 mm
Aspect ratio	3.16
Toroidal field	4.5 T
Plasma current	2.7 MA
Duration time	10 sec

Figure 2.3 shows the arrangements of the NB injectors and RF heating systems on JT-60. NB injectors consist of 8 co-injection units and 6 countor-injection units. Two injection units are mounted in one tower at top and bottom of it. The injection angle is 75° against the tangential direction of the torus. The NB injection system has been operated regularly with a injection power of about 20 MW at a hydrogen beam energy of 75 keV. The RF heating system consists of two schemes: three units of the LHRF system operated in a frequency range of 1.7-2.2 GHz and one unit of the ICRF system in a frequency range of 110-130 MHz. The frequency of the ICRF system corresponds to the second harmonics of the hydrogen ion cyclotron frequency in a toroidal magnetic field of about 4.5 T.

All TiC coated molybdenum limiters and divertor plates were replaced by the graphite tiles in May 1987. The surface area of the graphite wall corresponds to half the vacuum vessel area. The vacuum vessel is usually operated with wall temperature of 200-300°C after the replacement.

It was difficult to obtain a good H-mode in the configuration of outer X-point divertor. A new divertor coil was installed under the vacuum vessel to provide a lower X-point configuration in January 1988 [6]. Three configurations, i.e. limiter, outer X-point divertor and lower X-point divertor are provided on JT-60 as shown in Fig. 2.4.

Gas fueling is performed by gas puffing usually. A pneumatic pellet injector was installed in early 1988. This injector produced four hydrogen pellets with a velocity up to 2.3 km/s and with cylindrical sizes of 2.7 mm (diameter) × 2.7 mm (length) to 4.0 mm (diameter) × 4.0 mm (length).

Achieved and design parameters of JT-60 are summarized in Table 2.2.

Table 2.2 Achieved and design parameters of JT-60.

Parameter	Design	Achieved
Plasma current		
Limiter	2.7 MA	3.2 MA
Outer divertor	2.1 MA	2.7 MA
Lower divertor	2.2 MA	2.0 MA
Toroidal field (at R = 3 m)	4.5 T	4.8 T
Heating power (into torus)		
NBI	20 MW	25 MW
LHRF	15 MW	11 MW
ICRF	5 MW	3.1 MW
Wall material	TiC-Mo	TiC-Mo (before March 1987) Graphite (after June 1987)

2.2 JT-60 DIAGNOSTICS

In the large tokamak like JT-60, the diagnostics become more important not only for understanding the plasma characteristics but also for operating the machine safely. Each diagnostics is required to obtain the useful data with high resolution in time and space simultaneously and also to process the data quickly within few milliseconds in the on-line feedback loop and within few minutes (less than 10 minutes) in the shot-by-shot feedback loop.

JT-60 has 23 different kinds of diagnostics to measure the fundamental parameters of the plasma and three different ways to process the data in the computer system. Figure 2.5 shows a bird's-eye view of the JT-60 diagnostics [4]. In this Section, major diagnostics are described.

2.2.1 Electron Density Measuring System

The electron density is measured with the newly developed multi-channel CW118.8-μm CH_3OH laser/2-mm wave polari-interferometer. The FIR system employs 2 MHz beat-modulated twin CH_3OH lasers [5,6] with Michelson configuration providing 3 chords (R = 2.53, 3.04, and 3.55 m) in the

main plasma region and 2 chords in the divertor region [7]. 2-mm wave interferometer provides 2 chords at R = 2.19 and 3.25 m. The diagnostic chords are summarized in Fig. 2.6. After modification for lower X-point divertor, FIR interferometer at plasma center (R = 3.04 m) is not available owing to the new divertor coil.

2.2.2 Electron Temperature Measuring System

Two different kinds of diagnostics are used for the electron temperature measurement in JT-60. One is based on the electron cyclotron emission (ECE) and the other on Thomson scattering of multiples lasers (Fig.2.7).

(1) ECE measurement [8]

Three observing ports are dedicated to ECE system with the different angle of 7, 45 and 75 degrees to the horizontal plane, respectively. Presently the Michelson interferometer is installed at the diagnostic platform where it is possible to observe the plasma almost vertically using the 75 degree port. The rapid-scan Michelson interferometer measures the ECE in frequency range of 100-800 GHz with the resolution of ~3.5 GHz every 15 ms. The detector is a liquid-He cooled InSb detector. The system is calibrated using the liquid N_2 black-body source and a tunable microwave source with the known power.

(2) Thomson scattering system [9]

The electron temperature and density at six positions inside the JT-60 plasma are simultaneously measured by the Thomson scattering system with spatial resolution of ~10 cm. The light source is a ruby laser which can be operated by four different modes; (a) a single pulse with the energy of 20 J, (b) 10 J output at 0.25 Hz, (c) 5 J output at 0.5 Hz and (d) 2.5 J output at 1 Hz. A YAG laser with 1 J output at 100 Hz is also provided for the future extension improving the time resolution (10 ms) of the electron temperature and density measurement. The lasers locate at the peripheral room and the laser beam travels to JT-60 through the transmission pipe for 50 m buried in the floor. A Littrow type spectrometer is used to analyze the wave length of the scattered light into the 8 channels for each position. 48 photomultiplier-tubes (PMT) are used to detect the light and the optical fibers are used to connect between the spectrometer and the PMT.

The electron temperature profiles measured by the ECE system and the Thomson scattering system are examined each other and also cross-checked with one obtained from the soft X-ray spectrometer. The electron density profile is checked with the integrated density obtained by the interferometer.

2.2.3 Ion Temperature Measuring System

This system consists of charge-exchanged (CX) neutral-particle-mass energy analyzer, active beam scattering apparatus, and CX neutral-particle-energy analyzer array for space resolved measurement.

(1) CX neutral-particle-mass-energy analyzer [10,11].

Energetic neutral particles are produced by charge exchange reaction between plasma ions and neutral atoms in plasma and by recombination of plasma ions and electrons. These particles convey information of energy distribution for the ions, so that it is possible to infer ion temperature from measurements made on the energetic charge exchanged neutral atoms escaping from the plasma. The charge exchange diagnostics in JT-60 required the separation of three kinds of particles (H, D, He) over a wide range of energy, since energy distribution for each ion component is usually not identical. The E//B charge-exchanged-neutral-particle analyzer measures mass and energy distributions simultaneously, using parallel electric and magnetic fields. The basic principle of the analyzer is showed in Fig. 2.8. The analyzer consists of a stripping cell, a 180 degree deflection magnet and a set of electrostatic deflection plates. After the charge exchanged neutrals are ionized again in the gas cell filled with H_2 stripping gas, the ions enter perpendicularly into the magnetic field. The electric field is applied after the ions emerge from the magnetic field. Micro-channel plates, MCP, are used to detect the ions. The MCP has 32 channels of charge collector. These arrangements lead to a simple and compact analyzer.

(2) Active Beam Scattering Method [12-14].

The small angle neutral particle scattering method is provided in JT-60 for the ion temperature measurement in the central plasma region. The principle of the method is based on the energy broadening analysis of neutral particles, which is injected into plasma and scattered by plasma ions. A schematic of the system is shown in Fig. 2.9. According to the figure, the system consists of two main components. One is a diagnostic neutral beam source and the other is a scattered particle analyzer. Helium ions with 200 keV energy, 3.5 A current and 0.1 s duration are converted to helium neutral atoms by the charge exchange neutralizer, and a 0.6 A neutral helium beam is injected into the plasma. The neutral atoms, after being scattered through a small angle by collisions with plasma ions, enter the particle analyzer. The analyzer, 7° tilted against the injected beam line, is composed of a stripping

cell, an analyzing magnet with high momentum resolution, ion detectors and pulse counting electronics connected to the detectors.

(3) Spatial-Resolved Neutral-Particle Analyzer [15]

The multi-channel neutral particle energy analyzer consists of several identical electrostatic energy analyzers, covering a wide energy range of 0.2 through 110 keV with 2% resolution. It was installed in an oblique access port (IN2 port), viewing the different parts in a cross-sectional area of plasma (Fig. 2.10). A spatially resolved neutral particle energy spectrum can be obtained by this system.

2.2.4 Impurity Measuring System

Purposes of this system are to diagnose the behavior of impurity ions and to determine the plasma parameters (for example ion temperature) of the JT-60 plasma. This system has six spectrometers. The wavelength region of this system is from X-ray to visible region (0.15-700 nm). The spectrometers has been installed and operated.

In JT-60, it is required that spatial and time behaviors of many impurity lines are to be measured in one discharge. For that reason, a small-sized unit-type-grazing-incidence spectrometer was developed [16,17]. In this spectrometer, spectral lines are imaged on the flat plane, where the array detector is placed, by the holographic grating. The unit-type-grazing-incidence spectrometer and the set up view of the apparatus are shown in Fig. 2.11. This apparatus has two unit-type spectrometers. The specification of one unit is that the wavelength region is from 0.5 nm to 5 nm and the resolving power $\lambda/\Delta\lambda$ is 90 to 210 with 512-channel array detector. The other is that the wavelength region is from 0.5 nm to 50 nm and the resolving power $\lambda/\Delta\lambda$ is 10 to 363 with 1024-channel array detector. The 34 unit-type spectrometers can be installed in this apparatus. The spatial and time behaviors of many impurity lines can be measured by this apparatus simultaneously.

The Rowland-mount-type 3-m-grazing-incidence spectrometer and 1-m-Czerny-Terner-type visible spectrometer were installed at the same toroidal location above and below of JT-60.

The ion temperature is measured by the Doppler broadening of impurity lines. The ion temperatures at the middle and peripheral region of the JT-60 plasma are measured by Doppler broadening of forbidden lines with the 1.2-m-normal-incidence vacuum spectrometer. The specification of this spectrometer is that the wavelength region is mechanically from 0th order

light to 900 nm and the resolving power $\lambda/\Delta\lambda$ is about 20000 with 32-channel (channel pitch is 100 μm) array detector.

The ion temperature at the central region of the JT-60 plasma is measured by Doppler broadenings of heavy-impurity resonance-lines with the Johan-type crystal spectrometer [18]. This spectrometer has two crystals. One is SiO_2 for resonance line of nickel and the other is Si for titanium. The resolving powers of this spectrometer $\lambda/\Delta\lambda$ are respectively 15000 and 7000 with 32ch (channel pitch is 100 μm) array detector.

The impurity behavior in the neighborhood of the outer divertor is measured by the spectrometer using two unity-type grazing-incidence spectrometers.

Recently charge exchange recombination spectroscopy (CXRS) has been regarded as a powerful technique for tokamak plasmas to measure the radial profile of the ion temperature, toroidal rotation speed and light impurity densities. In JT-60 multichordal CXRS system was installed in March 1988 [18]. The CXR emissions in the beam line of NB are measured with 40 fiber optics bandle.

2.2.5 Radiation loss measuring system

The radiation losses are measured by four different types of instruments; the bolometer array, the soft x-ray pulse height analyzer, the soft x-ray intensity and Balmer α line measurement systems.

(1) Bolometer array system

The bolometer array system measures the total radiation flux from the plasma in order to investigate the energy balance of the plasma. This measurement system is described in Chapter 3.

(2) Soft x-ray pulse height analyzer

Soft x-ray pulse height analyzer (PHA) measures the soft X-ray spectra in the energy range of 3-60 keV with the high purity germanium detector. This measurement system is described in Chapter 4.

(3) Soft x-ray intensity measurement system

The soft X-ray intensities emitted from the plasma are measured by the PIN diode array. This measurement system is described in Chapter 5.

(4) Balmer α line measurement system

Balmer α line (Hα) emissions from the main and divertor plasmas are measured by photodiodes with Hα band-pass filters to investigate the particle balance. This measurement system is described in Chapter 5.

2.2.6 Peripheral Plasma and Wall Surface Measuring System

The peripheral plasma and the wall condition are observed by an infrared TV, a visible TV and a mirror-scanning spectrometer.

(1) Infrared TV system [19]

In several points of view, to monitor the temperature of divertor plates and the Hα emission at the divertor plates is equivalent to monitor the edge plasma. Since divertor plates are made of graphite, sputtering of carbon from the surface can cause a contamination of plasma. A sputtering yield is a function of temperature of the material. Thus measuring the temperature of the plate may be a good measure how much carbon is released. At the disruption large energy is released in a short period of time (several milliseconds). From the engineering points of view, it is important to know how the energy of the plasma is released to the divertor plate during the disruption. From physics points of view, heat flux to the divertor plate and the Hα emission at the divertor plates has a strong correlations to the confinement of the plasma and the recycling at the divertor plate.

A new divertor monitoring system was developed for lower-X point discharges. The system consists of an infrared TV camera, visible TV camera and the data acquisition system. Figure 2.12 shows schematic view of IR TV and Hα TV camera system. The half mirror is made of Si with anti-reflection coating for infrared. This half mirror behaves as a mirror for visible but as a transparency for infrared. Both IR TV camera and Hα camera have the identical field of view. It is limited by the port of the vacuum vessel and 51 cm × 10 cm at the divertor plate.

The calibration of IR camera system is carried out to obtain the attenuation factor of infrared by the half mirror and the vacuum window for the temperature range from 100°C to 1000°C. The attenuation factor of infrared by the half mirror and the vacuum window is 65% at 300°C and 75% at 800°C. The viewing fields of IR TVand Hα TV cameras are carefully measured at the setting up of this system. The sight of the line scan is set 3.5 cm from the side the divertor tile to prevent from seeing the enhance heat flux at the edge of the tile.

(2) Plasma TV [20]

The on-line TVs observes vertically and tangentially the visible light from the plasma using a TV camera. The viewing fields of those TVs are shown in Fig. 2.13. In the tangential TV, the plasma light is guided outside the vacuum vessel through a reflection mirror and three relay-lens. The support structure of the optics is composed of the ceramics, so called Macor, because of the reduction of the eddy-current effect in the toroidal field. The spatial resolution is about 10 mm at the plasma.

(3) Mirror-scanning spectrometer [21]

Mirror-scanning spectrometer is composed of two spectrometers; visible and ultraviolet spectrometers. The former measures the light having the wavelength of 400 nm ~ 700 nm, and the latter 200 nm ~ 400 nm. This system is mainly used for the measurement of the hydrogen and light impurity line radiation, and the bremsstrahlung radiation. The viewing chords of the mirror-scanning spectrometer is shown in Fig. 2.14.

2.2.7 Data Processing System

Data Processing System controls the diagnostics and collects data from the diagnostics, processes and stores the data [22,23]. The 50 million words of data (2 Bytes/word) are obtained by the diagnostics for one discharge, and some data are processed immediately and presented in the control room for the operators preparing next discharge. The major part of data are stored in the mass data recorder (MDR) which has the recording capability of 30 input channels, 4 Mbit per second for each channel simultaneously. Figure 2.15 shows the flow of the diagnostics data per shot. Inter shot processor (ISP) has one set of large computers to store and process data so that the sophisticated analysis is rapidly performed using a large amount of the stored data. The CAMAC standard [24] is used for the interface between the data processing system and the diagnostics. The CAMAC crates near the JT-60 machine are installed in an shield box which can reduce the electromagnetic noise by 60 dB. The components which are especially weak against the magnetic field are protected by placing in an iron box to avoid any malfunction.

(1) CAMAC system

CAMAC system makes not only an interface between each diagnostic apparatus and the large host computer, but also an interface between human operator and the apparatus.

The CAMAC system has following three major functions; (a) Control diagnostic apparatus under the ZENKEI, which is the control system of JT-60, operation sequence. (b) Collect diagnostics data and preprocess some of them using a microcomputer. (c) Transfer obtained the data to the host computer.

The CAMAC system consists of 23 diagnostic systems, and each system has two types of crates; one is the higher level crate which locates in the diagnostic room containing a microcomputer module, and the other is the lower level crate which is located in the torus hall containing modules for many purposes, for instance, A/D converter, I/O switch, transient memories, etc.

These two types of crates are connected by optical serial highways to prevent electromagnetic noise interferences, and to realize the high speed data transmission. The newly developed optical transit module BUAO (Byte serial Undefined port Adaptor with Optical) [25] has a function to regulate the accumulation of pulse jittering, and has the capability of 5 MB/sec data transfer by single optical fiber.

(2) Inter-shot processor

One of the main parts in the data processing system is the inter-shot processor system (ISP), which processes diagnostic data within the time interval between the discharges (shot interval).

The functions of this system are as follows; (a) Information exchange between ZENKEI and diagnostic systems for discharge sequence to get ready diagnostic systems toward the discharge. (b) Supplying the software and hardware environment for the analysis of collected data. (c) Supervise the diagnostics and monitor their status. Management of job schedule including synchronous/asynchronous job with discharge sequence.

The ISP system consists of a general purpose computer of FACOM M-360 dual processor. This system has dual CPU with 24 MB main memory and installs 24 disk-enclosures of 446 MB, 10.7 GB in total. The ISP system has many I/O devices and external storage unit, and those devices are connected individually to each CPU in order to ensure high reliability and quick I/O response.

A software in this system is classified into two categories, one is a basic software of general purpose computer and the other is an application use of a basic software. ISP has an special application software which is necessary not only to control diagnostic data acquisition under the discharge sequence, but also to manage the collected data.

(3) Real-time processor

The real-time processor (RTP) system has a role to supply the ZENKEI control computer with realtime feedback data got from diagnostic systems.

(4) Mass data recorder

In order to memorize the data amounting up to 100 MB/shot, which are created from a 10 second discharge, the MDR system has been developed using a high speed PCM tape recorder. MDR is a 30 track tape recorder, and has the capability to memorize 4 Mb/s data flow for each track. The storage capacity of one pack of the tape is 78 shots with 10 seconds duration, which amounts to 4.9 G Words.

REFERENCES TO CHAPTER 2

[1] JT-60 Team (presented by M. Yoshikawa), Plasma Phys. Controll. Fusion **28** (1986) 165.

[2] JT-60 Team (presented by S. Tamura), Plasma Phys. Controll. Fusion **28** (1986) 1377.

[3] JT-60 Team (presented by H. Kishimoto), J. Nucl. Mater. **145-147** (1987) 41.

[4] H.Yokomizo, H. Takeuchi, T. Sugie, N. Ogiwara, M. Sato, A. Nagashima, K. Ohasa, Y. Nakamura, T. Nishitani, Y. Neyatani, A. Sakasai, T. Fukuda, H. Kubo, K. Tobita, Y. Yamashita, M. Nemoto, S. Iida, K. Nagashima, Y. Uramoto, O. Yamashita, T. Tsugita, M. Shitomi, Y. Tsukahara, T. Ohshima, K. Yamagishi, S. Tahira, S. Konoshima, M. Shiho, H. Maeda and Y. Suzuki, Fusion Eng. Des. **5** (198) 117.

[5] T. Fukuda, A. Nagashima, S. Ishida, K. Haraguchi and T. Takahashi, Kakuyugo Kenkyu **59** Suppl. (1987) 16.

[6] T. Fukuda and A. Nagashima, Rev. Sci. Instrum. **60** (1989) 1080.

[7] T. Fukuda, H. Yoshida, A. Nagashima, S. Ishida, M. Kikuchi, H. Yokomizo and JT-60 Team, J. Nucl. Mater. **162-1164** (1989) 258.

[8] M. Sato, H. Yokomizo and A. Nagashima, Kakuyugo Kenkyu **59** Suppl. (1987) 47.

[9] H. Yokomizo, H. Yoshida, M. Sato and A. Nagashima, Kakuyugo Kenkyu **59** Suppl. (1987) 72.

[10] K. Hayashi, K. Hashimoto, H. Yamato, H. Takeuchi, Y. Miura, T. Nishitani, M. Shiho and H. Maeda, Rev. Sci. Instrum. **56** (1985) 359.

[11] Y. Kusama, K. Tobita, M. Nemoto and H. Takeuchi, Kakuyugo Kenkyu **59** Suppl. (1987) 119.

[12] H. Takeuchi, T. Matsuda, T. Nishitani, M. Shiho, C. Konagai, H. Kimura and H. Maeda, Jpn. J. Appl. Phys. **11** (1983) 1717.

[13] H. Takeuchi, K. Tobita, Y. Kusama, M. Nemoto, T. Itoh, Y. Tsukahara and JT-60 Team, Rev. Sci. Instrum. **59** (1988) 1652.

[14] K. Tobita, Y. Kusama, M. Nemoto, H. Takeuchi, T. Itoh, Y. Tsukahara, M. Shitomi, K. Watanabe and Y. Ohara, Kakuyugo Kenkyu **59** Suppl. (1987) 139.

[15] M. Nemoto, K. Tobita, Y. Kusama and H. Takeuchi, Kakuyugo Kenkyu **59** Suppl. (1987) 91.

[16] H. Kubo, T. Sugie, A. Sakasai, Y. Koide, N. Nishino, H. Yokomizo, H. Takeuchi and JT-60 Team, Rev. Sci. Instrum. **59** (1988) 1515.

[17] T. Sugie, H. Kubo, A. Sakasai, Y. Koide, N. Nishino, N. Akaoka and H. Takeuchi, Kakuyugo Kenkyu **59** Suppl. (1987) 157.

[18] A. Sakasai, Y. Koide, H. Kubo, T. Sugie, N. Akaoka, N. Nishino and H. Takeuchi, Kakuyugo Kenkyu **59** Suppl. (1987) 169.

[19] K. Itami, et al., to be submitted to J. Nucl. Mater.

[20] Y. Neyatani, K. Itami, Y. Yamashita, N. Ogiwara and H. Yokomizo, Kakuyugo Kenkyu **59** Suppl. (1987) 255.

[21] Y. Yamashita, Y. Neyatani, N. Ogiwara, Y. Yoshinari and H. Yokomizo, Kakuyugo Kenkyu **59** Suppl. (1987) 289.

[22] A. Ogata, R. Toyokawa, T. Nishitani, T. Kumahara, S. Tahira, T. Kambe, O. Mochizuki, N. Tahara, A. Fujioka and M. Fujita, in 9th Sym. Eng. Problems Fusion Research, Chicago, 1981.

[23] A. Nagashima, T. Tsugita, T. Aoyagi, S. Iida, T. Ohshima, S. Kakizaki and K. Ohasa, Kakuyugo Kenkyu **59** Suppl. (1987) 289.

[24] IEEE, Standard Serial Highway Interface System (CAMAC), 1976.

[25] T. Nishitani, K. Ohasa, K. Tsukada and Y. Ohgushi, J. Lightwave. Technol. **LT-3** (1985) 1717.

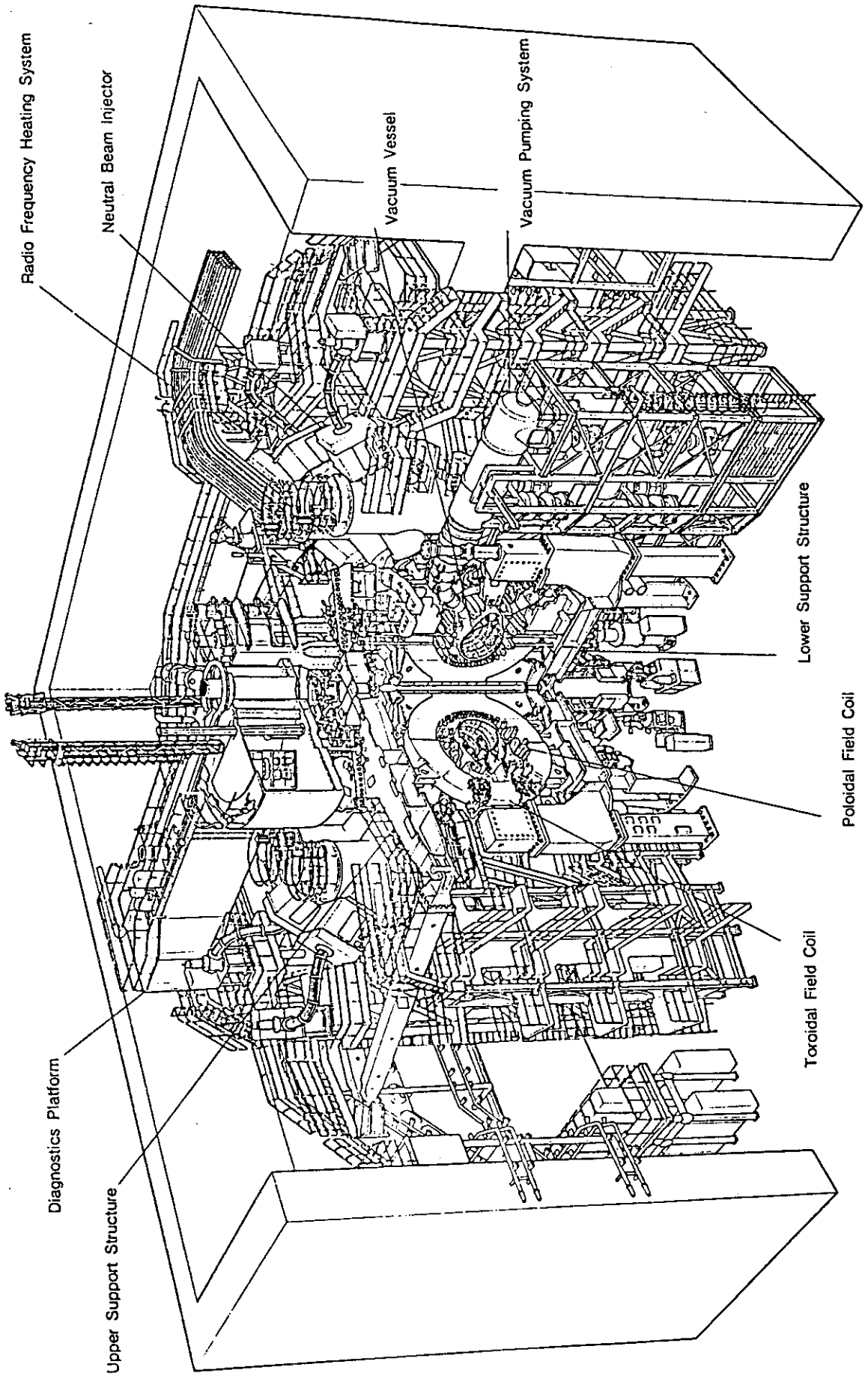

Fig. 2.1 Bird's-eye view of JT-60.

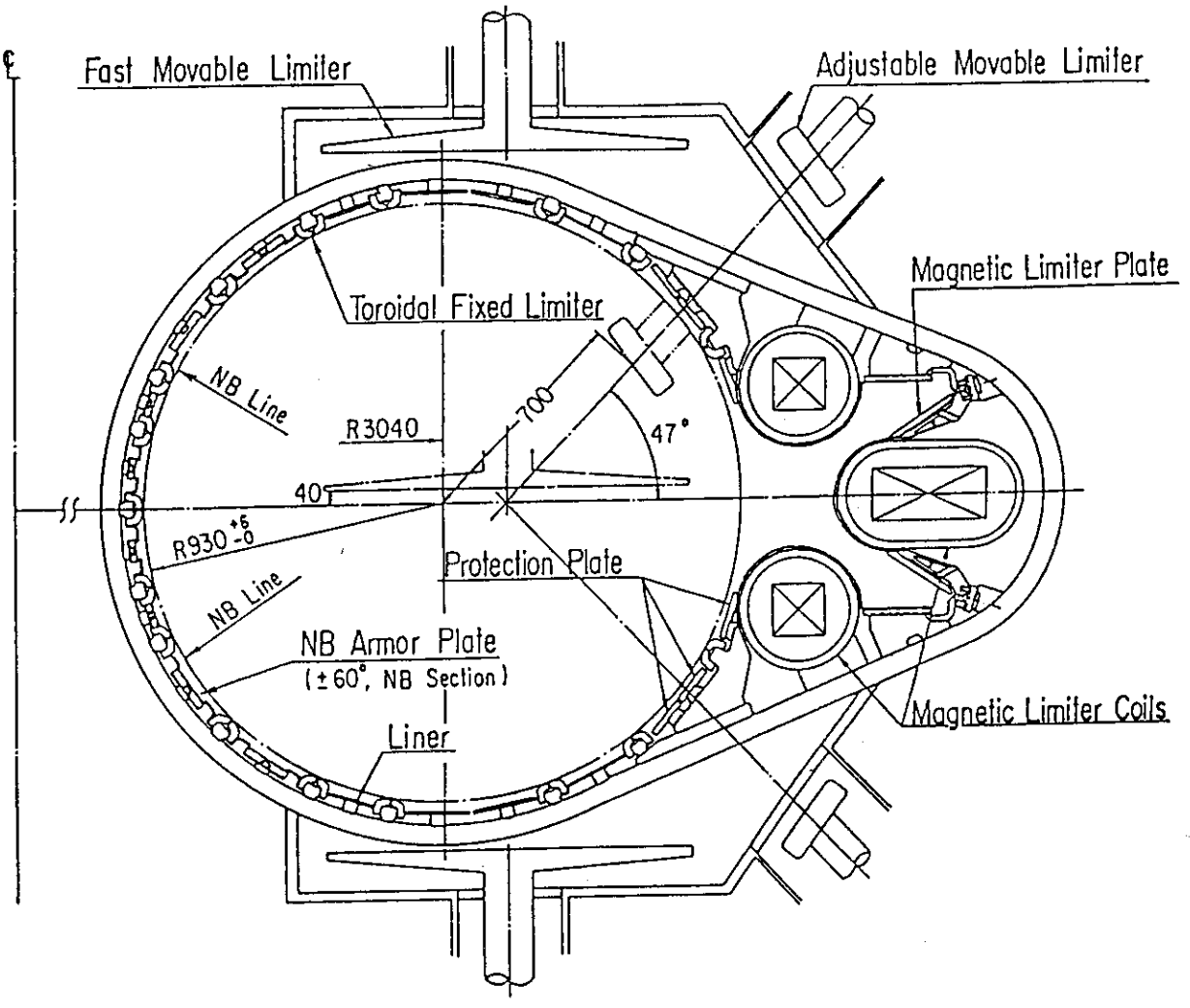

Fig. 2.2 Poloidal cross-sectional view of the original vacuum vessel.

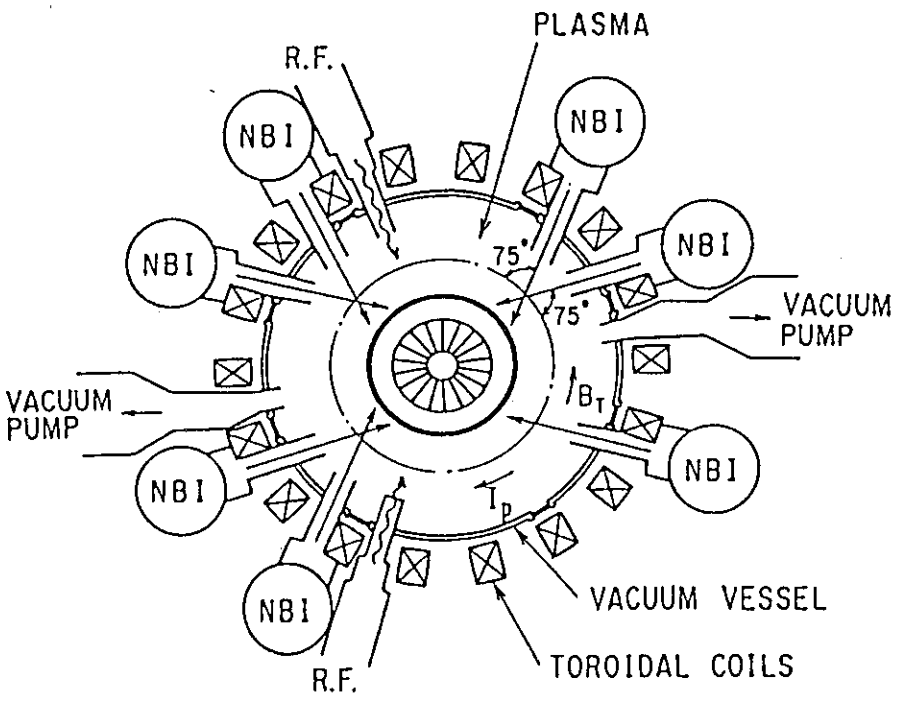

Fig. 2.3 Arrangements of the NB injectors and RF heating systems on JT-60.

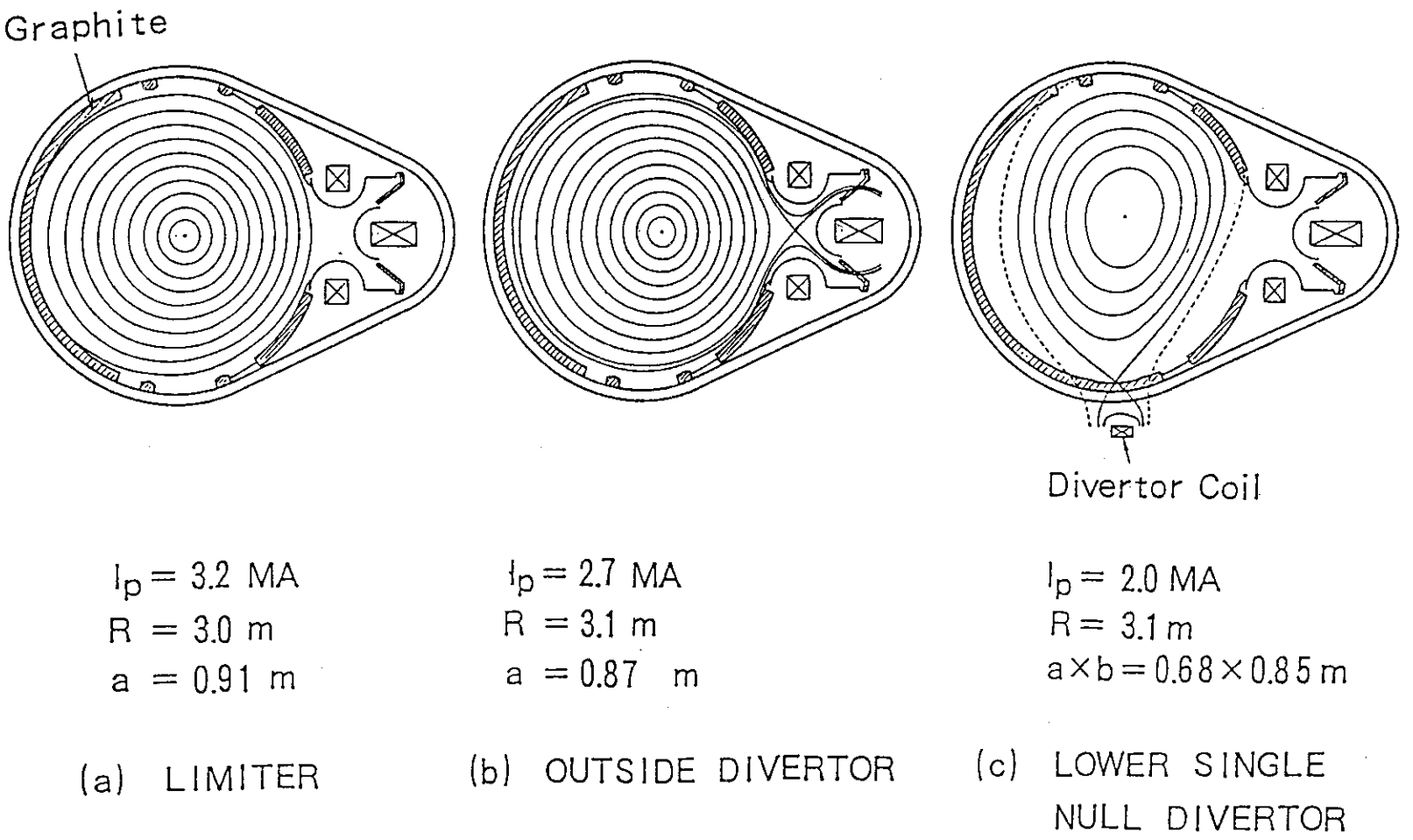

Fig. 2.4 Typical magnetic configurations of JT-60.

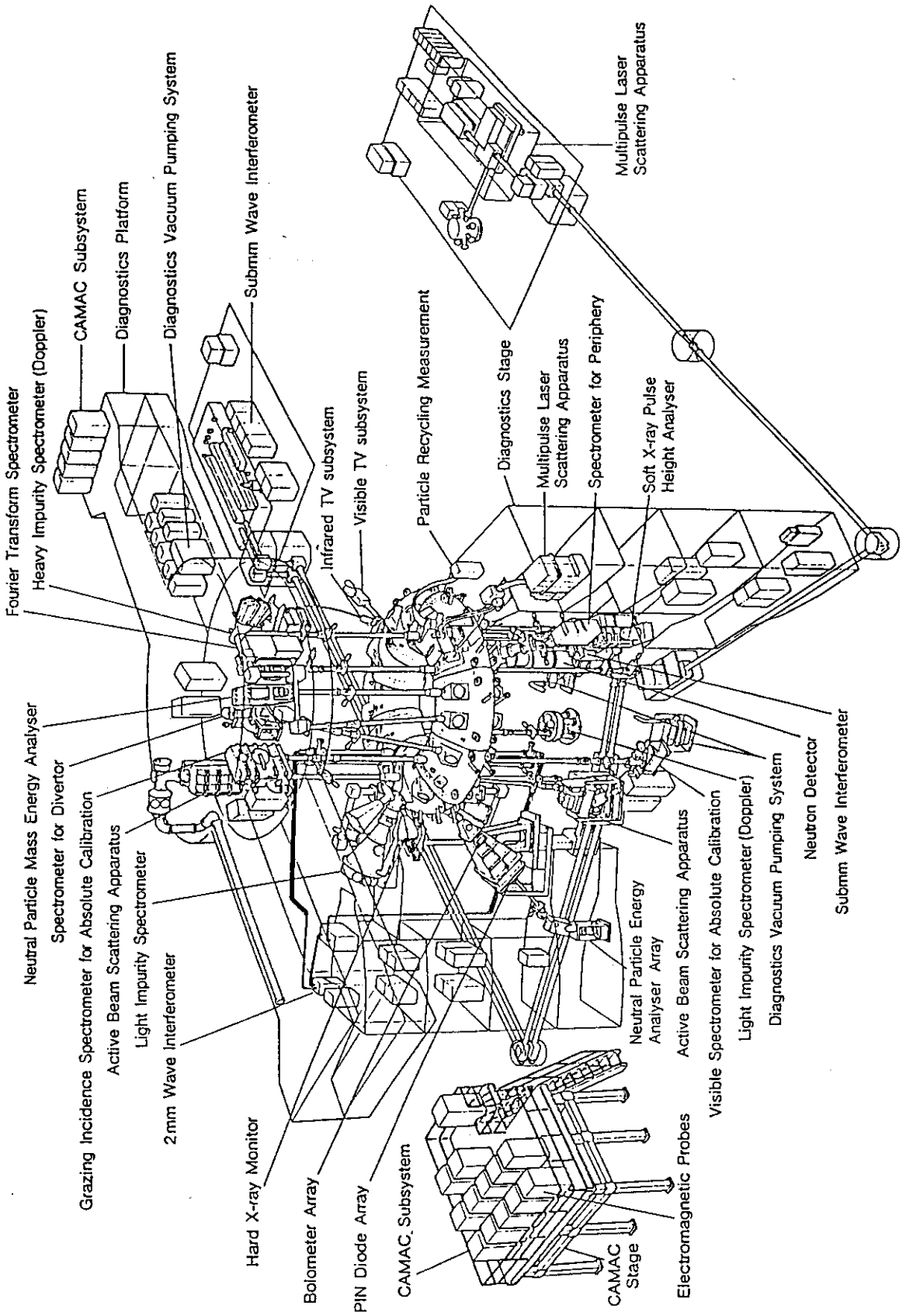

Fig. 2.5 Bird's-eye view of the JT-60 diagnostics.

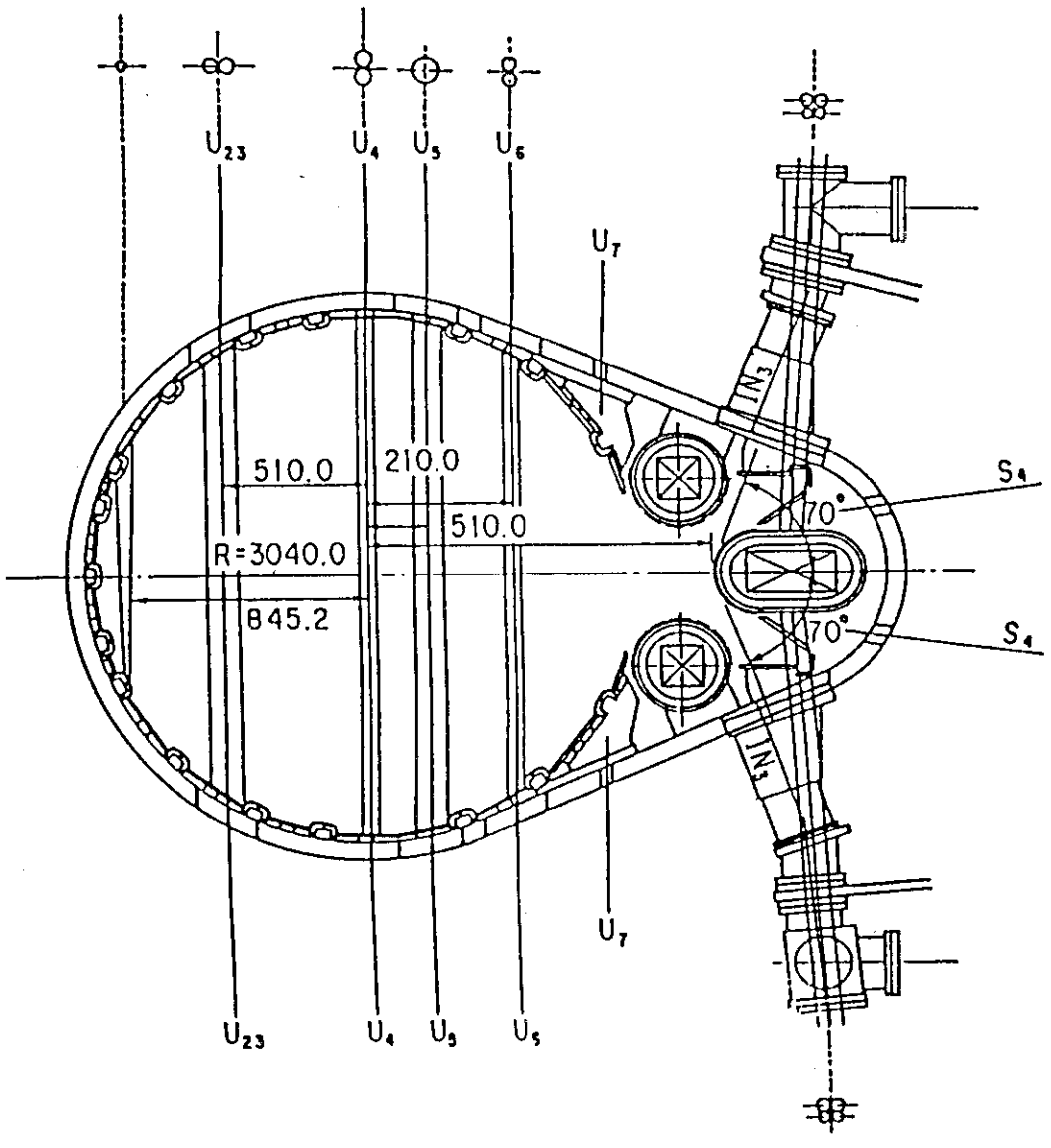

Fig. 2.6 Diagnostic chords of the interferometric measurements on JT-60.

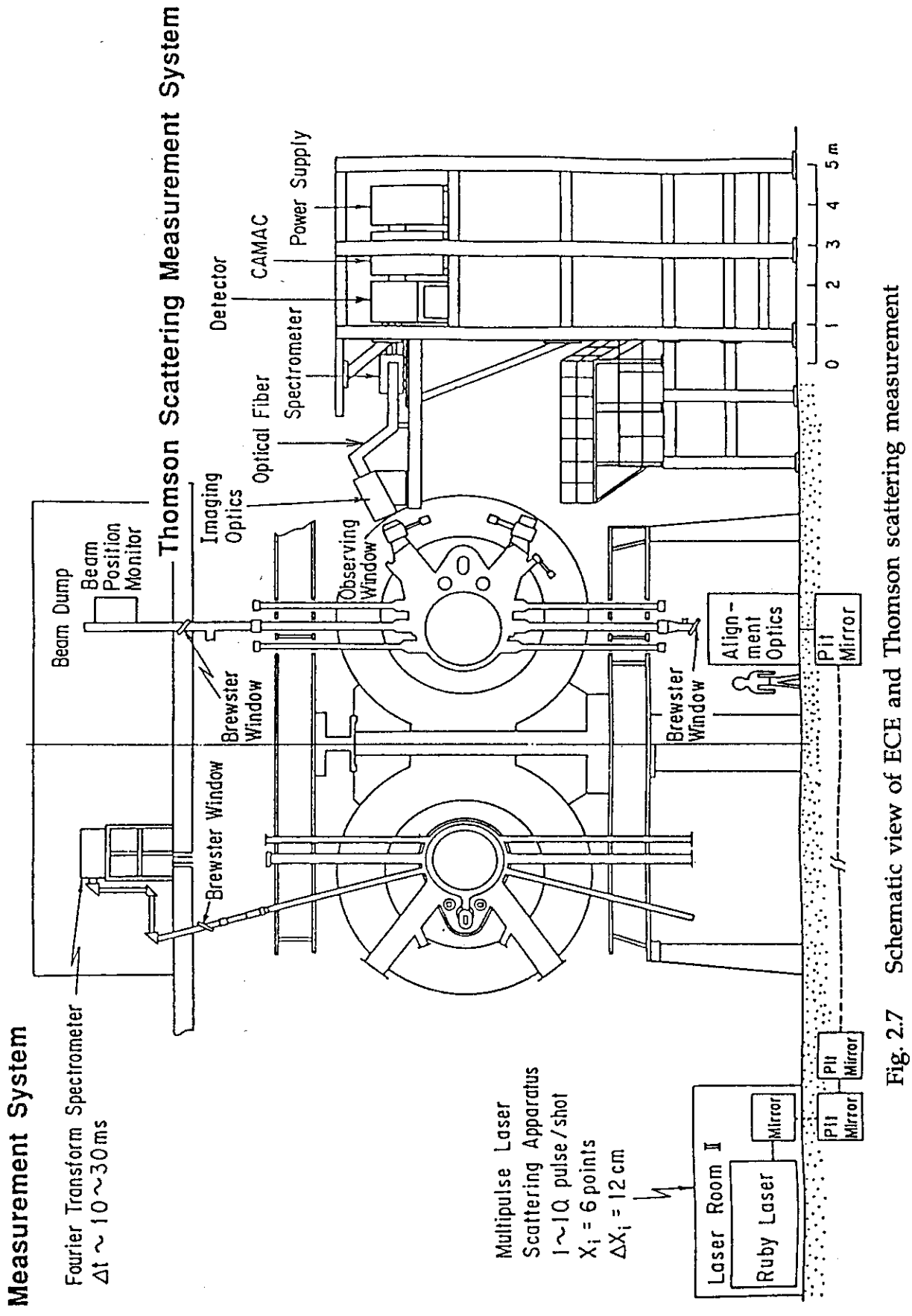

Fig. 2.7 Schematic view of ECE and Thomson scattering measurement systems.

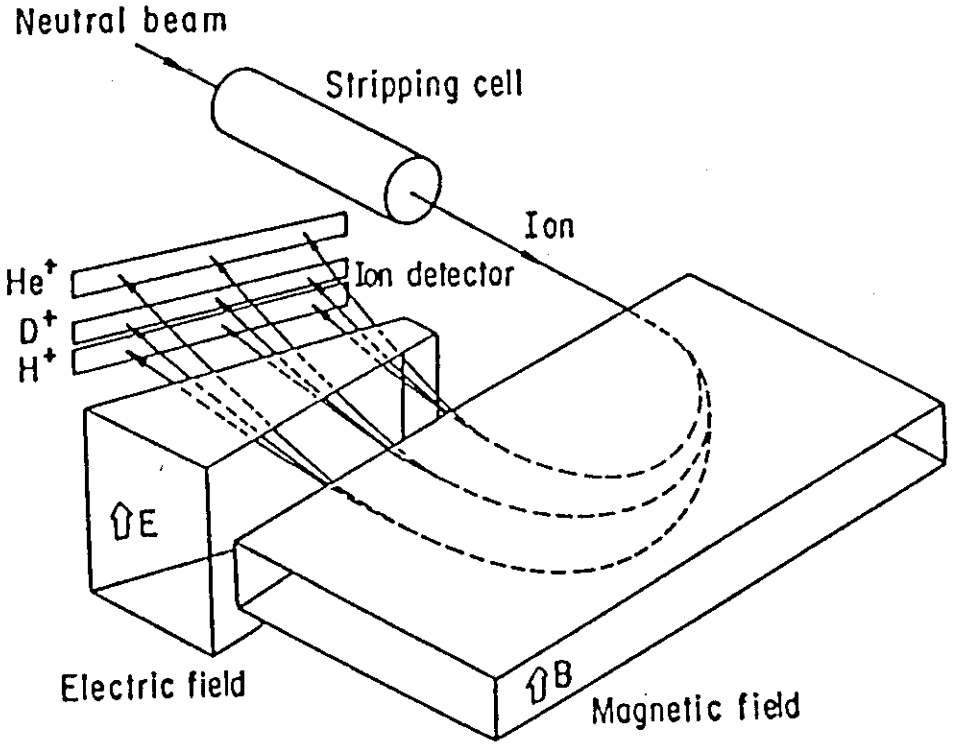

Fig. 2.8 Principle of the E//B type mass energy analyzer.

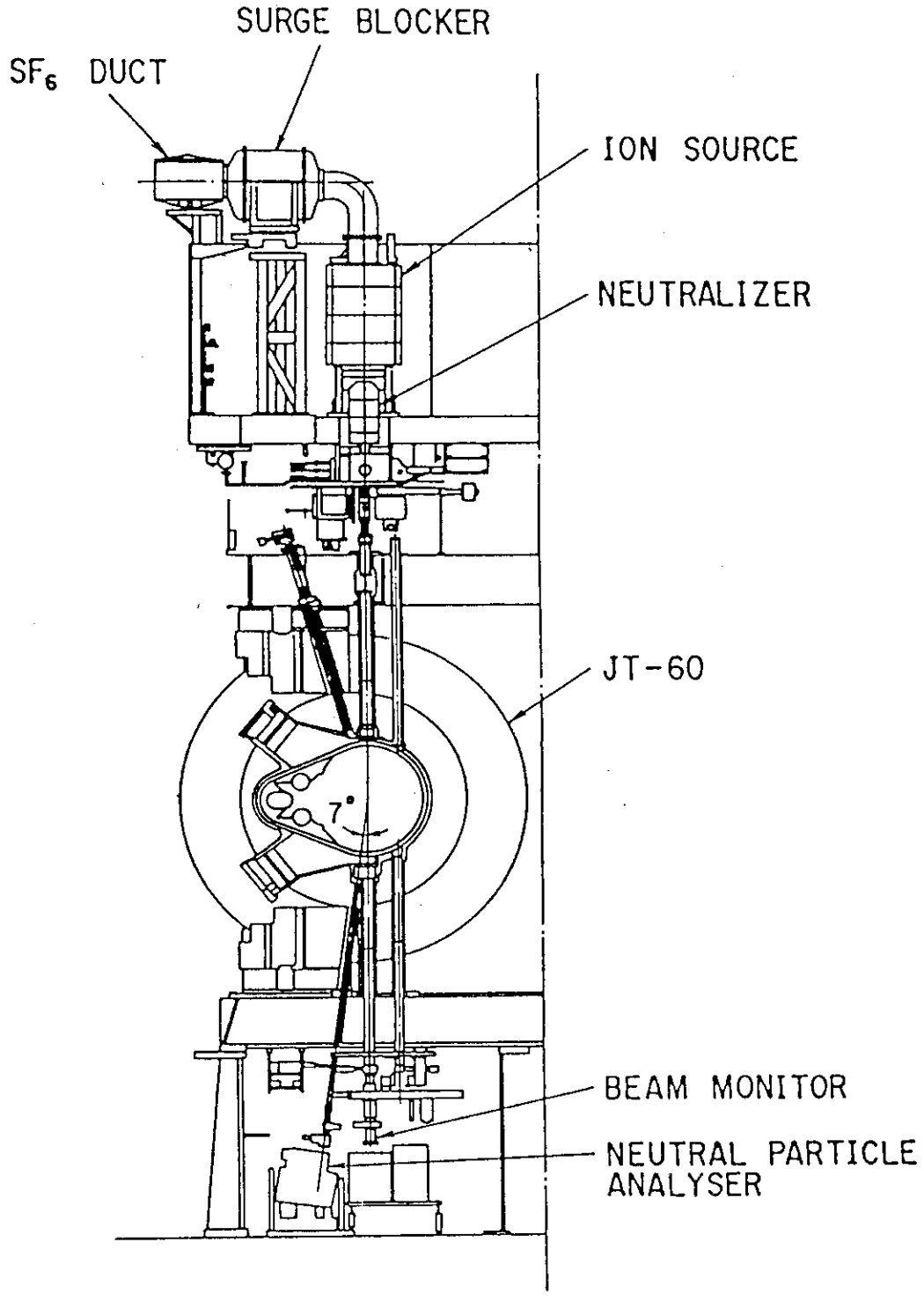

Fig. 2.9 Schematics of the active beam scattering system.

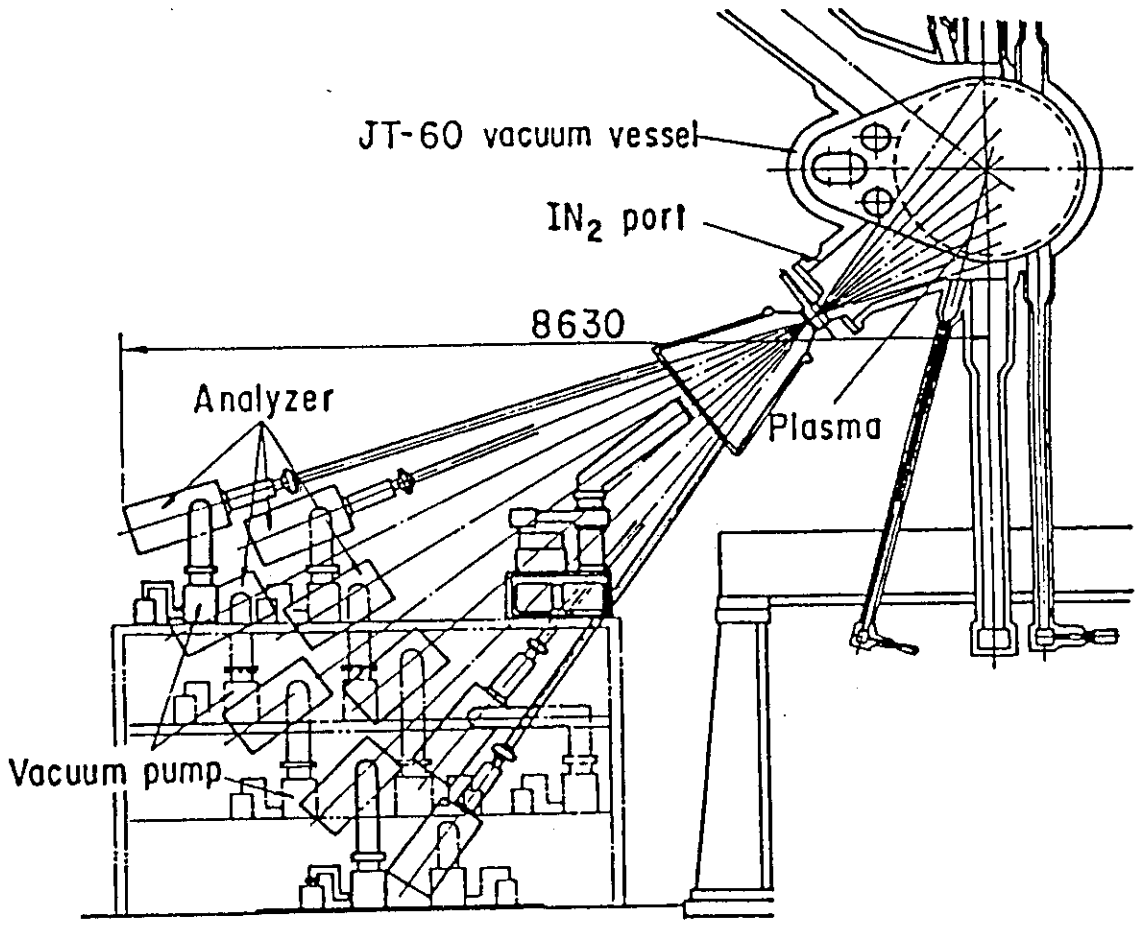

Fig. 2.10 Schematics of the neutral-particle energy analyzer array.

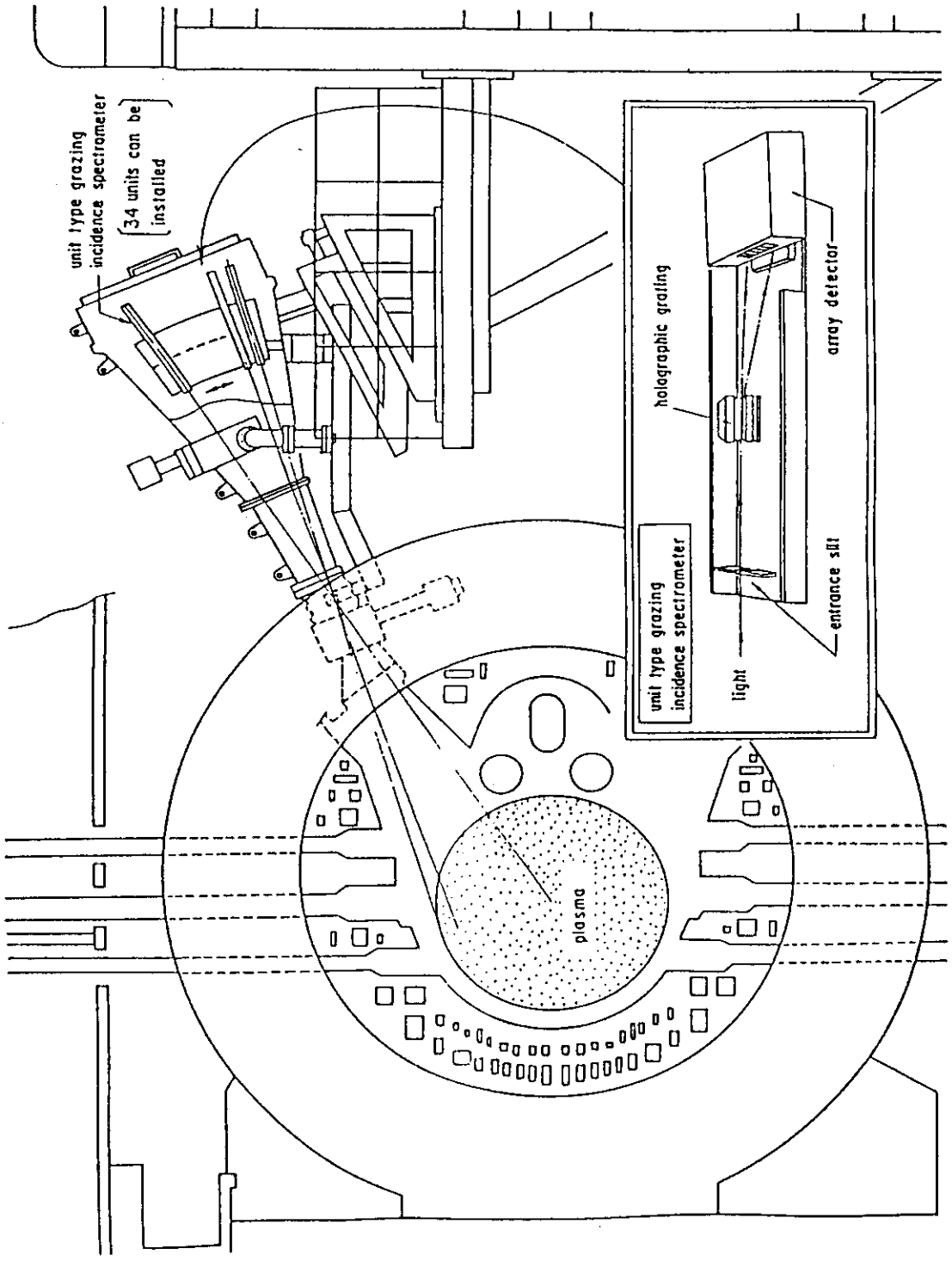

Fig. 2.11 Unit-type grazing-incidence spectrometer and the apparatus installing unit type spectrometers for spatial resolution.

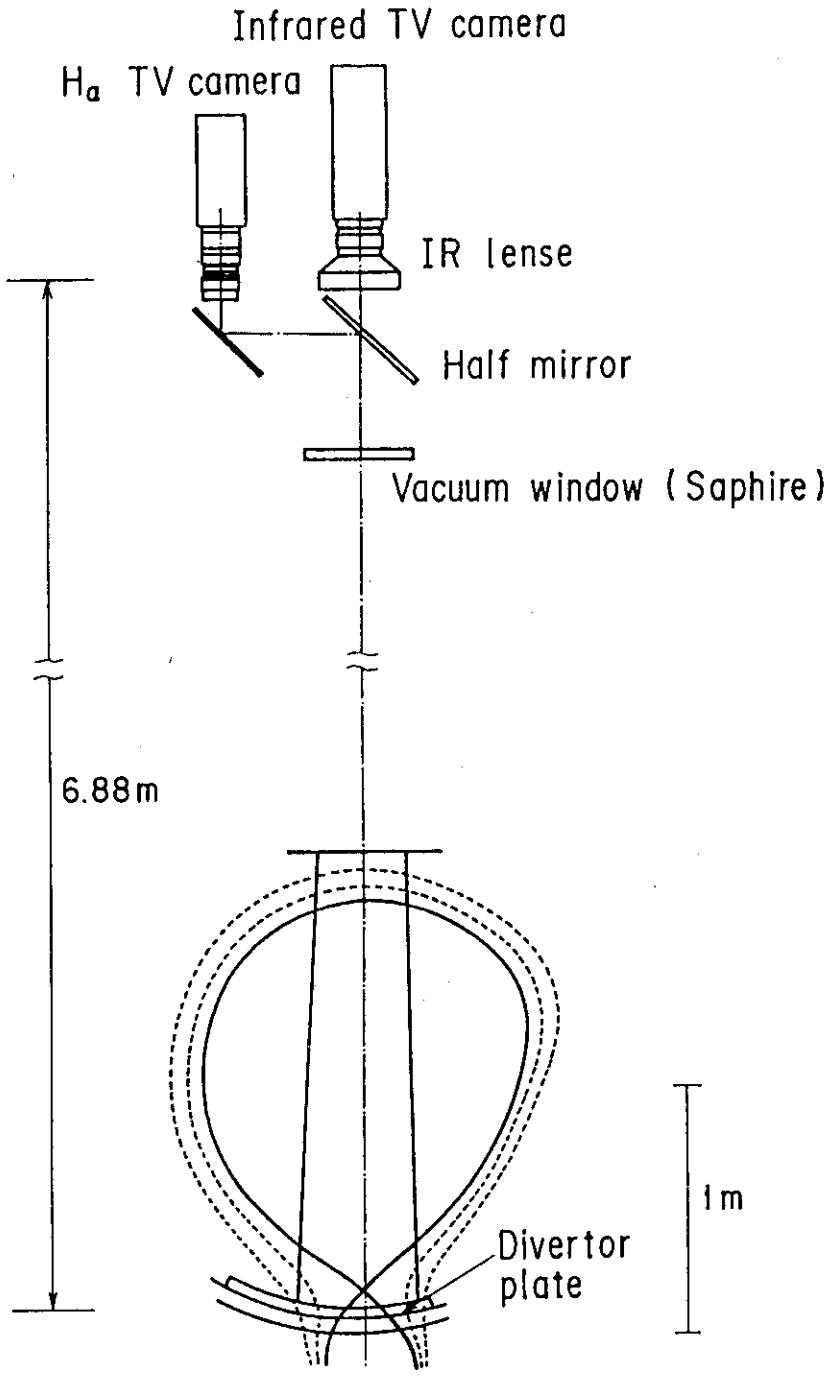

Fig. 2.12 Schematic view of IR TV and Hα TV cameras for lower X-point divertor.

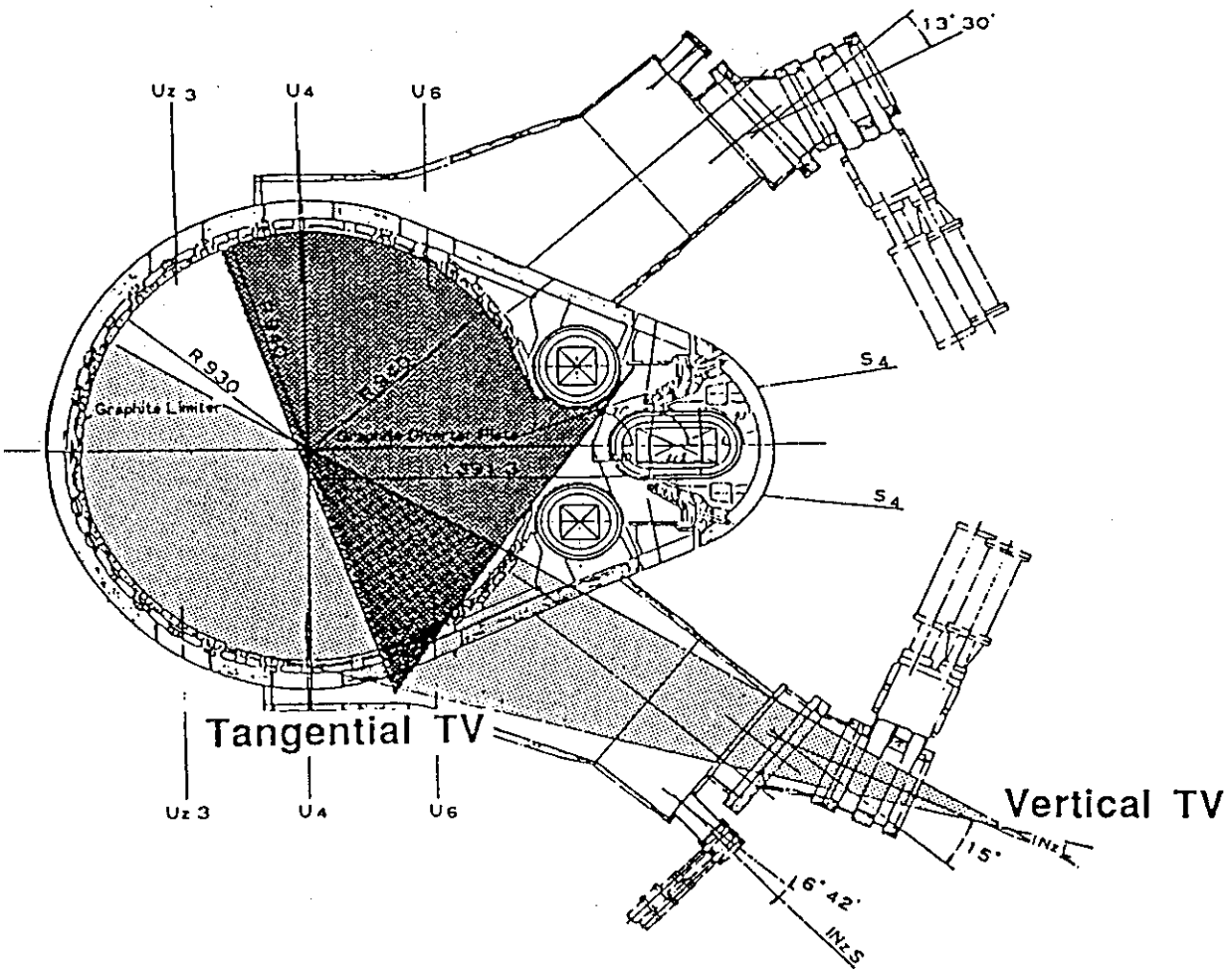

Fig. 2.13 Viewing fields of plasma TV cameras.

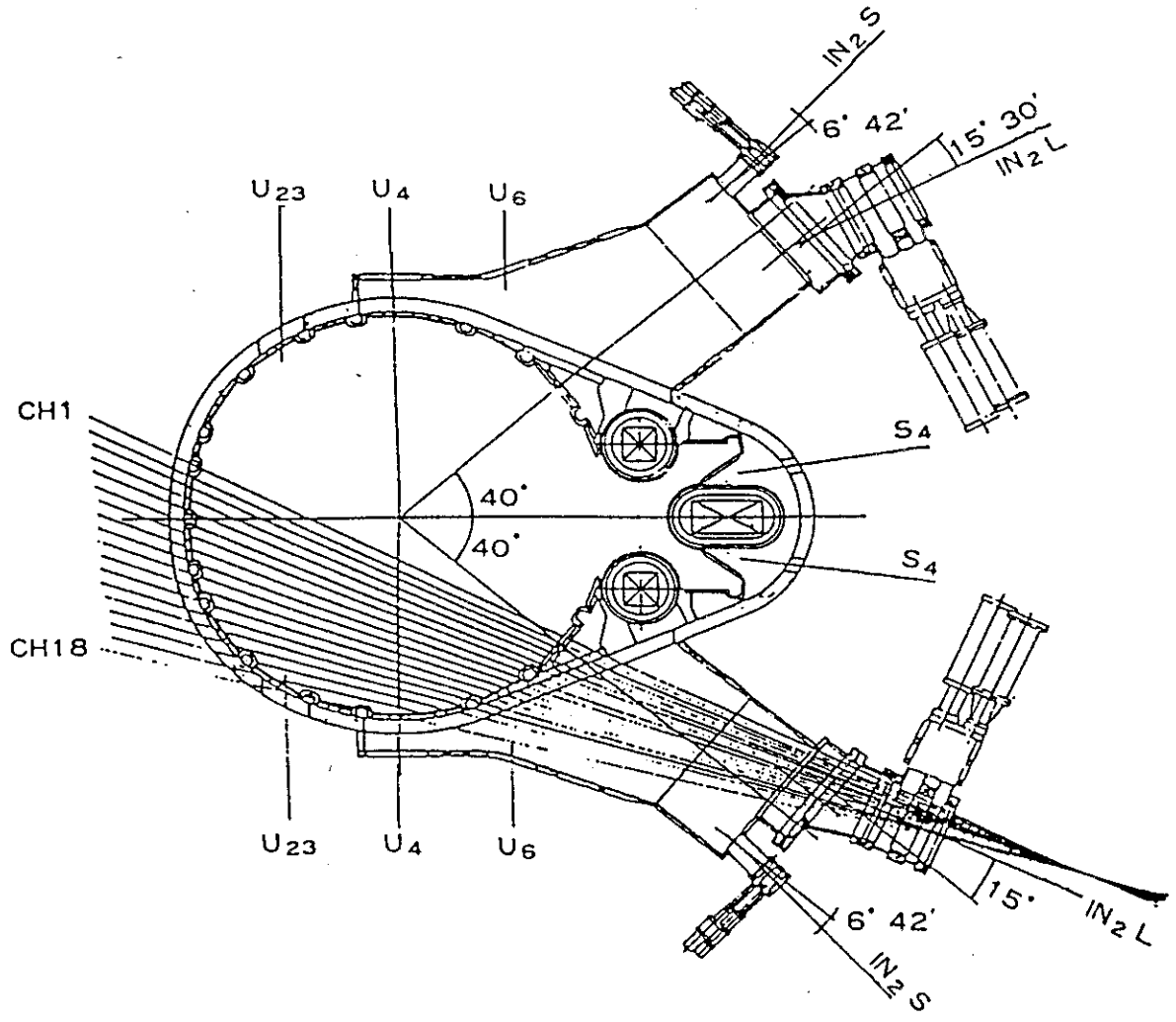

Fig. 2.14 Viewing chords of the mirror-scanning spectrometer.

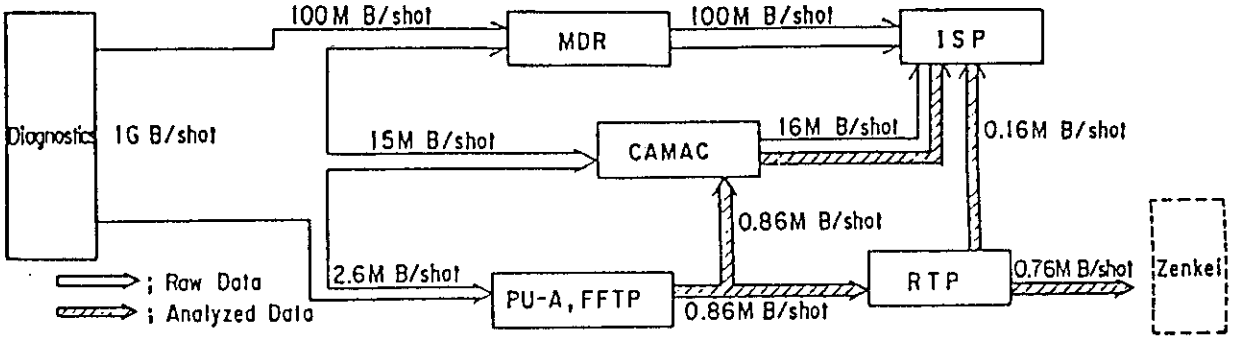

Fig. 2.15 Diagnostics data flow of each discharge in the data processing system.

3. Bolometric Measurement System of JT-60

3.1 INTRODUCTION

One of the main objectives of present-day tokamaks, such as JT-60, is to study the energy loss mechanisms of the magnetically confined plasma in order to develop techniques of controlling them. Line radiation and bremsstrahlung due to impurities mainly located in the VUV and soft X-ray region, and neutral particles by charge exchange process are important energy loss channels. These energy losses are measured with bolometric diagnostics. Radiation loss is important not only for global power balance study but also for local energy balance. The radiation profile has a decisive influence on the profiles of other parameters such as $T_e(r)$. To understand plasma parameter profiles, a knowledge of the radiation profiles is necessary.

The bolometer have to meet all of following requirements in JT-60: they have to be bakeable to 150° C; they have to meet high vacuum requirements; they have to reject background signals due to temperature changes of the mounting support, electromagnetic pickup and common-mode voltages; they have to be resistant to radiation damage by neutron and gamma radiation for DD discharges. The available detectors, the thermistor bolometer [1,2], the thermopile detector [3], the pyroelectric detector [4], and the thermographic method [5], do not meet all these requirements. So a new metal resistor bolometer was developed for JT-60. Similar bolometers are employed in ASDEX [6], JET [7], and TFTR [8].

Before modification for lower divertor, single array of 15 channel bolometers measured radiated power from main plasma and two bolometers measured that from outer X-point divertor. After the modification, two arrays of bolometer measured power from main plasma and a bolometer measured that from lower X-point divertor.

Section 3.2 describes the new metal resistor bolometer and electronics. Section 3.3 presents the arrangement of the bolometer arrays and data acquisition on JT-60. Analysis of the bolometer signal and calibration are described in Secs. 3.4 and 3.5, respectively. Section 3.6 presents the measurements on JT-60.

3.2 BOLOMETER AND ELECTRONICS

3.2.1 Selection of Bolometer

Pyroelectric detector [4] is one of the popular bolometer in tokamak experiments. The electric polarization of a ferroelectric crystal such as $LiTaO_3$ is a function of temperature and can measure the temperature of the detector foil. The detector supplies a current which is proportional to the temperature change, so that it can measure the input power directly. However, it have to be correct the cooling effect of the detector foil and the temperature change of the mounting support in the long duration discharge. Farther more the detector has severe difficulties of the radiation damage and the large time drift of the sensitivity. So it has less reliability as a bolometer for JT-60 and other large tokamaks.

Thermistor bolometer was a most popular detector in small and medium size tokamaks. In D-III [2] and JFT-2M [9], free standing thermistor (Veco's thinistor) are used for bolometer array to perform long cooling time of the detector. Thermistor has a large temperature coefficient dR/dT about -2% ~ -5% at room temperature, so that the sensitivity of the thermistor bolometer is large. Because the temperature dependence of the resistivity is non-linear as

$$R = A \exp\left(\frac{B}{T}\right) \tag{3.1}$$

where B is thermistor constant and T is temperature in Kelvin, data analysis of the bolometer signal is complicated. In JT-60, thermistor bolometers were employed for initial ohmic experiments. The bolometers were installed at the end of the vertical diagnostics port, 6 m away from the plasma center, so they

did not have to be bake-up. Figure. 3.1 shows the schematics of the thermistor bolometer. Thermistor chip is attached by epoxy resin back side of the copper absorber foil. Front side of the absorber is blackened to be sensitive to visible and infrared radiation. The sensor is sustained by only two platinum electrodes which have diameters of 25 μm, so that the long cooling time of about 19 s in vacuum is performed. The obtained characteristics of the thermistor bolometer is summarized in Table 3.1.

Metal resistor bolometer is employed for the bolometer array by following reasons: bolometer resistant to radiation damage should be developed for DD discharges; temperature coefficient of the resistivity is linear; it is bakeable up to 150°C; metal resistor bolometer is affected by electromagnetic noises less than thermistor, because resistant of metal bolometer is much lower then that of thermistor bolometer.

Table 3.1 Characteristics of the thermistor bolometer for JT-60 initial experiments.

Heat capacity C	0.75 mJ/°C
Cooling time in vacuum τ_{cool}	~19 s
Response time	9 ms
Electrical resistance R	1 MΩ

3.2.2 Theory of Metal Resistor Bolometer

Basically, metal resistor bolometer consists of three layers, (1) metal absorber, (2) dielectric sheet such as kapton and (3) metal resistor as shown in Fig. 3.2. The radiation absorbed by a thin metal foil results in a small temperature increase. The change of the resistance caused by the temperature increase is measured by electric circuit.

When the radiation P(t) input into the absorber, heat diffusion equations are given as

$$C_1 \frac{d}{dt} T_1 = P(t) - \frac{1}{R_1}(T_1 - T_2) - k_1 (T_1^4 - T_2^4) \tag{3.2}$$

$$C_2 \frac{d}{dt} T_2 = \frac{1}{R_1}(T_1 - T_2) - k_2 (T_2^4 - T_0^4) - \frac{1}{R_2}(T_2 - T_0) \tag{3.3}$$

where T_1 and T_2 are temperatures of absorber and metal resistor, respectively, C_1 and C_2 are heat capacitances of absorber and dielectric sheet, respectively, R_1 is thermal resistance between absorber and metal resistor, R_2 is one between metal resistor and electrode, k_1 and k_2 are radiation coefficients of absorber and metal resistor to circumstance, respectively. Here it is assumed that the metal resistor is very thin and its heat capacitance is negligible.

For estimation of the response time of the bolometer, cooling terms in Eqs. (3.2) and (3.3) can be neglected. If input power P(t) is delta function,

$$C_1 \frac{d}{dt} T_1 = -\frac{1}{R_1}(T_1 - T_2) \tag{3.2'}$$

$$C_2 \frac{d}{dt} T_2 = \frac{1}{R_1}(T_1 - T_2) \tag{3.3'}$$

are obtained. From Eqs. (3.2') and (3.3'), the differential equation with T_2 is given by

$$C_2 \frac{d^2}{dt^2} T_2 = \frac{1}{R_1}\left(1 + \frac{C_2}{C_1}\right) \frac{d}{dt} T_2 \tag{3.4}$$

The solution of Eq. (3.4) is given by

$$T_2(t) = T_2(t=0)\left(1 - e^{-\frac{t}{\tau_R}}\right) \tag{3.5}$$

where τ_R is the response time and given by

$$\tau_R = \frac{C_1 C_2 R_1}{C_1 + C_2} . \tag{3.6}$$

In order to obtain smaller response time, C_1 and C_2 should be smaller. Sufficient thickness of absorber is needed to stop soft X-rays, so that thinner dielectric sheet is needed to obtain fast response time.

For estimation of the cooling time of the bolometer, $T_1 \approx T_2$ can be assumed because the cooling time is much larger than the relaxation time of T_1 and T_2. By summing Eqs. (3.2) and (3.3) with neglecting radiative cooling terms,

$$(C_1 + C_2)\frac{d}{dt}T_2 = -\frac{1}{R_2}(T_2 - T_0), \tag{3.7}$$

is obtained. The solution of Eq. (3.7) is given by

$$T_2(t) = \{T_2(0) - T_0\} e^{-\frac{t}{\tau_c}} + T_0, \tag{3.8}$$

where τ_c is the cooling time and given by

$$\tau_c = (C_1 + C_2) R_2. \tag{3.9}$$

3.2.3 Metal Resistor Bolometer for JT-60

A schematic diagram of the metal resistor bolometer [10,11] developed for JT-60 is shown in Fig. 3.3. The sensor consists of three layers. A 11 × 16 mm^2, 5-μm-thick gold absorber is laminated on the front of 7-μm-thick polyimide sheet. A 0.1-μm-thick gold resistor is laminated on the back of the polyimide sheet. The resistor pattern is shown in Fig. 3.4. The manufacturing process is photoetching technique. The sensor foil is mounted on the stainless-steel frame. The bolometer is composed of two identical sensors. One is mounted behind the other via 1-mm-thick Teflon sheet. Front sensor faces to plasma. The backside sensor is shielded by front one and Teflon sheet, so that it operates as a reference sensor to compensate the change of room temperature.

Upper limit of the measurement range is determined by the stopping energy of the absorber foil. Stopping energy defined by 90% absorption is 10 keV. Lower limit of the measurement range is determined by the reflection of the absorber surface. Reflection coefficient of gold surface in the range from UV to visible is shown in Fig. 3.5. Reflection is almost constant 5 - 10 % in VUV range. So the measurement range of the bolometer is 1.2 - 2000 Å in wavelength.

The response time and cooling time of the bolometer were estimated from Eqs. (3.6) and (3.9) as follows. The response time is estimated by

$$\tau_R = \frac{C_1 C_2 R_1}{C_1 + C_2} = 3.5 \times 10^{-4}\ s \tag{3.10}$$

where $R_1 = \delta/\lambda A$, δ is a thickness of polyimide sheet (7×10^{-6} m), λ is a heat conductivity (0.156 J/s·m· °C), and A is an area of the resistor (1.2×10^{-4} m^2). Heat capacities C_1 and C_2 are respectively 2.35×10^{-3} J/°C and 2.04×10^{-3} J/°C from Table 3.2. The cooling time is estimated by

$$\tau_c = (C_1 + C_2) R_2$$

$$= 3.5 \times 10 \text{ s} \qquad (3.11)$$

where $R_2 = \delta/2\lambda A$, δ is a length of electrode wire (2×10^{-3} m), λ is a heat conductivity (314 J/s·m· °C), and A is a cross-section of the electrode wire (8.04×10^{-10} m^2).

Table 3.2 Heat capacitances of the bolometer components

	Mass (g)	Specific heat (J/g·°C)	Heat capacity (J/°C)
Absorber	1.85×10^{-2}	0.127	2.35×10^{-3}
Polyimide	2.04×10^{-3}	1.1	2.04×10^{-3}
Resistor	1.93×10^{-4}	0.127	2.45×10^{-5}
Electrodes	3.1×10^{-5}	0.127	3.9×10^{-6}

3.2.4 Electronics and Data Acquisition

Figure 3.6 shows a block diagram of the bolometer amplifier. The resistance change of the bolometer is converted to the corresponding voltage change through the bridge circuit. The bridge output is amplified by three stage operational amplifiers. The DC offset of the bridge output is automatically compensated by auto balance feedback circuit before plasma discharge. Figure 3.7 shows the data acquisition for the bolometer. The signal of the bolometer amplifier is sent to CAMAC transient recorder (LeCroy 8212A and 8800A) via fiber optics and stored in CAMAC memory with 3 ms sampling time throughout 10 s discharge. The data is transferred to the JT-60 data acquisition system and analyzed in the Inter-shot processor.

3.3 ARRANGEMENT OF BOLOMETERS ON JT-60

In the first period April 1985-March 1987, bolometer consisting of 15 channel bolometers was installed in the bottom diagnostics port outside of the vacuum vessel as shown in Fig. 3.8. The bolometer array was mounted in triangle vacuum chamber (IN2 vacuum chamber). The detectors were exposed to the plasma through a 4 cm × 6 cm rectangular aperture 3 m away from the center of the plasma. The viewing field covered more than a half of the plasma cross-section in the range of tangent radius from 0.73 to -0.19 m. The spatial resolution of the bolometer array in minor radius was about 0.12 m. A flash lamp was mounted near the aperture to test the detectors remotely. In the same vacuum chamber, X-ray imaging system, CX neutral particle analyzers and Hα monitor were installed. The three channel bolometers using thermistor with vertical sightlines were mounted on the diagnostics ports at R = 2.53, 3.04, and 3.55 m in the basement. One channel thermistor bolometer viewing near the X-point of the divertor was mounted on the diagnostics port tilted 75° against the midplane. A couple of the metal resistor bolometer on electron and ion drift sides measured the radiated power from the divertor chambers. These were mounted on the divertor pumping ports and 2.4 m away from the divertor plates.

In the second period May 1987 - October 1989, additional array consisting of 16 channel bolometers was installed in the top diagnostics port outside of the vacuum vessel as shown in Fig. 3.9. The radiated power from the lower divertor region was measured by single bolometer after the modification for lower X-point divertor. Note the viewing field of the divertor bolometer included the X-point in the typical divertor configuration. The three vertical bolometers and one viewing near the outer X-point were taken off for install of lower divertor coils.

3.4 ANALYSIS OF BOLOMETERS SIGNAL

If the radiation power P is incident on the bolometer, the time behavior of the temperature T is governed approximately by the simple differential equation

$$\frac{dT}{dt} = \frac{P}{C} - \frac{T - T_0}{\tau_c} , \tag{3.12}$$

where C is the heat capacity of the bolometer foil, T_0 is the initial temperature of the bolometer foil, and τ_c is the cooling time. By solving Eq. (3.12),

$$P = C\left(\frac{dT}{dt} + \frac{T - T_0}{\tau_c}\right) \tag{3.13}$$

is obtained. The output of the bolometer amplifier is proportional to the bolometer temperature, so that the chord integrated radiation along ith shightline is given by

$$\int P\, dl_i = \frac{1}{\Delta\Omega_i\, \varepsilon_i}\left\{\frac{d}{dt} V_i(t) + \frac{V_i(t) - V_i(0)}{\tau_c}\right\}, \tag{3.14}$$

where $V_i(t)$, $\Delta\Omega_i$ and ε_i are respectively the output, the slid angle and the sensitivity of the ith bolometer. Here dV/dT is obtained from the time derivative of the quadratic function fitted to V(t).

Generally, the total radiated power from the main plasma P_{rad}^{main} is obtained by the volume integral of P(r) which is the local radiation loss calculated by an Abel transformation from the chord-integrated radiated powers. However, an Abel transformation is not valid for the radiation profile which is poloidally asymmetric. The poloidal asymmetry of the radiation profile is expected in the divertor configurations on JT-60. P_{rad}^{main} is represented exactly by

$$P_{rad}^{main} = \int 2\pi R\left(\int P(R,Z)\, dZ\right) dR, \tag{3.15}$$

where P(R,Z) is the local radiation loss at point (R,Z) in the poloidal cross-section. The value in the large parentheses is the radiated power integrated along vertical chord. The number of the measurement chord is finite, and furthermore, the viewing chords of the bolometer array are not vertical. Therefore, simple form

$$P_{rad}^{main} = 2\pi R_P \sum_i \Delta r_i P_i \tag{3.16}$$

is employed as the approximation of Eq. (3.15). Here R_P is the plasma major radius, and Δr_i is the averaged width between ith and i+1th chords, and P_i is the radiated power integrated along ith chord.

A knowledge of the radiated power profile in the divertor region is necessary to estimate the radiated power from the divertor region. But sufficient information about the profile was not obtained. In the outer X-point divertor, the bolometers viewed near the separatrix hit line on the divertor plate only so that the divertor radiation loss P_{rad}^{div} power was assumed to be radiated only from the separatrix hit line. Thus P_{rad}^{div} was represented by

$$P_{rad}^{div} = P_{rad}^{div}\,(\text{electron side}) + P_{rad}^{div}\,(\text{ion side})$$

$$= \frac{2\pi R}{l} \cdot \frac{4\pi}{\Delta\Omega} \left\{ P_d\,(\text{electron side}) + P_d\,(\text{ion side}) \right\}, \qquad (3.17)$$

where R was the major radius of the separatrix hit line, l was the length of the separatrix hit line in the viewing field of the divertor bolometer, $\Delta\Omega$ was the solid angle from the separatrix hit line to the bolometer, and P_d was the received power of the divertor bolometer. In the lower X-point divertor, the bolometer viewed the divertor plasma of both electron and ion drift sides from the side diagnostics port, and did not view the surface of the divertor plate, so that P_{rad}^{div} power was assumed to be radiated from the divertor plasma uniformly. Thus P_{rad}^{div} was represented by

$$P_{rad}^{div} = 2\pi R_d\, Z_d \cdot \frac{4\pi}{\Delta\Omega} P_d, \qquad (3.18)$$

where R_d was the major radius of the X-point, Z_d was the height of the the viewing field of the divertor bolometer in the divertor region, $\Delta\Omega$ was the solid angle from the bolometer to the divertor plasma, and P_d was the received power of the divertor bolometer.

Generally, an Abel transformation is used to obtain the radiation profile P(r) from the chord-integrated radiated power. However, an Abel transformation is valid only for a poloidally symmetric radiation profile. It was estimated from the raw data of the bolometer array that the radiation profile had a poloidal asymmetry in the divertor discharges. So an Abel inversion was not available to obtain the radiation profiles. In TiC molybdenum wall period, additional three-channel vertically-viewing

bolometers and one channel bolometer viewing near the X-point were available, so that the reconstruction of the radiation profile was tried by using an asymmetric Abel inversion. Intense asymmetric radiation around the outer X-point had been found in the divertor configuration. The radiation profile was assumed to be simple form as

$$P(r,\theta) = P_0(r) + P_1(r)\cos^m\theta \,, \tag{3.19}$$

where $\theta = 0°$ was the direction of major radius. Here following function was employed as $P_1(r)$:

$$P_1(r) = \alpha \sin^n\left(\frac{\pi}{2} \cdot \frac{r}{a}\right) \left(\text{for } -\frac{\pi}{2} \le \theta \le \frac{\pi}{2}\right)$$

$$= 0 \quad \left(\text{for } -\pi < \theta < -\frac{\pi}{2},\ \frac{\pi}{2} < \theta \le \pi\right), \tag{3.20}$$

where parameters α, m, and n represent respectively the intensity, width in radial direction, and extent in the θ direction. These parameters was determined so that the reconstructed profile most likely reproduced the data measured by the bolometer array and four bolometers by an iteration method.

3.5 CALIBRATION OF BOLOMETERS

Response time of the bolometer τ_R was estimated from the response to flush lamp. The response of the bolometer V(t) for impulse input is given by

$$V(t) = V_0 \left(1 - e^{-\frac{t}{\tau_R}}\right), \tag{3.21}$$

where V_0 is the saturation voltage. If the pulse width is comparable with the response time, Eq. (3.21) is not valid and replaced by

$$V(t) = C \int_0^t f(t') \left(1 - e^{-\frac{t' - t}{\tau_R}}\right) dt' \,, \tag{3.22}$$

where f(t) is the time history of the input pulse. The pulse width of the flush lamp was about 2 ms, so that it could not be regarded as a impulse input. Rise time τ_R was determined so that Eq. (3.22) most likely reproduced the

bolometer response by using flush lamp waveform f(t) which was measured by a photodiode with 10 μsec response time. Thus response time of 1.4 msec was obtained. This value is four times larger than expected one of Eq. (3.10). It is probably because heat capacity of the dielectric sheet out of the absorber area can not be neglected.

Cooing time of the bolometer was estimated in situ from the time evolution of the bolometer output signal after the termination of the flash lamp in the vacuum chamber using Eq. (3.8). Thus cooling time of about 8 s was obtained. This value is four times smaller than expected one of Eq. (3.11). It is probably because radiative cooling effect and heat diffusion to the dielectric sheet out of the absorber area can not be neglected.

Sensitivity of the bolometer was calibrated by a He-Ne laser. Schematic diagram of the calibration is shown in Fig. 3.10. The laser beam which was calibrated by the power meter was put on the bolometer with the incident angle of 45°. The power reflected by the bolometer surface was measured by the power meter. The sensitivity of the bolometer ε was given by

$$\varepsilon = \frac{dV / dt}{P_{input} - P_{reflect}}, \tag{3.23}$$

where dV/dt is the time derivertive averaged in 0 - 200 ms after open of the incident shutter, and P_{input} and $P_{reflect}$ were the powers of input and reflected laser beam, respectively. Thus the sensitivity of 1.75 V/mW was obtained in the case that the bias of the bridge was 5 V, and the gain of the amplifier was 5000. The measurement uncertainty of the sensitivity was estimated to be 7%.

The calibrated data and other characteristics of the metal bolometer is summarized in Table 3.3 . The cooling time of the bolometer is about 160 time longer than that of JET (0.2 s) and the heat resistance is larger than that of JET (90 °C/W). Therefore high sensitvity is performed.

Table 3.3 Calibrated data and other characteristics of the metal bolometer.

Response time	1.4 ms
Cooling time in vacuum τ_{cool}	~8 s
Heat capacity C	4.4 mJ/°C
Heat resistance τ_{cool}/C	1800 °C/W
Sensitivity (V_{bias} = 5 V, Gain = 5000)	1.75 V/mW
Electrical resistance R	7 kΩ

3.6 APPLICATION ON JT-60

By bolometric measurements, the radiation losses and global power balance of JT-60 plasmas was investigated. These experimental results are described in Chapters 6 and 7. Typical results of bolometric measurement is shown in this section.

Figure 3.11 shows the typical waveforms of plasma current I_P, line averaged electron density $\bar{n}_e$, injected NB power P_{NB}, and radiated power from the main plasma P_{rad}^{main} in the outer divertor discharge. The radiated power from the main plasma increased proportionally to $\bar{n}_e$ in OH phase. When the NB of 20 MW was injected from 6 to 7 s, P_{rad}^{main} was in creased according to P_{NB} to be about 2 MW which was 10% of P_{NB}. The time evolution of the bolometer signals around the NB injection is shown in Fig. 3.12. Channels 1 and 12 viewed the bottom and center of the plasma, respectively. The radiated power in the chords passing through the core region was dominant, so that a center-peaked radiation profile was provided if the radiation profile was axisymmetric. That was not consistent with the theoretical prediction and the results of other tokamaks such as TFTR [12] and JET [13]. The radiation loss around the X-point was expected to be enhanced. The chord-integrated radiation profile in Fig. 3.12 might be explained by the asymmetric radiation enhanced around the X-point because the sightlines of high channel number bolometers were viewing near the X-point. The line averaged radiated powers measured with the three vertical bolometers and one viewing near the X-point plotted against the major radius of the sightline are shown in Fig. 3.13, where major radius of the chord viewing near the X-point is defined as 3.04 m plus the tangent radius of the chord. This figure indicates that the intense poloidal asymmetry exists outside of the torus. Then, the poloidally asymmetric radiation profiles were reconstructed for the

outer X-point discharge with NB heating by the technique described in Sec. 3.4. The result of the reconstruction shown in Fig. 3.14 indicates an intense poloidal asymmetry near the X-point. The radiation emissivity in the asymmetry reached up to 200 kW/m^3 in this case. The width of the asymmetry in the radial direction was approximately 0.25 m. The integrated powers of the symmetric and asymmetric components were 730 ± 150 and 720 ± 140 kW, respectively. It was found from the reconstructions with different $\overline{n}_e$ that the asymmetry became remarkable for $\overline{n}_e$ larger than 2×10^{-19} m^{-3}. The chord integrated emissivities calculated from the reconstructed profile agreed with the measured data within 25%. It is considered that these errors are caused by an insufficient number of bolometers with vertical viewing chords and systematic error of the sensitivities between the metal bolometers and thermistor bolometers.

3.7 CONCLUSION

A new metal resistor bolometer was developed for JT-60. It is composed three layers, 5-μm-thick gold absorber, 7-μm-thick polyimide and 0.1-μm-thick gold resistor. This bolometer with bridge amplifier shows a linear response to radiation power, including both neutral particle emission and electromagnetic radiation in the range from UV to soft X-ray. Very long cooling time and high sensitivity are performed in this bolometer. The bolometer meets the requirements of present-day tokamak experiments. The sensitivities of the bolometers were calibrated by a He-Ne laser. The long cooling time and high sensitivity of the bolometer are performed.

Before modification for lower divertor, single array of 15 channel bolometers measured radiated power from main plasma and two bolometers measured that from outer X-point divertor. After the modification, two arrays of bolometer measured power from main plasma and a bolometer measured that from lower X-point divertor. Intense poloidal asymmetries of the radiated power localized near the X-point outside the torus were observed in divertor discharges. The profiles of the radiated power were reconstructed by the Abel inversion with an asymmetric term.

REFERENCES TO CHAPTER 3

[1] H. Hsuan, K. Bol and R.A. Ellis, Nucl. Fusion **15** (1975) 657.

[2] C.L. Hsieh (private communication).

[3] L.E. Sharp, L.S. Holmes, P.E. Stott and D.A. Aldcroft, Rev. Sci. Instrum. **45** (1974) 378.

[4] C.E. Bush and J.F. Lyon, Oak Ridge National Laboratory Report ORNL/TM-6148 (1977).

[5] TFTR Group, J. Nucl. Mater. **93 & 94** (1980) 377.

[6] E.R. Müller and F. Mast, J. Appl. Phys. **55** (1984) 2635.

[7] K.F. Mast and H. Krause, Rev. Sci. Instrum. **56** (1985) 969.

[8] J. Schivell, G. Renda, J. Lowrance and H. Hsuan, Rev. Sci. Instrum. **53** (1982) 1527.

[9] H. Tamai, M. Maeno,T. Matsuda and T. Matoba, Japan Atomic Energy Research Institute Report JAERI-M 88-120 (1988).

[10] T. Nishitani, K. Nagashima, T. Sugiyama, M. Hara, H. Takeuchi and JT-60 Team, Rev. Sci. Instrum. **59** (1988) 1866.

[11] T. Nishitani, K. Nagashima, T. Sugiyama, S. Koide and H. Takeuchi, Kakuyugo Kenkyu **59** Suppl. (1987) 243.

[12] J. Schivell, Rev. Sci. Instrum. **56** (1985) 972.

[13] P.H. Rebut, D.V. Bartlett, G. Bäumel, K. Behringer, et al., in Plasma Physics and Controlled Nuclear Fusion Research (*Proc. 10th Int. Conf. London, 1984*) Vol.1, IAEA, Vienna (1985) 11.

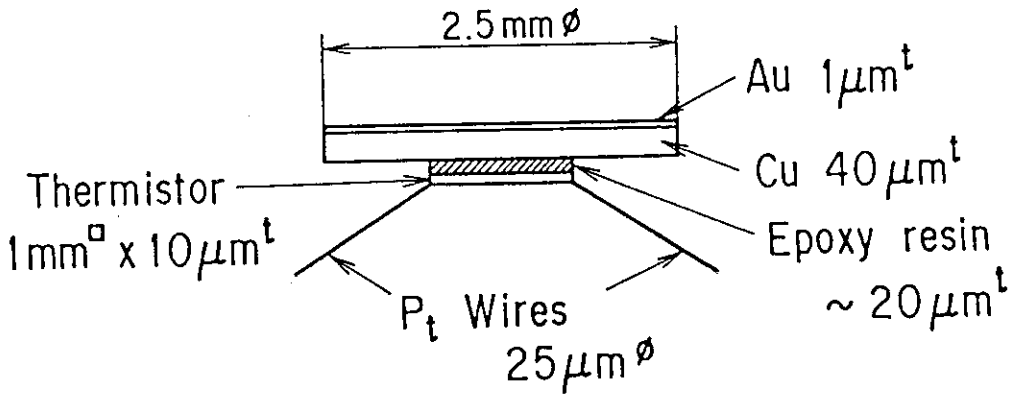

Fig. 3.1 Schematic diagram of the thermistor bolometer used on JT-60 initial experiments.

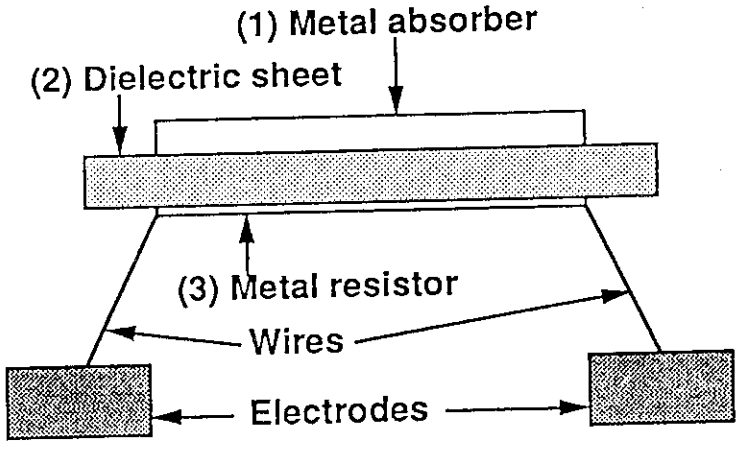

Fig. 3.2 Principle of metal resistor bolometer.

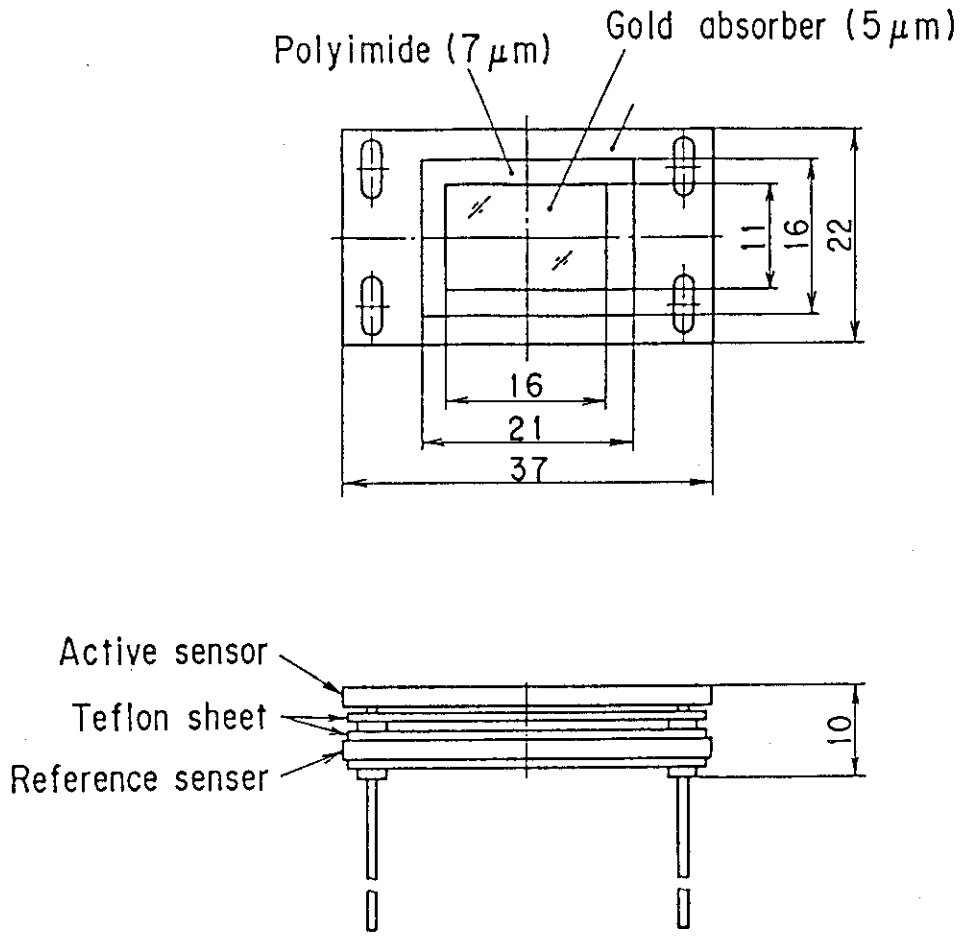

Fig. 3.3 Schematic diagram of the metal resistor bolometer developed for JT-60.

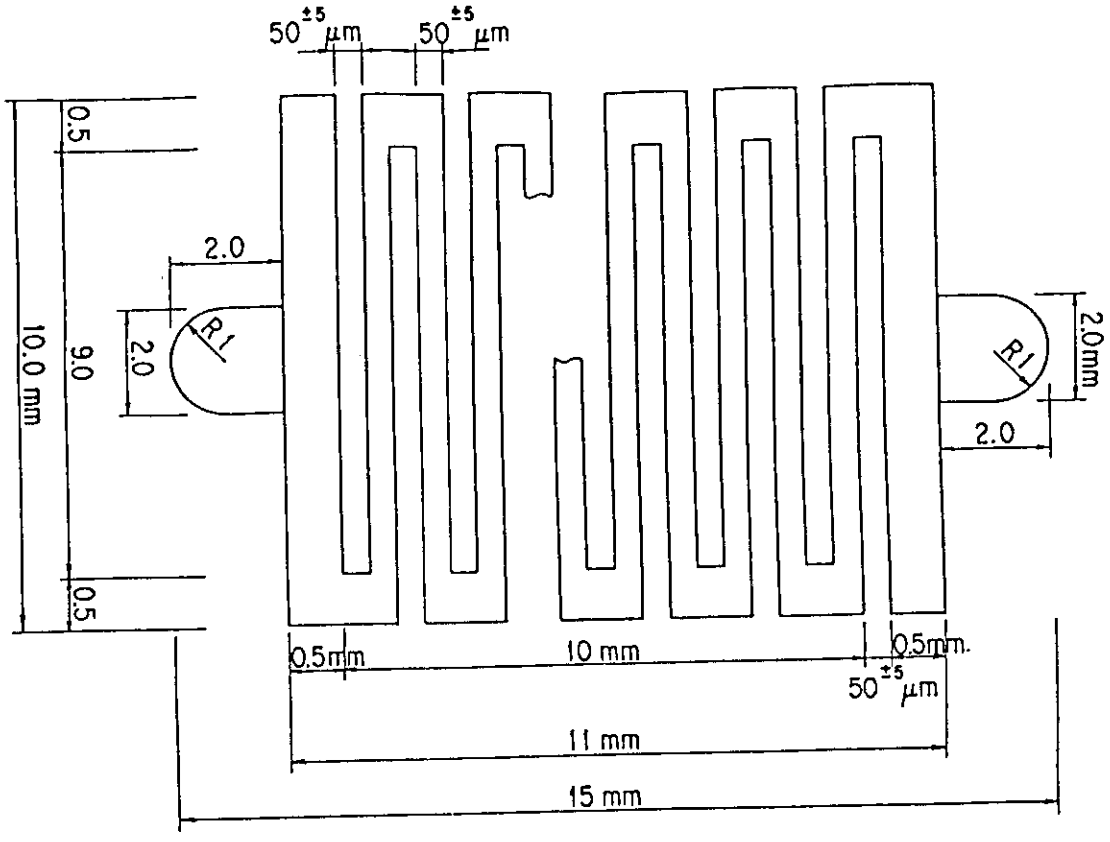

Fig. 3.4 Resistor pattern of the metal resistor bolometer.

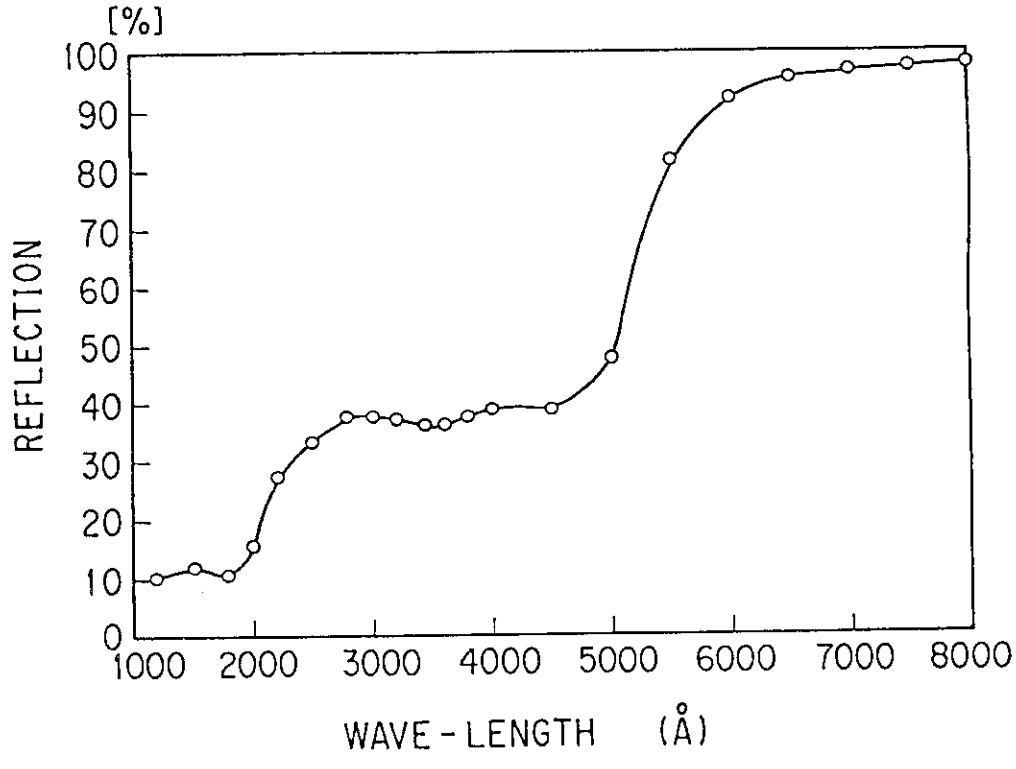

Fig. 3.5 Reflectivity of gold in the spectral range 1000 Å to 8000 Å.

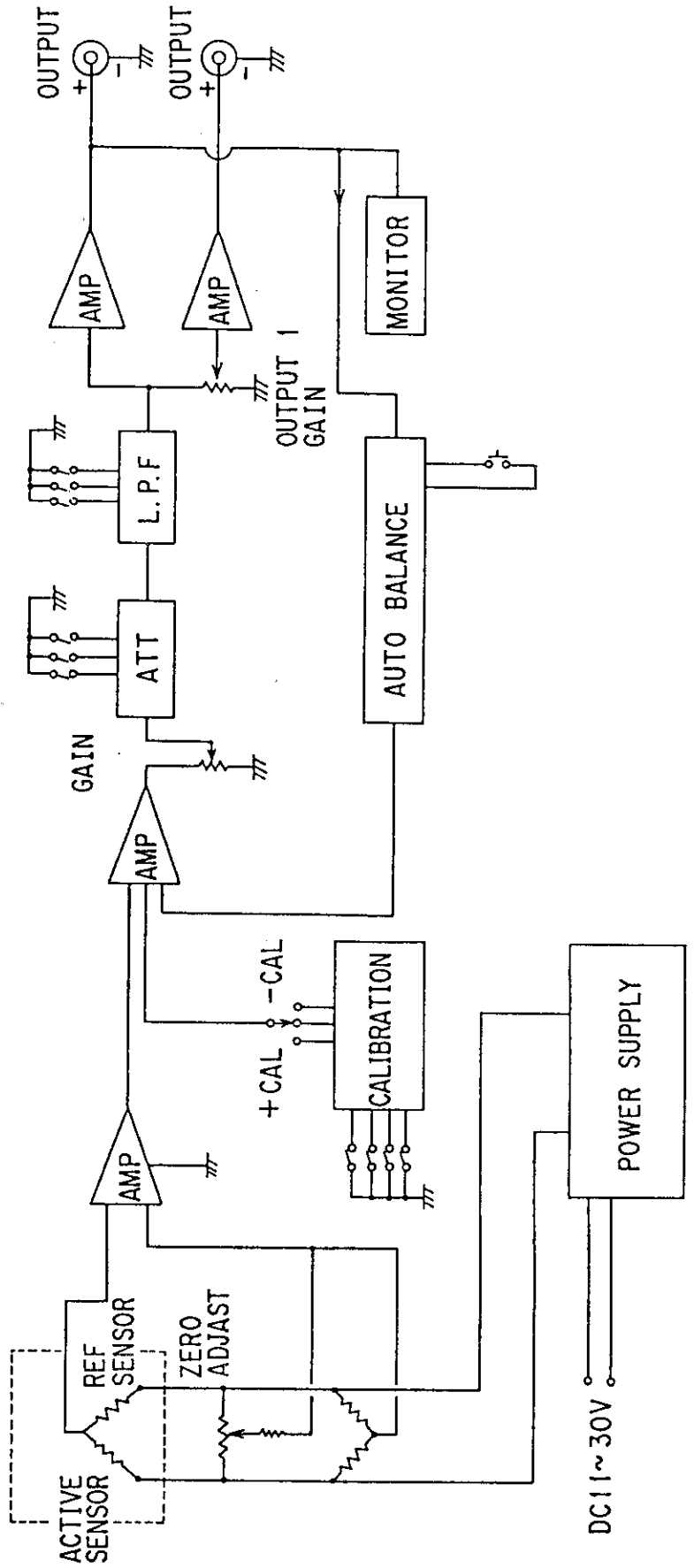

Fig. 3.6 Block diagram of the bolometer amplifier.

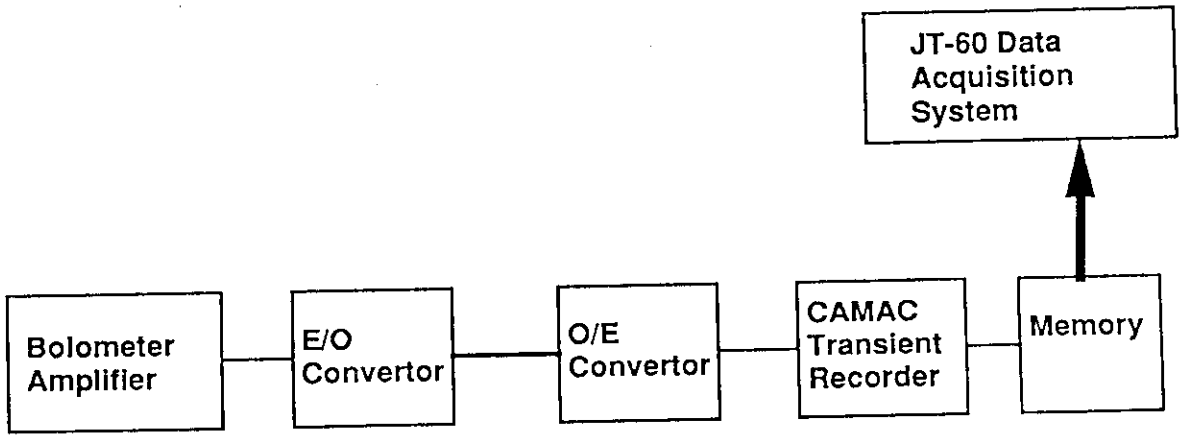

Fig. 3.7 Block diagram of the data acquisition for bolometric measurement.

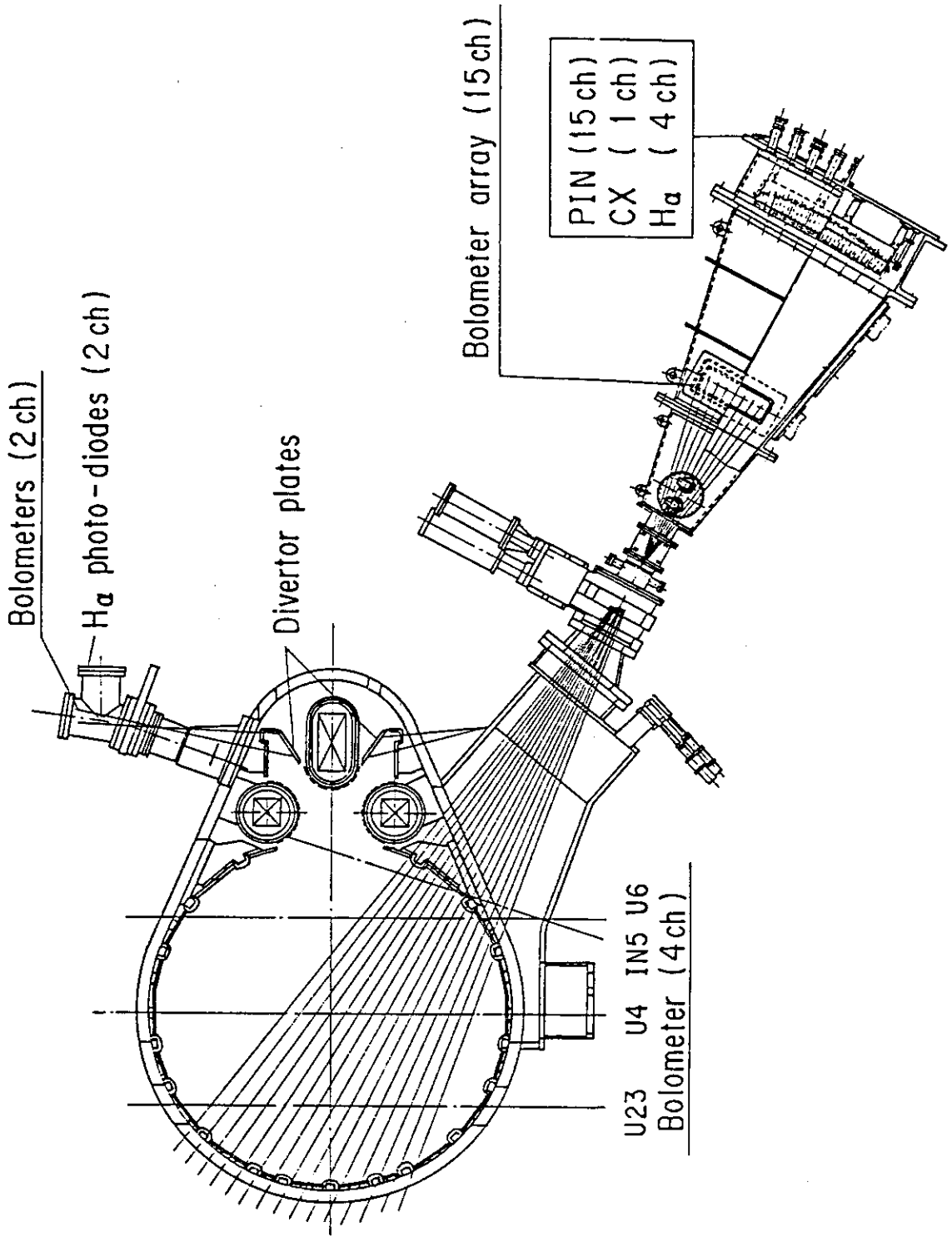

Fig. 3.8 Arrangement and sightlines of the bolometers in the period April 1985 - March 1987.

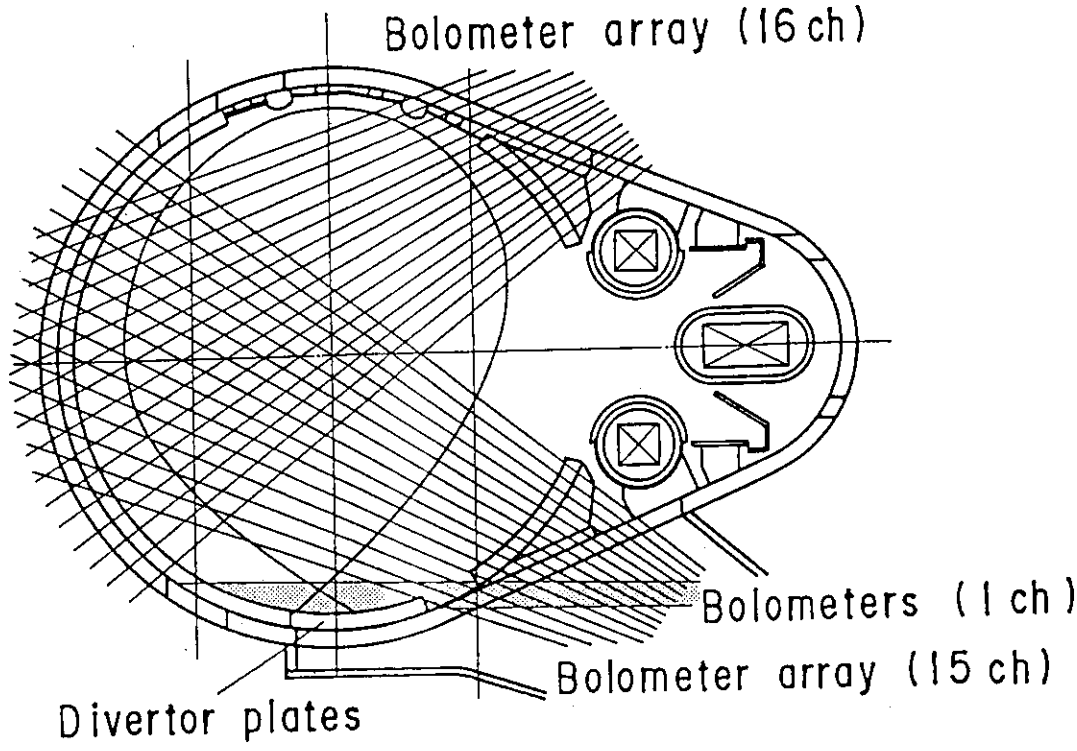

Fig. 3.9 Sightlines of the bolometers in the period May 1987 - October 1989.

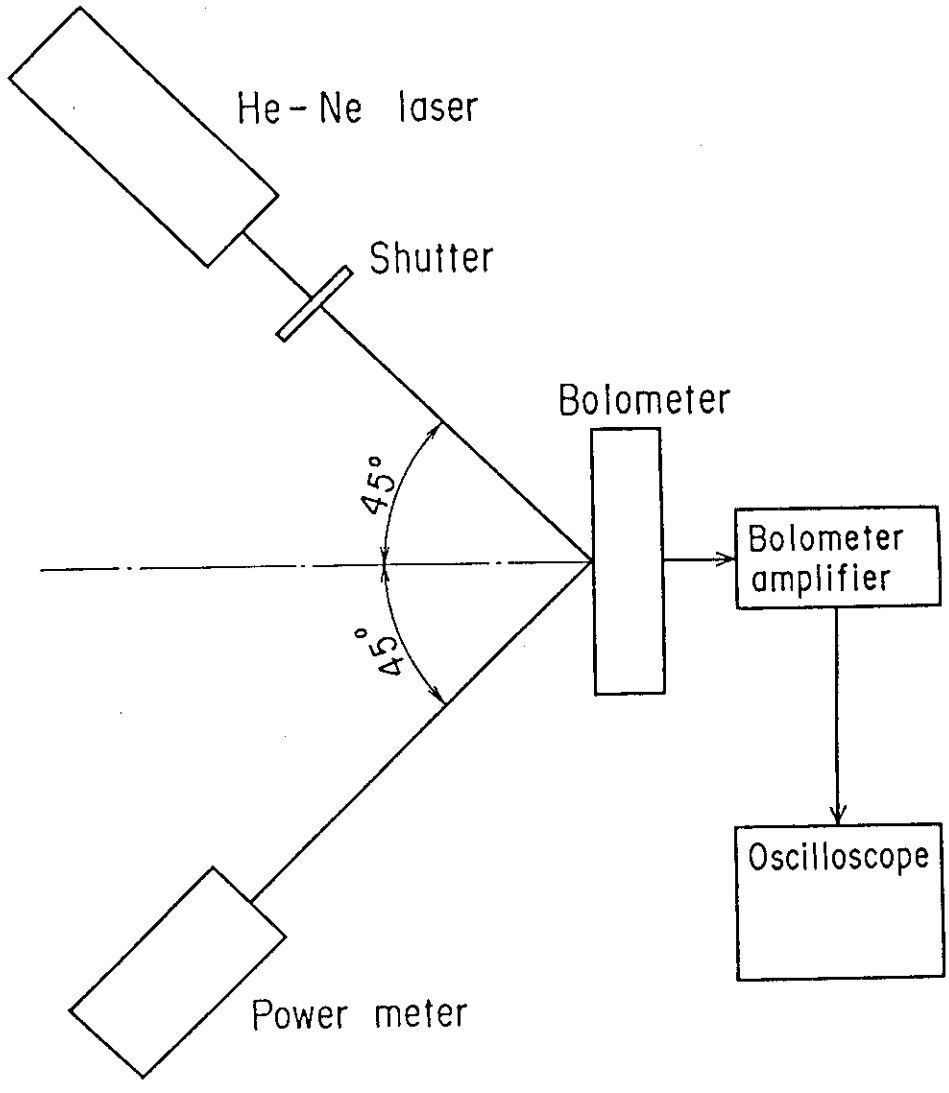

Fig. 3.10 Schematic diagram of the sensitivity calibration using He-Ne laser.

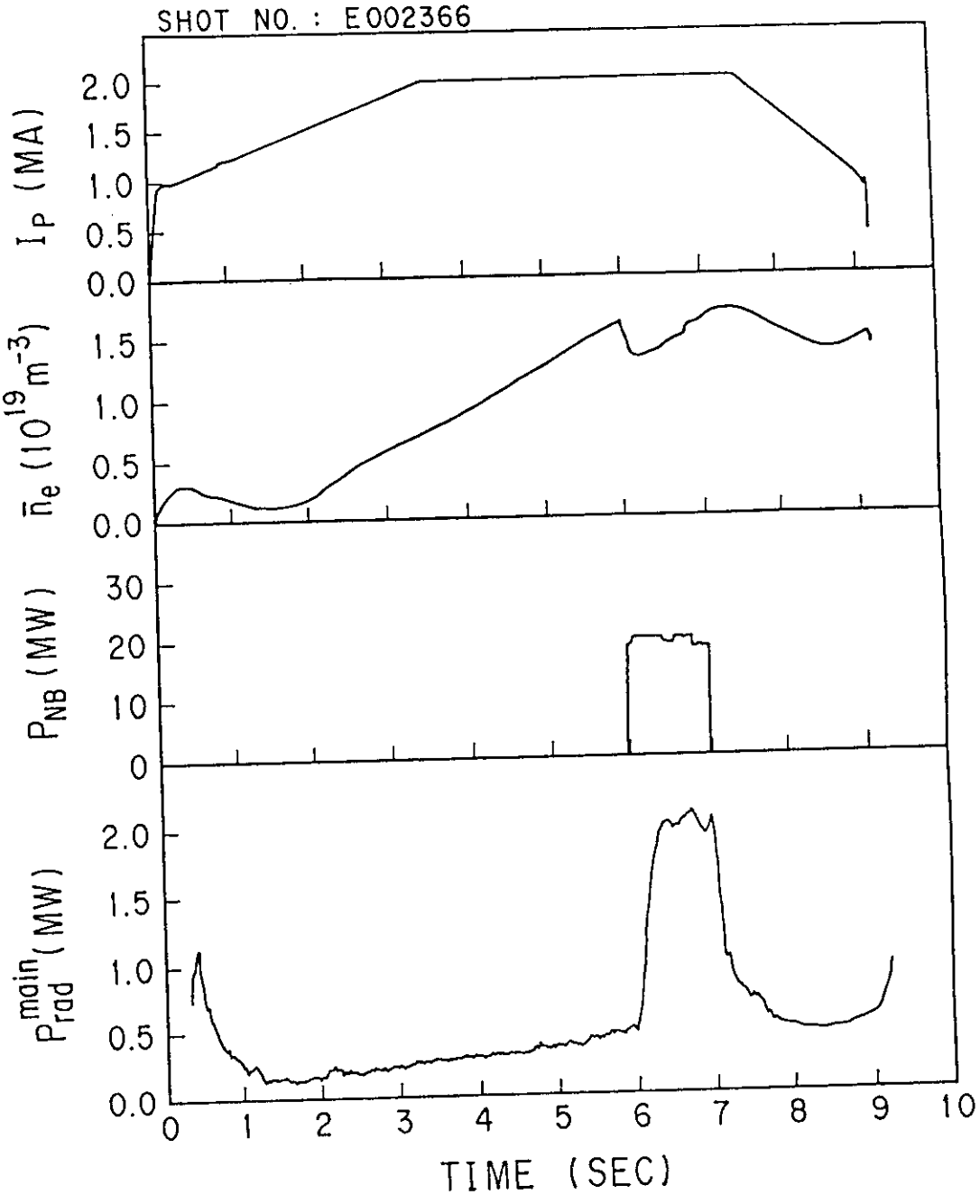

Fig. 3.11 Typical waveforms of plasma current I_P, line averaged electron density $\bar{n}_e$, injected NB power P_{NB}, and radiated power from the main plasma P_{rad}^{main} in the outer divertor discharge with NB heatings.

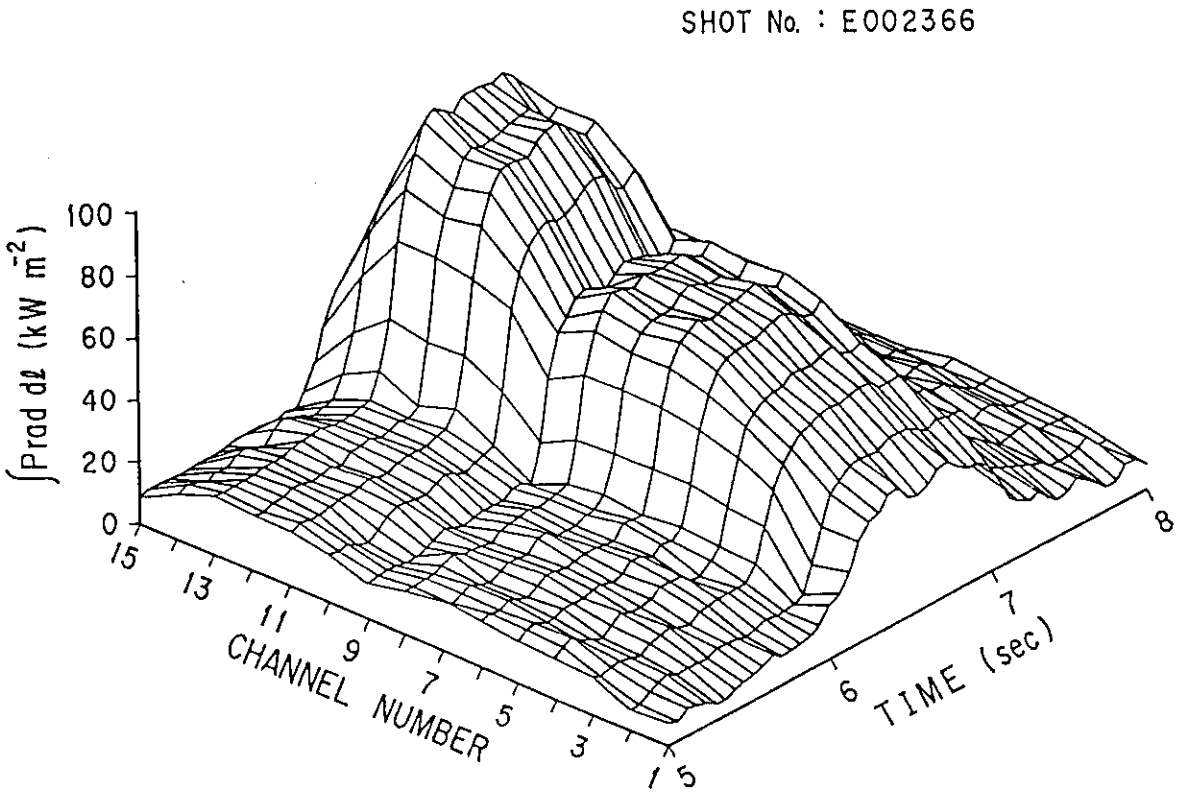

Fig. 3.12 Time evolution of the bolometer signals as a function of channel around the NB injection

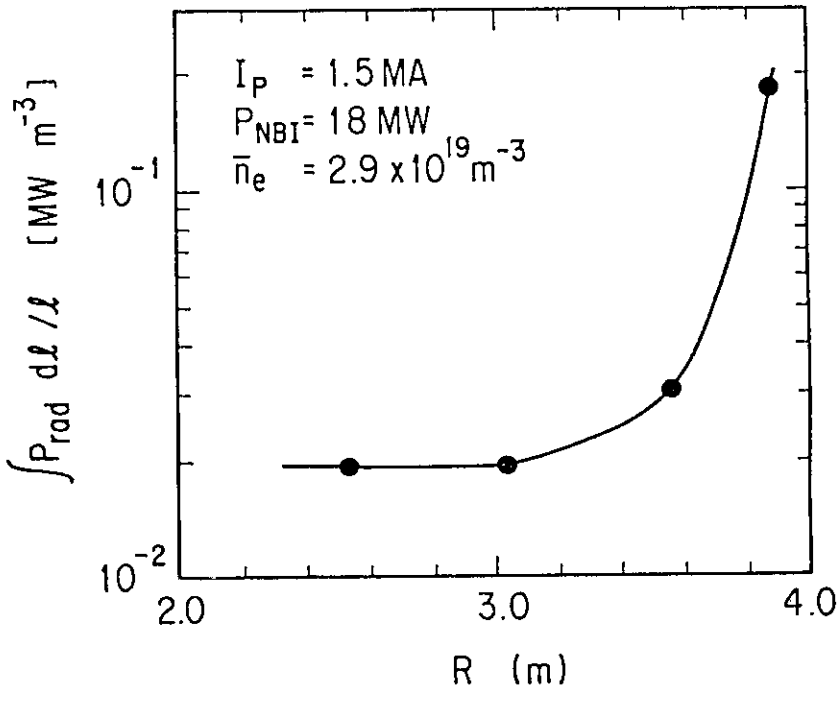

Fig. 3.13 Line averaged radiated powers measured with the three vertical bolometers and one viewing near the X-point plotted against the major radius of the sightline.

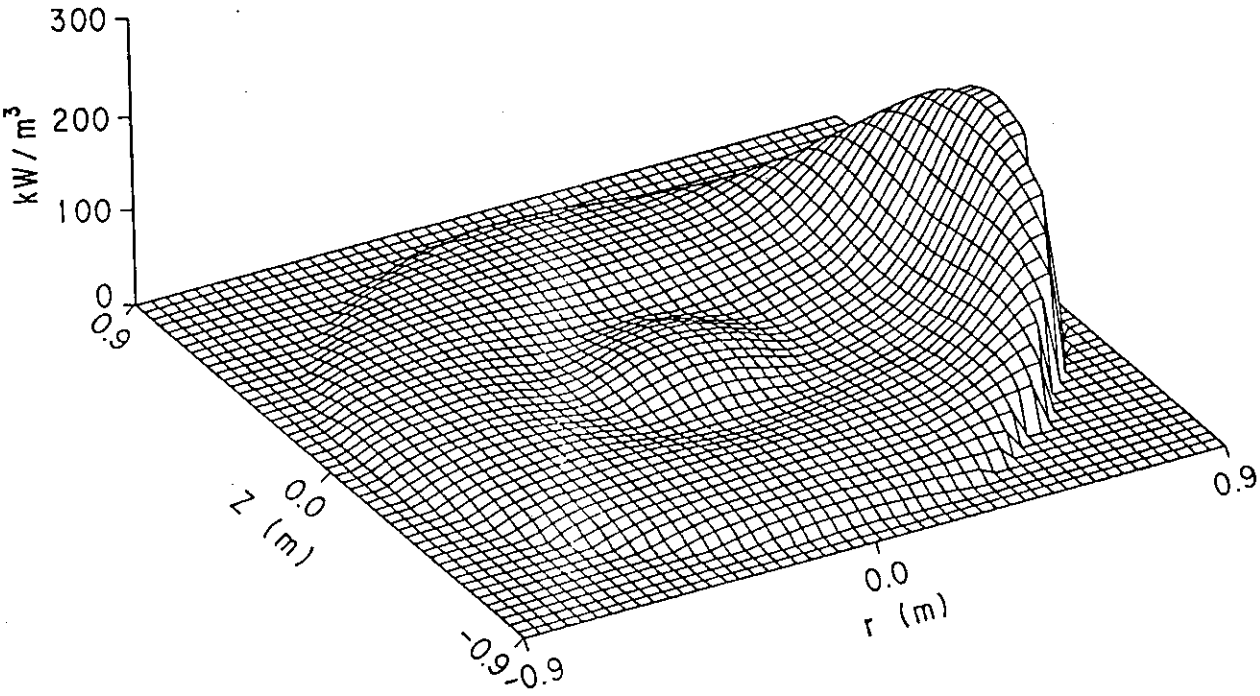

Fig. 3.14 Asymmetric radiation profile reconstructed by an Abel inversion with asymmetric term for NB-heated divertor discharge with $\bar{n}_e$ of 2.9×10^{-19} m^{-3}.

4. Soft X-ray Measurements by Pulse Height Analysis on JT-60

4.1 INTRODUCTION

The evolution of electron temperature and the behavior of impurities are important parameters in tokamak fusion plasmas. Soft x-ray spectrum has an information of electron temperature, low- and high-Z impurities. Moderate resolution x-ray spectroscopy is a powerfull tool for studing these parameters [1,2]. In order to estimate the electron temperature and to investigate the basic performance of impurities in JT-60, the x-ray pulse height analyzer (PHA) was constructed. The high purity germanium detector cooled by liquid-nitrogen is used to measure the soft x-ray spectra in the 3-60 keV energy range with time resolution of 100 ms. The x-ray spectrum consists of an exponentially decreasing continuum spectrum, due to bremsstrahlung and recombination radiation, and line radiation of high Z impurities. Electron temperature can be derived from the inclination of the continuum spectrum, and the concentrations of low- and high-Z impurities can be derived from the absolute measurements of the continuum and line radiation.

The experimental set-up of the PHA system is described in detail in Sec. 4.2. The analysis procedure of soft x-ray spectrum is reviewed in Sec. 4.3. In Sec. 4.4 the experimental results for measurements of electron temperature and the impurity concentrations are presented.

4.2 MEASUREMENT SYSTEM

4.2.1 Arrangement and Detector

The spatial arrangement of the PHA on JT-60 is shown in Fig. 4.1. The PHA is installed under the lower structure and views the center of the plasma through the vertical diagnostics port. The detailed view of the pulse-height analyzer system is shown in Fig. 4.2. The PHA is connected to the vacuum vessel of the JT-60 by about 4 m long inconel tube and the differetial pumping system using a turbo molecular pump.

The high purity germanium detector arranged at the bottom of this system is cooled by liquid nitrogen using the J-shaped cold finger. The high purity germanium crystal is mounted behind 0.025 mm thick beryllium window which keeps it vacuum isolated from the vacuum environment of JT-60. The crystal has an active area of about 80 mm^2 and thickness of 10 mm. The detector is most sensitive to photons in the rang 2-100 keV as shown in Fig. 4.3.

The detector views the plasma through the collimator and the thin-foil filter placed in front of the detector. The collimator is made of the 5mm-thick lead disk covered by 5 mm aluminium side by side, on which eight different diameter apertures are arranged. The x-ray intensity incident on the detector is remotely controlled by this rotating collimator disk. The apertures provides a large dynamic range of 10^3 in count rate to adjust the various conditions of the JT-60 plasma. A set of filters, which consists of 4 beryllium foils and 4 aluminium foils displaced on the aluminium disk, can be set remotely to adjust the cut off energy of the incident photons. The probability of pulse pile up is increased by too many photons incident on the detector. Figure 4.4 shows normal and pile up spectra of soft x-ray measured on JT-60. The pulse pile up becomes remarkable at count rate more than 40 kcps for this detection system. Therefore, the count rate has to be kept 10-40 kcps by choosing the suitable aperture and foil. Checking source of 3.7 MBq ^{241}Am is mounted between the filters and collimator to do *in-situ* energy calibration. The checking source is inserted on the viewing line remotely.

Ceramic breaks in front of the gate valve isolates the supporting structure of the PHA from the differential pumping system and the vacuum vessel electrically. Furthermore, the detector is isolated from the supporting structure by a poli-ether-ether-keton break which was can be use instead of a conflat type gasket and to be baked up to 180°C. The 30 mm-thick iron cylinder

surrounds the detector and the pre-amplifier, which are prevented against the influence of the leakage magnetic field from JT-60 and the electro-magnetic noise. Lead plates on the iron cylinder shields hard x-rays which are generated by collisions of runaway electrons with the limiters.

4.2.2 Electronics and Data Acquisition

The block diagram of the electronics is shown in Fig. 4.5. Charges generated by a x-ray photon in the detector are integrated by the charge sensitive pre-amplifier which is mounted to the detector directly. The first atage FET is cooled by liquid nitrogen to reduce thermal noises. The time constant of the pre-amplifier is made as short as possible in order to get higher count rate. The gain of the linear amplifier is adjusted so high that the energy range of measurement is from 3 to 60 keV typically. Though the amplifier has the pile up rejection circuit, it is not used in this experiment. Because the gain is set to be high in this experiment, the pile-up rejector is triggered by the thermal noise and then generates the event pulses of pulse pile up continuously. Shorter shaping time constant makes count rate higher, however, degrades an energy resolution. So the shaping time constant of the amplifier is set to be 1 μs.

The pulse height of the linear amplifier is analized by a CAMAC type spectroscopic ADC (pulse height analizer). The conversion gain of the ADC is selectable among 256, 512 and 1024. The degitized data by the ADC was transferred to four 32 KW histogram memories. The conversion gain of 1024 channels is employed typically, so that the spectrum is measured with time resolution of 100 ms throughout 10 s. The scalar recorded the total count rate of the pulses above a discrimination level which is same as that of the ADC. Furthermore, the dead time of the PHA system is estimated from the difference between the count rate of the scalar and that of the ADC.

4.2.3 Calibration of Detector

The absolute detection efficiency of the detector was calibrated by ^{55}Fe x-ray source whose energy was 5.9 keV. The phton emissivity of the source was calibrated to be $5.7 \times 10^5 \pm 5\%$ phton s^{-1} $4\pi^{-1}$ (at Sep. 2, 1985) by standard radiation source at the Electrotchnical Laboratory, Tsukuba. By correction the absorbtion of air between the detector and x-ray source, the absolute efficiency of 0.81 ± 0.08 was ontained for 5.9 keV photon. Energy calibration was carried

out by using checking sources of ^{55}Fe and ^{241}Am. The energy resolution of the detector was 0.38 keV of FWHM for 5.9 keV and 0.51 keV for 59.5 keVusing a 1-μs shaping time.

4.3 ANALYSIS OF SOFT X-RAY SPECTRUM

The spectral distribution of the soft x-ray emission in tokamak discharges can yield the valuable information on the electron temperature, impurity concentrations and the presence of runaway electrons. The electron temperature is obtained from the slope of soft x-ray spectrum in a semilogarismic plot, but the interpretation is complicated by radial profile effect, because the measured spectra are the line integral signals. The absolute intensity of the continuum radiation compared to only hydrogen bremsstrahlung is represented by the enhancement factor ζ, which characterizes the impurity concentrations in a plasma, as well as the effective ionic charge Z_{eff}. Typical soft x-ray spectrum consists of a continuum spectrum with a few impurity K- and L-lines. If the runaway electrons are produced substantially in the discharges, the high energy runaway tails become prevalent in the continuum spectrum. The metallic impurity concentrations can be estimated from the K- or L-lines spectra, and the residual light impurity concentrations from the enhancement factor ζ.

The x-ray emission from a plasma consists of a continuum of free-free bremsstrahlung and free-bound recombination radiation, and of a bound-bound line radiation. The energy spectrum of bremsstrahlung radiation for a Maxwellian plasma is [2]

$$\frac{dP_{ff,ij}(T_e,E_v)}{dE_v} = 3 \times 10^{-15}\, n_e\, n_i \frac{n_{ij}}{n_i} Z_{ff,ij}^2\, T_e^{-1/2}\, \bar{g}_{ff,ij} \exp(-\frac{E_v}{T_e}) \qquad (4.1)$$

$$[keV/keV \cdot cm^3 \cdot sec],$$

where i, j represent an i-impurity ion species and j-charge state. E_v, n_e, T_e represent the photon energy, electron density and electron temperature, respectively. $Z_{ff,ij}$ is the effective ionic charge for free-free bremsstrahlung, which is nearly equal to the nuclear charge [3]. $\bar{g}_{ff,ij}$ is the averaged free-free gaunt factor which is averaged over a Maxwellian electron velocity distribution, and is a function depending on the electron temperature and

photon energy, n_i is the total density of the i-impurity species, and n_{ij}/n_i is the relative density ratio of the j-ionic charge state of the impurity.

The formula of free-bound radiative recombination [2], which is obtained from the Kramers formula for the hydrogenic ions, is

$$\frac{dP_{fb,ij}(T_e,E_v)}{dE_v} = 3\times10^{-15}\, n_e\, n_i \frac{n_{ij}}{n_i} Z_{ij}^2\, T_e^{-1/2}\, \beta_{ij} \exp(-\frac{E_v}{T_e}) , \tag{4.2}$$

$$\beta_{ij}(T_e,E_v) = \frac{\xi}{n^3}\bar{g}_{fb,ij}\frac{I_{ij}}{T_e}\exp(\frac{I_{ij}}{T_e})\,\theta\,(E_v - I_{ij})$$

$$+\sum_{\alpha=1}\frac{2}{(n+\alpha)}\bar{g}_{fb,ij}\frac{Z_{ij}^2\cdot I_H}{(n+\alpha)^2\,T_e}\exp(\frac{Z_{ij}^2\cdot I_H}{(n+\alpha)^2\,T_e})\,\theta\,(E_v - I_{ij,n+\alpha}) ,$$

where Z_{ij} is the charge of ij-ion before recombination, and I_H and I_{ij} are the ionization potentials of hydrogen and the recombined electron in a ground state, respectively. The first term in β_{ij} represents the recombination to the valence shell-n with empty spaces ξ and the second term is the contribution to the quantum states $(n+\alpha)$. As the photon energy is the sum of the kinetic and binding energies of the recombining electron, the spectrum has the recombination steps at the energies equal to $I_{ij,n+\alpha}$nd is indicated by the step function $\theta(E_v - I_{ij,n+\alpha})$. $\bar{g}_{fb}$ is the averaged free-bound gaunt factor and assumed to be unity in most cases [8].

From Eqs. (4.1) and (4.2), total x-ray spectrum is given using the enhancement factor ζ as

$$\frac{dP_{tot}(T_e,E_v)}{dE_v} = \sum_i\sum_j\left(\frac{dP_{ff,ij}}{dE_v}+\frac{dP_{fb,ij}}{dE_v}\right)$$

$$= 3\times10^{-15}\,\zeta\,\bar{g}_{ff,H}\,n_e^2\,T_e^{-1/2}\,\exp(-\frac{E_v}{T_e}) . \tag{4.3}$$

Here we define the factor γ_{ij} as well as in Ref. [3], and the relation between γ_{ij} and ζ is given as

$$\frac{dP_{tot,ij}}{dE_v} = \gamma_{ij}\frac{dP_{ff,ij}}{dE_v} , \tag{4.4}$$

$$\gamma_{ij} = \frac{\beta_{ij} \cdot Z_{ij}^2}{\bar{g}_{ff,ij} \cdot Z_{N,i}^2} + 1 \quad , \tag{4.5}$$

$$\gamma_i = \sum_j \gamma_{ij} \frac{n_{ij}}{n_i} \quad , \tag{4.6}$$

$$\zeta = \frac{1}{\bar{g}_{ff,H}} \sum_i \frac{n_i}{n_e} \gamma_i \bar{g}_{ff,i} Z_{N,i}^2 \quad . \tag{4.7}$$

The charge state fractions of an i-ion are unknown, which is dominated by the balance between ionization and recombination, and in considerably affected by the radial direction particle transport. But for the light impurities, it can be assumed that all ions are stripped perfectly.

The dominant processes of the bound-bound line radiation are through to be electron collisional excitation and dielectronic recombination [6]. For metallic impurities, K- or L-line photons are emitted in the energy range where the PHA detectors are sensitive, which characterize the impurity elements and their concentrations. The photon emissivity of i-ion S_i [photons/$cm^3 \cdot s$] is represented by

$$S_i = n_e n_i \sum_j \frac{n_{ij}}{n_i} \langle \sigma v \rangle_{ij} \quad , \tag{4.8}$$

where $<\sigma v>_{ij}$ is the total excitation rate averaged over a Maxwellian velocity distribution [6,7]. The line integrated value is

$$S_L = \left(\frac{\overline{n_i}}{\overline{n_e}} \right) \int n_e(r)^2 \langle \sigma v \rangle_i \, dl \quad , \tag{4.9}$$

where $\sum_j \left(n_{ij} / n_i \right) \langle \sigma v \rangle_{ij} = \langle \sigma v \rangle_i$ and $\left(\overline{n_i / n_e} \right)$ is the averaged impurity density for the x-ray emitting high temperature region. This value is related to the detected photon count rate C [count/s] as

$$C = \varepsilon_f \varepsilon_d S_d \frac{\Delta \Omega}{4\pi} S_L \tag{4.10}$$

where ε_f, ε_d, S_d, and $\Delta\Omega/4\pi$, represent respectively the filter transparency, the detection efficiency, the detector sensitive area and the solid angle.

The neutrality of plasma is represented by

$$n_e = n_p + \sum_{i \neq p} Z_i \, n_i \quad , \tag{4.11}$$

where n_p is proton density. Therefore the effective ionic charge Z_{eff} is given by

$$Z_{eff} = 1 + \frac{\sum_{i \neq p} \left(Z_i^2 - Z_i\right) n_i}{n_e} \quad . \tag{4.12}$$

4.4 EXPERIMENTAL RESULTS

4.4.1 Soft X-ray Spectrum

Figure 4.6 shows the typical spectrum of the soft x-ray emitted from the main plasma in the JT-60 divertor discharge. In the spectrum, Kα and Kβ lines of titanium and Kα of nickel were identified. The former is the coating material of the first wall and the latter is the base metal of inconel 625, of which the JT-60 first wall is made. No significant lines of molybdenum, which was the base material of the limiter, were observed in the normal discharges except outer divertor discharges with high-power NB heating. The following sections describe the electron temperature and the impurity concentration from the soft x-ray PHA measurements.

4.4.2 Electron Temperature

Figure 4.7 shows the time evolution of the plasma current, electron density and electron temperature from PHA for the divertor discharge of I_p=1.5 MA, B_T=4.5 T. The electron density was increasing gradually and reached its peak at about 7.0 s, when inversely the electron temperature showed minimum value. This tendency was more remarkable in Fig. 4.8. This data was obtained from the plasma current flat top phases. As the electron density increased, the effective ionic charge decreased. So the ohmic input power decreased and therefore the electron temperature decreased.

The PHA measures the line integrated spectrum along the viewing chord and it represents central high temperature region. The profile effect is approximately less than 10% in the central electron temperature. In Fig. 4.9 the temperature obtained by PHA is compared with the central electron temperature measured by Thomson scattering. In this figure, PHA temperature was a little higher than Thomson scattering temperature. But the good agreement was obtained in the statistical error range.

4.4.3 Impurity Concentration and Effective Ionic Charge

In the JT-60 plasma, the dominant metal impurity species were titanium, nickel and chromium. In Fig. 4.6 these impurity lines are seen except chromium line, of which K_α-line is overlapped on Ti-K_β line. During the strong NB heating discharges, the Mo-K_α line which was generated on the divertor plate was observed and these discharges were often terminated by the hard radiation energy loss.

Figure 4.10 shows the effective ionic charge Z_{eff} as the function of electron density. As the electron density increased, Z_{eff} approached asymptotically the value of 1. The dependence of Z_{eff} on the plasma current was not clear, but the values of limiter discharges were far larger than those of divertor discharges. No difference between the ohmic and NB heating discharges can be seen and this result is supported by the visible bremsstrahlung spectroscopy [9]. The value of Z_{eff} estimated by PHA was 1.2 at $\bar{n}_e = 3.0 \times 10^{19}$ m^{-3}, but the values obtained by the other diagnostics, the visible bremsstrahlung spectroscopy [9] and the active beam scattering system [10], were about 1.5 at the same electron density. This deviation is under examination. In order to calculate Z_{eff}, titanium and nickel were included as the dominant metal impurities and oxygen was assumed to be only light impurity because of the lack of enough spectroscopic information. The electron density and temperature profile were given from the 4 channel interferometers and 6 channel Thomson scattering measurements, respectively.

In Fig. 4.11, the titanium concentrations of the divertor and limiter discharges which were estimated from Ti-K_α photons are shown as the function of electron density. The symbol of He shows the helium discharges and all the others are hydrogen discharges. To calculate the excitation rate coefficient, the dominant three processes were considered; the electron collisional excitation [6,7], the dielectronic recombination and the radiative

recombination into the K-shell. The titanium concentrations of NB heating discharges were about factor 2 larger than those of ohmically heating. The values of helium discharges were far larger than those of hydrogen discharges, but the exponentially decreasing features with the increasing of electron density were seen in all discharges.

Figure 4.12 shows oxygen concentration as the function of electron density. It decreased with the increasing of electron density as well as titanium concentration, but its decline was smaller than one of titanium. The oxygen concentrations of limiter discharges were about factor 5 larger than those of divertor discharges, but no clear difference could be seen between ohmic and NB heating discharges for the divertor discharges. These value estimated by PHA were not about factor 2 smaller than those obtained by the active beam scattering system.

4.5 DISCUSSION AND CONCLUSION

The x-ray pulse height analysis was performed using a liquid-nitrogen cooled high germanium detector and by this measurement the electron temperature and impurity concentrations were estimated. The electron temperature measured by PHA, which was not the central electron temperature strictly but represented the central high temperature region, corresponded to the temperature measured by Thomson scattering system within the statistical error range. The titanium concentration was decreasing exponentially with the increasing of electron density and its typical value was 1.0×10^{-3}% at $\overline{n}_e = 3.0 \times 10^{13}$ m^{-3}. About the effective ionic charge Z_{eff} which was dominated by light impurities in the JT-60 plasma, there was the unnegligible difference between the PHA measurement and others; the visible bremsstrahlung spectroscopy and the active beam scattering system. This difference may be due to the ambiguity of the atomic cross section considered in the calculation process or due to the system calibration error.

REFERENCES TO CHAPTER 4

[1] K.W. Hill, M. Bitter, M. Diesso, L. Dudek, S. Von Goeler, S. Hayes, L.C. Johnson, J. Kiraly, E. Moshey, G. Renda, S. Sesnic, N.R. Sauthoff, F. Tenney and K.M. Young, Rev. Sci. Instrum., **56** (1985) 840.

[2] E.H. Silver, M. Bitter, K. Brau, D. Eames, A. Greenberger, K.W. Hill, D.M. Meade, W. Roney, N.R. Sauthoff and S. Von Goeler, Rev. Sci. Instrum. **53** 1198(1982) 1198.

[3] S. Von Goeler, W. Stodiek, H. Eubank, H. Fishman, S. Grebenshchikov and E. Hinnov, Nucl. Fusion **15** (1975) 301.

[4] K.W. Hill, M. Bitter, N.L. Bretz, M. Diesso, P.C. Efthimion, S. Von Goeler, J. Kiraly, A.T. Ramsey, N.R. Sauthoff, J. Schivell and S. Sesnic, PPPL-2309 (1986).

[5] K.H. Behringer, P.G. Carolan, B. Denne, G. Decker, W. Engelhardt, M.J. Forrest, R. Gill, N. Gottardi, N.C. Hawkes, E. Källne, H. Krause, G. Magyar, M. Mansfield, F. Mast, P. Morgan, N.J. Peacock, M.F. Stamp and H.P. Summers, Nucl. Fusion **26** (1986) 751.

[6] C. Breton, C. De Michelis and M. Mattioli; J. Quant. Spectrosc. Radiat. Transfer **19** (1978) 367.

[7] C. De Michelis and M. Mattioli, Nucl. Fusion **21** (1981) 677.

[8] A. Costescu and N. Mezincescu, Phys. Lett. A **29** (1984) 459.

[9] H. Kubo, T. Sugie, A. Sakasai, Y. Koide, N. Nishino, T. Hirayama, T. Nishitani, K. Nagashima, N. Akaoka and JT-60 Team, Nucl. Fusion **29** (1989) 571.

[10] H. Takeuchi, K. Tobita, Y. Kusama, M. Nemoto, T. Itoh, Y. Tsukahara and JT-60 Team, Rev. Sci. Instrum. **59** (1988) 1652.

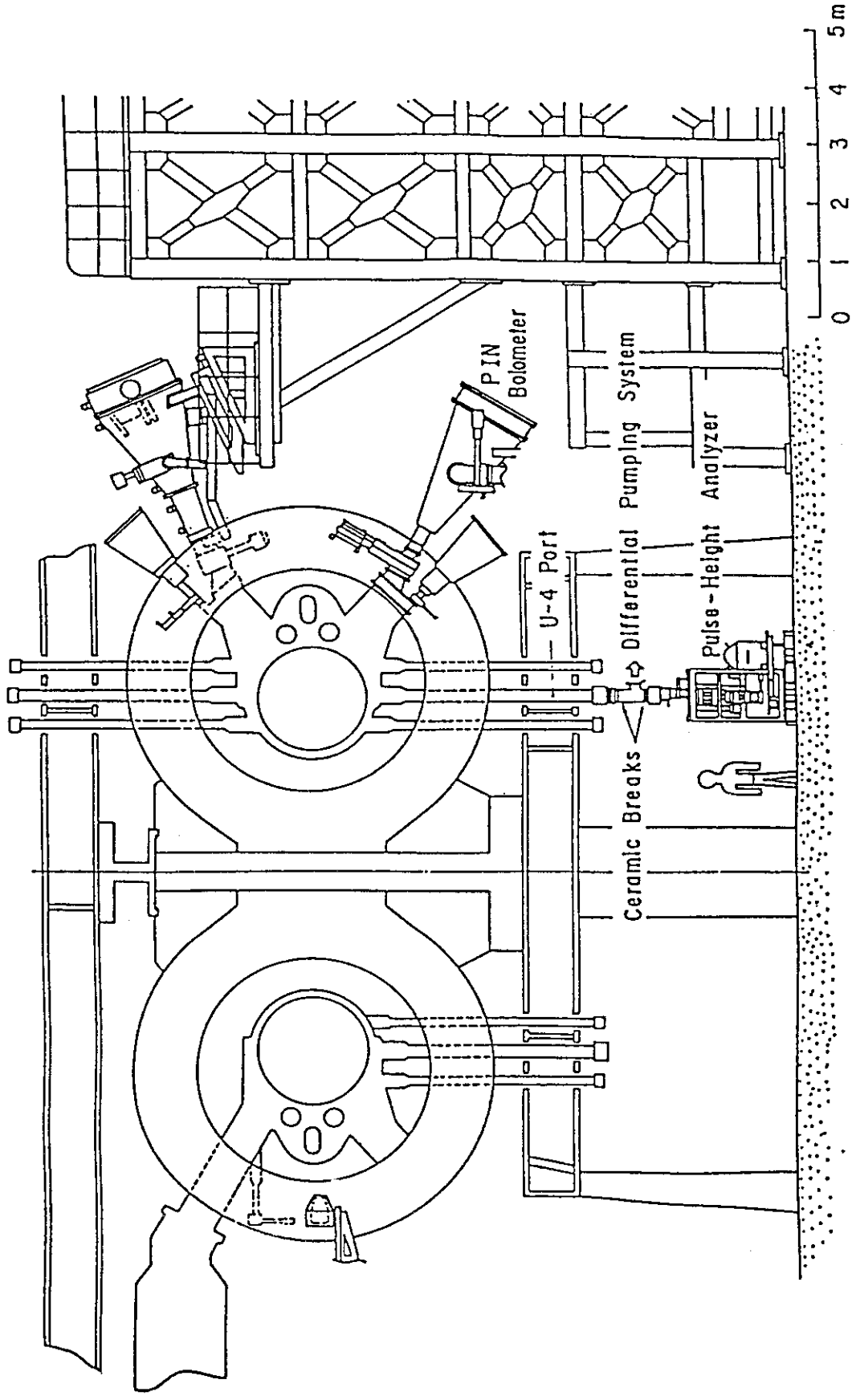

Fig. 4.1 Schematic view of the pulse height analyzer on JT-60.

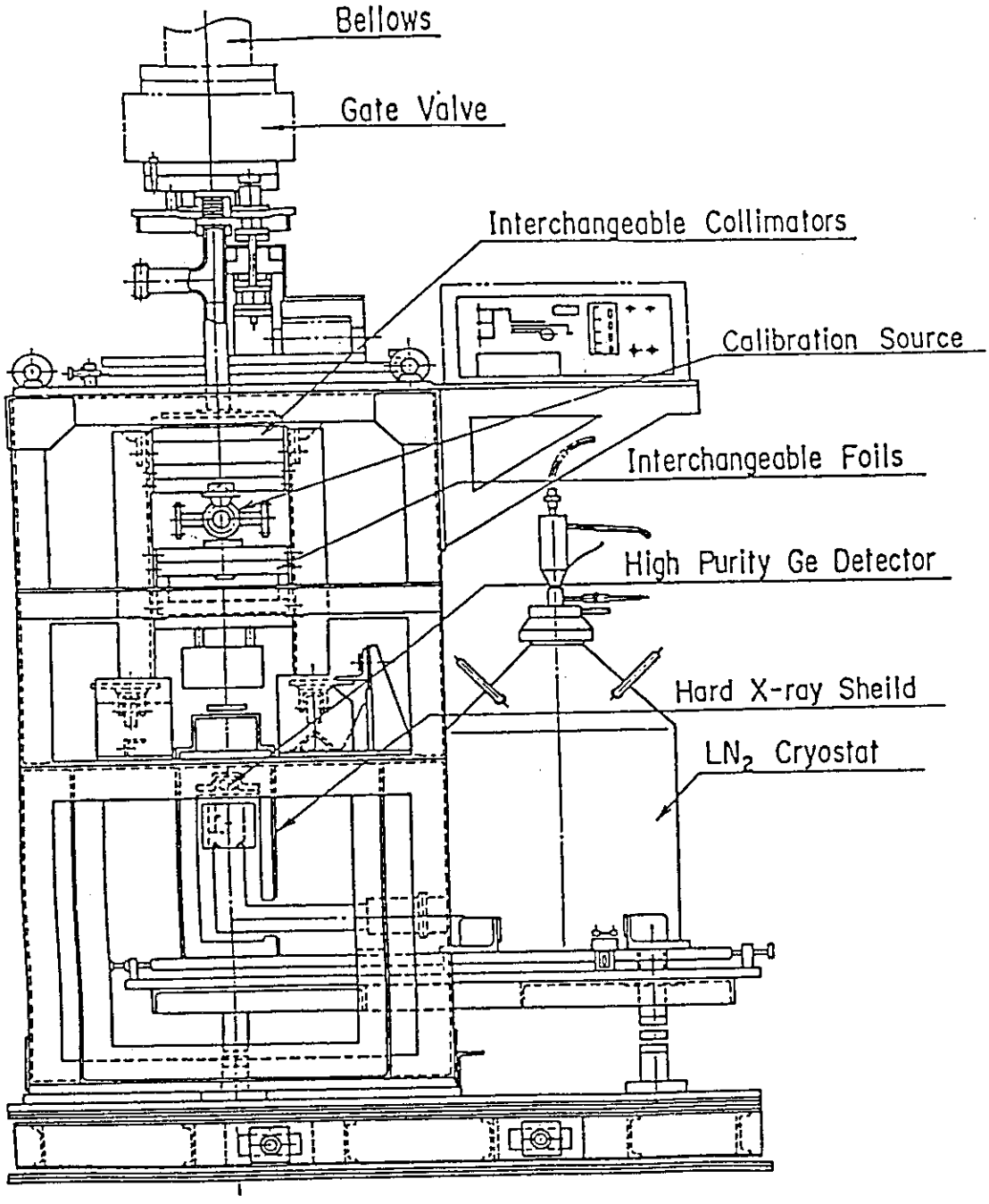

Fig. 4.2 Detailed constitution of the pulse height analyzer.

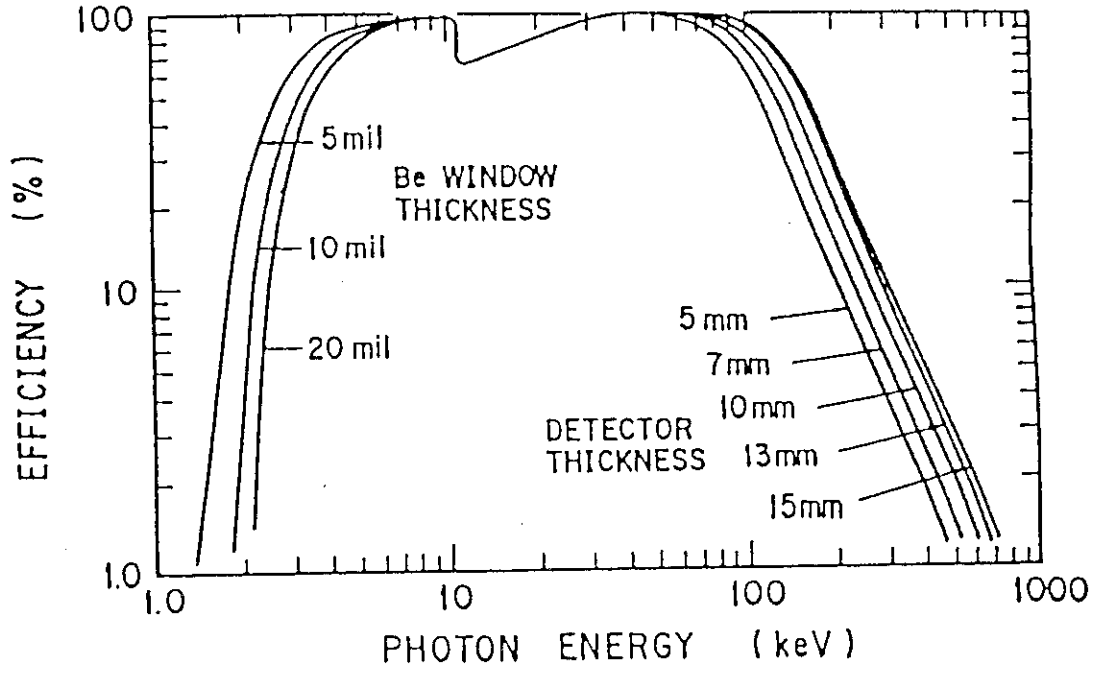

Fig. 4.3 Detection efficiencies of plena type germanium detector with various window thickness.

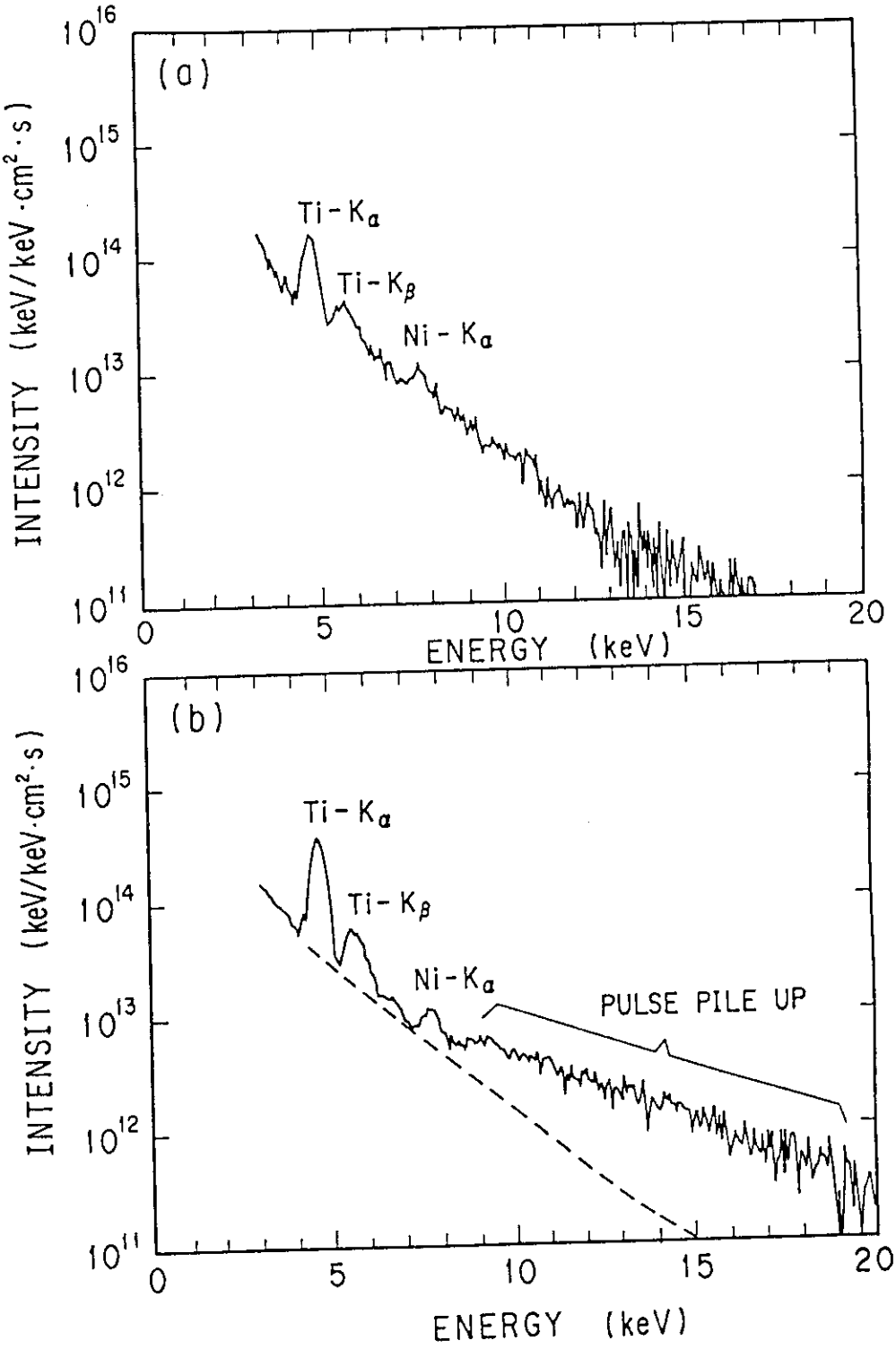

Fig. 4.4 Typical spectra with and without pulse pile-up.

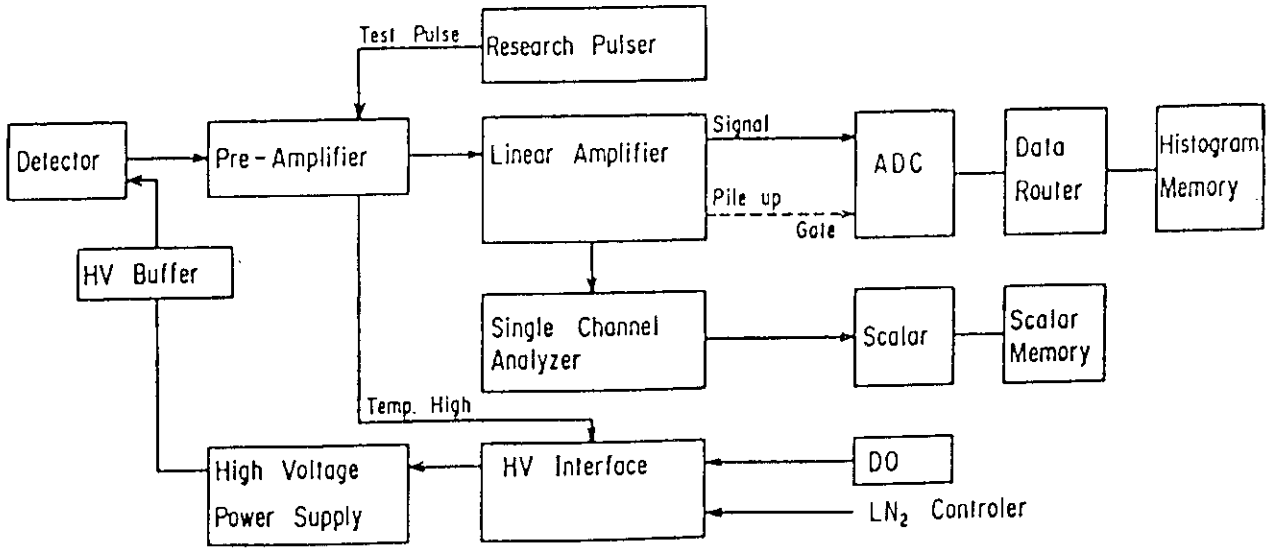

Fig. 4.5 Block diagram of the electronics for the pulse height analyzer.

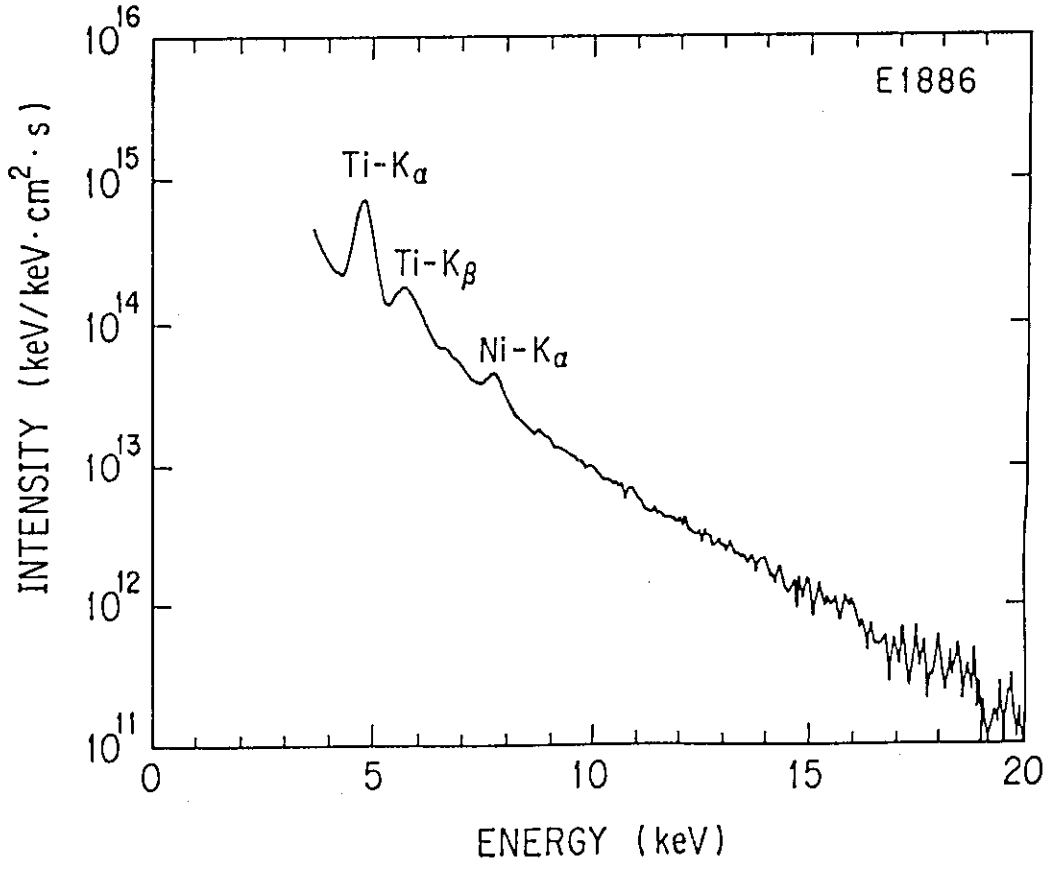

Fig. 4.6 Typical soft x-ray spectrum of 1.5 MA divertor discharge. Titanium and nickel lines were identified on continuum radiation spectrum.

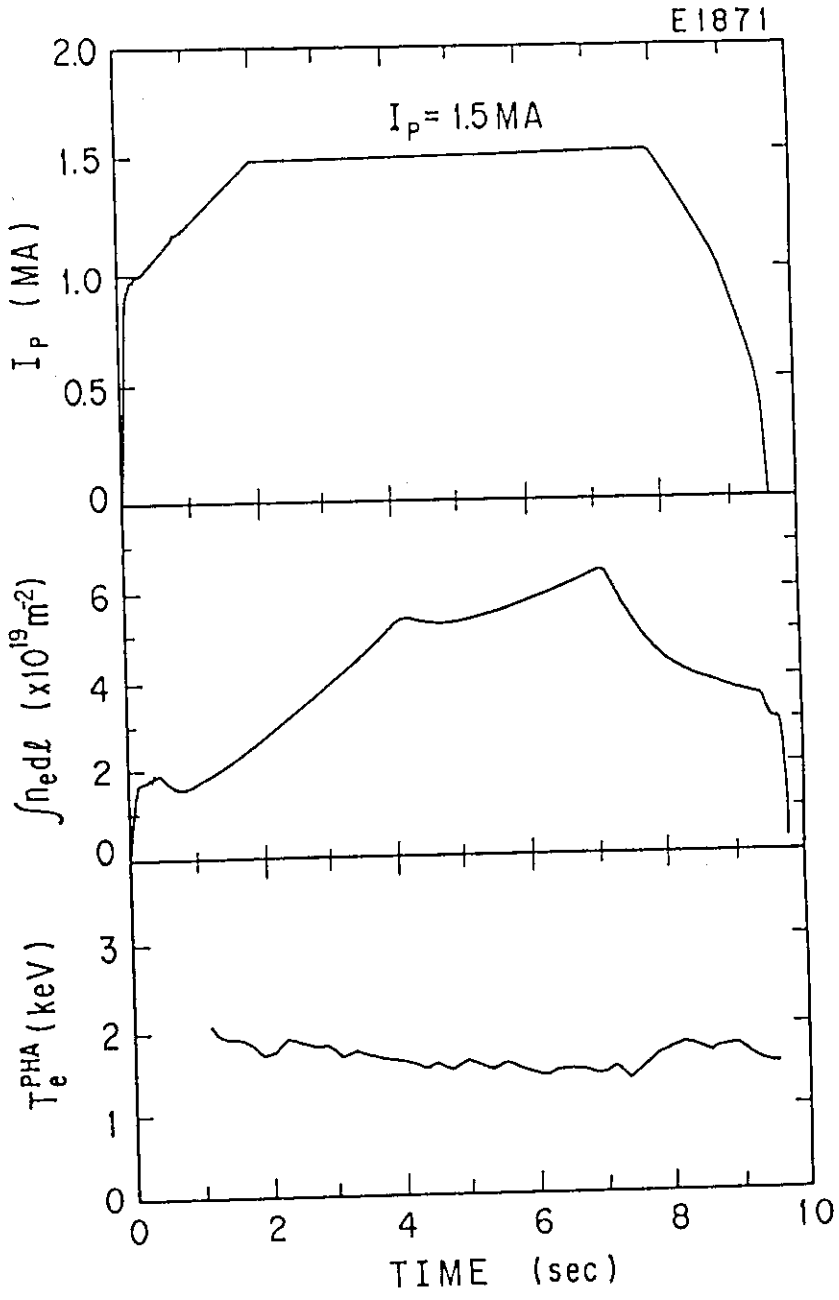

Fig. 4.7 Time evolution of plasma current, line electron density and electron temperature measured by PHA.

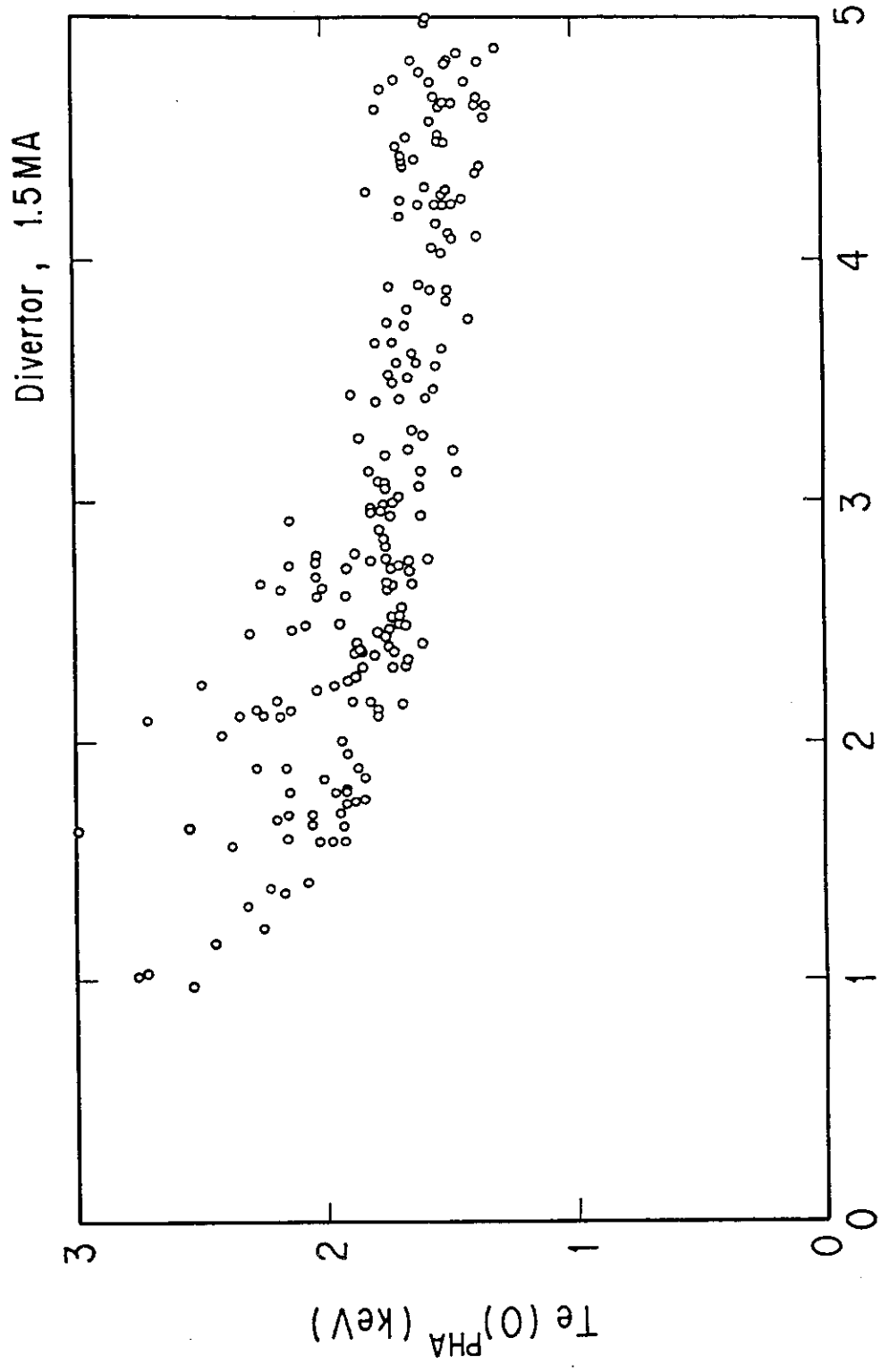

Fig. 4.8 Electron temperature measured by PHA as a function of central electron density on the condition of I_P = 1.5 MA and B_T = 4~4.5 T.

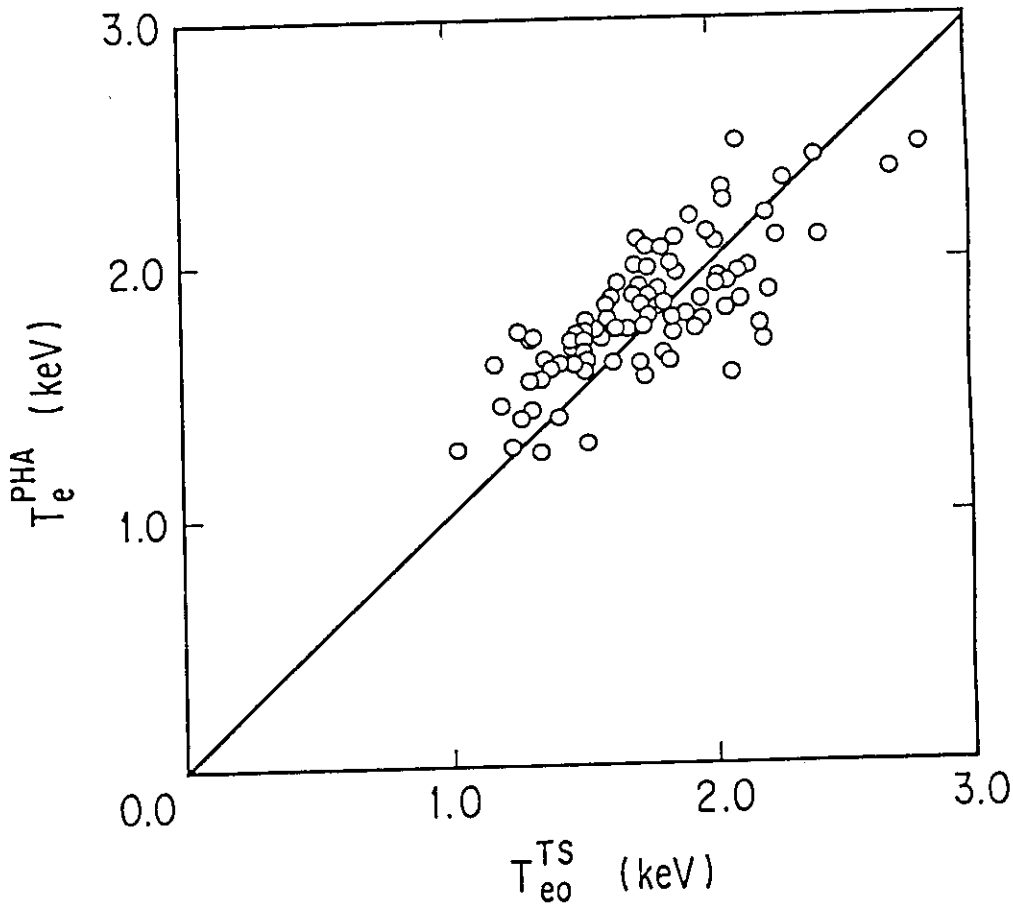

Fig. 4.9 Electron temperature measured by PHA versus that by Thomson scattering.

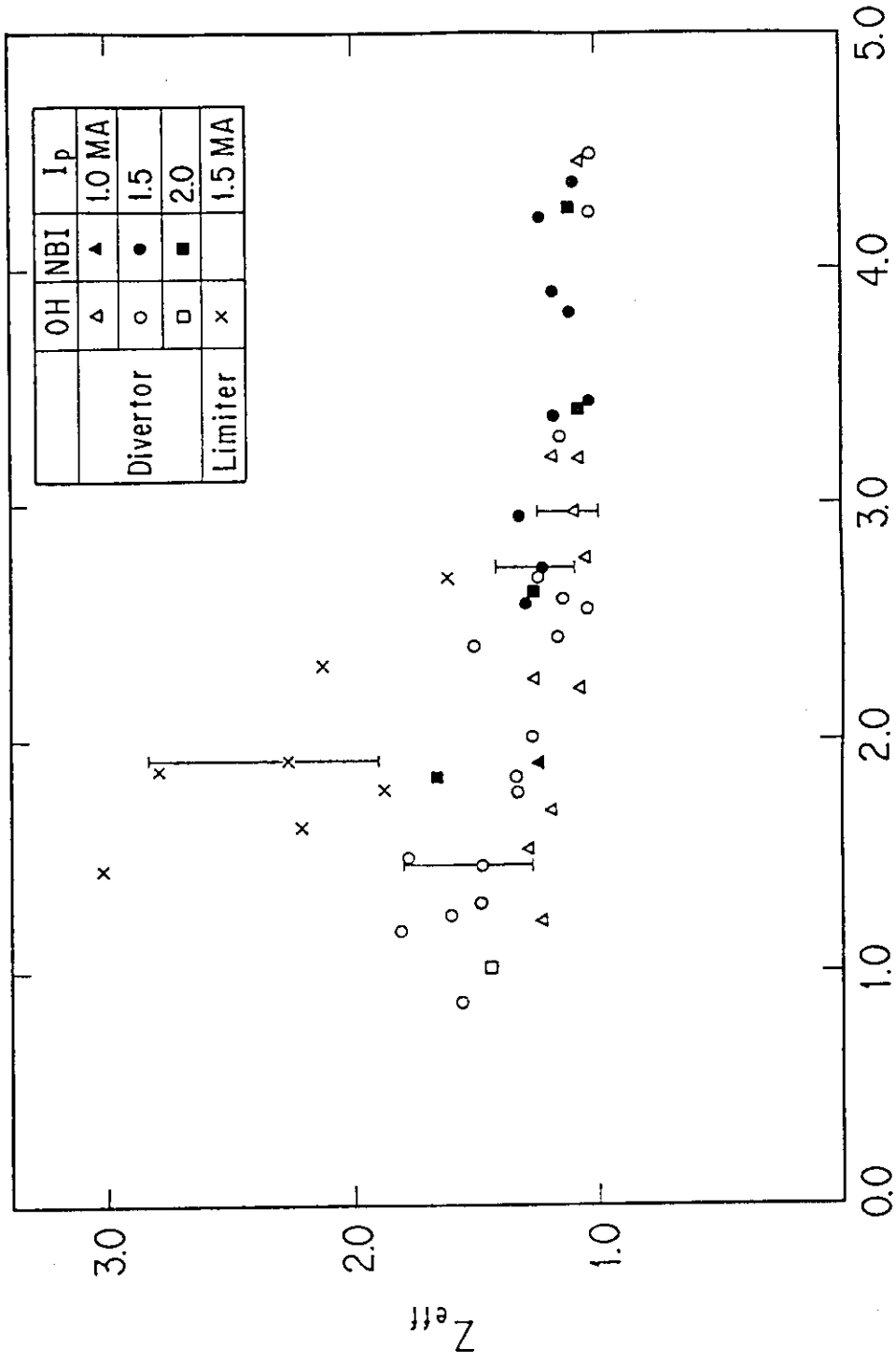

Fig. 4.10 Effective ionic charge Z_{eff} as a function of line averaged electron density.

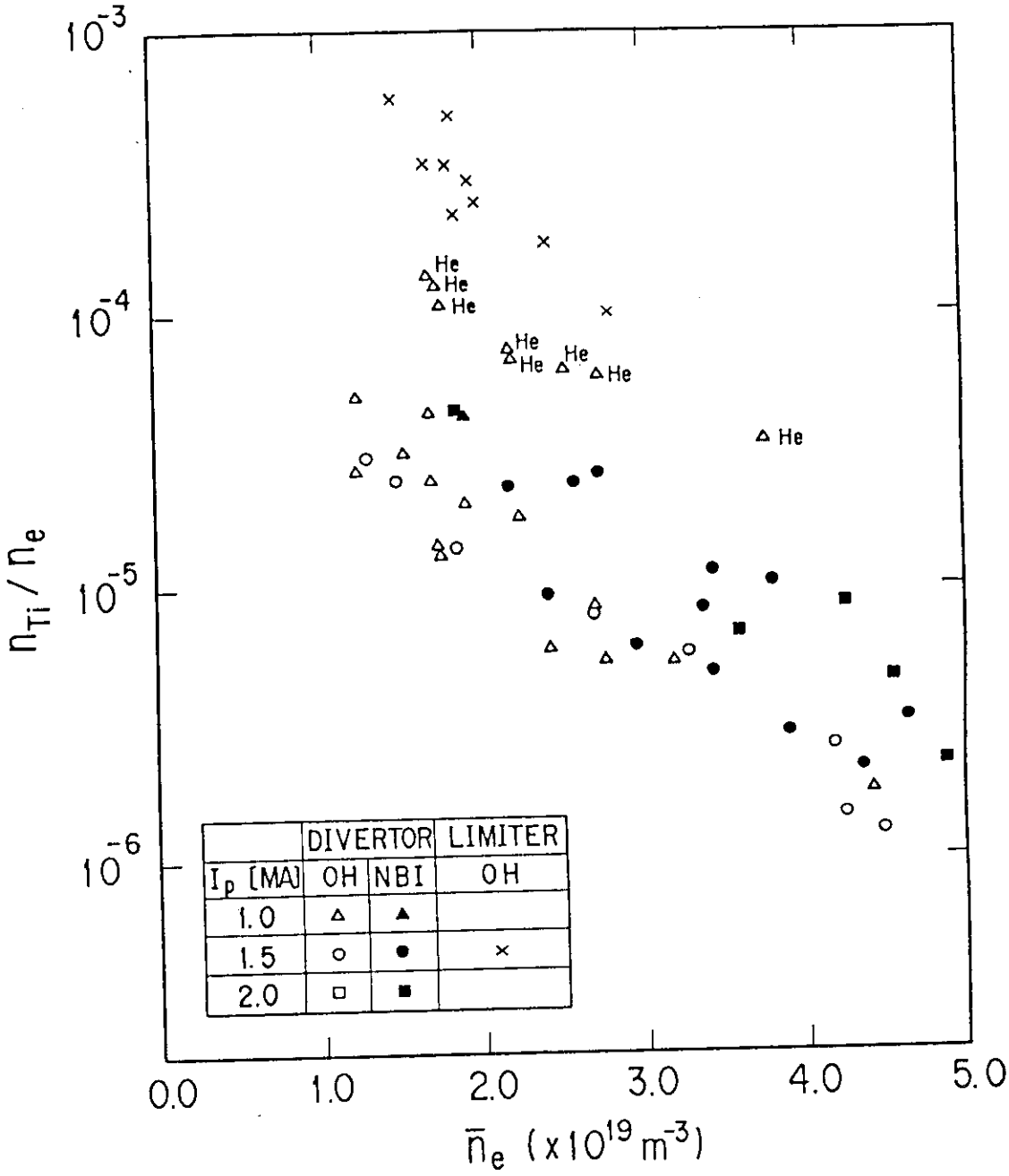

Fig. 4.11 Titanium concentration as a function of line averaged electron density.

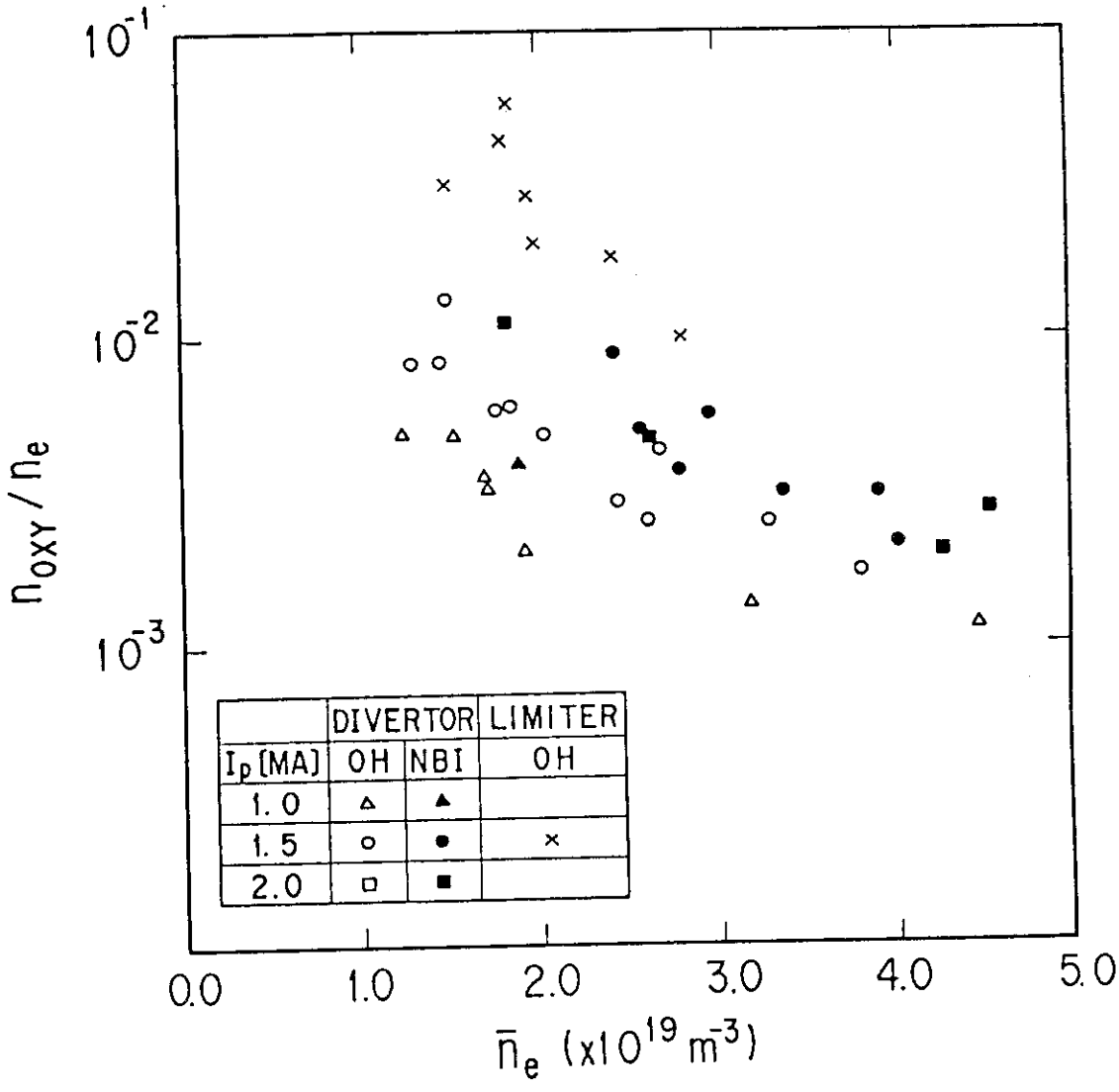

Fig. 4.12 Oxygen concentration as a function of line averaged electron density. Oxygen was considered as the only light impurity.

5. Soft X-ray Intensity and Balmer α Line Measurement Systems on JT-60

5.1 SOFT X-RAY INTENSITY MEASUREMENT SYSTEM

5.1.1 Introduction

One-dimensional imaging of soft x-ray intensity (x-ray imaging) can provide several interesting parameters of tokamak plasmas with excellent spatial and temporal resolutions in spite of the simple mechanism. So the x-ray imaging has been applied to most tokamaks [1-8]. The most common use of the x-ray imaging is to study magnetohydrodynamic (MHD) instabilities. Especially, sawtooth study originated at the ST tokamak using a single detector [9] has been evolved via poloidal/toroidal mode analysis [10] to be a MHD study using a tomography technique [11-14]. Other uses of the x-ray imaging have been studies of the radiated power and rapid transport of impurity ions in the plasma, the electron thermal conductivity from the heat pulse propagation in the sawtooth oscillations, the electron temperature profile using a filter absorption technique, and the toroidal rotation velocity from the frequency of the m = 1 oscillations.

In JT-60, thirty channels of PIN diode detectors with the changeable multi-absorption filters were installed as the x-ray imaging system.

5.1.2 Theory of Measurement

The soft x-rays radiated from the plasma consists of a continuum radiation and line radiations of impurity ions. As discussed in Sec. 4.3, the continuum radiation spectrum is represented by

$$\frac{dP_{tot}(T_e,E_v)}{dE_v} = 3\times10^{-15}\,\zeta\,\bar{g}_{ff,H}\,n_e^2\,T_e^{-1/2}\,\exp(-\frac{E_v}{T_e}) \quad , \tag{5.1}$$

where each notation is same as in Eq. 4.3. The soft X-ray intensity is a function of the electron density, electron temperature and contents of impurity ions, however, the intensity in the range $E_v > T_e$ is most sensitive to the electron temperature.

Chord-integrated x-ray intensity received by the PIN diode is given by

$$P_{DET} = S_D \frac{\Delta\Omega}{4\pi} \int dl \int \varepsilon_d\,\varepsilon_f \left(\frac{d\,P_{con}}{d\,E_v} + \sum \frac{d\,P_i}{d\,E_v} \right) d\,E_v \quad , \tag{5.2}$$

where ε_d is an absorption rate of the detector, ε_f is a transmissivity of the detector, S_d is an active area of the detector, and $\Delta\Omega$ is a solid angle of the detector. The intensity of line radiation from impurity ion is represented by

$$P_i = E_i \left(\frac{n_i}{n_e}\right) n_e^2 \langle \sigma\, v \rangle_i \quad , \tag{5.3}$$

where $<\sigma v>$ is an excitation coefficient and n_i is an impurity ion density. So the spectrum of the line radiation is given by

$$\frac{dP_i}{dE_v} = E_i \left(\frac{n_i}{n_e}\right) n_e^2 \langle \sigma\, v \rangle_i\, \delta(E_i - E_v) \quad , \tag{5.4}$$

where E_i is an excitation energy.

The detection efficiency of the detector is determined by $\varepsilon_d \cdot \varepsilon_f$. Figure 5.1 shows the detection efficiency as a function of the beryllium filter thickness for the detector with the depletion layer of 10 μm and the dead layer of 0.3 μm. Lower cutoff energy defined by 1/e transmission of the peak value increases with the filter thickness.

The detected x-ray intensity is enhanced by impurity ions. Figure 5.2 shows the enhancement ratio to pure hydrogen plasma on the case $\eta_i = (n_i/n_e)/\zeta = 1 \times 10^{-5}$ of titanium where ζ is the enhancement factor. Here the total excitation coefficient of the impurity ion is calculated from corona model. The enhancement by titanium increases with the beryllium filter thickness, and has a maximum value around 1500 μm. The enhancement decreases with the electron temperature larger than 1 keV.

5.1.3 Measurement System

(1) Detector array

PIN-type silicon photodiode (PIN diode) was employed for the detector of x-ray imaging system on JT-60. The dead layer of a silicon surface barrier diode (SBD) is so thin that it is suitable to measure the soft x-ray of the energy lower than 1 keV. Therefore SBD is popular for the detector in small and middle size tokamaks. The thick dead layer of PIN diode is no problem in the large tokamak such as JT-60, where electron temperature is higher than 1-2 keV and the absorption filter has the cutoff energy more 2-3 keV. And PIN diode is less expensive than SBD. So the PIN diode is suitable for x-ray detector on JT-60. Table 5.1 summarizes the characteristics of the PIN diode used in the x-ray imaging system.

Table 5.1 Characteristics of the PIN diode used in the x-ray imaging system.

Type	Hamamatsu S1723
Active area	100 mm^2
Maximum bias voltage	50 V
Bias voltage (in JT-60)	15 V
Dark current (30 V biased)	100 nA
Surface dead layer	~0.2 μm
Depletion layer	~100 μm
Measurement energy range	1-20 keV

Figure 5.3 shows the schematic of the x-ray imaging system. The 30 channels of the x-ray detector were mounted in the same vacuum chamber as the bolometer array. The changeable absorption filters having four kinds of filter were mounted in front of the detectors. Each cutoff energies are shown

in Table 5.2. The detectors view the plasma through the 2×4 cm^2 rectangular aperture. The detector and aperture sizes were chosen to provide adequate spatial resolution and sufficient x-ray intensity to give statistic for sampling period of 20 μs. The viewing field coveres more than a half of the plasma cross-section in the range of tangent radius from 0.86 to -0.09 m as shown in Fig. 5.4. The spatial resolution of the bolometer array in minor radius is about 3.5 cm. A x-ray tube is mounted near the aperture to test the detectors remotely.

Table 5.2 Absorption filters.

Material	Thickness (mm)	Cutoff energy (keV)
Al	150	10.1
Be	1000	4.5
Be	250	2.9
Be	25	1.4

(2) Electronics and data acquisition

Figure 5.5 shows a block diagram of the detector amplifier. The amplifier consists of two stages of operational amplifier. The current of the PIN diode is converted to voltage signal by the first operational amplifier. The feedback resistivity of the first operational amplifier is changeable among 51 kΩ, 470 kΩ and 4.7 MΩ by a CAMAC command. The DC offset due to the leakage current of the detector is automatically compensated by auto balance feedback circuit in the second operational amplifier 1 min before plasma discharge.

Figure 5.6 shows the data acquisition for the x-ray imaging system. The output of the amplifier is converted to 12 bit digital signals and modulated to optical signals in the A/D-E/O module. The O/E-D/A module has both digital and analog outputs. The digital signals are stored in MDR (see Sec. 2.2.3) via MDR interface module (IMDR) with 20 μs sampling time throughout 10 s discharge. The analog signals are stored in CAMAC transient recorder (LeCroy 8212A and 8800A) with 3 ms sampling time.

5.1.4 Experimental Results

The details of the MHD studies using the x-ray imaging system are described in Ref. [15-17]. This section presents the typical results of the x-ray imaging system.

A typical sawtooth activity is shown in Fig. 5.7 for a 2 MA divertor discharge with B_T of 4.5 T. Figure 5.7 (a) illustrates the temporal evolutions of the plasma current, soft x-ray intensity and the line electron density from 2 mm-wave interferometer. The sawtooth oscillations started at around 3-4 s in this discharge. The expanded waveforms of the soft x-rays and the line electron density for 6.0-6.5 s are shown in Fig. 5.7 (b). The presence of compound sawteeth, whose period was typically ~100 ms, was found together with successor oscillations following the complete and the partial relaxations. From the soft x-ray signals, such oscillations were found to result from the rotation of the mode with am m = odd (possibly m = 1) structure localized on the q = 1 surface as shown in Fig. 5.8.

The toroidal rotation velocity, v_φ, can be estimated from the frequency of the m = 1 mode, $f_{m=1}$, as $v\varphi = 2\pi R_P f_{m=1}$, where R_P denotes the major radius. The toroidal rotation velocity is plotted against the absorbed beam power distinguishing the direction such as co and counter, as shown in Fig. 5.9. The velocity was apt to increase with the beam power. The scattering of the plots in the same beam power is seemed to be due to the difference of the electron density. The general tendency that the counter -injection experiments appear to generate higher velocity than the co-injection is explained by taking into account the Ohmic plasma rotation.

From the inversion radius of the sawtooth, r_I, obtained from the chord-integrated signals of the soft-x-ray emission, the radius of the q = 1 surface, r_s, can be inferred assuming that the inversion radius of the soft x-ray emissivity profile in the plasma is approximately equal to the q = 1 radius. By correcting the chord integral effect and the width of the viewing field, $r_s \approx 1.4\, r_I$ was obtained. In accordance with the above statement, the q = 1 radius normalized by the minor radius as a function of the the inverse q_{eff} value for Ohmic discharges was obtained as shown in Fig. 5.10. Here q_{eff} is the effective safety factor at the plasma edge defined by

$$q_{eff} = q_a \left[1 + \left(\frac{a_P}{R_P}\right)^2 \left\{ 1 + \frac{\left(\beta_P + l_i / 2\right)^2}{2} \right\} \right], \qquad (5.5)$$

where q_a is the cylindrical safety factor at the plasma edge. This figure includes the data on compound and single sawteeth, and shows the relationship of

$$\frac{r_s}{a} \equiv \frac{1}{q_{eff}} \tag{5.6}$$

independent of the plasma species. The same scaling was obtained in other tokamaks such as TFTR [18] and DIVA with limiter configuration [19].

The electron thermal conductivity can be estimated by the heat pulse propagation method of the sawtooth oscillation [20-22]. Figure 5.11 shows the relationship between the heat pulse propagation time, t_p, and the diffused area of the heat pulse, Δr^2. Here, Δr^2 is defined as

$$\Delta r^2 = r^2 - (\sqrt{2}\, r_s)^2 . \tag{5.7}$$

The electron thermal conductivity is given by $\chi_e = (1/8)\,(d\Delta r^2/dt_p)$. Two solid lines in Fig. 5.11 represent respectively the fastest and slowest propagations, in 5.5-5.6 s in a discharge. So the χ_e of 1.3-2.2 $\times$ 10^4 cm^2/s was obtained in this case.

The electron temperature profile was obtained by the absorption filter method [23] for the successive two discharges assuming the reproducibility. The electron temperature profile was derived from the ratio of the soft x-ray emissivities provided by Abel inversion from the chord-integrated intensities with different filters. The 25 μm-thick beryllium filters were used in one discharge and the 1000 μm-thick beryllium filters were used in another discharge. Figure 5.12 shows the obtained electron temperature profile (solid line) comparing with that from Thomson scattering measurement. Those electron temperatures coincide each other within ± 20%. The absorption filter method could not provide the electron temperature in the peripheral region where the x-ray intensity was not sufficient due to the low electron temperature.

5.1.5 Conclusion

To measure the soft x-ray intensity profile of JT-60 plasma, thirty channels of PIN diode detectors were arranged with the changeable multi-absorption filters. The x-ray imaging system was able to operate with the temporal resolution of 20 μs and the spatial resolution of 3.5 cm. The x-ray

imaging system was helpful to study the MHD behavior and other plasma characteristics. The toroidal rotation velocity was estimated from the frequency of the m = 1 mode. The velocity was apt to increase with the beam power. The q = 1 radius was estimated from the inversion radius of the sawtooth oscillation. The relationship $r_s/a \approx q_{eff}^{-1}$ was confirmed in JT-60. The electron conductivity was estimated from the heat pulse propagation method of the sawtooth oscillation. The absorption filter method assuming the reproducibility of successive two discharges provided the electron temperature profile with good agreement with that from Thomson scattering measurement. So the additional x-ray imaging system consisting of the parallel detector arrays with different thickness filters were installed recently for the absorption filter method, which provided the time evolution of the electron temperature profile with the high temporal resolution of 0.1-1 ms.

5.2 BALMER α LINE MEASUREMENT SYSTEM

5.2.1 Introduction

The operational gas is neutralized on the surface of the first wall and returns to the plasma via a reionizing process, which is named as a particle recycling. The particle recycling diagnostics are important to study a particle confinement, density control and improving energy confinement such as H-mode. Particle behavior has been studied in numerous tokamaks with or without divertor [24-29]. These studies have revealed the fact that refuelling of hydrogen gas neutralized at the divertor plates plays an important role in the divertor configuration, while, in the limiter configuration, the particle dynamics is dominated by recycling at the limiter surface. The plasma density was controlled satisfactory by gas puffs in medium size tokamaks, because of the low recycling of refuelling rate. In the large tokamaks with a carbon graphite wall and long plasma duration, however, plasma density control has become more difficult. In the early experiments of JET [29] and TFTR, the electron density remained constant without any additional gas during the plasma current flat-top, because of high recycling from full loading of the limiter surface by the hydrogen gas. It is well known that Balmer α line (Hα) drops rapidly in the H-mode transition. And D-III experiments [30] shows that the control of particle recycling has proved to be very important in creating good H-mode discharges.

Balmer α line (Hα) is one of line radiations of a hydrogen atom. The particle recycling flux via reionization process can be estimated by the Hα intensity, because the ratio of the Hα emission to the ionization is known. The particle behaviors of the ohmically and NB heated plasmas have been investigated by measuring Hα emissions from the main and divertor plasmas on JT-60.

5.2.2 Particle Balance of the Tokamak Plasma

A schematic particle-flow pattern for the outer divertor configuration is shown in Fig. 5.13. The charged particle diffusing from the main plasma into the scrape-off layer outside the separatrix surface are transported into the divertor chamber where they are neutralized in collisions with divertor plates. These particle losses are mainly compensated by the refuelling of the hydrogen gas flowing back from the divertor chamber and the gas puff. In the NB heating experiments, the NB injector acts as an additional particle source. The behavior of the plasma density is dominated by the balance of these particle flows. In the limiter discharge, local recycling around the toroidal limiter plays an important role in the particle balance, instead of the refuelling process taking place in the divertor discharges.

Neglecting the impurity contribution to the total number of electrons in the main plasma, the global particle balance of equation is given by

$$\frac{dN_e}{dt} = \eta_G S_G + S_B + S_I - \frac{N_e}{\tau_p}, \tag{5.8}$$

where Ne is the total number of electrons in the main plasma, S is the fuelling rate of neutral or charged particles, η is the fuelling efficiency, and τ_p is the global particle confinement time. The subscript G, B and I designate gas puff, NB injection and refuelling, respectively. A recycling coefficient is defined as $R = S_I/(N_e/\tau_p)$. Since the effective particle confinement time tp* corresponding to the decay constant of the electron density is related to the particle confinement time via the expression $\tau_p^* = \tau_p/(1-R)$, Eq. (5.8) can be rewritten as

$$\frac{dN_e}{dt} = \eta_G S_G + S_B - \frac{n_e}{\tau_p^*}. \tag{5.9}$$

If the particle recycling is toroidally uniform, the number of recycling particles can be determined from the measurement of the Hα emission at a single toroidal location as follows:

$$S_I = \int \phi(r,R)\,\varepsilon(n_e)\,dV \qquad (5.10)$$

where, $\phi(r,R)$ is the Hα emission profile in the poloidal cross-section, $\varepsilon(n_e)$ is the number of ionization events per Hα emission and V is the plasma volume. The ionization-per-Hα ratio, ε, was already analyzed by Johnson-Hinov [31] as shown in Fig. 5.14. The ε for T_e above 20 eV is nearly independent of the electron temperature and varies from 10 to 50 in the range of the electron density (0.5-10) × 10^{19} m^{-3}.

The Hα emission profile is calculated by Monte Carlo method to understand its properties and to introduce a simple expression for it [32]. A contour map of the calculated Hα emission profile is shown in Fig. 5.15. The entire Hα emission occurs in the edge region of the plasma and the emission is enhanced outside the torus. A simple formula showing these features of the Hα emission profile is introduced to estimate the parameters characterizing the particle behavior, which consists of the axisymmetric function $\phi_1(r)$ and a nonlinear function in the major radius direction $\phi_2(R)$, as

$$\phi(r,R) = N_0\,\phi_1(r)\,\phi_2(R)\,, \qquad (5.11)$$

where N_0 is a constant. Here,

$$\phi_1(r) = 1 + A\,(r/a)^m - (A+1)\,(r/a)^n \qquad (5.12)$$

is employed as the axisymmetric function. The parameters A, m and n are fixed to be 500, 8 and 24, respectively, so that the position of the maximum and its FWHM agree with the results of the numerical simulation. The monotonically increasing function in the major radius direction,

$$\phi_2(R) = 1 + \frac{B\left[1 + (R-R_P)/a\right]^4}{\left[1 + (R-R_P)/a\right]^4 + C} \qquad (5.13)$$

is employed as the nonlinear function. Where R_P is the major radius, and B and C are constants determined to reproduce the measured Hα intensities.

The electron density in JT-60 increases almost linearly with constant gas puff during steady state of the plasma current and decays immediately after termination of the gas feed. The fuelling efficiency of the gas puff is determined from the time derivatives of the electron density before and after the gas feed termination by

$$\eta_G = \left[\left(\frac{dN_e}{dt}\right)_{before} - \left(\frac{dN_e}{dt}\right)_{after}\right] / S_G . \qquad (5.14)$$

The fuelling rate by the NB injection, S_B, is derived from the net absorbed NB power, which is defined as $(1-\eta_s)P_{NB}$ where η_s is the shinethrough ratio of the NB injection.

The total number of electrons is obtained from the volume integration of the electron density profile $n_e(r)$, which is derived by fitting of line densities along three chord at R = 2.53, 3.04 and 3.55 m to the parabolic form as

$$n_e(r) = [1-(r/a)^2]^m . \qquad (5.15)$$

5.2.3 Measurement System

(1) Detectors and arrangements

It is popular in other tokamaks that the Hα emission is measured with a visible spectrometer. A photodiode detector with a Hα interference filter is very compact, less expensive, and easy to calibrate the absolute sensitivity, so that it is suitable as a Hα detector. The wavelength resolution of the detector is not so good, typically 1-10 nm, that the contamination of other lines in the measurement window have to be checked by a spectrometer. In JT-60, Hα emissions form the main and divertor plasmas have been measured by several channels of the photodiode detector with a Hα interference filter.

The detector is the PIN photodiode which is same as that of the x-ray imaging system (see Table 5.1). The catalog value of the sensitivity for Hα line (656.3 nm) is 0.35 A/W or 1.06×10^{-19} A/Photon. The typical transmissivity of the original interference filters measured by a spectrophotometer is shown in Fig. 5.16 (a). The FWHM was about 4.5 nm. In the wavelength range from 656.3 - 4.5/2 nm to 656.3 + 4.5/2 nm, a dominant line radiation was Hα only, which was confirmed by the visible spectrometer. After the replacement of the first wall from TiC coated molybdenum to carbon graphite tiles, the improved divertor confinement (IDC) characterized by an enhanced radiation in the divertor plasma was found. The enhancement of CII line (657.8 nm) was

observed in the divertor plasma on the IDC discharges as shown in Fig. 5.17. In order to omit the CII line, all filters were replaced by the filters with FWHM of 1 nm. The typical transmissivity of new filters is shown in Fig. 5.16 (b).

Figure 5.18 shows the sightlines of the Hα detectors. The four channel Hα detectors are mounted at the same vacuum chamber as the bolometer array and the x-ray imaging system. The three channel Hα-detectors with vertical sightlines at R = 2.53, 3.04, and 3.55 m, and one detector viewing near the X-point of the divertor are mounted on the diagnostics ports under the vacuum vessel. A couple of the detectors on electron and ion drift sides measures Hα emissions on the divertor plates.

After the modification for the lower X-point divertor, the Hα emission from the lower divertor region is measured by single detector with same viewing chord as the divertor bolometer (see Fig. 3.9). The three vertical detectors were rearranged at top of the diagnostics ports above the vacuum vessel. And one detector viewing near the outer X-point was taken off for the install of lower divertor coils.

(2) Electronics and data acquisition

Figure 5.19 shows the block diagram of the data acquisition for the Balmer line measurement system. The amplifier is similar to that of x-ray imaging system shown in Fig. 5.5 except feedback resistivities. The output of the amplifier is converted to 12 bit digital signals and modulated to optical signals in the A/D-E/O module. The analog outputs of the O/E-D/A module are stored in CAMAC transient recorder (LeCroy 8212A and 8800A) with 400 μs sampling time throughout 10 s discharge. The data is transferred to JT-60 data acquisition system.

5.2.4 Experimental Results

Figure 5.20 shows the time evolutions of Hα intensities in the ohmically heated outer-divertor discharge with large gas puff rate. The Hα intensities increased with the increase of the electron density. The relationship between the Hα intensity and line-averaged electron density at the vertical chord of R = 3.04 m is shown in Fig. 5.21. This figure indicates that the Hα intensity is proportional to $\overline{n}_e^{1.5}$.

Fuelling efficiencies of the gas puffs are plotted against the $\overline{n}_e$ in Fig. 5.22. The fuelling efficiency was almost independent of $\overline{n}_e$, and 0.32 in limiter discharges and 0.25 in divertor discharges.

Figure 5.23 shows the global particle confinement time of OH and additional heated plasmas as a function of $\overline{n}_e$. The global particle confinement time of the OH plasma was about 150 ms at low electron density and decreased with $\overline{n}_e$. The τ_p of the NB heated plasma was about 2/3 of that of the OH plasma at same electron density. There was not significant difference between the NB heated plasmas and plasmas with combined heating of the NB and LHCD. The τ_p of the NB heated plasmas decreased with the NB power as shown in Fig. 5.24.

5.2.5 Conclusion

The particle behaviors of the ohmically and NB heated plasmas have been investigated by measuring Hα emissions from the main and divertor plasmas using Hα filtered photodiodes. The Hα intensity from the main plasma was proportional to $\overline{n}_e^{1.5}$ approximately. The fuelling efficiency was almost independent of $\overline{n}_e$. The global particle confinement time of the OH plasma was about 150 ms at low electron density and decreased with $\overline{n}_e$. The τ_p of the NB heated plasma was about 2/3 of that of the OH plasma at same electron density. The τ_p of the NB heated plasmas decreased with the NB power.

REFERENCES TO CHAPTER 5

[1] N.R. Sautoff, S. von Goeler, and W. Stodiek, Princeton University, Plasma Physics Laboratory Report PPPL-1379, 1978.

[2] J.L. Dunlap, B.A. Carreras, V.K. Pare, J.A. Holmes, S.C. Bates, J.D. Bell, H.R. Hicks, V.E.Lynch and A.P. Navarro, Phys. Rev. Lett. **48** (1982) 538.

[3] G.L.Johns, M. Soler, B.V. Waddel, J.D. Callen and H.R. Hicks, Nucl. Fusion **18** (1978) 609.

[4] R. Petrasso, M. Gerassimenko, F.H. Seguin, J. Ting, R. Krogstad, P. Gauthier, W. Hamilton, A.T. Ramsey, P. Bustein and R. Granetz, Rev. Sci. Instrum. **51** (1980) 585.

[5] K.W. Hill, S. von Goeler, M. Bitter, W. Davis, L. Dudek, E. Fredd, L.C. Johnson, J. Kiraly, K. McGuire, J. Montague, E. Moshey, N.R. Sauthoff and K.M. Young, Rev. Sci. Instrum. **56** (1985) 830.

[6] A.W. Edwards, H.-U. Fahrbach, R.D. Gill, R. Grantz, E. Oord, G. Schramm, S. Tsuji, A. Weller and D. Zashe, Rev. Sci. Instrum. **57** (1986) 2142.

[7] K. Nagashima, T. Nishitani and H. Takeuchi, Kakuyugo Kenkyu **59** Suppl. (1987) 215.

[8] S. Tsuji, Y. Nagayama, K. Miyamoto, K. Kawahata, N. Noda and S. Takahashi, Nucl. Fusion, **25** (1985) 305.

[9] S. von Goeler, W. Stodiek and N.R. Sauthoff, Phys. Rev. Lett. **33** (1974) 1201.

[10] N.R. Sautoff, S. von Goeler and W. Stodiek, Nucl. Fusion, **18** (1978) 1445.

[11] R.S. Granetz and J.F. Camacho, Nucl. Fusion, **25** (1985) 727.

[12] A.W. Edwards, D.J. Campbell, W.W. Engelhardt, H.-U. Fahrbach, R.D. Gill, R. Grantz, S. Tsuji, B.J. Tubbing, A. Weller, J. Wesson and D. Zashe, Phys. Rev. Lett. **57** (1986) 210.

[13] J.A. Wesson, Plasma Phys. Controlled Fusion, **28** (1986) 243.

[14] Y. Nagayama and S. Tsuji, Phys. Rev. Lett. **61** (1988) 1839.

[15] H. Shirai, K. Nagashima, T. Nishitani and JT-60 Team, Japan Atomic Energy Research Institute Report JAERI-M 87-014, 1987.

[16] S. Ishisda, H. Shirai, K. Nagashima, T. Nishitani, T. Fukuda and JT-60 Team, Plasma Phys. Controlled Fusion, **30** (1988) 1069.

[17] S. Ishida, T. Nishitani, K. Nagashima, S. Iida, T. Matoba and JT-60 Team, Nucl. Fusion **28** (1988) 2225.

[18] K. McGuire, R. Colchin, E. Fredrickson, et al., Rev. Sci. Instrum. **57** (1986) 2136.

[19] DIVA Group, Nucl. Fusion **20** (1980) 271.
[20] G.L. Johns, M. Soler, B.V. Waddel, J.D. Callen and H.R. Hicks, Nucl. Fusion **18** (1978) 609.
[21] M. Soler and J.D. Callen, Nucl. Fusion **19** (1979) 703.
[22] E.D. Fredrickson, et al., Nucl. Fusion **26** (1986) 849.
[23] T.P. Donaldson, Plasma Phys. **20** (1978) 1279.
[24] E.S. Marmar, J. Nucl. Mater. **76 & 77** (1978) 59.
[25] H.-M. Mayer. F. Wagner, G. Becker, K. Behringer, D. Campbell, et al., J. Nucl. Mater. **111 & 112** (1982) 205.
[26] H.F. Dylla, W.R. Blanchard, R. Budny, R.J. Fonck, D.K. Owens and G.L. Schmidt, J. Nucl. Mater. **111 & 112** (1982) 211.
[27] M. Shimada, A.T. Ramsey, D.K. Owens, H.F. Dylla, R.V. Budny, P.H. Lomarche, J.F. Schivell, R.J. Groebner, D. Heifetz and M. Murakami, J. Nucl. Mater. **145 - 147**(1987) 544.
[28] G. Haas, M. Kaufmann, R.S. Lang, the ASDEX Team and the Pellet Team, J. Nucl. Mater. **145 - 147** (1987) 519.
[29] A. Tanga, C.W. Gowers, C.A. Hugenholtz, P. Morgan and F.C. Schüller, Joint European Torus Report JET-P-84-09, 1985.
[30] M. Nagami, M. Kasai, A. Kitsunazaki, T. Kobayashi, S. Konoshima, T. Matsuda, N. Miya, H. Ninomiya, S. Sengoku, M. Shimada and H. Yokomizo, Nucl. Fusion **24** (1984) 183.
[31] L.C. Johnson and E. Hinnov, J. Quant. Spectrosc. Radiat. Transfer **13** (1973) 333.
[32] K. Yamada, S. Tsuji, K. Shimizu, T. Nishitani, K. Nagashima and the JT-60 Team, Nucl. Fusion **27** (1987) 1203.

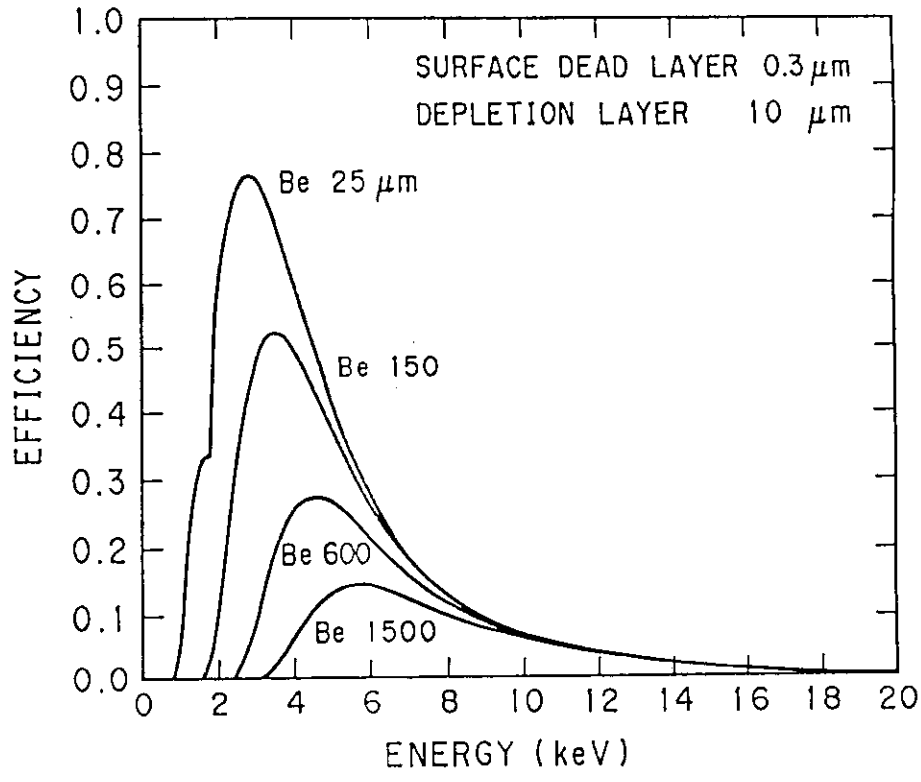

Fig. 5.1 Detection efficiency of PIN diode with beryllium filter.

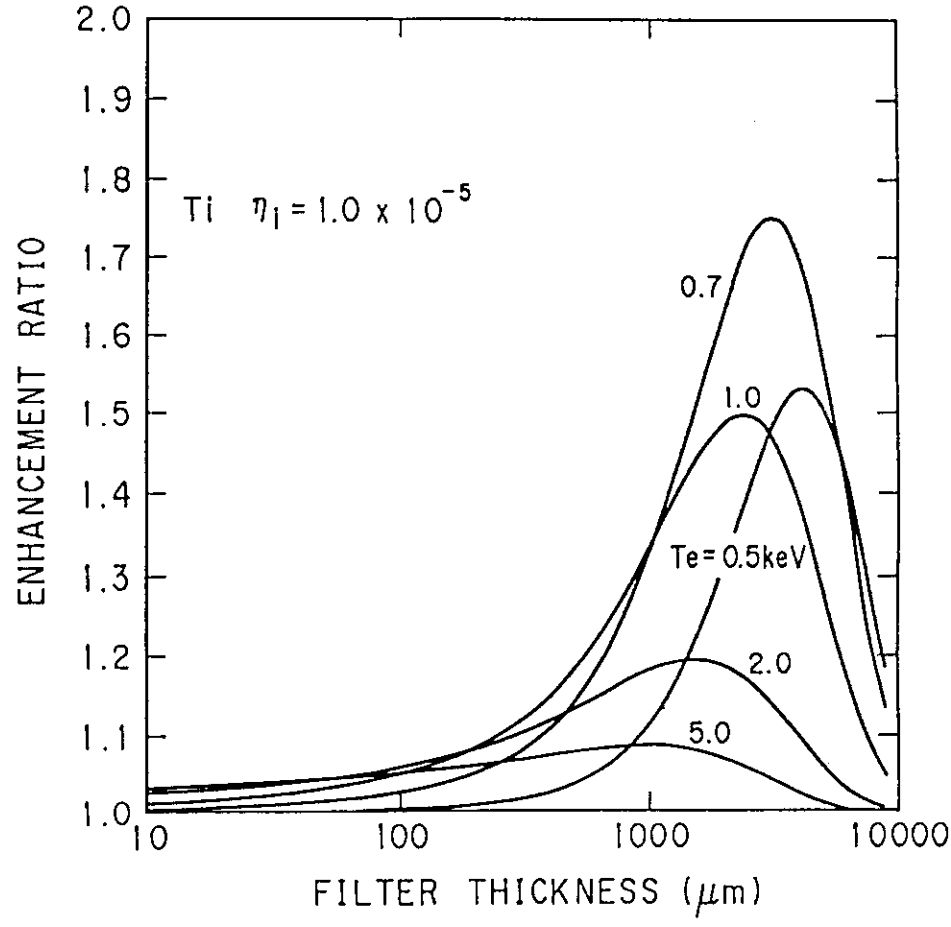

Fig. 5.2 Enhancement ratio of the soft x-ray intensity from the plasma with titanium impurity to that from pure hydrogen plasma.

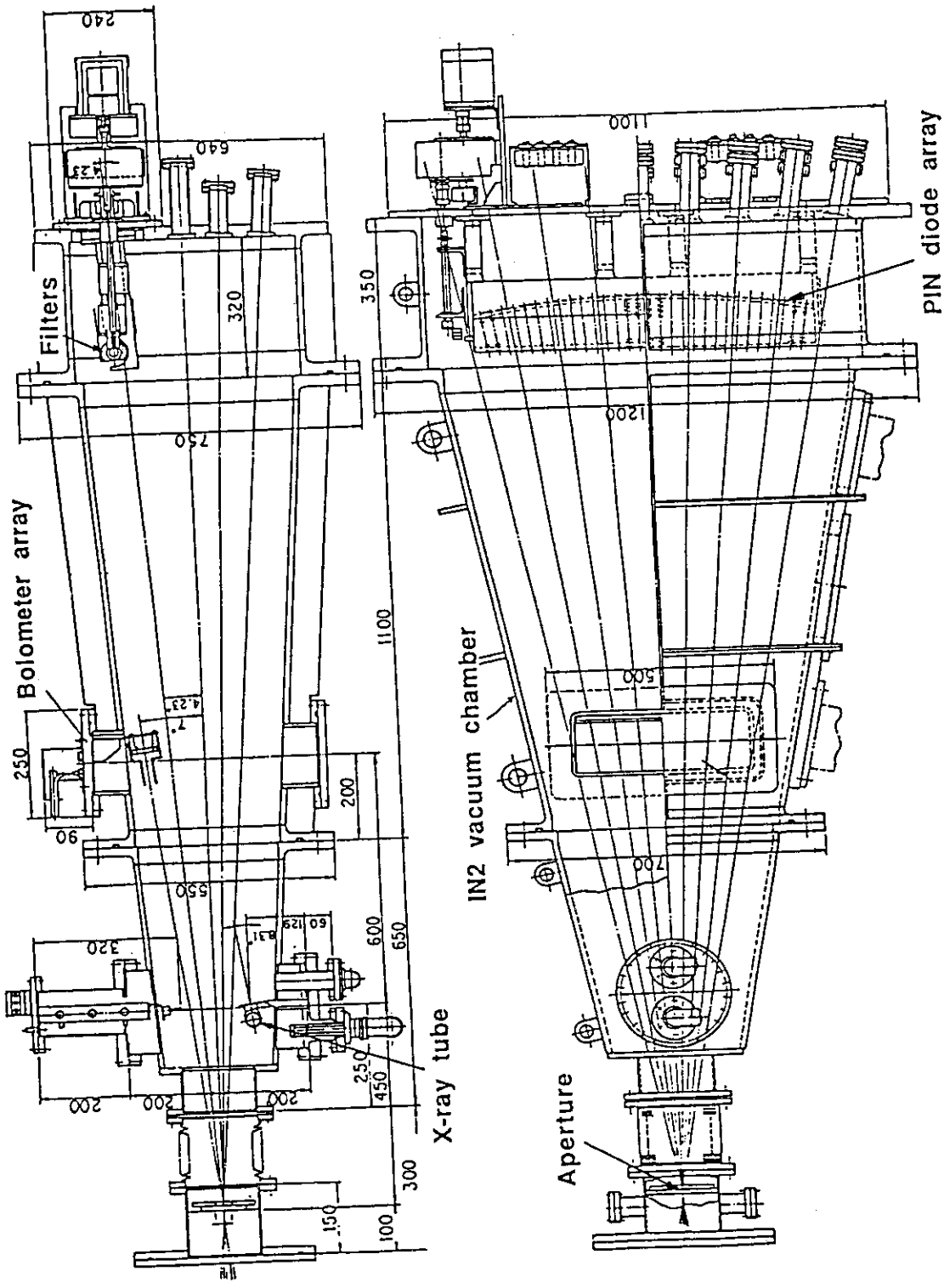

Fig. 5.3 Schematic of the x-ray imaging system. The fan array of the 30 channel detectors were mounted in the vacuum chamber.

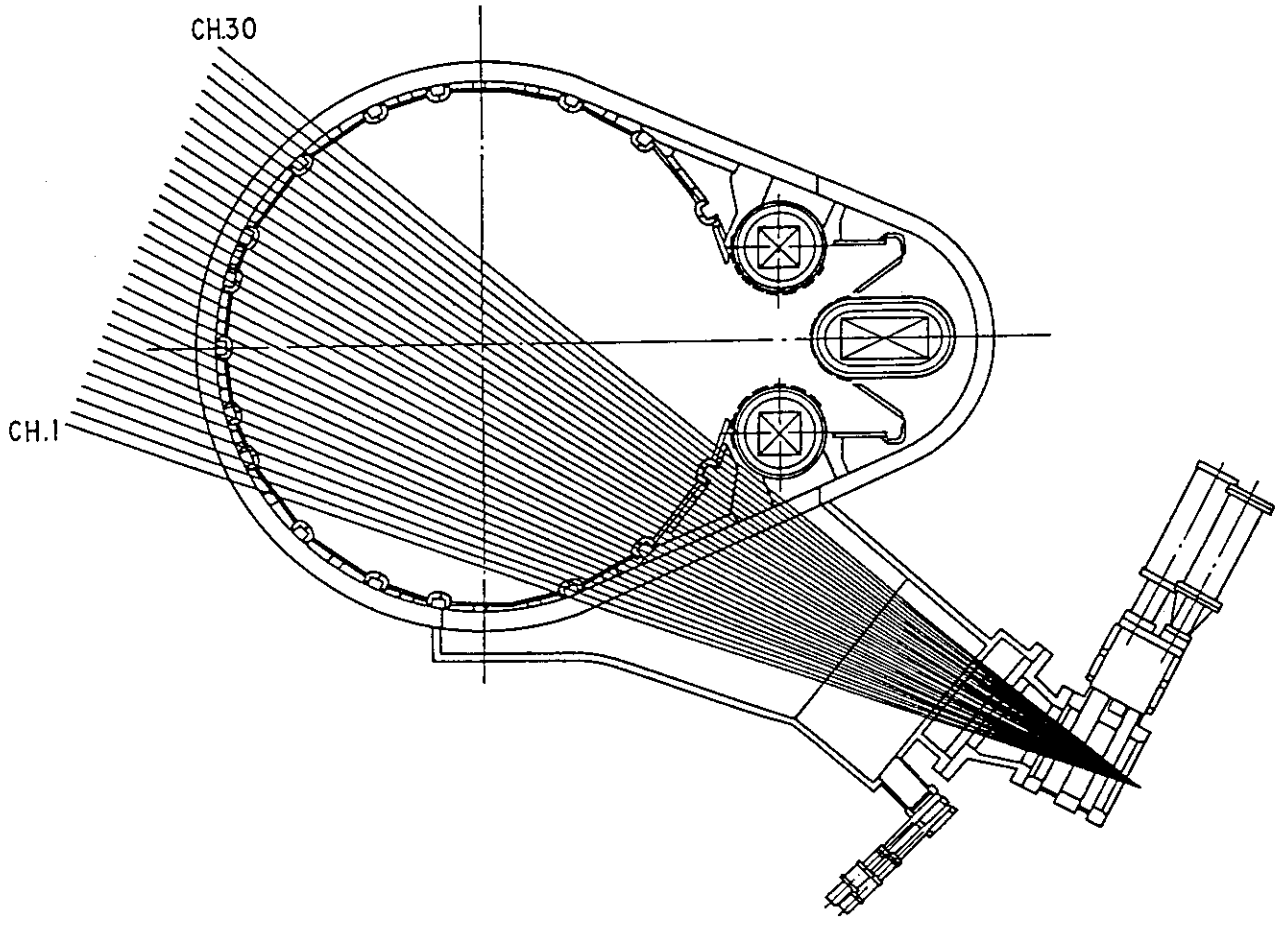

Fig. 5.4 Sightlines of the x-ray imaging system. The viewing field covered more than a half of the plasma cross-section in the range of tangent radius from 0.86 to -0.09 m

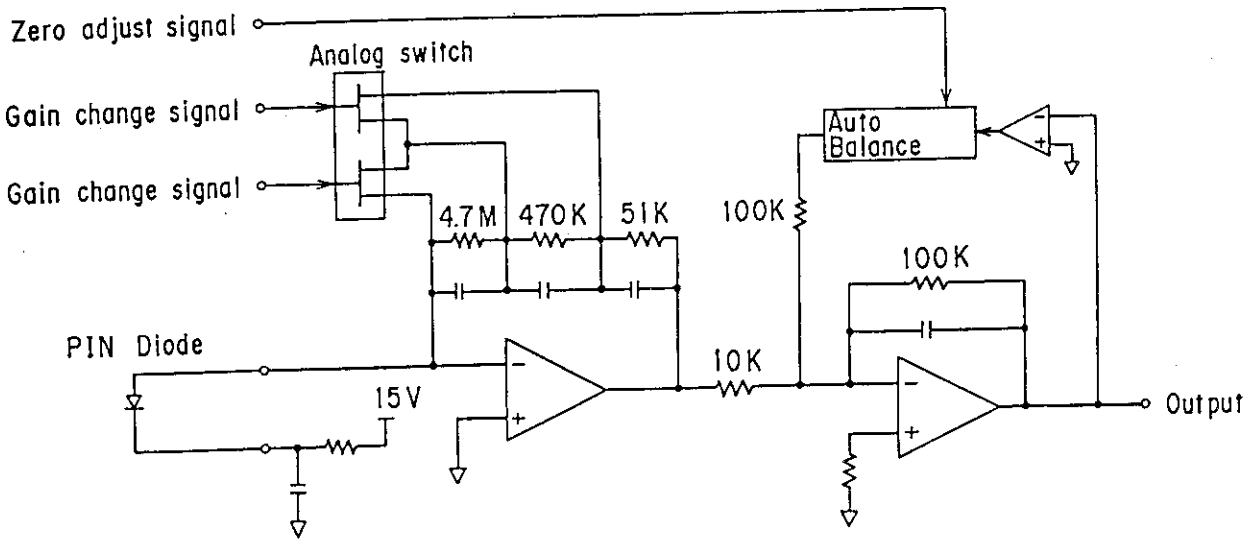

Fig. 5.5 Block diagram of the amplifier for the PIN diode detector.

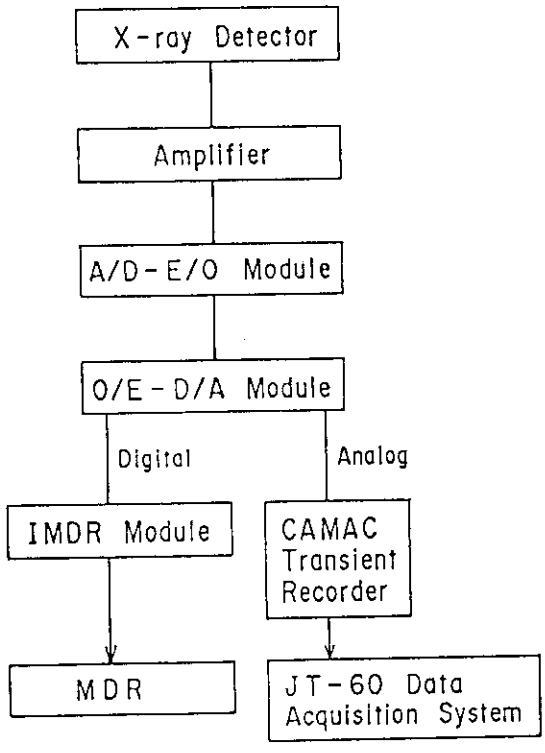

Fig. 5.6 Block diagram of the data acquisition for the x-ray imaging system.

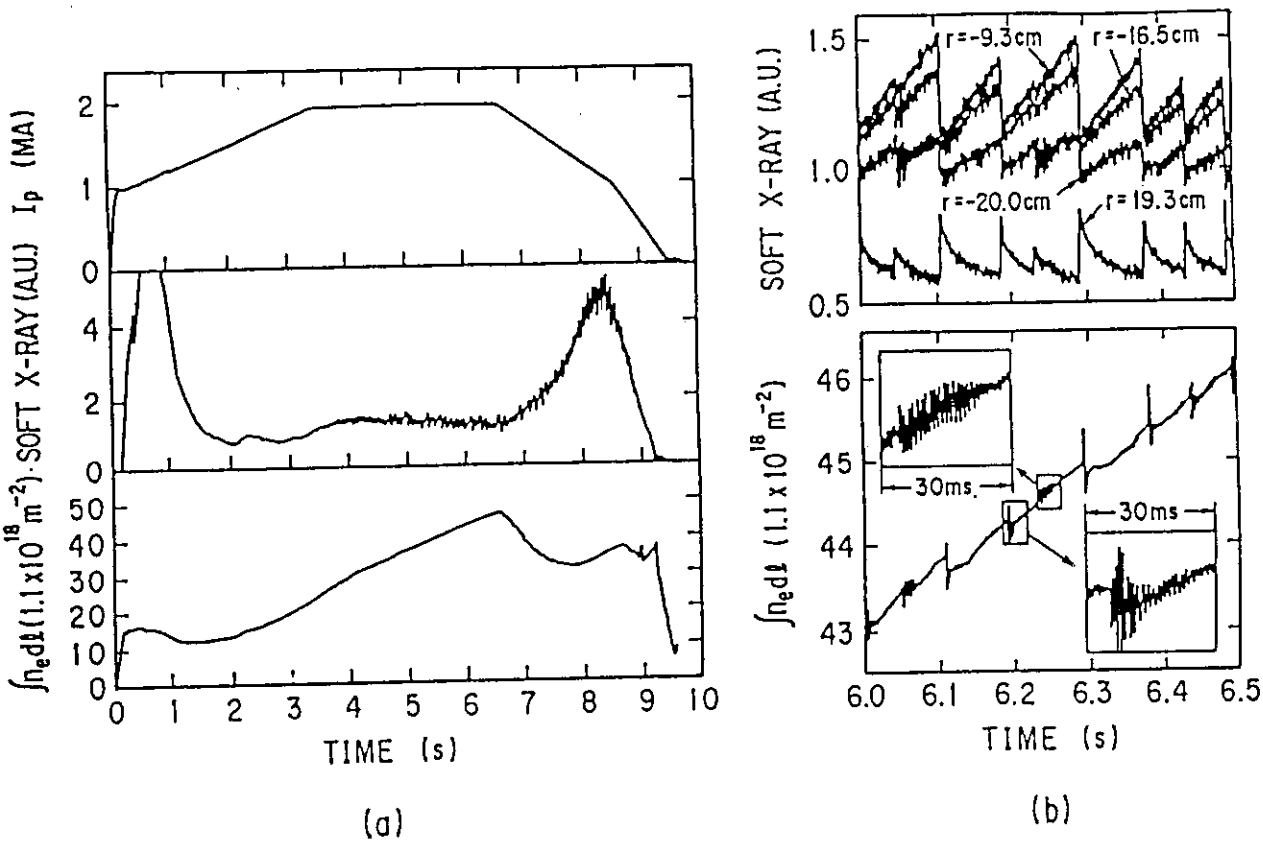

Fig. 5.7 A typical sawtooth activity in a 2 MA divertor discharge with B_T = 4.4 T: (a) time evolution of the plasma current, the soft x-ray intensity and the line electron density; (b) expanded waveforms of t he soft x-ray intensities and the line electron density, showing compound and single sawteeth with corresponding successor oscillations.

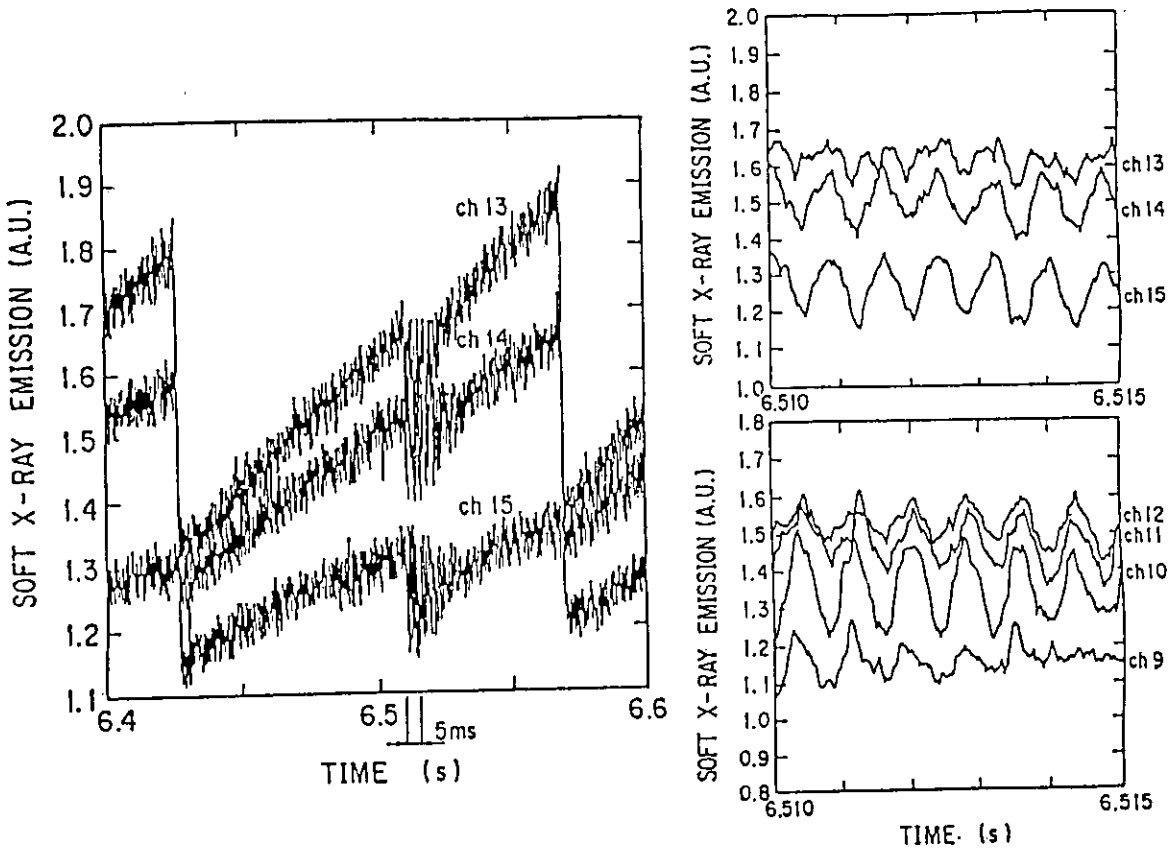

Fig. 5.8 Waveforms of soft x-ray intensities showing m = 1 structure in the plasma with I_P = 2 MA and B_T = 4.5 T.

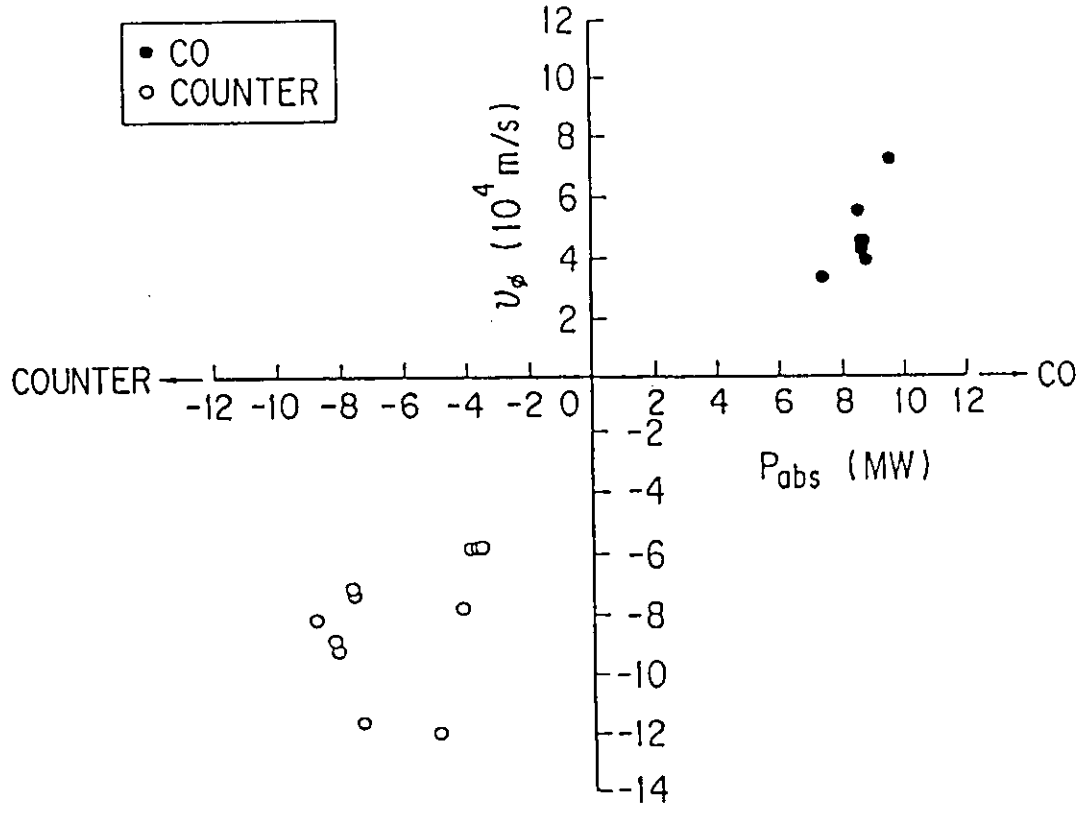

Fig. 5.9 Toroidal phase velocity inferred from the frequency of the m = 1 oscillations as a function of the NB power for co- and counter-injection experiments.

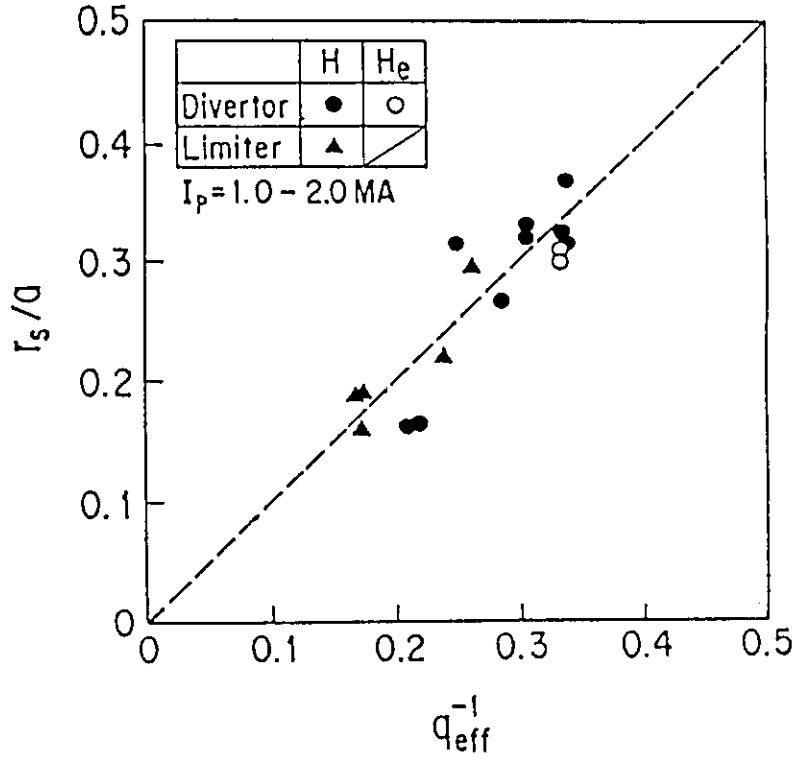

Fig. 5.10 The q = 1 radius normalized by the minor radius as a function of the the inverse q_{eff} value.

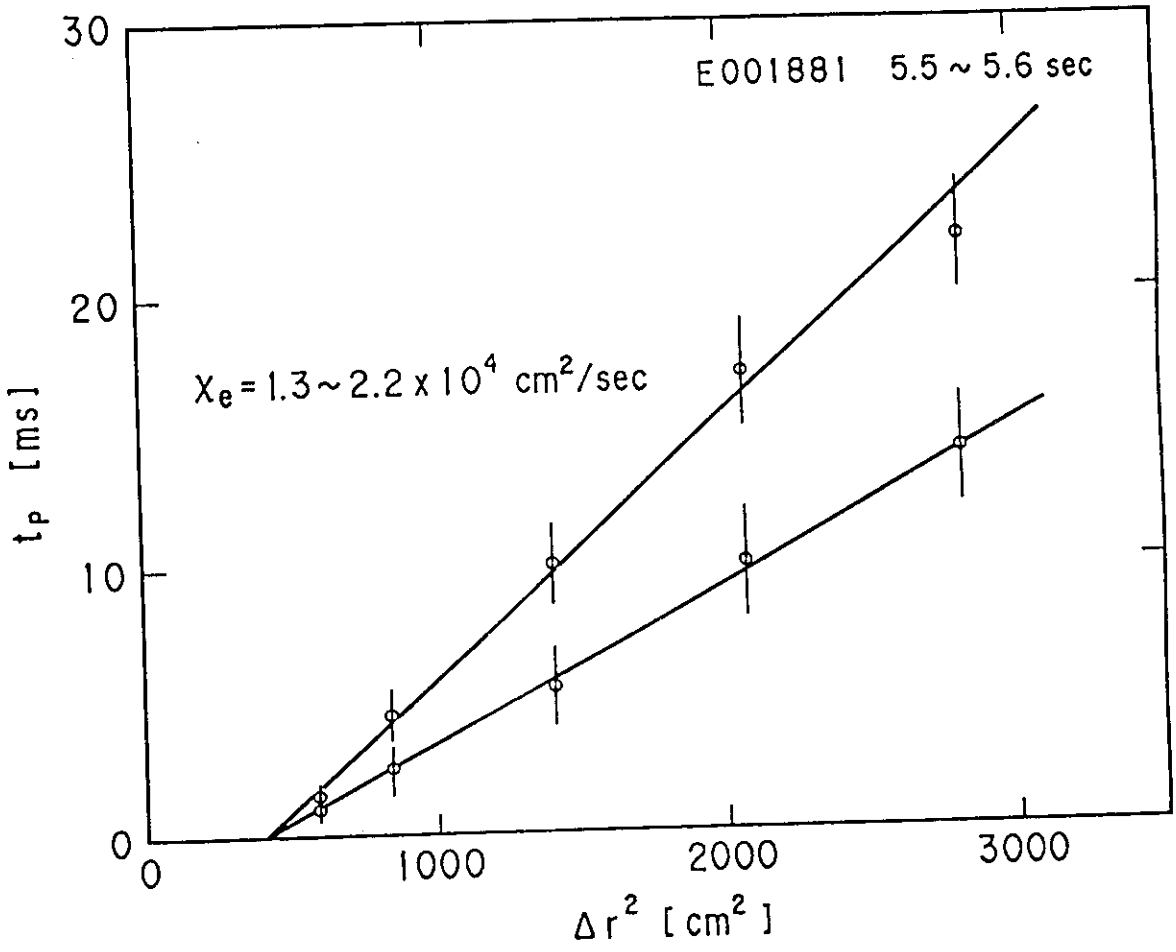

Fig. 5.11 The electron thermal conductivity estimated by the heat pulse propagation method. Two solid lines represent respectively the fastest and slowest propagations, in 5.5-5.6 s in a discharge.

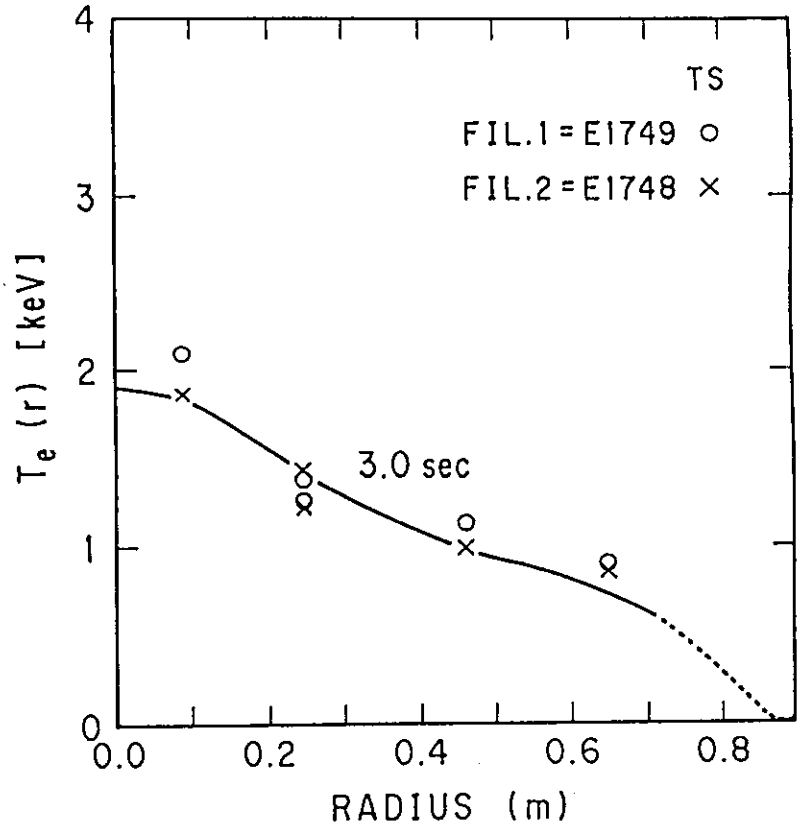

Fig. 5.12 Electron temperature profile obtained by the absorption filter method for the successive two discharges assuming the reproducibility, comparing with the results of the Thomson scattering measurement.

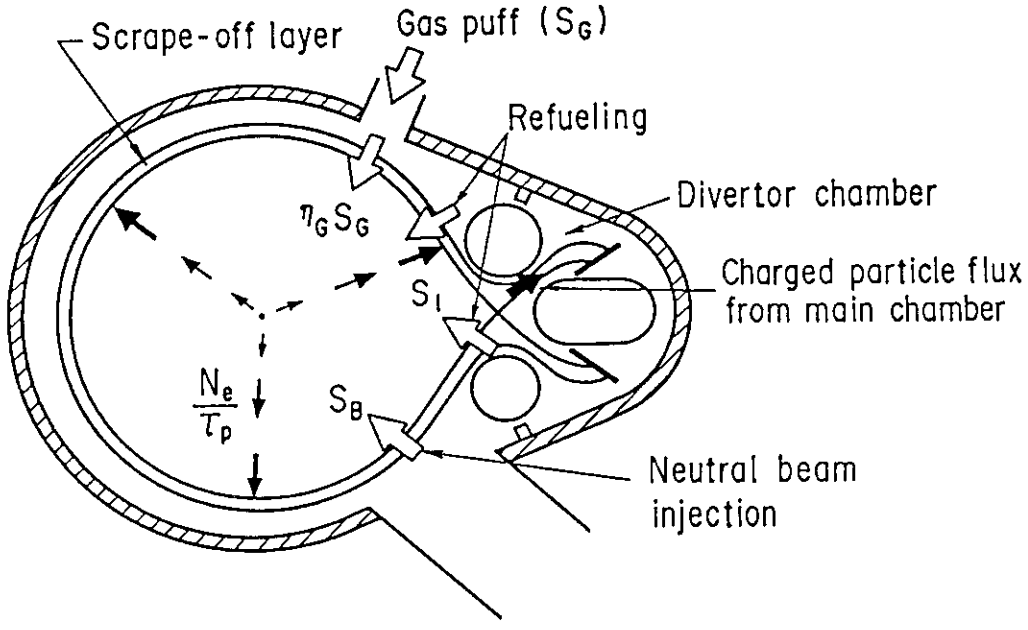

Fig. 5.13 Schematic particle flow pattern for diverted plasma with NB injection.

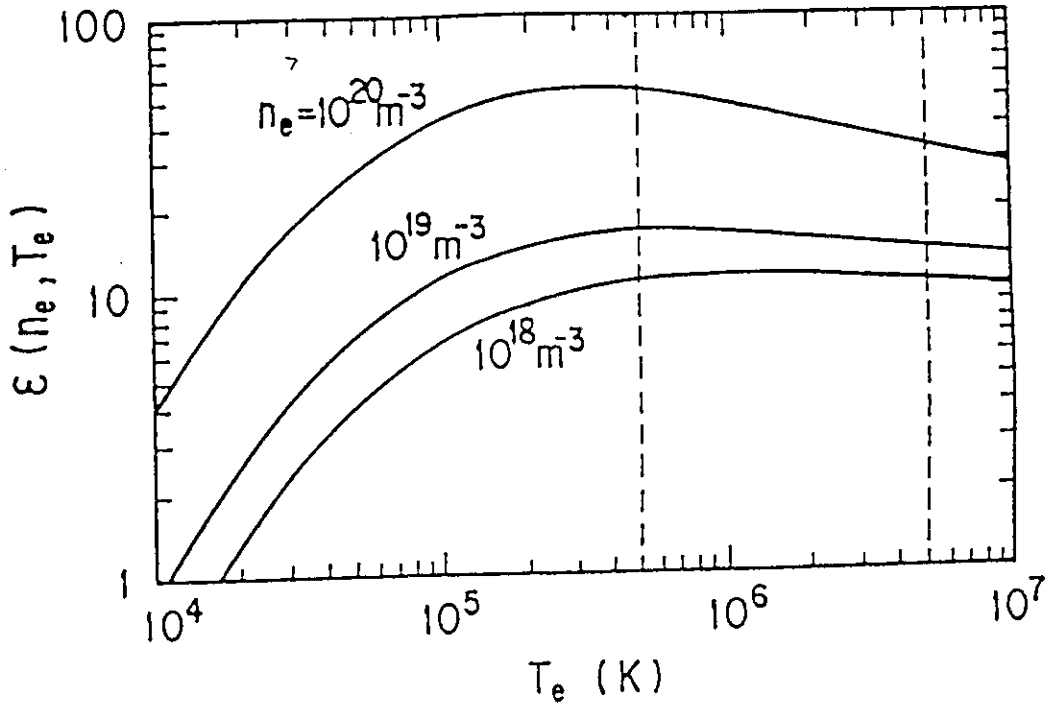

Fig. 5.14 Number of ionization events per Hα emission as a function of the electron temperature.

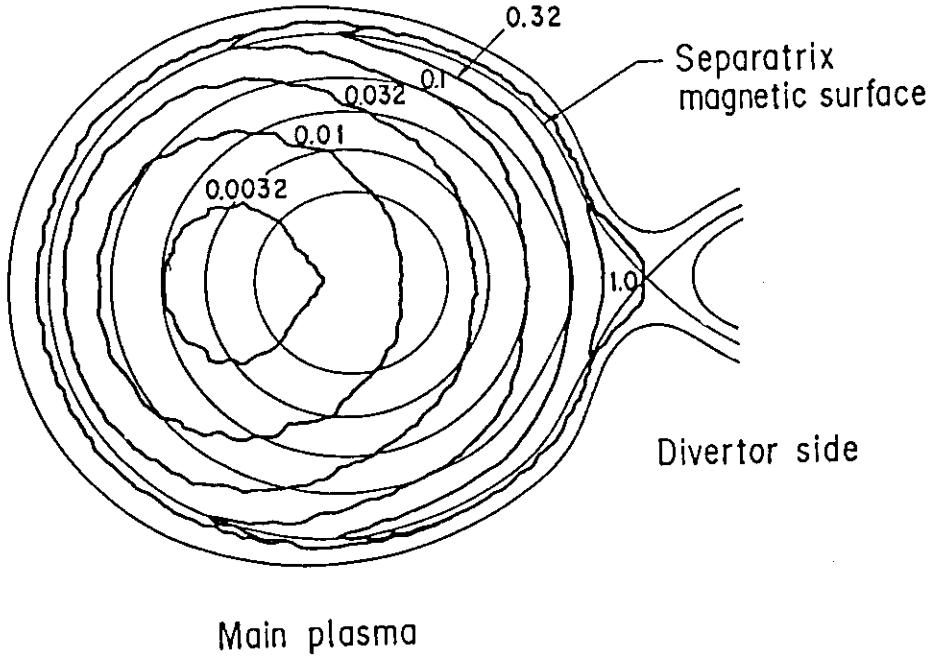

Fig. 5.15 Two-dimensional Hα radiation distribution in poloidal cross-section calculated by neutral particle transport and line radiation c calculation codes.

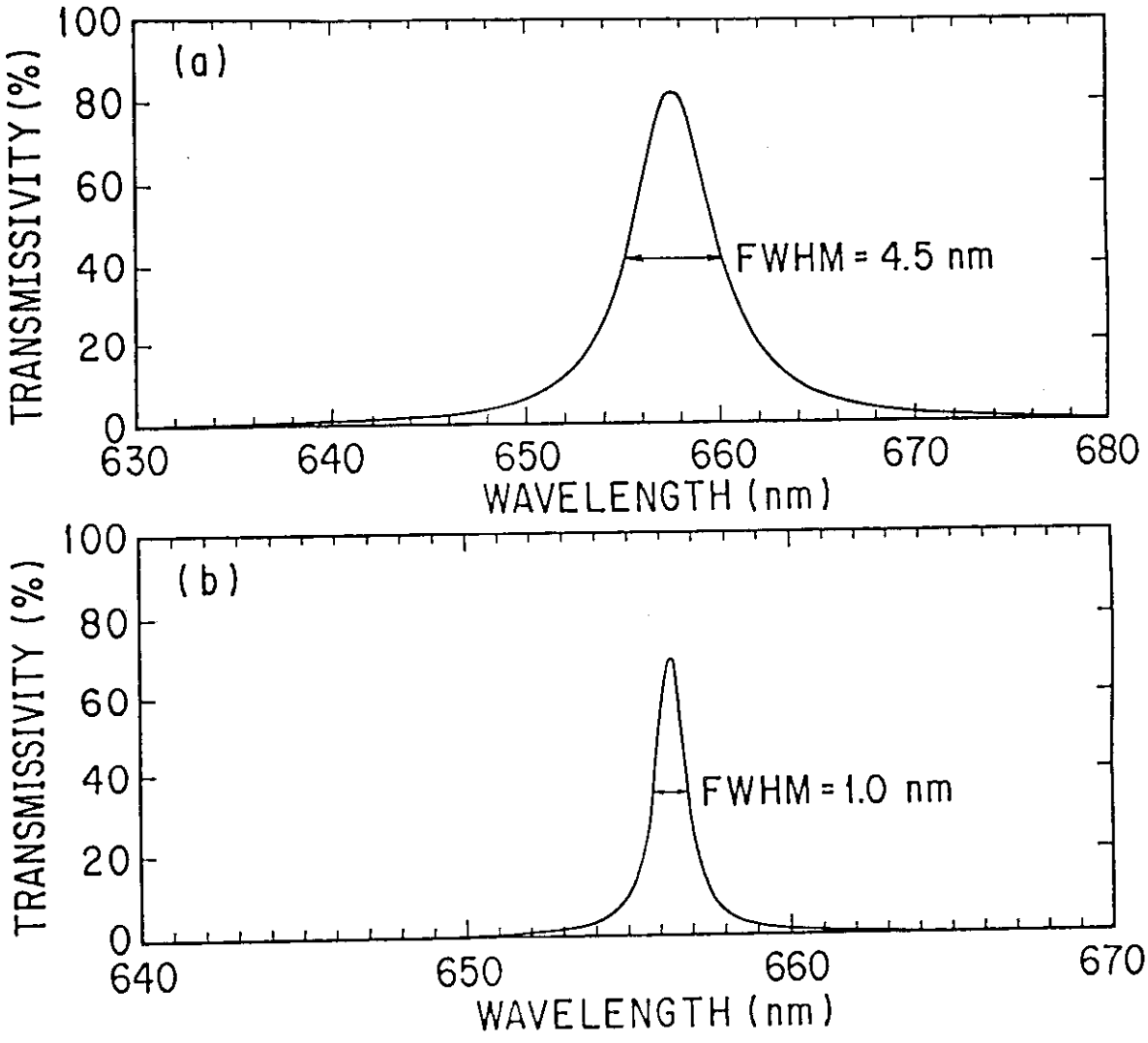

Fig. 5.16 Transmissivities of Hα filters as a function of wavelength: (a) original filter with FWHM = 4.5 nm; (b) new filter with FWHM = 1 nm.

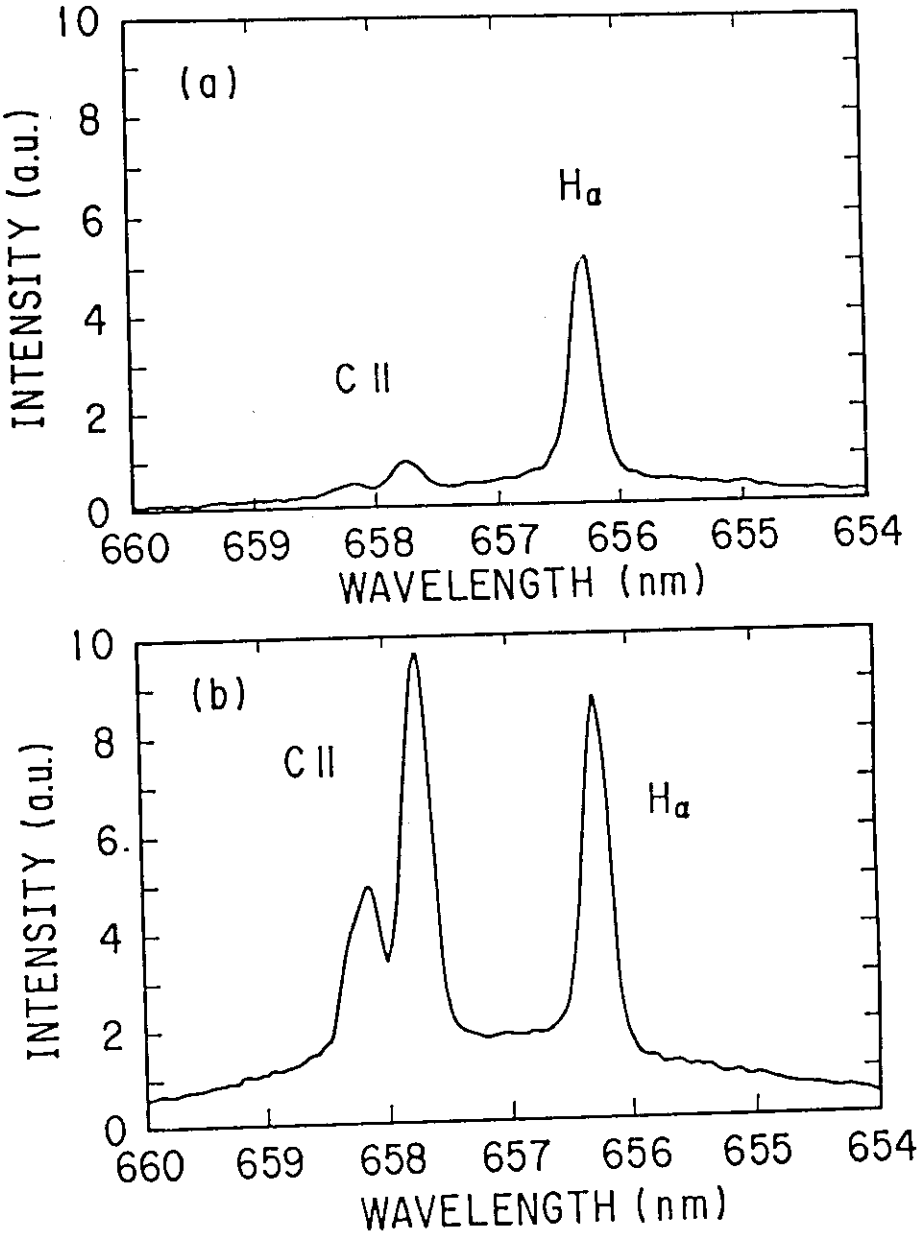

Fig. 5.17 Radiation spectra around Hα line from divertor plasma in (a) non IDC plasma and (b) IDC Plasma.

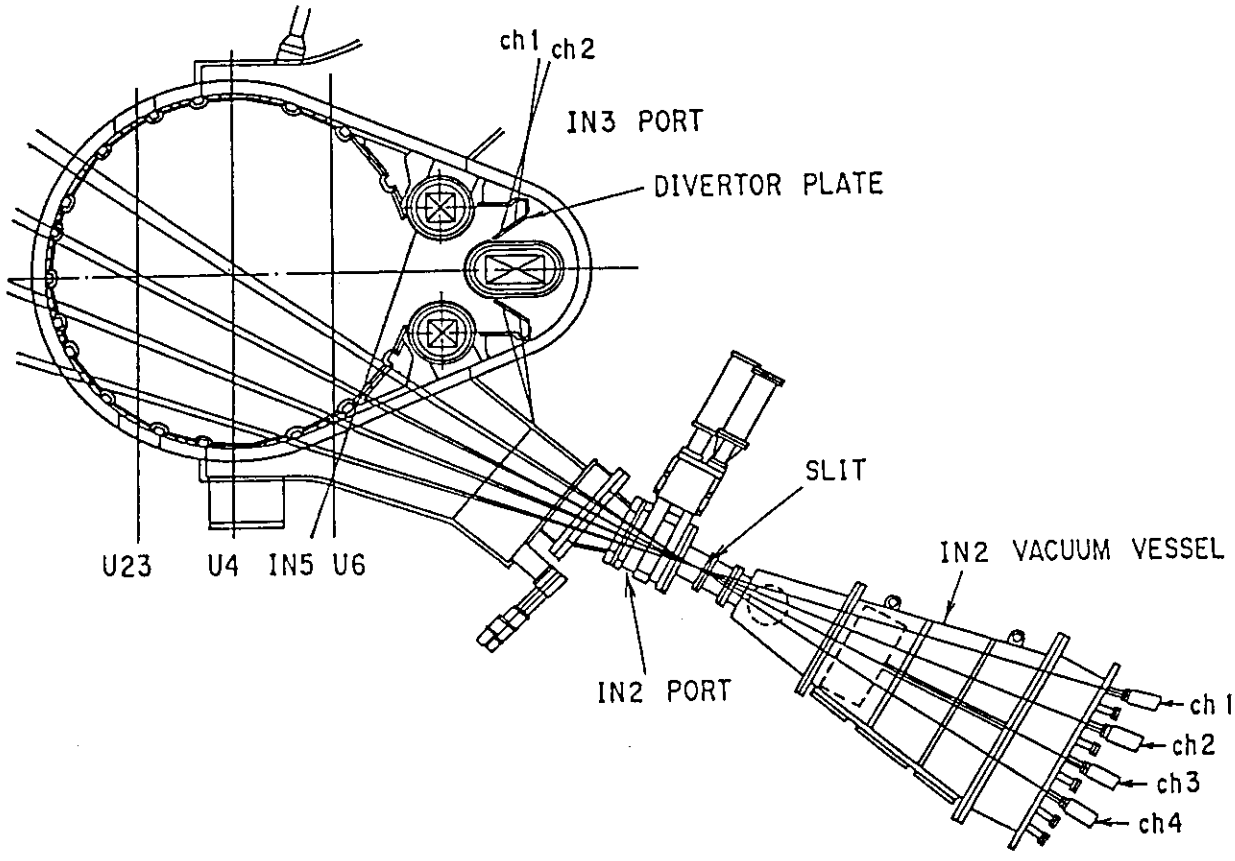

Fig. 5.18 Sightlines of the Hα detectors. The four channels of the Hα detector were mounted at the same vacuum chamber as the bolometer array and x-ray imaging system. The three channel Hα-detectors with vertical sightlines at R = 2.53, 3.04, and 3.55 m, and one detector viewing near the X-point of the divertor were mounted on the diagnostics ports under the vacuum vessel. A couple of the detectors on electron and ion drift sides measured Hα emissions on the divertor plates.

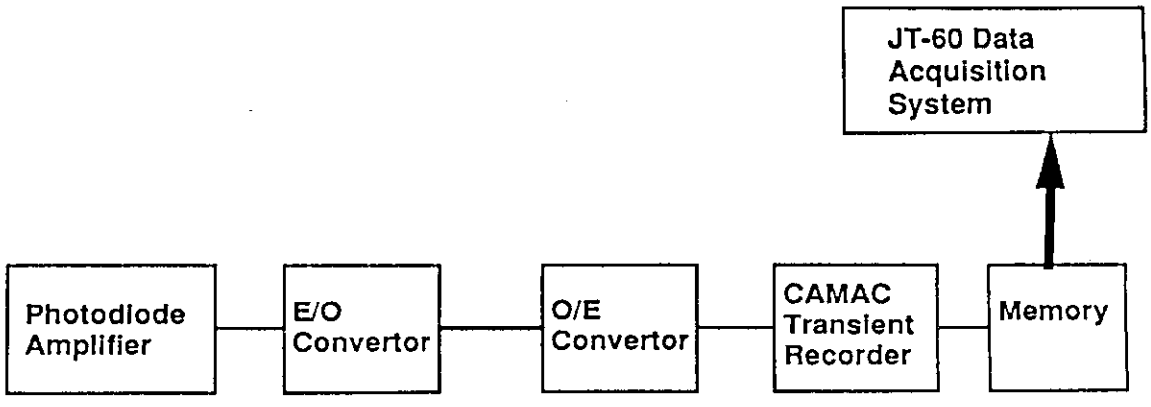

Fig. 5.19 Block diagram of the data acquisition for the Balmer line measurement system.

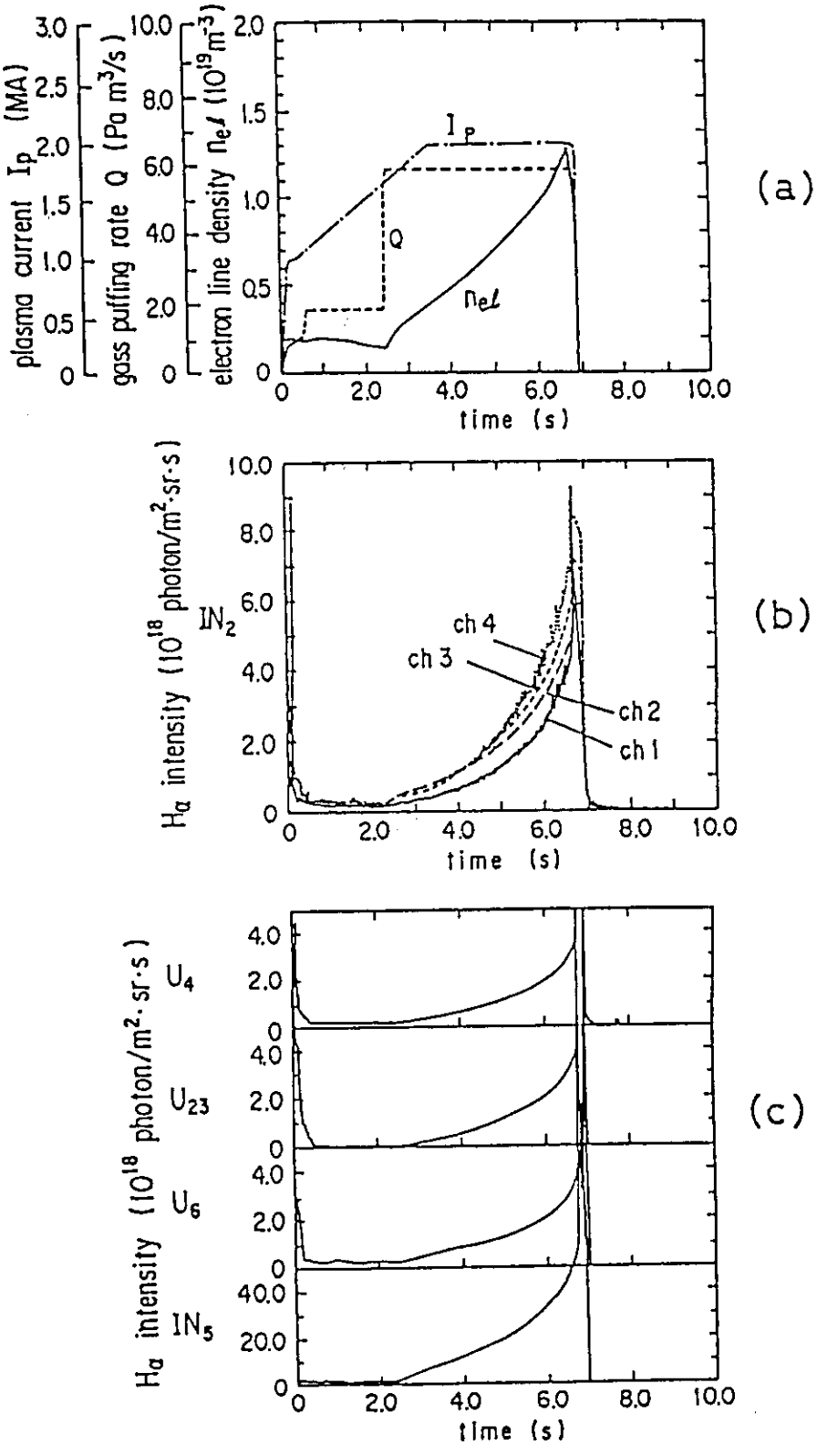

Fig. 5.20 Time evolutions of Hα intensities in the ohmically heated outer-divertor discharge with large gas puff rate.

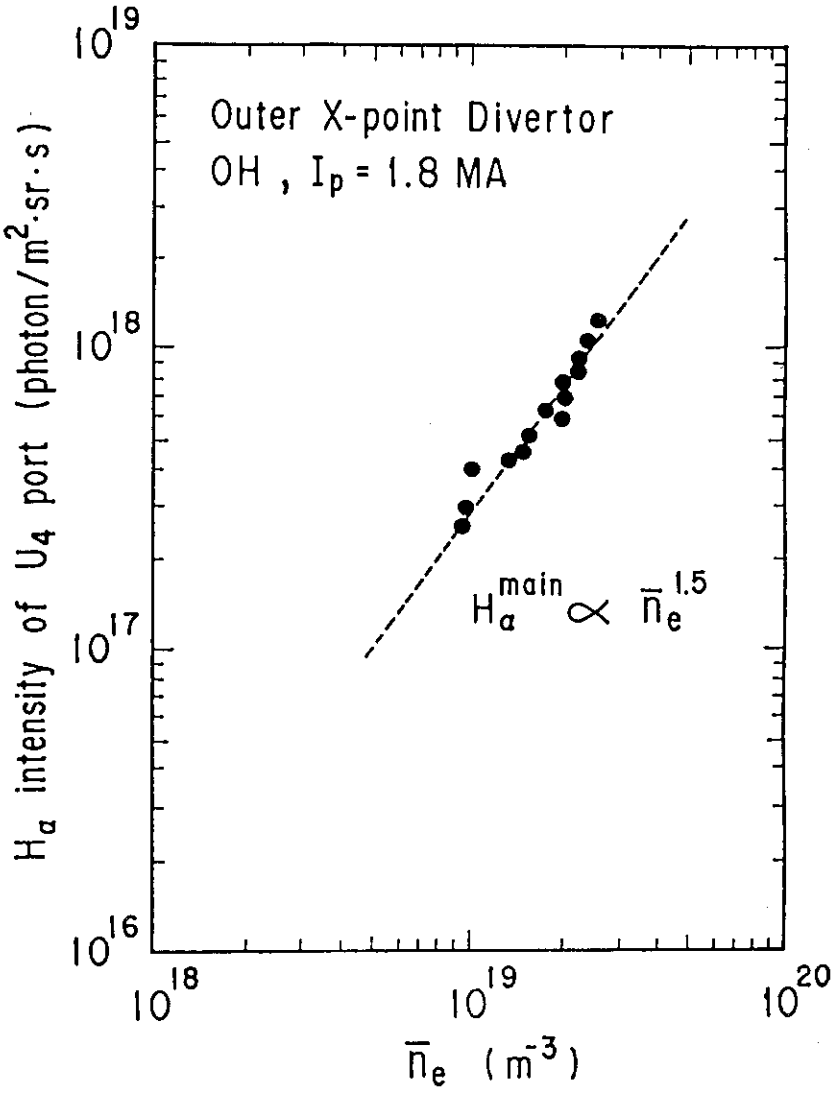

Fig. 5.21 The relationship between the Hα intensity and line-averaged electron density at the vertical chord of R = 3.04 m.

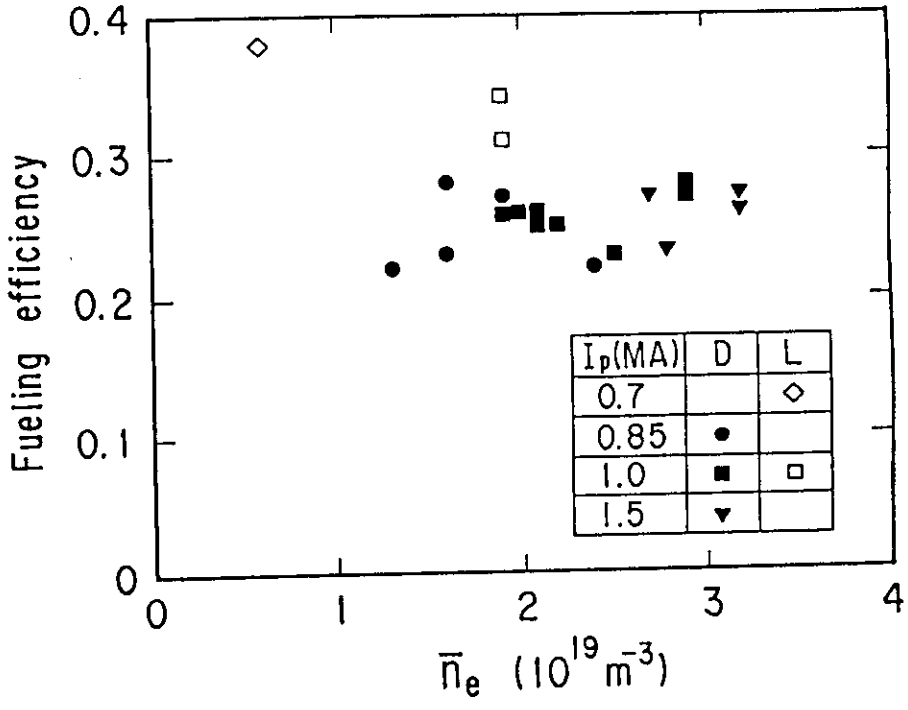

Fig. 5.22 Fuelling efficiency of gas puff as a function of $\bar{n}_e$.

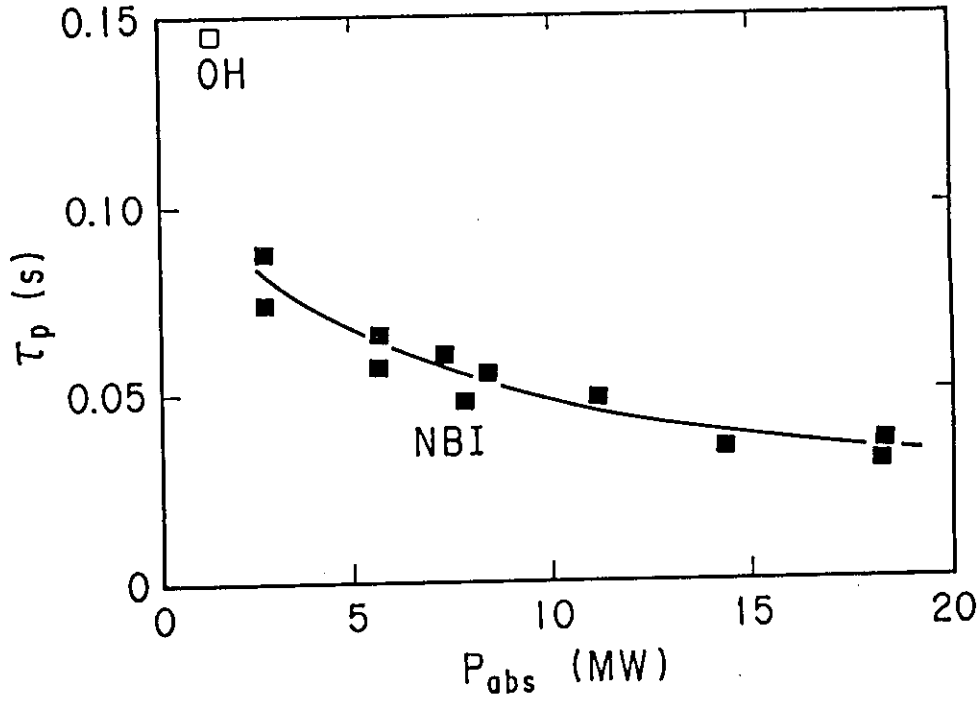

Fig. 5.24 Global particle confinement time of NB heated plasmas as a function of the NB power.

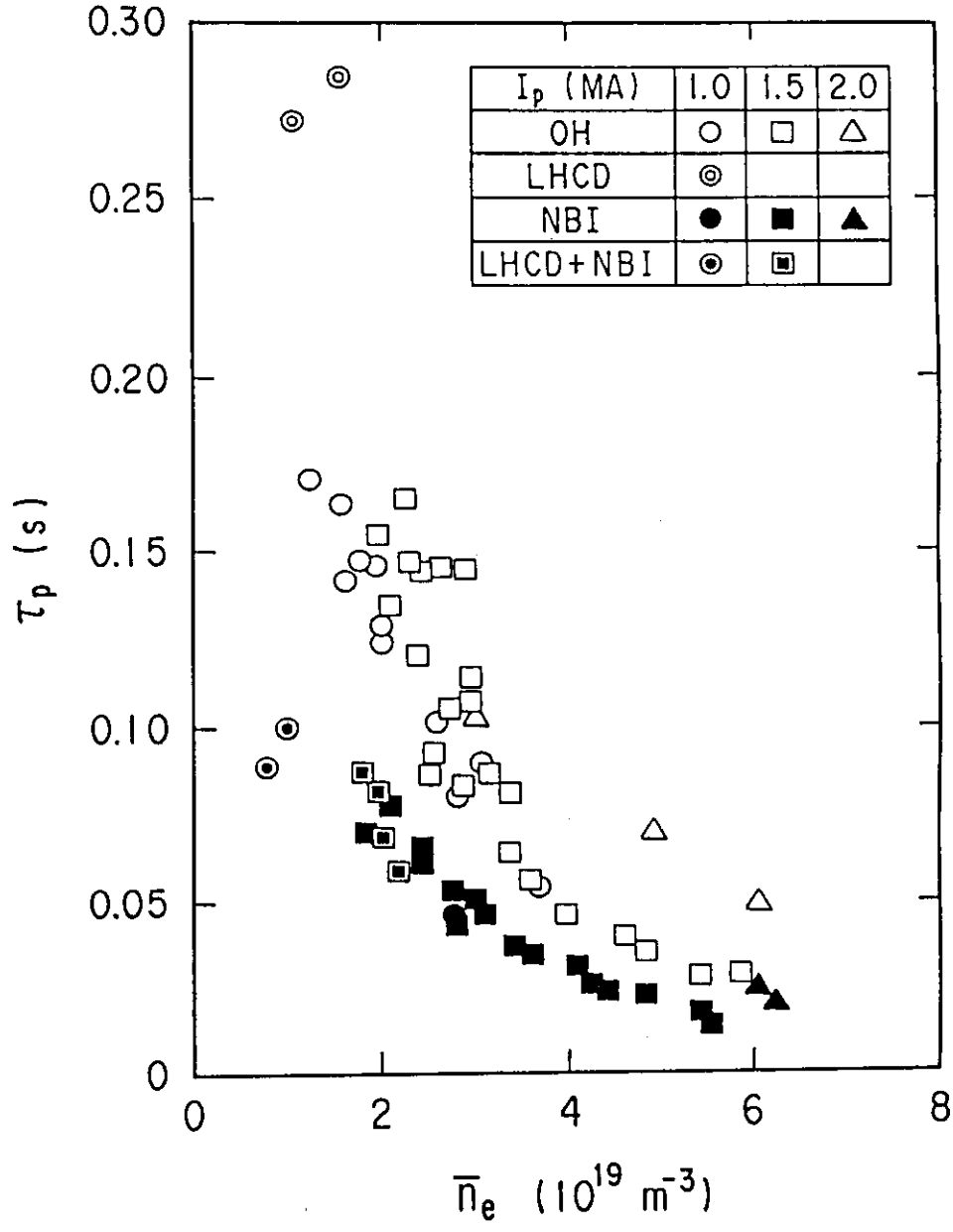

Fig. 5.23 Global particle confinement time of OH and additional heated plasmas as a function of $\bar{n}_e$.

6. Radiation Losses and Global Power Balances of JT-60 Plasmas

6.1 INTRODUCTION

The accumulation of impurities and the accompanying radiation losses in a core plasma are serious problem to achieve a reactor grade plasma not only because the radiation losses degrades the energy confinement of the core plasma but also because the impurities dilute the reacting plasma to reduce reaction rate. Whereas, appropriate radiation loss localized in the peripheral plasma is sometimes favorable to reduce the heat load onto the first wall and influx of impurities from the wall by cooling edge plasma namely remote radiative cooling. The poloidal divertor is one of the most effective methods of the impurity control as described in Chapter 1. Radiation losses, charge-exchanged neutral particles and heat load on the divertor plates are main mechanism of the energy loss from the plasma with divertor configuration. Measurement of the radiation losses is important not only for the power balance study but also for impurity study. The power balance studies have been performed in various tokamaks in large range of size and heating power [1-10].

JT-60 is a unique device among the three large tokamaks, having a closed divertor chamber. Original feature of JT-60 was a large tokamak device with a single null divertor outside the torus and with TiC coated molybdenum

limiter and divertor plates which demonstrated impurity and particle control successfully [11,12]. The characteristics of the outer X-point divertor is described in Refs. [13,14]. TiC coated molybdenum limiters were replaced by the graphite tiles. A new divertor coil was installed under the vacuum vessel to provide a lower X-point configuration in 1987. Radiation losses and global power balance of ohmic and high power NB heating up to 25 MW with three types of magnetic configuration and with two types of first wall have been investigated consistently in one device by using bolometer arrays, thermocouples in the divertor plates, and a IR TV camera on JT-60.

Section 6.2 reviews the JT-60 hardware and the diagnostics systems used in this study. Experimental results of radiation losses and global power balance are described is section 6.3. Reconstructed radiation profiles are presented in Section 6.4. Section 6.5 discusses the simulation of radiation losses for outer X-point discharges and the comparison with the results of spectroscopic measurements.

6.2 EXPERIMENTAL ARRANGEMENTS

In the first period April 1985-March 1987, the vacuum vessel of JT-60 was covered with armor plates of Inconel 625, toroidal limiters and divertor plates of TiC coated molybdenum (see Fig. 2.2). The study of radiation loss and global power balance was carried out mainly by bolometric measurement. In this period, radiated power from the main plasma was measured with the lower array of bolometer consisting of 15 channels and three channel vertically viewing bolometers and one channel bolometer viewing near the X-point (see Fig. 3.8). Radiated power from the divertor chambers were measured with a couple of bolometer on electron and ion drift sides. Heat load onto the divertor plates was measured with a set of thermocouples in the plates

All of the TiC coated molybdenum limiters and divertor plates were replaced with graphite tiles in May 1987. And new divertor coils were installed under the vacuum vessel in order to make a lower X-point configuration in December 1987. Radiated power from the main plasma is measured by two fan arrays of bolometer and that from the divertor region is measured by single bolometer after the replacement (see Fig. 3.9). Note the viewing field of the divertor bolometer includes the X-point in the typical divertor configuration. An IR TV camera measures the temperature of the divertor plates from the top of the vacuum vessel in order to obtain the heat load onto the divertor plates (see Fig. 2.12).

The electron density of the main plasma is measured with FIR interferometers along the three vertical chords of R=2.53 m, 3.04 m, and 3.55 m (see Fig. 2.6). After the modification for the lower X-point divertor, the central chord (R=3.04 m) has not been available on account of the new divertor coil. Instead of the FIR interferometer, new 2 mm wave one was installed. Hα emissions from the main plasma are measured with photodiodes with Hα interference filter. Visible and VUV spectrometers measures impurity lines in the ranges of 50-122 nm and 0.5-50 nm, respectively, with temporal resolution of 15 ms in the same toroidal section as the bolometer array (see Fig. 2.11). Hα emission and impurity lines in the divertor plasma are measured with similar Hα monitors and visible spectrometer via fiber optics, respectively, with the same viewing chord as divertor bolometer in outer X-point configuration.

6.3 GLOBAL POWER BALANCE

6.3.1 Limiter and Outer X-point Discharges with TiC Coated Molybdenum Wall

The ratios of the radiated power from the main plasma in ohmically heated discharges are plotted against the line averaged electron density $\overline{n}_e$ in Fig. 6.1. The plots shows that the radiation loss of the limiter discharges is more than 70% of the ohmically input, which is consistent with the results of ASDEX in limiter discharges (P_{rad}/P_{OH} = 45-85%) [5], JET (P_{rad}/P_{OH} = 70-90%) [9], and TFTR (P_{rad}/P_{OH} ~ 80%). The outer X-point configuration, however, fractional radiated power from the main plasma to the ohmically input P_{rad}^{main} / P_{OH} was 20% for hydrogen plasma and 15% for helium in the range of $\overline{n}_e$ 1-5 × 10^{19} m^{-3} and increased gradually with $\overline{n}_e$ in 1.5 MA discharges. For the 1.5 MA helium discharge with $\overline{n}_e$ of 4 × 10^{19} m^{-3}, heat load onto divertor plates $P_{T/C}^{div}$ was estimated from the thermocouples to be about 50% of the ohmically input, and radiated power from the divertor chambers was 15% of the ohmically input. In ASDEX, P_{rad}^{main} / P_{OH} and P_{rad}^{div} / P_{OH} are typically 20% and 50%, respectively [5]. P_{rad}^{div} / P_{OH} of JT-60 is about one third of that of ASDEX. The I_P dependence of the fractional radiation loss is shown in Fig. 6.2. P_{rad}^{main} / P_{OH} decreases with the increase of I_P. P_{rad}^{main} / P_{OH} of the helium plasma was smaller than that of hydrogen plasma in 1.5MA and 2MA divertor

discharges. Whereas, 1MA helium plasma was very radiative similar to the limiter plasma.

NB heating up to 20MW was carried out in the limiter and outer X-point discharges with TiC coated molybdenum limiter and divertor plates. Figures 6.3 (a) and 6.3 (b) show the global power balance of the NB-heated limiter and outer X-point discharges as function of the absorbed power P_{abs} which is defined as $P_{OH}+P_{NB}-P_{shinethrough}$ where $P_{shinethrough}$ is the NB power passing through the plasma. In the limiter discharges, P_{rad}/P_{abs} was about 60% and 90% for hydrogen and helium plasma, respectively. In the outer X-point discharges, however, P_{rad}^{main} / P_{abs} and P_{rad}^{div} / P_{abs} for hydrogen plasma were 10% and 15%, respectively. And those for helium plasma and 20% and 5%, respectively. Heat load onto the divertor plate was about 60% of the absorbed power for both hydrogen and helium plasmas. The global power balance was almost independent of the absorbed power. It is remarkable that very low radiation loss of main plasma was realized in the outer X-point discharge with metallic wall and divertor plates in NB heating more than 20 MW.

Figure 6.4 shows the global power balance of the outer X-point discharges with NB heating as a function of $\overline{n}_e$. With the increase in $\overline{n}_e$, the reduction of the fractional heat load onto the divertor plates was observed. The behaviors of radiated power from the ion and electron drift sides with increasing $\overline{n}_e$ are different as shown in Fig. 6.5. Radiated power from the electron drift side increased with the increase in $\overline{n}_e$, whereas that from the ion drift side had a maximum value at $\overline{n}_e$ of $4 \times 10^{19} m^{-3}$ and decreased steeply with $\overline{n}_e$ above $4 \times 10^{19} m^{-3}$. Both of the heat load onto the divertor plates of the ion and electron drift sides decreased with $\overline{n}_e$. Simple divertor simulation was performed to interpret the behavior of the divertor radiation. The calculational results is presented in Section 6.5. The missing power increased with $\overline{n}_e$ as shown in Fig. 6.4. Three channel bolometers with vertical viewing chord at R=2.53 m, 3.04 m, and 3.55 m were added in order to investigate the poloidal asymmetry of the radiation profile in the R direction. Those bolometers indicated that an enhanced radiative region existed outside of the main plasma and the asymmetric radiation increased with electron density. The bolometer array and the divertor bolometers did not view the X-point region which existed outside of the torus, so the most of the missing power was considered to be the radiation loss from the X-point region.

The plasma was disrupted frequently by the burst of the radiation loss in high power NB injection. Soft x-ray spectra obtained by the PHA measurements in the NB heated divertor discharge with the radiation burst

are shown in Fig. 6.6. Before NB heating and initial phase of the NB heating without the radiation burst (t = 3-3.2 s), a molybdenum line was not observed although titanium and nickel lines were observed. During the burst (t = 3.3-3.5 s) and after the burst (t = 3.5-3.8 s), a significant peak of molybdenum line was observed. It was revealed that the radiation burst was caused by the molybdenum influx. The origin of the molybdenum burst was guessed to be the melting of the divetor plates in the NB heating, so that the sweep of the separatrix on the divertor plates were tried to reduce the heat load onto the divertor plates. The sweep successed to suppress the radiation burst as shown in Fig. 6.7. In spite of the separatrix sweeping, the injection time of the NB was restricted to be one second more or less. Therefore all of the TiC coated molybdenum limiters and divertor plates were replaced with graphite tiles in May 1987, which cover the half of the vacuum vessel area.

6.3.2 Outer X-point and Limiter Discharges with Graphite Wall

Figure 6.8 shows the global power balance of the NB heated outer X-point discharges with graphite wall as a function of $\overline{n}_e$ in the case of Ip = 2.4-2.7MA and P_{NB} = 17-22MW. With the increase in $\overline{n}_e$ radiated power from the main plasma increased from 15% to 25% of the absorbed power, that of the divertor plasma kept constant to be 15%, whereas the heat load onto divertor plates decreased from 50% to 30%. Radiation loss of the main plasma was larger than that of TiC coated molybdenum case, however, that of the divertor plasma was smaller that of TiC coated molybdenum case.

In NB heated limiter discharges with graphite wall, radiated power was 25% of the absorbed power in the range of $\overline{n}_e$ from 1 to 6 $\times$ $10^{19}m^{-3}$ independent of the plasma current as shown in Fig. 6.9, which is not so inconsistent with the results of JET (P_{rad}/P_{abs} = 30-60%) [10] and TFTR (P_{rad}/P_{abs} ~ 20%) [8]. With the increase in $\overline{n}_e$ larger than 6 $\times$ $10^{19}m^{-3}$, radiation loss increased steeply. In these plasma radiated power from the peripheral region contributed the increase of the total radiated power. Near the density limit, marfe [15] appeared on the inside wall [16]. The radiation loss of the plasma with marfe reached up to 90% of the absorbed power. The marfe had not been observed in TiC molybdenum wall except a few discharges. After replacement of the wall by graphite tiles it has observed frequently in high Ip and high $\overline{n}_e$ of limiter discharges with NB heating. The characteristics of the marfe is described in Chapter 7.

6.3.3 Lower X-point Discharges with Graphite wall

The improved divertor confinement (IDC) [17] regime has been obtained in NB heated lower X-point discharges with graphite wall. The characteristics of IDC is described in Chapter 7. Figure 6.10 is the global power balance of the NB heated lower X-point discharges with and without IDC as a function of $\overline{n}_e$ where Ip=1MA and B_T=3.3T. Closed and open symbols represent IDC and non IDC discharges. Radiated power from the main plasma was approximately 20% of the absorbed power almost independent of the electron density. With the increase in $\overline{n}_e$, radiated power from the divertor region increased. Similar increase of P_{rad}^{div} with $\overline{n}_e$ was reported in ASDEX [5]. The increase of the power in the IDC was larger than that of non IDC discharge. The heat load onto the divertor plates of the IDC discharge was smaller than that of the non IDC discharge in the same electron density. The total output power, the radiation losses and the heat load onto divertor plates, was not so different between IDC and non IDC discharges. It indicates that the remote radiative cooling in the divertor region is enhanced in the IDC discharges, which reduces the heat load onto the divertor plates.

6.4 RADIATION PROFILES

It was estimated from the raw data of the bolometer array that the radiation profile had a poloidal asymmetry in the divertor discharges. So an Abel inversion is not available to obtain the radiation profiles. In the period of TiC molybdenum wall, additional three channel vertically viewing bolometers and one channel bolometer viewing near the X-point were available, so that the reconstruction of the radiation profile was tried by using asymmetric Abel inversion as described in Sec. 3.4. Figure 6.11 shows the radiation profiles on the midplane for outer X-point discharges with different $\overline{n}_e$. The radiation near the X-point is enhanced in the higher $\overline{n}_e$ case. Whereas the radiation power density of central region in the lower $\overline{n}_e$ case was larger than that in higher $\overline{n}_e$ case, which is consistent with the results of spectroscopic measurements that the titanium concentration decreases with $\overline{n}_e$ and the radiation loss in central region is considered to be due mainly to titanium [18].

6.5 DISCUSSION

6.5.1 Simulation of Divertor Radiation Losses in Outer X-point Discharges

The behavior of the radiated power from the divertor chamber with $\bar{n}_e$ was so curious as shown in Fig. 6.5, that simulation of the divertor plasma was carried out [14]. The simulation model employed here consists of the tokamak transport code combined with a divertor fluid model, which solved the transport of the scrape-off layer plasma and divertor plasma consistently. The model is based on: (1) one-dimensional fluid equation particle, momentum and energy transport of the divertor plasma along the magnetic field lines, and (2) a two dimensional Monte Carlo method for the particle, momentum and energy source due to ionization and charge exchange reaction of neutral particles. The model geometry for the simulation analysis is illustrated in Fig. 6.12, together with the divertor plasma model of width δ_S and length L_1 which is projected onto the poloidal plane. The effective pumping rate of particles f_{pump} includes the bypass component to main chamber through the duct, wall absorption and exhaust from the divertor chamber. In this model, only hydrogen atoms are treated in the Monte Carlo calculation, and only hydrogen line radiation estimated by a collisional radiative model is assumed as a source of radiation loss from the divertor plasma. Figure 6.13 shows the simulation result for NB heated discharge (P_{NB} = 20MW) comparison with the experimental results. The calculated P_{rad}^{div} increases abruptly with $\bar{n}_e$ in the range of 1-4 $\times$ 10^{19} m^{-3}. The saturation and decrease of P_{rad}^{div} are observed both in simulation and experiment, which is due to the low temperature of the divertor plasma caused by high recycling. Here measured P_{rad}^{div} is total radiated power from ion and electron drifts sides. The measured P_{rad}^{div} is by a factor of about two smaller than the calculated value in the wade range of $\bar{n}_e$. More detailed measurements for both divertor and scrape-off layer plasmas in the main chamber are needed to investigate this discrepancy.

6.5.2 Comparison with Spectroscopic Measurements

Though the bolometric measurement is convenient for the investigation of the global power balance and for monitoring plasma performance, the

information of impurities causing radiation loss can not be obtained by the bolometric measurement only. In order to interpret the data from the bolometric measurements, the results of the spectroscopic measurements must be referred. The impurity contents, Z_{eff}, and radiation losses of JT-60 plasmas are summarized in Table 6.1 [18], where the results for NB heated hydrogen discharges at $\bar{n}_e = 4 \times 10^{19}$ m^{-3} are represented. In NB heated divertor discharges with TiC coated molybdenum wall, Z_{eff} was 1.6, and concentrations of oxygen, carbon and titanium were respectively about 1%, 0.1% and 0.006% of $\bar{n}_e$. The radiation loss due to oxygen was dominant there. The concentration of metallic impurities decreased drastically when the TiC coated molybdenum wall was replaced by graphite tiles. The titanium concentration after the replacement was 1/3 - 1/10 of that before the replacement, and the contribution of metallic impurities to the radiated power was less than 1%, even in NB heated limiter discharges. The increase of the carbon concentration in NB heated divertor discharges was by a factor of four after the replacement. In the limiter discharges with graphite wall, the carbon concentration increased to 5% and Z_{eff} increased up to 3 comparison with the divertor discharges.

Table 6.1 Impurity contents and radiation losses in NB heated JT-60 Plasmas.

		Divertor	Limiter
TiC coated	Z_{eff}	1.6	
molybdenum	C	0.1%	
first wall	O	1%	
	Ti	0.006%	
	P_{rad}^{main}/P_{abs}	10%	≥60%
Graphite	Z_{eff}	2.2	3.0
first wall	C	0.4%	5%
	O	2%	1%
	Ti	0.0005-0.002%	0.0005-0.002%
	P_{rad}^{main}/P_{abs}	20%	25%

For hydrogen plasmas at $\bar{n}_e = 4 \times 10^{19}$ m^{-3}

Figure 6.14 shows the radiated power from the main chamber calculated from the spectroscopic data as function of $\overline{n}_e$ comparison with that of bolometric measurement in NB heated discharges with graphite wall. In limiter discharges (Fig. 6.14(a)), the radiated power from carbon is the same as that from oxygen. In divertor discharges (Fig. 6.14(b)), the contribution of oxygen to the radiated power is dominant. The contribution from metallic impurities is estimated to be less than 1% in this case. The radiated power calculated from the spectroscopic data is consistent with that measured with the bolometer array, typically within a factor of two.

The bolometer is sensitive to charge exchange (CX) neutral particles same as to radiations. So the measured radiated power includes CX losses. The charge exchange loss is estimated to be less than 2-3% of the absorbed power by CX neutral particle analyzers.

6.6 CONCLUSION

Radiation losses and global power balances of the plasmas in the NB heated plasmas with different inner hardware, and with different plasma configurations have been investigated by bolometric measurements, thermocouples and IR TV camera on the JT-60 tokamak.

Very low radiation loss of the main plasma (10% of the absorbed power) was realized in NB heated outer X-point discharges with TiC coated molybdenum wall. The radiation loss due to oxygen was dominant in this case. Whereas, the limited plasmas with TiC coated molybdenum limiters were very radiative where the radiated power was more than 60% of the absorbed power in ohmically and NB heated discharges. In the discharges with graphite wall, radiated power from the main plasma was 20 - 25% for both of limiter and lower X-point configurations. The radiated power from the divertor region increased from several percent to 40% of the absorbed power with the increase of $\overline{n}_e$. The titanium concentration of discharges with graphite wall was 1/3 - 1/10 of that of TiC coated molybdenum wall. The dominant contributor to the radiation loss was oxygen in lower X-point discharges, and carbon same as oxygen in limiter discharges.

The improved divertor confinement (IDC) regime was obtained in NB heated lower X-point discharges with graphite wall where the energy confinement time was improved up to 20%. In IDC discharges the radiation loss from the divertor region increased to be up to 40% (typically 10 MW) of

the absorbed power. Whereas, that from the main plasma and the heat load onto divertor plates decreased in IDC.

The radiation profiles were reconstructed by an Abel inversion with an symmetric term for the outer X-point discharges. Intense poloidal asymmetries of radiated power localized near the outer X-point were observed. The asymmetry was enhanced with the increase of $\bar{n}_e$.

The behavior of P_{rad}^{div} with $\bar{n}_e$ in outer X-point discharge was simulated by simple divertor model. The simulation indicated that the increase of P_{rad}^{div} with $\bar{n}_e$ was saturated due to the low temperature of the divertor plasma caused by high recycling in the divertor.

Finally, this study revealed that the most clean plasma was obtained in the metallic first wall with the divertor on JT-60. This fact is suggesting the capability of the metallic material for the first wall of next devices such as ITER and FER.

REFERENCES TO CHAPTER 6

[1] H. Hsuan, K. Bol and R.A. Ellis, Nucl. Fusion **15** (1975) 557.

[2] J.W. Paul, K.B. Axon, J. Burt, A.D. Cring, S.K. Erent, et al., in Plasma Physics and Controlled Nuclear Fusion Research (*Proc. 6th Int. Conf. Berchtesgaden, 1976*) Vol. 2, IAEA, Vienna (1977) 269.

[3] EquipeTFR, ibid., Vol 1, 35.

[4] A.B. Berlizov, G.A. Bobrovskij, A.A. Bagdasarov, N.L. Vasin, A.N. Vertiporokh, et al., et al, ibid., Vol. 1 3.

[5] E.R. Müller, K, Behringer and H. Niedermeyer, H., Nucl. Fusion **22** (1982) 1651.

[6] P.C. Efthmion, N. Bretz, M. Bell, M. Bitter, W.R. Blanchard, et al., in Plasma Physics and Controlled Nuclear Fusion Research (*Proc. 10th Int. Conf. London, 1984*) Vol.1, IAEA, Vienna (1984) 29.

[7] J. Schievell, Rev. Sci. Instrum. **56** (1985) 972.

[8] K.W. Hill, V. Arunsalam, M.G. Bell, M. Bitter, W.R. Blanchard, et al., in Plasma Physics and Controlled Nuclear Fusion Research (*Proc. 11th Int. Conf. Kyoto, 1986*) Vol.1, IAEA, Vienna (1987) 207.

[9] K.H. Behringer, A.A. Maanen, J. Bonnerue, A. Bulliard, et al., in Plasma Physics and Controlled Nuclear Fusion Research (*Proc. 10th Int. Conf. London, 1984*) Vol.1, IAEA, Vienna (1985) 291.

[10] K.H. Behringer, A. Boileau, F. Bombarada, B. Denne, W. Engelhart, et al., in Plasma Physics and Controlled Nuclear Fusion Research (*Proc. 11th Int. Conf. Kyoto, 1986*) Vol.2, IAEA, Vienna (1987) Vol.1, IAEA, Vienna (1987) 197.

[11] JT-60 Team (presented by M. Yoshikawa), ibid, Vol. 1, 11.

[12] JT-60 Team (presented by H. Takeuchi), ibid., Vol.1, 217.

[13] H. Nakamura, T. Ando, H. Yoshida, S. Niikura, T. Nishitani and K. Nagashima, Nucl.Fusion **28** (1988) 43.

[14] H. Yoshida, S. Niikura, S. Shimizu, T. Ando, H. Nakamura, T. Nishitani, K. Nagashima and JT-60 Team, Nucl Fusion **28** 1988) 318.

[15] B. Lipschultz, Nucl. Mater. **145-147** (1987) 15.

[16] T. Nishitani and S. Ishida, *Study of Marfe Phenomena on JT-60*, Rep. JAERI-M 89-209, Japan Atomic Energy Research Institute, Ibaraki-ken (1989).

[17] S. Tsuji, M. Akiba, T. Ando, et al., in Plasma Physics and Controlled Nuclear Fusion Research (*Proc. 12 the Int. Conf. Nice 1988*) Vol. 1, IAEA, Vienna (1989) 265.

[18] H. Kubo, T. Sugie, A. Sakasai, Y. Koide, N. Nishino, T. Hirayama, T. Nishitani, K. Nagashima, N. Akaoka, H. Takeuchi and JT-60 Team, Nucl. Fusion **29** (1989) 571.

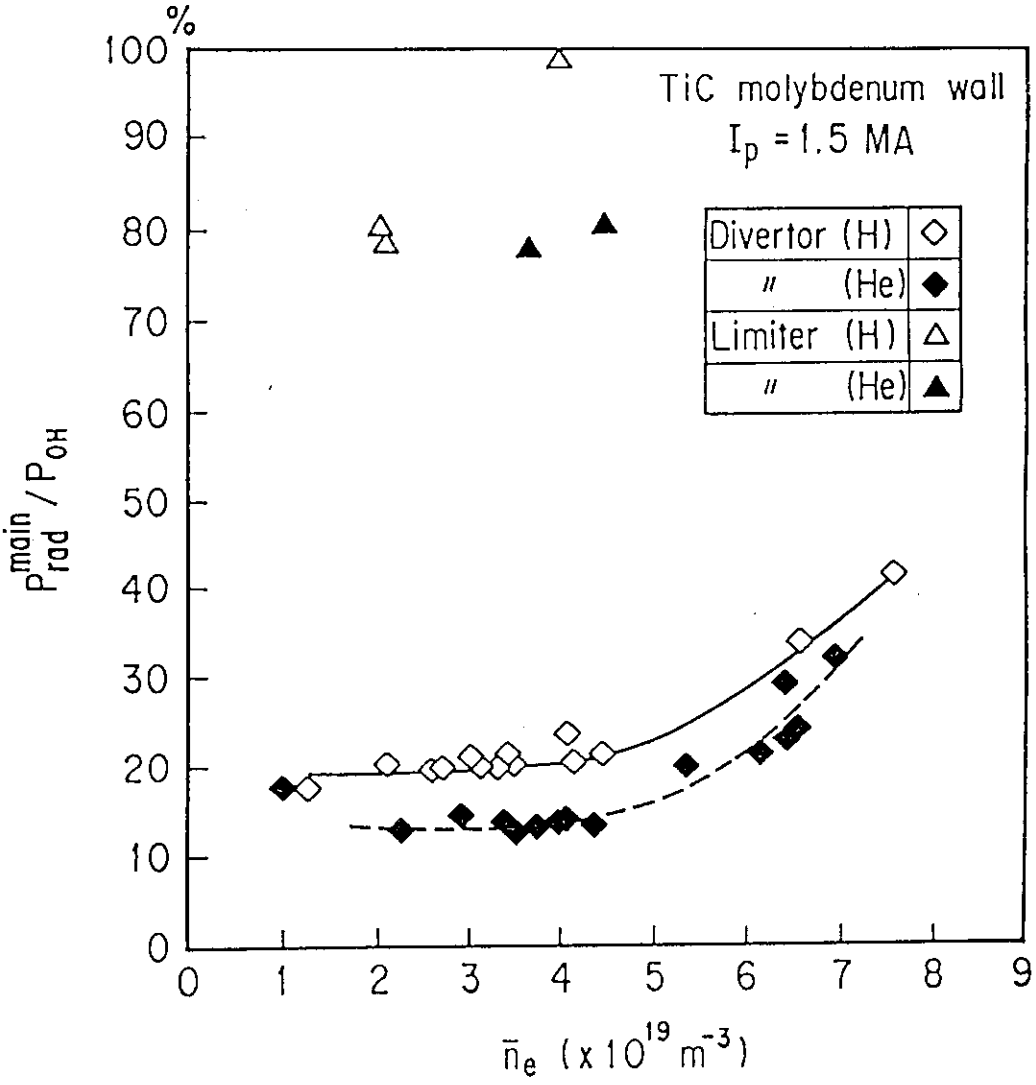

Fig. 6.1 The ratios of the radiated power from the main plasma to the input power in ohmically heated discharges with TiC coated molybdenum wall as a function of $\bar{n}_e$.

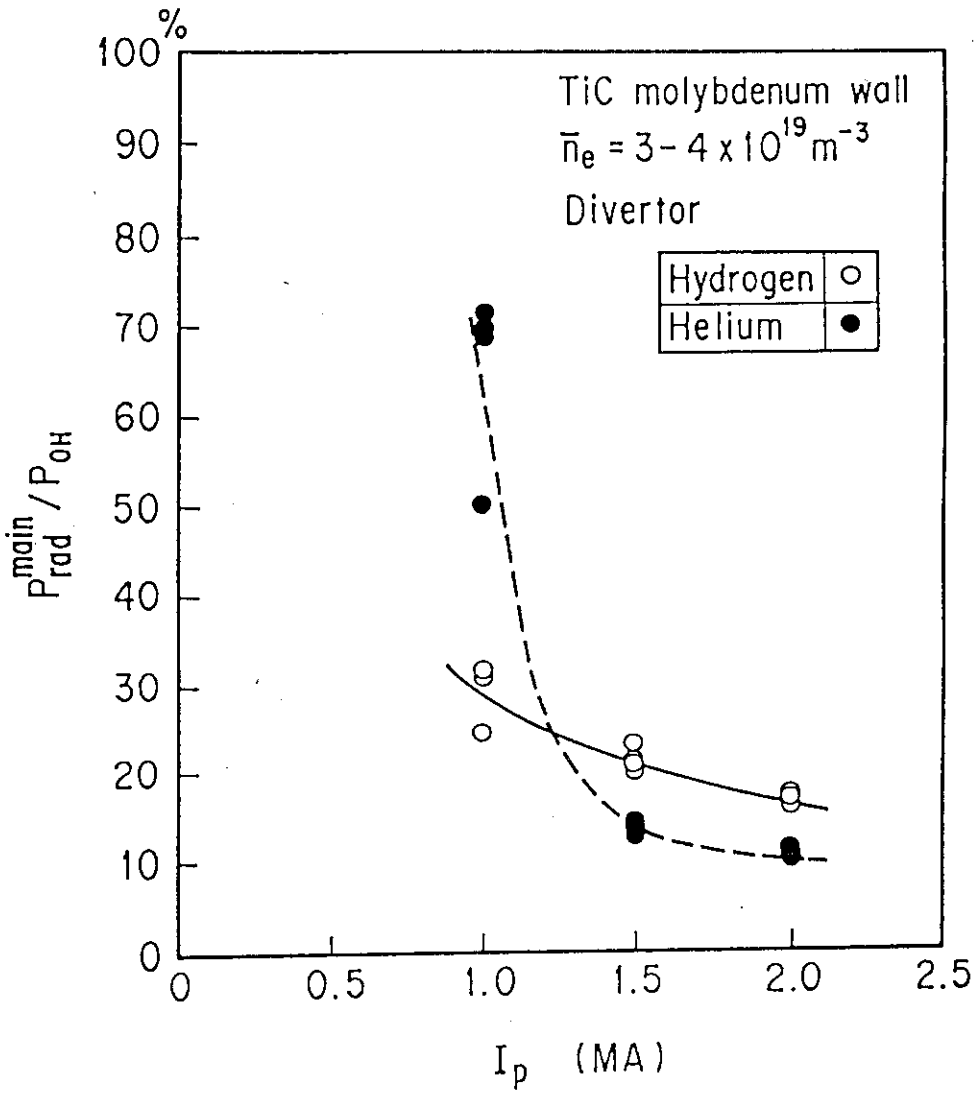

Fig. 6.2 The ratios of the radiated power from the main plasma to the input power in ohmically heated outer X-point discharges with TiC coated molybdenum wall as a function of I_P.

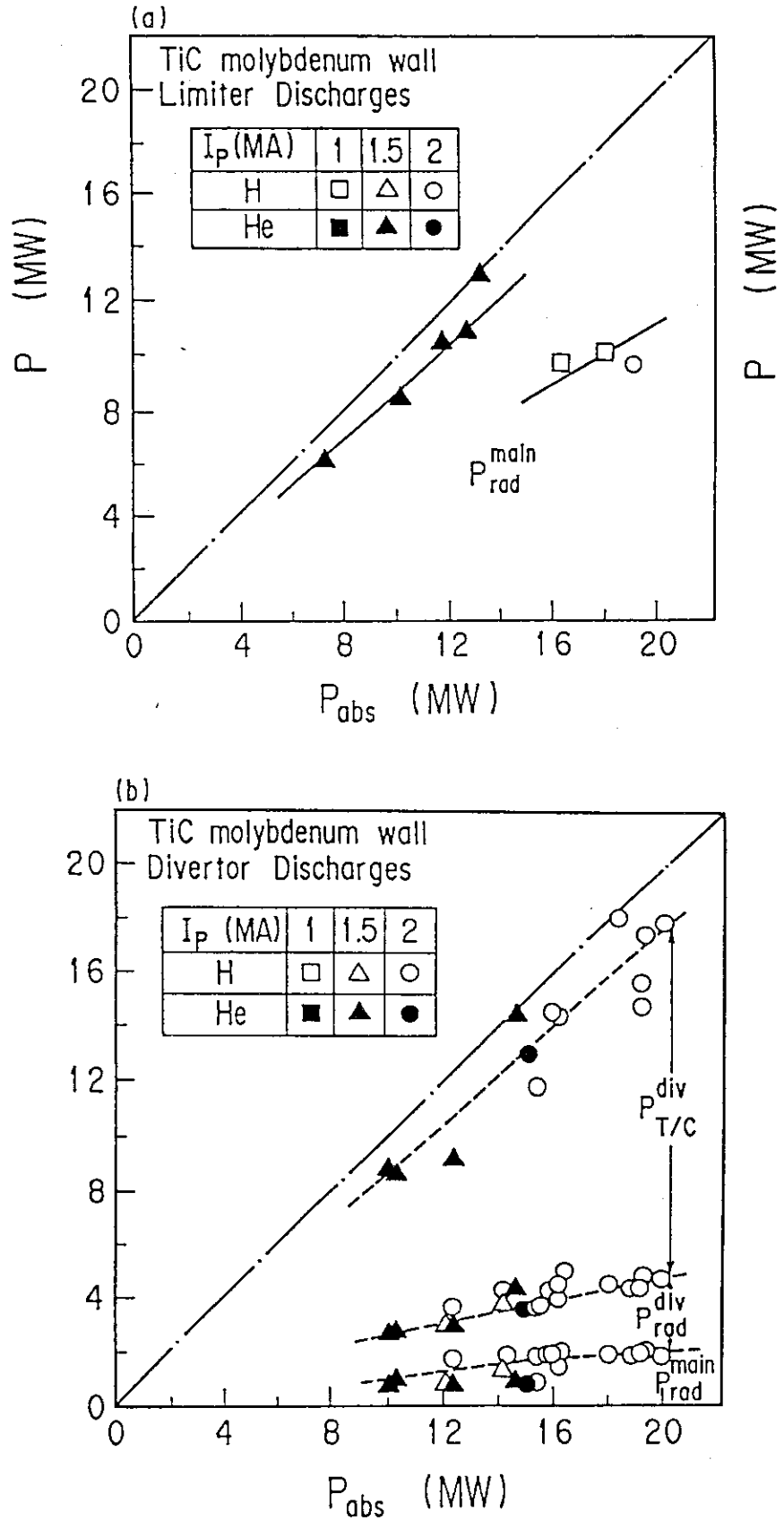

Fig. 6.3 Global power balance of NB-heated discharges with TiC coated molybdenum wall as a function of neutral beam power for (a) limiter and (b) outer-Xpoint discharges.

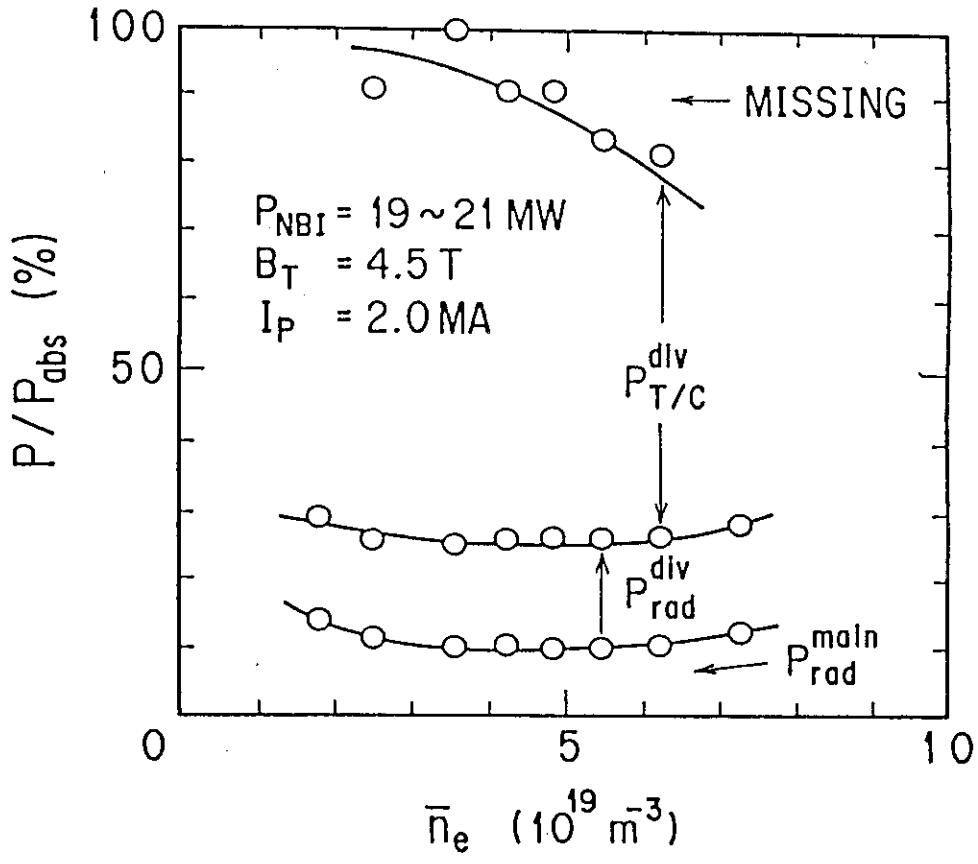

Fig. 6.4 Global power balance of NB-heated outer X-point discharges with TiC coated molybdenum wall as a function of $\bar{n}_e$.

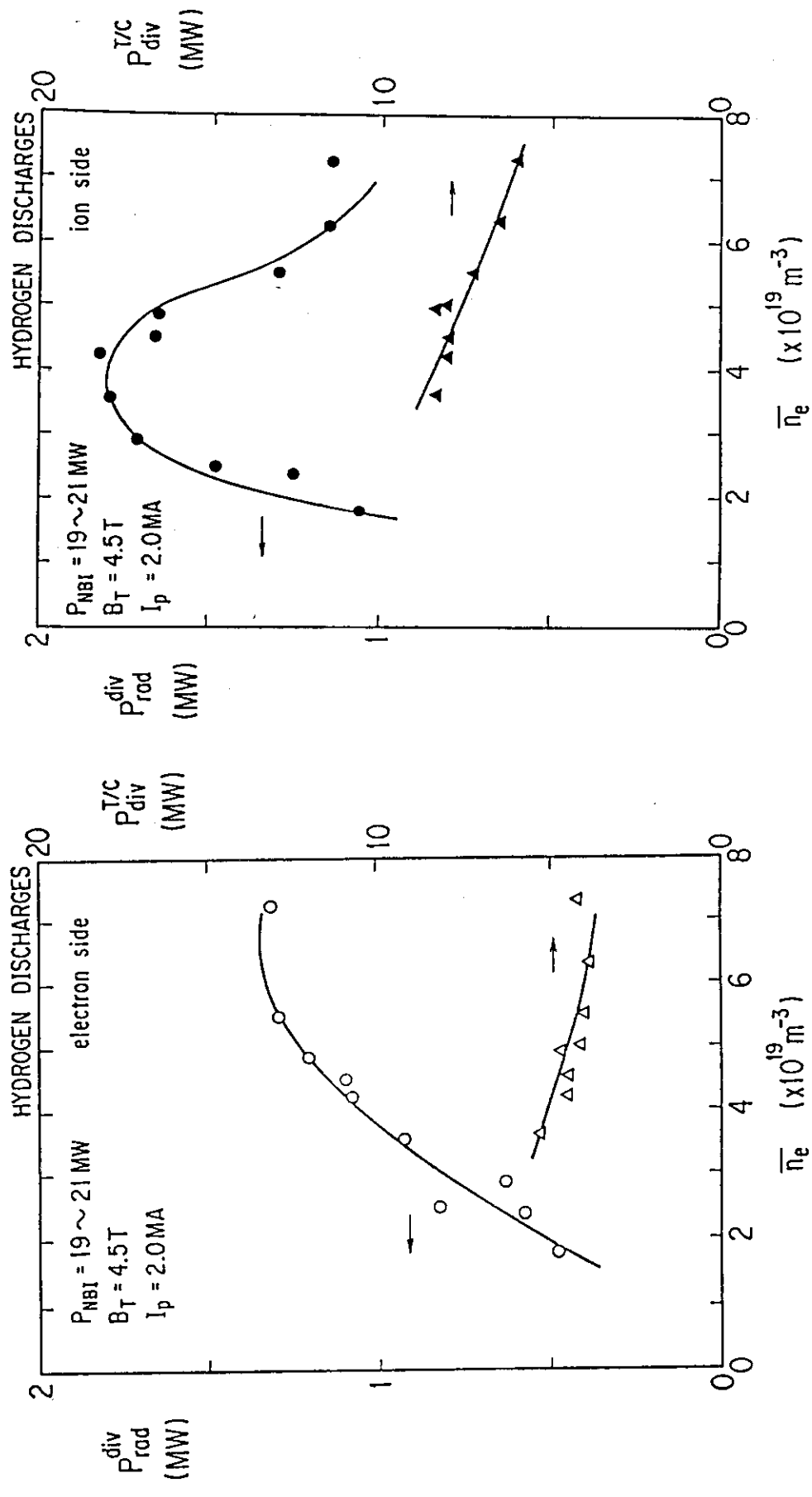

Fig. 6.5 The radiated powers from (a) ion and (b) electron drift sides as a function of $\bar{n}_e$ on NB-heated outer X-point discharges.

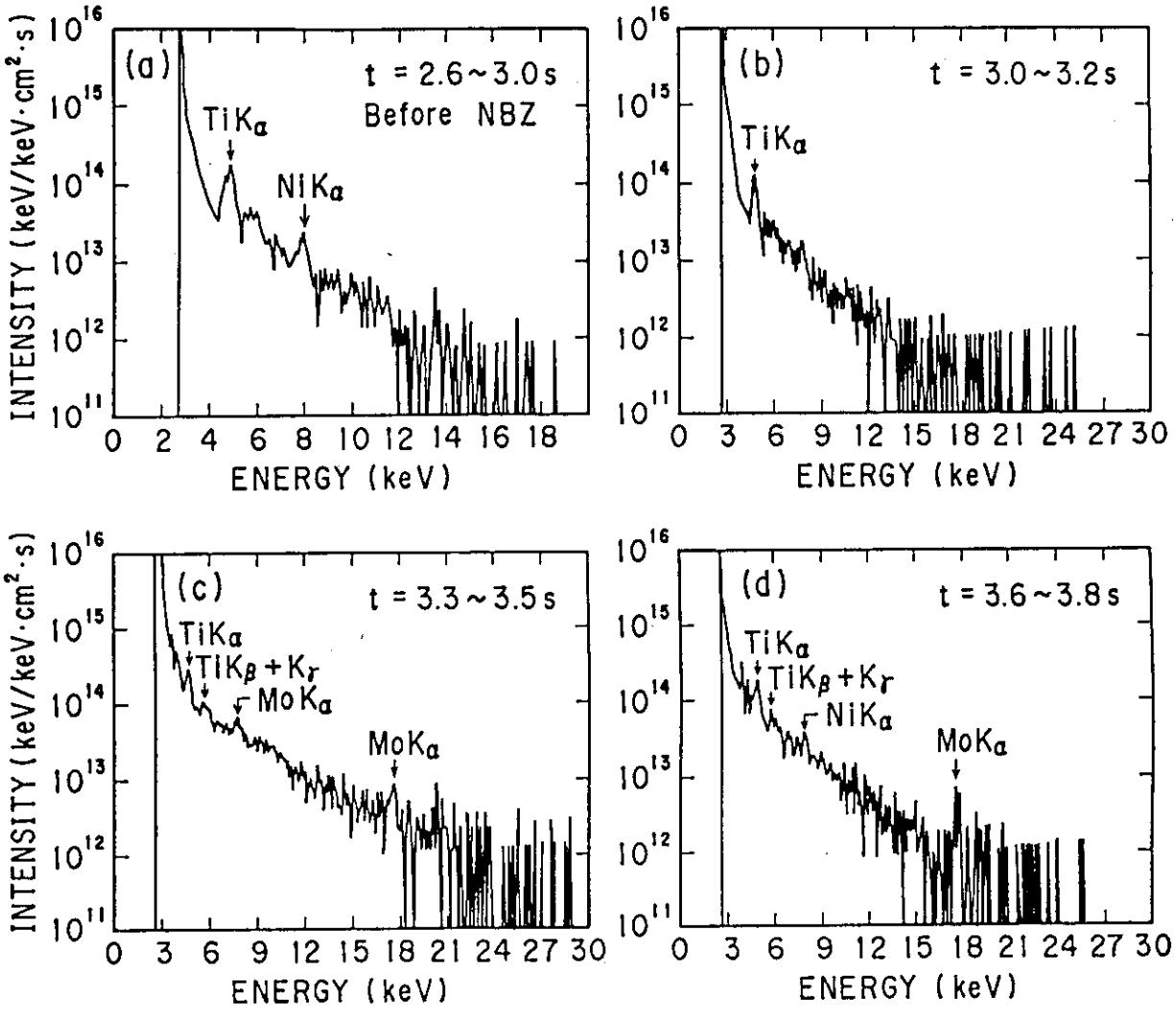

Fig. 6.6 Soft x-ray spectra obtained by the PHA measurements in the NB heated divertor discharge with the radiation burst. Before NB heating and initial phase of the NB heating without the radiation burst (t = 3-3.2 s), molybdenum line was not observed although titanium and nickel lines were observed. During the burst (t = 3.3-3.5 s) and after the burst (t = 3.5-3.8 s), significant peak of molybdenum line was observed.

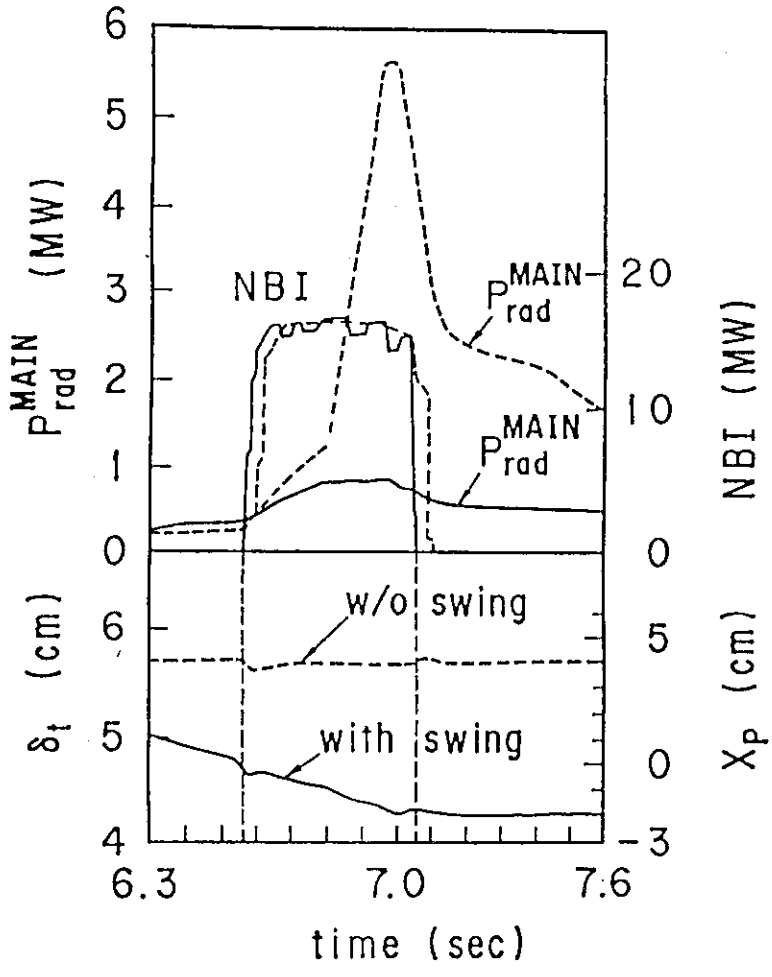

Fig. 6.7 Time evolutions of the radiation losses from the main plasma in the NB heated divertor discharges with and without separatrix sweep. Here δt is the distance between the separatrix surface and the can of the main divertor coil at the divertor throat. Xp is the distance between the X-point and the can of the main divertor coil, Xp in the standard configuration is defined to be 0.

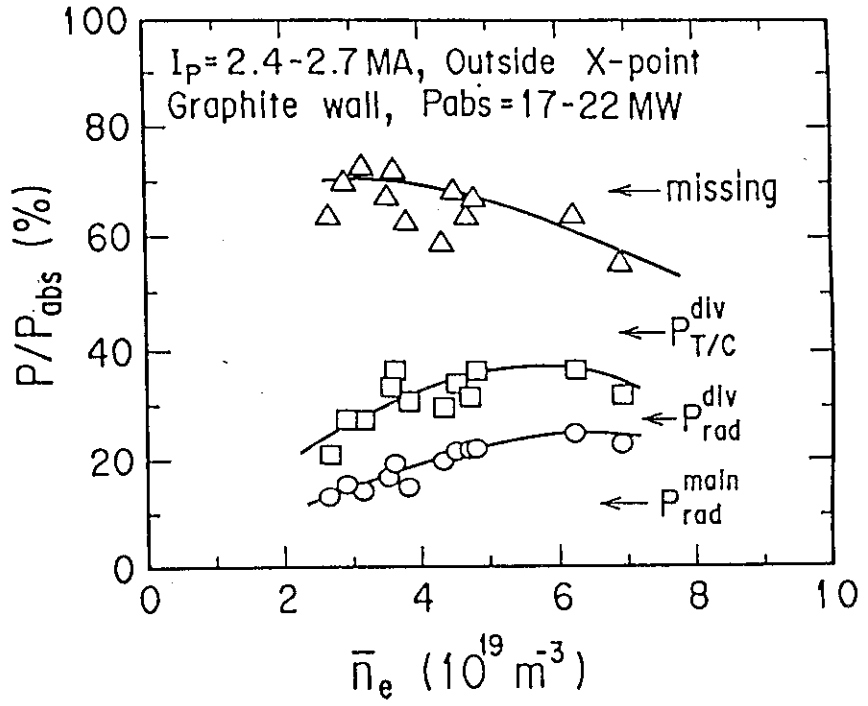

Fig. 6.8 Global power balance of NB-heated outer X-point discharges with graphite first wall as a function of $\bar{n}_e$.

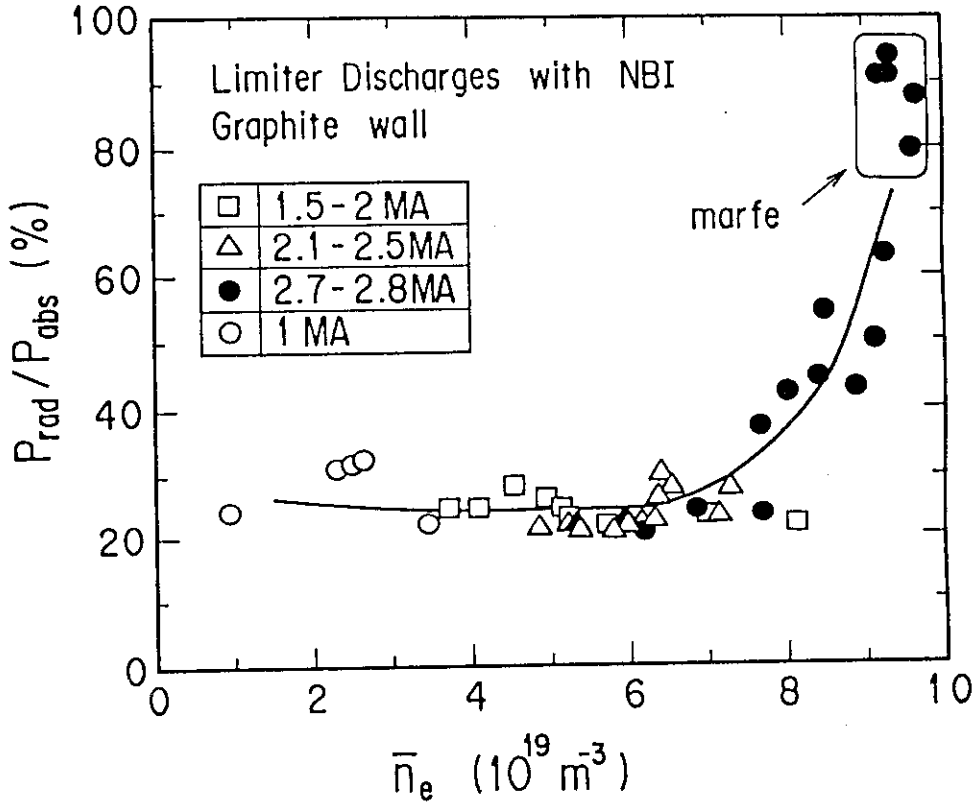

Fig. 6.9 Global power balance of NB-heated limiter discharges with graphite first wall as a function of $\bar{n}_e$. With the increase in $\bar{n}_e$ larger than $6 \times 10^{19} m^{-3}$, radiation loss increased steeply.

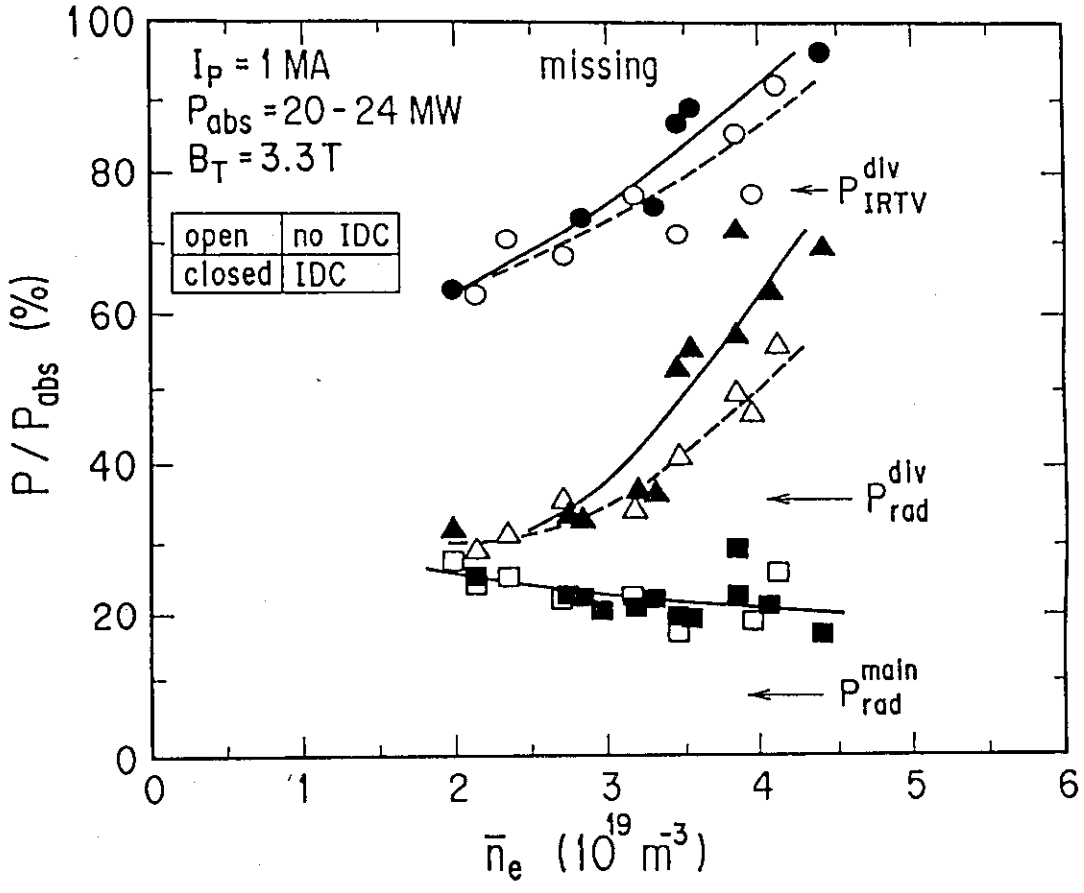

Fig. 6.10 Global power balance of NB heated lower X-point discharges with and without IDC as a function of $\bar{n}_e$.

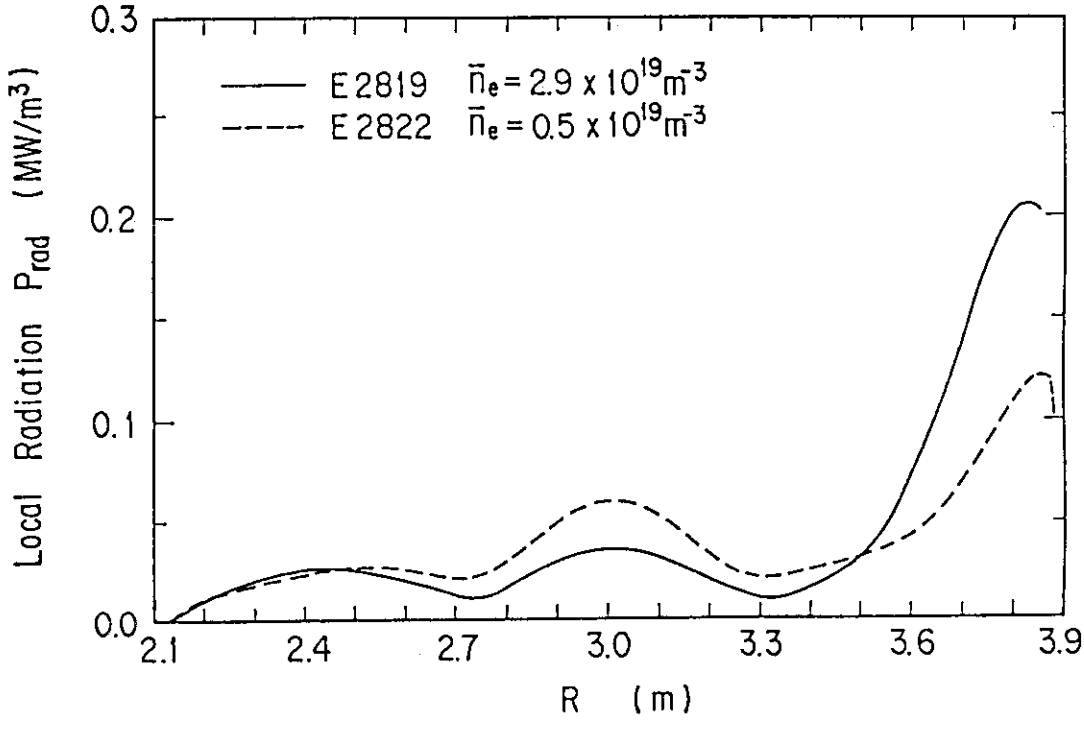

Fig. 6.11 Radiation profiles on the midplane for outer X-point discharges with different $\bar{n}_e$.

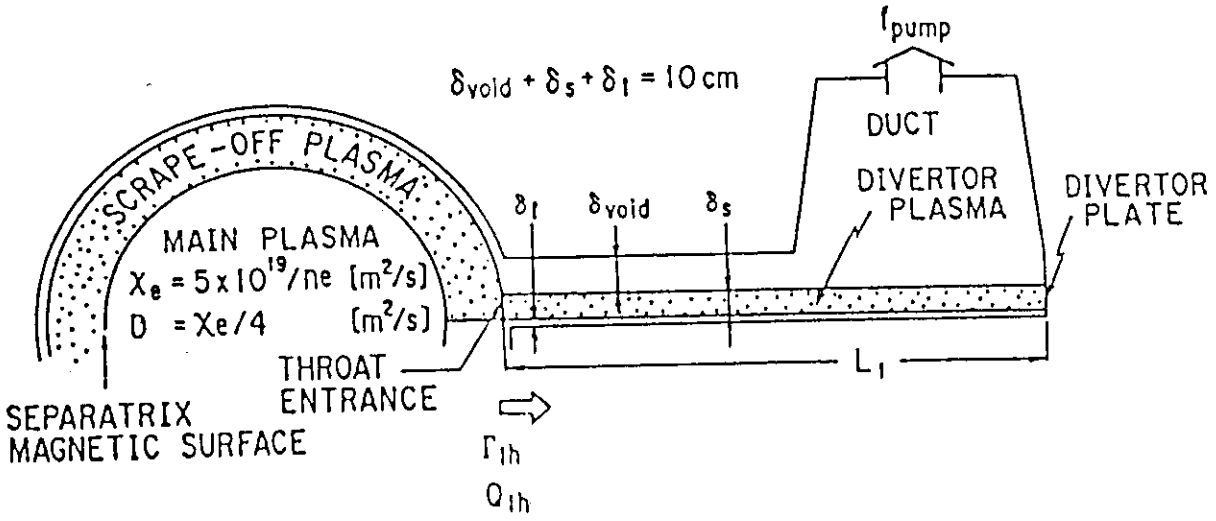

Fig. 6.12 Model geometry for the simulation analysis. Parameters used in the simulation : distance between the divertor throat and plate L_1 = 60 cm, width of divertor scrape-off layer plasma δ_s = 3 cm, width of vacuum area δ_{void} = 2.5 cm and the effective pumping rate f_{pump} = 0.2.

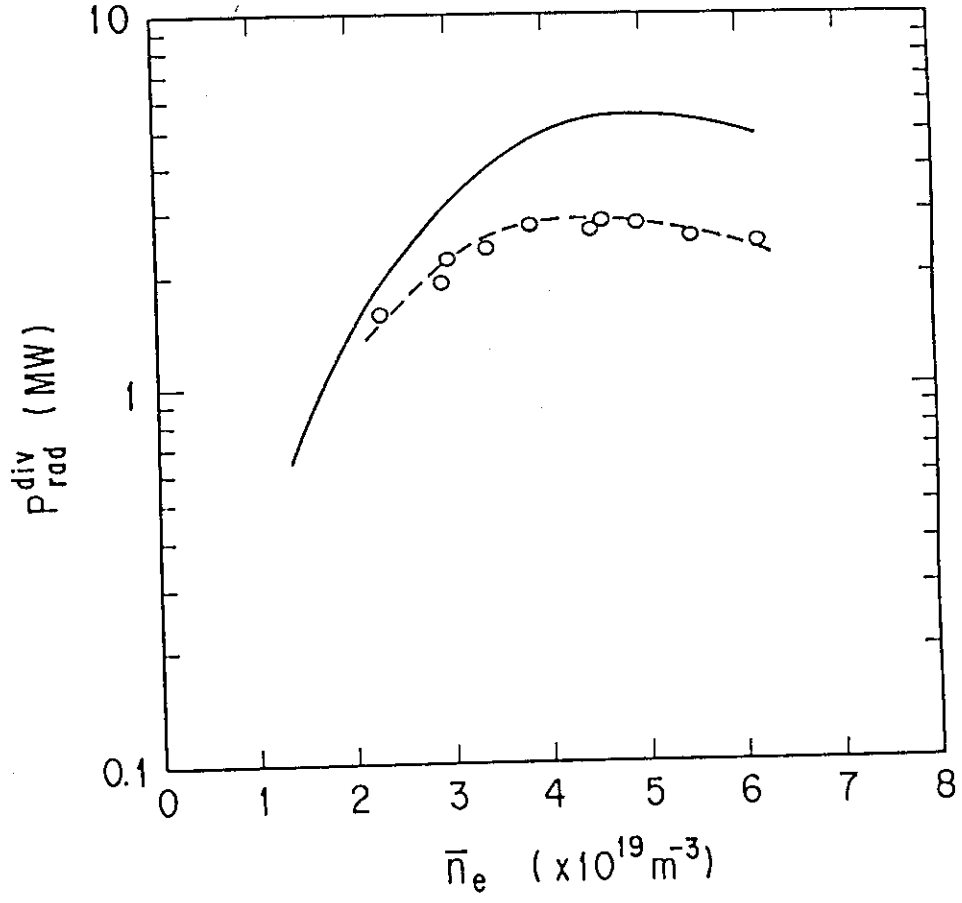

Fig. 6.13 Comparison of radiated power from the divertor plasma, P_{rad}^{div}, of experiment (open circles) and simulation (solid curve) for high power NB heated 2 MA hydrogen discharge. Only hydrogen line radiation was assumed in the simulation.

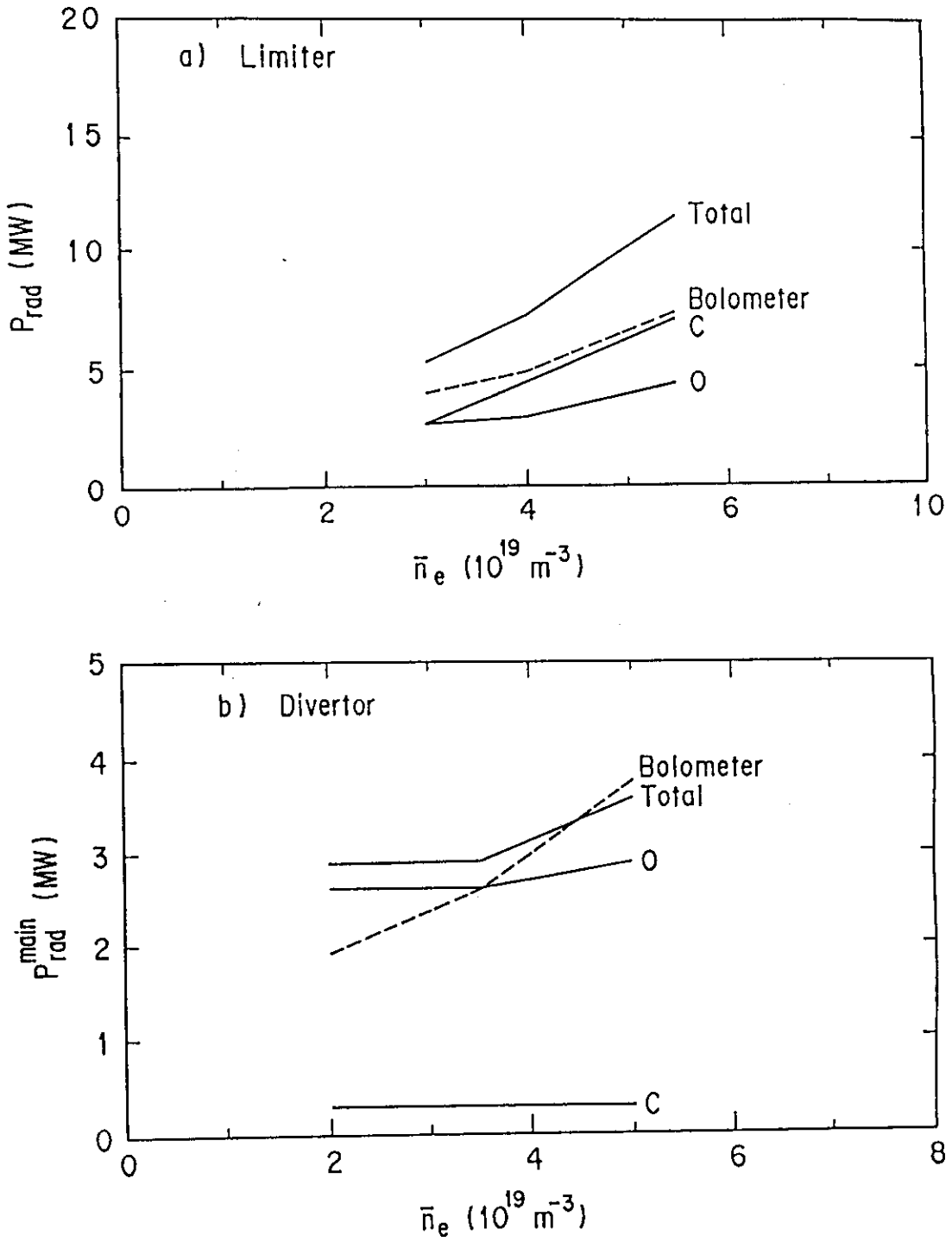

Fig. 6.14 Radiated power from the main plasma, P_{rad}^{main}, calculated from spectroscopic data for NB heated with graphite wall comparison with that from bolometer array for (a) limiter discharges and (b) outer X-point discharges.

7. Radiative Thermal Instability in the Peripheral Plasma on JT-60

7.1 INTRODUCTION

The edge plasma has been studied from the point of view of the plasma surface interactions such as sputtering or sublimation of the first wall and the impurity control such as divertor. Recently it has been revealed that the improvement of the energy confinement such as H-mode [1,2] and IOC [3,4] is related with the edge plasma conditions. So the importance of edge plasma physics has been recognized as an improving effect on core plasma confinement.

A marfe, multifaceted asymmetric radiation from the edge, is one of the edge plasma phenomena regarded as a radiated thermal instability. As shown in Fig. 7.1, a marfe is a toroidally symmetric and poloidally asymmetric radiating belt localized on the inside wall near the midplane where is the high field edge of the plasma. The width of the marfe is 15-30° of poloidal angle. The phenomena was reported at ASDEX [5,6] and D-III [7] previously, and Lipschltz [8] investigated it precisely in ohmically heated Alcator-C plasma and named it marfe. Now the marfe is a common phenomena among the middle and large size tokamak such as JET [9-11], TFTR [12-14] and FT [15]. Though the marfe in ohmically heated limiter discharges has been reported in many

tokamaks, the marfe in diverted discharges has been observed only on ASDEX [5]. The marfe in the plasma with intense NB heating has not reported.

On JT-60 the marfe had not been observed in the discharges with TiC coated molybdenum first wall except only several ones in the high density ohmically heated discharges. After the replacement of TiC coated molybdenum first wall by graphite tills, a marfe has been observed frequently in high Ip, 2.5-3.2 MA, limiter discharges with high power NB heating of 10 - 20 MW. Though the marfe occurs close to the density limit and reduced the $\bar{n}_e$, it does not affect the central electron temperature and the energy confinement. Recently a marfe has been observed in the relatively low Ip and $\bar{n}_e$ which results in improvement of energy confinement time up to several % accompanied with the increase of electron density. It has been reported that the marfe grows up to be detached plasma in some tokamaks [14-16]. The detached plasma is characterized by large amounts of radiation from its boundary layer which is poloidally symmetric different from the marfe. The temperature of the radiative layer is so low that the hot plasma is effectively detached from the limiter. The detached plasma has never been observed on JT-60.

Recently IDC (improved divertor confinement) was found in the NB heated lower X-point discharges with graphite wall which was the enhanced radiation loss in the divertor region resulting in the energy improvement on the main plasma. IDC may be regarded as one of the radiative thermal instability in the divertor region.

Section 7.2 describes the diagnostics concerned with marfe observation. The characteristics of the marfe observed in JT-60 are shown in Section 7.3. Section 7.4 shows the characteristics of IDC. Section 7.5 discusses the marfe modeling and the estimation of light impurity concentration in the region of the enhanced radiation. Section 7.6 is the summary and conclusion.

7.2 DIAGNOSTICS CONCERNED WITH MARFE

The behavior of the marfe can be observed by a bolometer array most effectively. The viewing chords of the bolometer array are shown in Figs. 3.8 and 3.9. Four channel of Hα monitors (see Fig. 5.8) and two channel of VUV spectrometers (see Fig. 2.11) measures Hα emissions and impurity lines, respectively in the same toroidal section as the bolometer arrays. Note that the Hα monitor signals involves the CII line of 657.6 nm because the Hα bandpassing filters had 4.5 nm of the FWHM centered at 656.3 nm. Additional

bolometers and Hα monitors are installed at three vertical diagnostics ports at R=2.53, 3.04, and 3.55 m. A visible TV is a helpful to see the marfe behavior directly. On JT-60 a visible TV camera is installed in the top diagnostics port outside the vacuum vessel and views the inside wall vertically against the magnetic axis (see Fig. 2.13). The electron density of the main plasma is measured with FIR interferometers with three vertical chords (R=2.53, 3.04, and 3.55 m) and 2 mm wave interferometer at R=2.2 m where is the marfe region (see Fig. 2.6).

7.3 PHENOMENOLOGY OF MARFE ON JT-60

7.3.1 Outline of Marfe Phenomena

The marfe had not been observed in the discharges with TiC coated molybdenum first wall except several ohmically heated discharges with new configuration where the plasma had a separatrix line and touched to the inboard limiter by exciting the divertor coil weakly. This experiment was carried out from January to March 1987 just before the replacement of the first wall to the graphite tiles. Figure 7.2 shows the typical configuration of the discharges. The typical waveforms of the marfe in ohmically heated plasma are shown in Fig. 7.3. The radiated power increases rapidly at 5.7 s. The gas puffing keeps constant from 1 to 7 s. The line-integrated electron density which is increasing until 5.7 s saturates from 5.7 to 6.2 s and began to increase steeply. The enhanced radiation from 5.7 to 8.5 s is the marfe, which is indicated clearly by the time evolution of the chord-integrated radiation losses shown in Fig. 7.4. The radiation is enhanced around channel 11 which views inside wall 28.5° above the midplane. There is not enhancement of the intensity of the bolometer signal with vertical viewing chord passing the plasma center and the increase of Hα intensity is most remarkable among the three vertical Hα monitors. These facts indicates that the enhanced radiation is localized near the inside wall. The light impurity spectrometers were not operated routinely in the period, so the information of the light impurity behavior in the marfe was not obtained.

After replacement of TiC coated molybdenum first wall to graphite tills, marfe was observed frequently in high Ip, 2.5 - 3.2 MA, limiter discharges with high power NB heating of 10 - 20 MW. Figure 7.5 shows the typical waveformes of the parameters of the discharge with the marfe. The marfe occurs at 6.6 s. Then the intensities of the bolometer and the Hα monitor

viewing the inner wall on the midplane increase steeply. Remarkable changes are not observed in the one turn voltage, SX intensities and sawtooth activity. Though the gas puffing is continuous, the increase of the electron density saturates at the marfe onset. It is suggesting that the marfe degrades the fueling efficiency of the gas puffing. Figure 6.7 shows the time evolution of the chord-integrated radiation losses measured with the bolometer array. The intensity of the ch. 1 bolometer is increasing during 5.5 - 6.6 s with the increase of the electron density. The intensities of the ch. 5 - ch. 10 increase rapidly at the same time as the decrease of the ch. 1 intensity. The enhance radiation is kept for about two seconds until the NB offset.

7.3.2 Onset Position and Poloidal Motion

If the marfe is assumed to be localized on the inner wall, the poloidal spread of the marfe can be estimated from the chord-integrated radiation profile such as Fig. 7.6. The poloidal extent of the marfe is shown in Fig. 7.7. The center of the marfe was about 10° above the midplane and the FWHM of the radiative band was 15° of poloidal angle. The visible TV camera observed the bright emission of the toroidal band corresponding to the radiative band as shown in Fig.7.8. The marfe occurred on the midplane ($\theta \sim 180°$) in ASDEX, FT and D-III, and above the midplane ($\theta \sim 120°$) in Alcator-C, and below the midplane ($\theta \sim 235°$) in TFTR and JET. Though the radial extent of the marfe has not been measured directly on JT-60, it is said generally to be about 10% of the plasma minor radius [21]. The radiation power density in the marfe was estimated to be more than 30 MW/m^3 from Fig. 7.7 if the radial extent of the marfe assumed to be 0.1 m.

The marfe sometimes moved upward in JT-60. The drift motion appeared often while the plasma current was ramping down and/or NB power was reduced fully or partially. Figures 7.9 and 7.10 show the two dimensional plot and contour plot of the time evolution of the chord-integrated radiation losses of the marfe when the NB power reduced 50% and the configuration was changed from the outer-X-point-divertor configuration to the limiter one. The marfe drifted from 174° to 150° of the poloidal angle with the angular velocity of about 30°/s which was much slower than that of other tokamaks such as Alcator-C. In TFTR the direction of the drift motion was correspond to the $\mathbf{B}\times\nabla\mathbf{B}$, which was confirmed by the reverse of the toroidal field. Whereas the direction of the drift motion was upward independent of the B_T direction in JT-60.

7.3.3 Impurity Behavior

The time evolutions of light impurity brightness in the marfe measured by the normal incidence spectrometer are shown in Fig. 7.11. Major lines of low-ionized light impurities were saturated before the marfe onset, so that relatively week lines were employed here. In this discharge, the marfe occurred at 7 s triggered by the 25% turnoff of the NB injection. Then the brightnesses of CII, CIII and OII lines increased steeply to be saturated. Whereas, the brightnesses of CIV and Lyβ lines decreased to be unsaturated level from saturation one. It is suggested that the low-ionized carbon and oxygen are major radiation source in the marfe. In JET, enhancement factors of low-ionized carbon and oxygen by marfe onset was investigated quantitatively [21] as shown in Fig. 7.12. The enhancement factors of CIII, OII and OIII are largest, so that the electron temperature in the marfe is estimated to be about 30 eV from those ionization potentials. Figure 7.13 shows diagnostics wave forms of the marfe in relatively low density and plasma current with NB heating on JT-60 including the time evolutions of CVI and OVIII brightnesses measured with VUV spectrometer viewing the plasma center. The brightness of CVI increased according to the increase of electron density in the marfe period, however, that of OVIII decreased. It can be estimated that the concentration of oxygen reduces with the marfe onset. Those impurity behaviors are similar to that of IDC as described in Section 7.5.

7.3.4 Density Behavior

The increases of chord-integrated electron densities along the three vertical chords at R=2.53, 3.04 and 3.55 m were saturated with same manner at the marfe onset in spite of continuous gas puffing as shown in Fig. 7.14 (a). In the discharge shown in Fig. 7.14 (b), the chord-integrated density decreased once at the marfe onset and kept rising within the marfe period resulting in a major disruption at density limit, which was a only rare case. The density degradation by the marfe was helpful to avoid the density limit disruption in many cases on JT-60. Similar density degradation has been observed in center and outer side of the TFTR plasma [18]. However, the density in the vicinity of the marfe increases. In JT-60, the density behavior in the vicinity of the marfe could not investigated because the 2 mm interferometer at R = 2.2 m could not be available due to the fringe counting error by the large density gradient at the peripheral region. In relatively low density and current plasmas with NB

heating, the density increased in the marfe period as shown in Fig. 7.13. Similar density increase have been observed in Alcator-C [12] and ASDEX [11]. The mechanisms of these two types of density behaviors are unknown at present.

7.3.5 Onset Condition

The Hugill diagram of the plasma at the marfe onset and the plasma disrupted by density limit is shown in Fig. 7.15. It was indicated that the marfe was observed in the vicinity of the density limit. Figures 7.16 (a) and 7.16 (b) show the time trajectories of the plasmas with marfe onset at constant I_P phase and decreasing I_P phase, respectively. In the constant I_P, the marfe occurred on the density limit, whereas the marfe occurred in the density region higher than the density limit in decreasing I_P where the drift motion was observed frequently.

The threshold electron density for the marfe onset is plotted against the plasma current normalized by the poloidal cross-section of the plasma in Fig. 7.17. Defining ρ to be $\bar{n}_e/(I_P/\pi a^2)$, $\rho = 0.55 \pm 0.05$ for ohmically heated plasma and $\rho = 0.90 \pm 0.15$ for NB heated plasma on JT-60. The scatter of the ρ is seemed to be due to the NB power and condition of plasma current (rising, flattop, and falling). The comparison of the ρ with that of the other tokamaks is summarized in Table 7.1 as Lipschultz showed in Ref. [21]. The ρ is about 0.5 and 0.9 for ohmic and NB heated plasma, respectively in various tokamaks, which is consistent with the results of JT-60.

The NB power dependence of the threshold density for the marfe onset was investigated in several discharges where the NB powers were different but the other conditions were almost same. The threshold density increased with the increase in the NB power as shown in Fig. 7.18. In other words, the marfe was suppressed by the NB injection. The empirical scaling of the marfe onset taking account of the NB power is derived from Fig. 7.18 as

$$\bar{n}_e = (\rho_{OH} I_P + \rho_{NB} P_{NB})/\pi a^2 , \qquad (7.1)$$

where

$$\rho_{OH} = 0.55 \pm 0.05 \ \ (10^{20}/\mathrm{MAm}) ,$$

$$\rho_{NB} = 0.07 \pm 0.01 \ \ (10^{20}/\mathrm{MWm}).$$

This scaling is useful to predict the marfe onset condition in NB heated discharges on JT-60. The validity of the scaling would be confirm for the other tokamaks.

Table 7.1 Threshold Density of Marfe Onset Normalized by the Poloidal Cross-section on Various Tokamaks

Machine	R (m)	a (m)	B_T (T)	$\rho = \bar{n}_e/(I_P/\pi a^2)$	Comments
JT-60	3.04	0.9	4	0.55 ± 0.05	OH
	3.04	0.9	4.75	0.9 ± 0.15	NBI
Alcator-C	0.64	0.165	6-10	0.5 ± 0.05	OH
ASDEX	1.65	0.4	2.2	0.7 ± 0.05	OH, diverted
	1.65	0.4	2.2	0.85 ± 0.05	NBI
D-III	1.4	0.4	2	0.45	OH
JET	2.96	1.25	2.5--3.4	0.55 - 0.3	OH
TFTR	2.5	0.82	4	0.4 ± 0.05	OH
FT	0.83	0.2	6-8	0.75 ± 0.05	OH, I_P down

7.3.6 Total Radiation Loss and Energy Confinement

In general, the total radiated power is derived from the volume integration of the radiation profile, $P_{rad}(r)$, which is provided by the Abel inversion of the bolometer array signals, where the radiation profile is assumed to be axisymmetric. The method, however, is not valid for the plasma with poloidally asymmetric radiation profile like marfe. Therefore symmetric component and marfe component of the total radiated power were calculated individually by separating the bolometer signals to each component as shown in Fig. 7.7, where symmetric component of the marfe viewing channel was estimated from that of the other channels by interpolation. The time evolutions of the symmetric and marfe components of the total radiated power for the plasma as for Fig. 7.5 are shown in Fig. 7.19. In this discharge, the power radiated from the marfe was up to 50% of the total radiated power, however, it was 20-50% usually in other discharges. The total radiated power from the plasma with marfe reached up to 90% of the absorbed power as shown in Fig. 6.9.

Figure 7.20 shows the time evolutions of the stored energy measured by the diamagnetic loop, the electron temperature measured from the ECE emission, and other parameters as for Fig. 7.5. Both stored energy and electron temperatures did not changes by the marfe onset at 6.6 s in spite of the intense radiation loss. In the marfe of relatively low density and I_P, the stored energy increased accompany with the increase in the electron density as shown in Fig. 7.21. Reducing the increase of stored energy due to decreasing NB shinethrough with the increase of density, the energy confinement time was improved about 5%. The effect of marfe on the energy confinement has not been referred in papers of other tokamaks. But it was presented from Alcator-C in Ref. [8] that the influx of molybdenum was suppressed by the marfe. One possibility of the improvement by the marfe is that the marfe reduces the temperature of the edge plasma except marfe region and suppresses the particle recycling and impurity influx from the first wall.

7.4 IMPROVED DIVERTOR CONFINEMENT (IDC)

Recently IDC was found in the NB heated lower X-point discharges with graphite wall accompanied with the enhanced radiation loss in the divertor region. Figure 7.22 shows the typical wave forms of IDC. The IDC begins at about 5.7 s. In IDC, P_{rad}^{div} and $\bar{n}_e$ increase gradually and chord integrated radiated power from the plasma center decrease. The light impurity behavior in IDC is characterized by the increase of CVI (33.74 nm) and the decrease of OVIII (18.97 nm). The decrease of the radiated power from the main plasma corresponds to the decreases of the OVIII brightness in main plasma. Though the electron density of the main plasma increased in IDC, the central electron temperature did not decrease. So the energy confinement time was improved 10-20% in IDC discharges. The time evolution of the chord-integral intensities of the bolometers as a function of channel in the IDC discharge are shown in Fig. 7.23, where channel 1-13 and channel 14-25 correspond to the lower and upper arrays, respectively. The intensity of the lowest channel which was nearest to the X-point increased steeply in IDC, whereas central ones somewhat decreased. This figure indicates that the enhance radiation is localized in the divertor region. And Section 6.3.3 describes that the remote radiative cooling in the divertor region is realized in the IDC discharges, which reduced the heat load onto the divertor plates.

The radiated power from the main and divertor plasmas in IDC discharges are plotted against the absorbed power for different B_T in Fig. 7.24.

increased steeply with the P_{abs} than 20MW. The increase in the radiated power was enhanced by the increase of the toroidal field.

Figure 7.25 shows the radiated power from the divertor region plotted against the delta Xp which is the distance between the X-point and the divertor plate for IDC discharges of I_P = 1MA and B_T = 3.3T. The radiated power from the divertor region increased as the delta Xp was increased. Thus, Figs. 7.24 and 7.25 indicate that the radiated power from the divertor region increased according to the connection length of the divertor which was the length of the field line from the X-point to the divertor plate.

As described above, IDC is characterized by the strong enhancement of the radiation loss from the divertor region. So the global energy confinement time of the IDC plasmas is plotted against the radiated power from the divertor region in Fig 7.26. Global energy confinement time increases with the increase of the radiated power from the divertor region.

7.5 DISCUSSION

7.5.1 Modeling of Marfe

The marfe is considered to be a result of a radiative thermal instability due to light impurity in the peripheral plasma. The radiation loss of an impurity is given by

$$P_{rad} = n_e n_I L(T_e) , \tag{7.1}$$

where n_e is the electron density, n_I is the impurity density, and $L(T_e)$ is the radiation cooling rate at the electron temperature T_e. Because the L of light impurity such as carbon and oxygen has a negative value of dL/dT, the temperature becomes lower and lower once it decreases. Here the simulation of marfe was performed by a simple model of the thermal equilibrium.

The thermal equilibrium of the edge plasma is given by

$$\frac{\kappa_\perp}{\Delta^2} n_e T_e + n_e n_I L = \frac{P_{in}}{4 \pi^2 R a \Delta} , \tag{7.2}$$

where $\kappa_\perp$ is a perpendicular thermal conductivity, Δ is the width of the scrape-off layer, and P_{in} is the input power to the plasma. The first and second terms of the left hand side in Eq. (7.2) are heat losses by thermal conduction and radiation, respectively. The right hand side of Eq. (7.2) is the heat flow from

the main plasma to the scrape-off layer. The width of the scrape-off layer Δ is represented approximately by

$$\Delta = R\,q\,\sqrt{\frac{\kappa_\perp}{\kappa_{||}}}\,, \tag{7.3}$$

where q is the safety factor at the plasma edge and $\kappa_{||}$ is a parallel thermal conductivity. The transport at edge region is assumed to be Bohm type as

$$\kappa_\perp = \frac{1}{16}\frac{T_e}{B}\,, \tag{7.4}$$

and $\kappa_{||}$ of the classical transport

$$\kappa_{||} = 3.16\,\frac{T_e\,\tau}{m_e} \tag{7.5}$$

is used. Here τ is the electron collision time given by

$$\tau = \frac{3.5\times 10^4}{(\lambda/10)}\,\frac{T_e^{3/2}}{Z_{eff}\,n_e}\,, \tag{7.6}$$

where λ is the Coulomb logarithm.

Dominant impurity in the marfe is assumed to be carbon. The radiative cooling rate of carbon around T_e = 10 eV is approximated by simple functions as

$$\begin{aligned} &L \approx 10^{-31}\,(Te/10)^{-4} && \text{for } T_e \geq 10 \text{ eV}\,,\\ &L \approx 10^{-31} && \text{for } 6 \text{ eV} < T_e < 10\text{eV},\\ &L \approx 10^{-31}\,(Te/6)^3 && \text{for } T_e < 6 \text{ eV}\,. \end{aligned} \tag{7.7}$$

The condition of the thermal instability is

$$\frac{\partial}{\partial T_e}\left(\frac{\kappa_\perp}{\Delta^2}\,n_e\,T_e + n_e\,n_I\,L\right) < 0\,. \tag{7.8}$$

The solution of Eq. (7.2) under the condition of Eq. (7.8) gives the criterion of the marfe onset. Figure 7.27 shows the marfe onset plasma in the Hugill diagram calculated by the criterion for the NB heated plasma assuming the carbon concentration of 0.3-1%. The density n is the local electron density in the marfe region. Therefore this calculation result (Fig. 7.27) could not be compared with the experimental one (Fig. 7.15) in the strict sense, but they have a good agreement in the case of the carbon concentration of ~0.5%.

7.5.2 Estimation of Light Impurity Concentration in the Enhanced Radiative Region of the IDC Plasmas

In the typical IDC discharge, radiated power from the divertor region reachs up to 10 MW which corresponds to the power density of approximately 10 MW/m^3. The spectroscopic measurement of the divertor plasma revealed that the brightness of carbon lines increased with the similar manner to the radiated power from the divertor region in IDC. So the dominant contributor of radiation loss in the IDC divertor plasma seems to be carbon. Though the spectrometer was calibrated absolutely, the carbon concentration in the IDC divertor plasma could not be obtained for lack of the knowledge of n_e and T_e in the divertor region. Therefore the carbon concentration was estimated by using simple model of the scrape-off layer [22] form the radiated power from the divertor region.

A one dimensional model of the scrape-off layer is considered. The heat conduction equation along the field line is given by

$$q = -\kappa_{||} \frac{dT}{dx} , \tag{7.9}$$

where q is heat flux density along the field line, $\kappa_{||}$ is the heat conduction coefficient long the field line, which is given by

$$\kappa_{||} = \kappa_0 T^{5/2} , \tag{7.10}$$

where κ_0 = 12.5 $Wcm^{-1}eV^{-7/2}$, T is electron temperature in eV, and x is the coordinate along the field line. The convection heat loss is neglected.

The radiation power P_{rad} by impurity ions is given by

$$\frac{dq}{dx} = P_{rad} = -n^2 f L(T) \quad , \tag{7.11}$$

where n is electron density, f is the impurity fraction, and L is the radiative cooling rate. By multiplying Eq. (7.9) by Eq. (7.11) and by using Eq. (7.10), The equation

$$\begin{aligned} \frac{1}{2}\frac{d}{dx}q^2 &= k_0 T^{5/2} n^2 f L(T) \frac{dT}{dx} \\ &= k_0 f p^2 T^{1/2} L(T) \frac{dT}{dx} \end{aligned} \tag{7.12}$$

is obtained, where p is the electron pressure(= nT). By assuming that f and p are constant along the field line, Eq. (7.12) can be integrated as follows;

$$q_s^2 - q_d^2 = f p^2 (g(T_s) - g(T_d)) \quad , \tag{7.13}$$

where

$$g(T) = 2k_0 \int_0^T T^{1/2} L(T) dT \quad , \tag{7.14}$$

where the suffix s means the separatrix, and the suffix d means the divertor plate. From Eq. (7.13),

$$f = \frac{q_s^2 - q_d^2}{p^2 (g(T_s) - g(T_d))} \tag{7.15}$$

is obtained. The typical parameters of the IDC discharges in JT-60 are:

R = 3 m (major radius)

$P_{in} - P_{rad}^{main}$ = 16 MW (total power from the main plasma)

P_{rad}^{div} = 10 MW(radiative power in the divertor))

θ = 0.1 (pitch of the field line)

δ = 0.05 m (thickness of the scrape-off layer)

d = 0.06 m (distance from the x point to the divertor plate)

$l = d/\theta$ = 0.6 m (length of the field line)

$$q_s = \frac{P_{in} - P_{rad}^{main}}{4\pi R\theta\delta} = 8.5 \times 10^7 \ W/m^2 ,$$

$$q_d = \frac{P_{in} - P_{rad}^{main} - P_{rad}^{div}}{4\pi R\theta\delta} = 3.2 \times 10^7 \ W/m^2 .$$

It is estimated that

$$T_d = 10 \ eV ,$$

$$n_d = \frac{q_d}{e\gamma T_d \left(\frac{eT_d}{m}\right)^{1/2}} \approx 0.8 \times 10^{20} \ m^{-3} ,$$

where γ= 8 (heat transmission coefficient at the sheath), e is electron charge, and m is the proton mass. T_s is approximately given by

$$T_s = \left(\frac{7q_s l}{2\kappa_0}\right)^{2/7} \approx 110 \ eV$$

$$n_s = \frac{2n_d T_d}{T_s} \approx 1.5 \times 10^{19} \ m^{-3} .$$

Figure 7.28 shows the g(T) as function of electron temperature T_e for carbon calculated from the non-coronal radiative cooling rate [20], where τ is the particle confinement time of the impurity. If $n\tau$ is assumed to be $10^{17} m^{-3} s$,

$$g(T_s) = 8 \times 10^{-27} \ W^2 m^2 / eV^2 >> g(T_d),$$

$$p = 1.6 \times 10^{21} \ m^{-3} \ eV.$$

are obtained. By using these parameters,

$$f \cong \frac{q_s^2 - q_d^2}{p^2 \, g(T_s)} \cong 30\%$$

is obtained. The averaged ionic charge of carbon is 2-4 for T_e = 10-110 eV at $n\tau$ = $10^{17} \ m^{-3}$. So the carbon concentration of 30% means that the ion of the divertor plasma in the IDC discharge is almost carbon.

7.6 CONCLUSION

The marfe characteristics in the high-power NB heated plasmas has been investigated on the JT-60 tokamak. The marfe is a poloidally asymmetric radiation band localized near the inside midplane and is a common phenomenon among middle and large size tokamaks. In JT-60, the marfe has been observed frequently in high-Ip and high density limiter discharges with NB heating after the replacement of the first wall from TiC coated molybdenum tiles to graphite ones.

The marfe occurred around the midplane on the inside wall and the poloidal extent of the radiative band was about 10° of poloidal angle. The poloidal drift motion of the marfe has been observed frequently in the discharges during I_P rump down and/or reducing P_{NB}. The direction of the drift motion was upward independent of the B_T direction and drift angular velocity was typically 30° s^{-1}.

The marfes occurred near the density limit of the JT-60 plasmas. The threshold electron density for the marfe onset has been investigated on ohmically and NB heated discharges in JT-60. Defining ρ to be $\bar{n}_e / (I_P/\pi a^2)$, marfe onset condition was $\rho = 0.55 \pm 0.05$ for ohmically heated plasma and $\rho = 0.90 \pm 0.15$ for NB heated plasma which was consistent with the results of other tokamaks. The threshold electron density increased with P_{NB}. The empirical scaling of the marfe onset taking account of the NB power was obtained as $\bar{n}_e = (\rho_{OH} I_P + \rho_{NB} P_{NB})/\pi a^2$ where $\rho_{OH} = 0.55 \pm 0.05$ (10^{20}/MAm) and $\rho_{NB} = 0.07 \pm 0.01$ (10^{20}/MWm). This scaling was useful to predict the marfe onset condition in NB heated discharges on JT-60. The threshold electron density for marfe onset during I_P rump down was found to be higher than that in constant I_P.

The marfe was modelled based on the radiative thermal instability. The simple model can explain the marfe onset condition.

The increases of chord-integrated electron densities along the three vertical chords at $R=R_P - a/2$, R_P and $R_P + a/2$ were saturated with same manner in the marfe period in spite of continuous gas puffing. The marfe may degrade the fuelling efficiency of the gas puffing.

The radiation power density in the marfe was estimated to be 20-30 MW/m^3 typically if the radial extent of the marfe assumed to be 0.1 m. The increases in the brightness of CII, CIII and OII lines were observed in the marfe. The major contributors to the large emissively in the marfe were estimated to be carbon and oxygen in low charge states.

The power radiated from the marfe reached 20-50% of the total radiated power. The radiated power from the plasma with marfe was about 90% of the absorbed power. Both stored energy and central electron temperatures did not change by the marfe onset in spite of the such intense radiation loss. The marfe onset in relatively low Ip improves energy confinement time up to several % accompanied with the increase of electron density. The marfe was helpful to avoid the density limit disruption by reducing the rate of the electron density increase. So the plasma with marfe might be favorable operational regime in the high density region for the limiter discharges.

The improved divertor confinement (IDC) regime was obtained in NB heated lower X-point discharges with graphite wall where the energy confinement time was improved up to 20%. In IDC discharges the radiation loss from the divertor region increased up to 40% (typically 10MW) of the absorbed power. Whereas, that from the main plasma and the heat load onto divertor plates decreased in IDC. It was indicated that the strong remote radiative cooling was realized in the IDC discharges. Radiation losses from the divertor region increased with the toroidal magnetic field and the distance between the X-point and the divertor plates, which suggested that it increased with the connection length of the divertor. The strong radiated power from the divertor region in IDC (typically 10MW) can be explained with a dense and cold carbon plasma in the divertor region by using simple model of the scrape-off layer. Though the improvement of the energy confinement in IDC is not so remarkable (only several % to 20%), it is suitable operational regime to long pulse or steady state operation in future devices because IDC does not concentrate impurities to the core plasma like as H-mode.

REFERENCES TO CHAPTER 7

[1] F. Wagner, G. Becker, K. Behringer, D. Campbell and A. Eberhagen, Phys. Rev. Lett. **49** (1982) 1408.

[2] N. Ohyabu, G. Jahns, R. Stambough and E. Strait, Phys. Rev. Lett. **58** (1982) 120.

[3] F. Söldner, E. Müller, F. Wagner, et al., Phys. Rev. Lett. **61** (1988) 1105.

[4] G. Fussmann, O. Gruber, H. Ntedermeyer, et al., in Plasma Physics and Controlled Nuclear Fusion Research 1988 (*Proc. 12 the Int. Conf. Nice 1988*) Vol. 1, IAEA, Vienna (1989) 145.

[5] H. Niedermeyer, K. Behrimger, K. Bernhardi, A. Eberhagen, G. Fusmann, et al., Max-Planck-Institute für Plasmaphysik, Garching Report IPP-III/90 (1983).

[6] H. Niedermeyer, R. Bartiromo, G. Becker, H.S. Bosch, H. Brocken et al., in *Proc. 12th European Conf. on Controlled Fusion and Plasma Physics, Budapest, Hungary, 1985,* contributed papers, Part I, P. 159.

[7] D.R. Baker, R.T. Snider and M. Nagami, Nucl. Fusion **22** (1982) 807.

[8] B. Lipschults, B. LaBonbard, E.S. Markar, M.M. Pichkrell, J.L. Terry, R. Watterson and S.M. Wolfe, Nucl. Fusion **24** (1984) 977.

[9] J. Wesson, C. Gowers, W. Han, F. Mast, F. Nave, M. Turner and M. Watkins, in *Proc. 12th European Conf. on Controlled Fusion and Plasma Physics, Budapest, Hungary, 1985,* contributed papers, Part I, P. 147.

[10] J. O'Rourke, D. Campbell, B. Denne, A. Gondhalker, N. Gottardi, H. Krause, G. Magyar, M. Malacarne, F. Mast, P. Morgan, M.F. Nave, F.C. Schüller, M. Stamp and D. Summers, ibid, P. 155.

[11] P.G. Carolan, M.J. Forrest, N.C. Hawkwes and N.J. Peacock, ibid, P. 263.

[12] F.P. Boody, C.E. Bush, S.S. Medley, H.K. Park and J.F. Schivell, J. Nucl. Mater. **145-147** (1987) 196.

[13] J. Schivell and C.E. Bush, Rev. Sci. Instrum. **57** (1986) 2081.

[14] J. Schivell, Rev. Sci. Instrum. **58** (1987) 12.

[15] F. Alladio, R. Bartiromo, B. Casali, P. Buratti, F. De Marco, , M. De Pretis, R. Giannellla, M. Grolli, L. Pieloni, A Tanga, A. Tuccillo and O. Tudiso, Phys. Lett. **90A** (1982) 405.

[16] J.D. Strachan et al., in *Proc. 12th European Conf. on Controlled Fusion and Plasma Physics, Budapest, Hungary, 1985,* contributed papers, Part I, P. 339.

[17] J.D. Strachan, F.P. Boody, C.E. Bush, S.A. Cohen, B. Grek, L. Grisham, F.C. Jobes, D.W. Johnson, D.K. Mansfield, S.S. Medley, W. Morris, H.K. Park,

J.F. Schivell, G. Taylor, K.L. Wong, S. Yoshikawa, M.C. Zarnstorff and S.J. Zweben, J. Nucl. Mater. **145-147** (1987) 186.

[18] G.M. McCracken, J. Allen, K. Axon, R. Barnsley, S.J. Firlding, D.H. goodall, N. Hawkels, J. Hugill, P.C. Johnson, G.F. Matthews and C.S. Pitcher, J. Nucl. Mater. **145-147** (1987) 181.

[19] T.E. Stringer, in *Proc. 12th European Conf. on Controlled Fusion and Plasma Physics, Budapest,* Hungary, 1985, contributed papers, Part I, P. 86.

[20] P. Carolan and V. Piotrowicz, Plasma Phys. **25** (1983) 1065.

[21] B. Lipschultz, J. Nucl. Mater. **145-147** (1987) 15.

[22] M. Shimada, M. Nagami, et al., Nucl. Fusion **22** (1982) 643

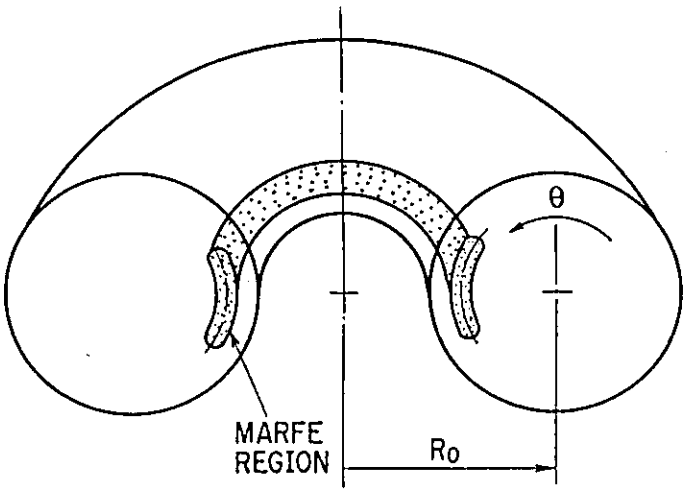

Fig. 7.1 Illustration of the marfe. The poloidal angle, θ, is measured from the outside midplane.

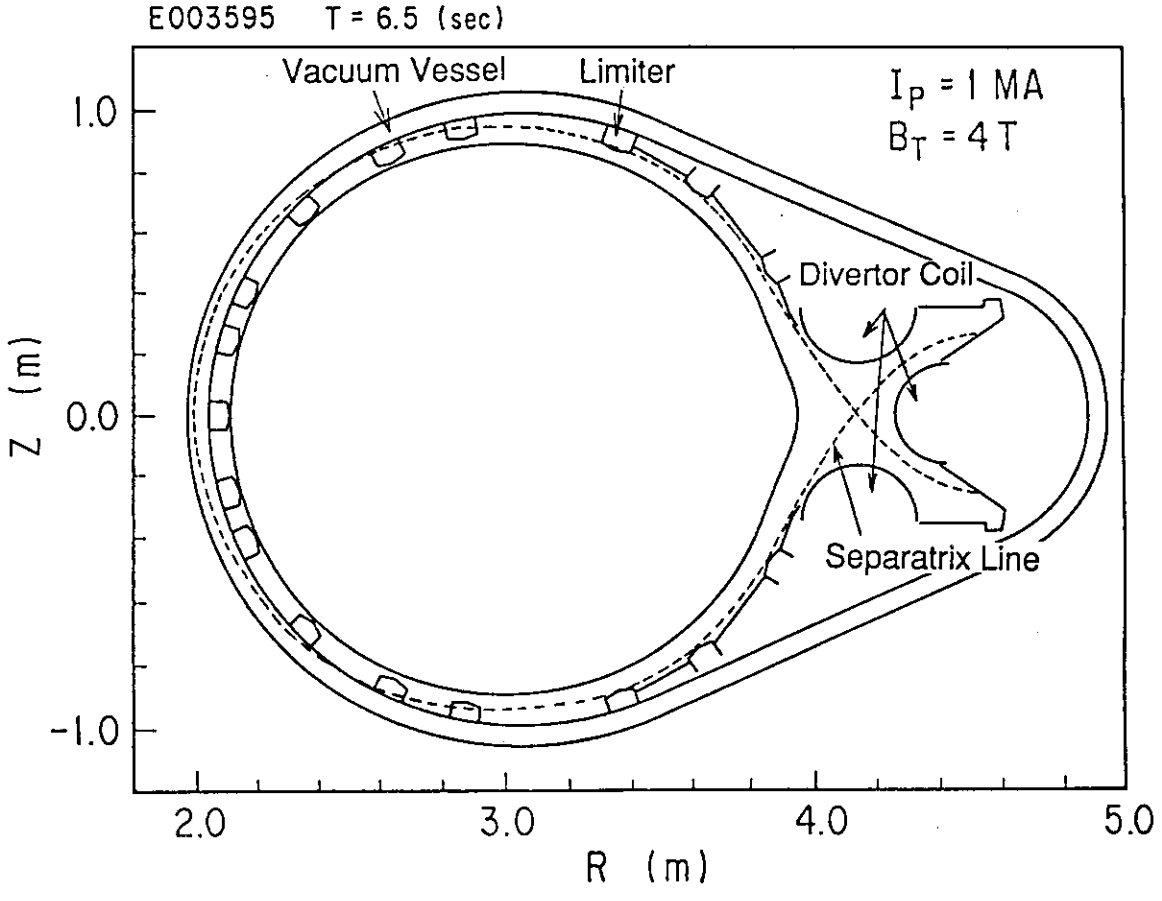

Fig. 7.2 Magnetic configuration of the ohmic discharge with the marfe. The plasma had a separatrix line and touched to the inboard limiter by exciting the divertor coil weakly.

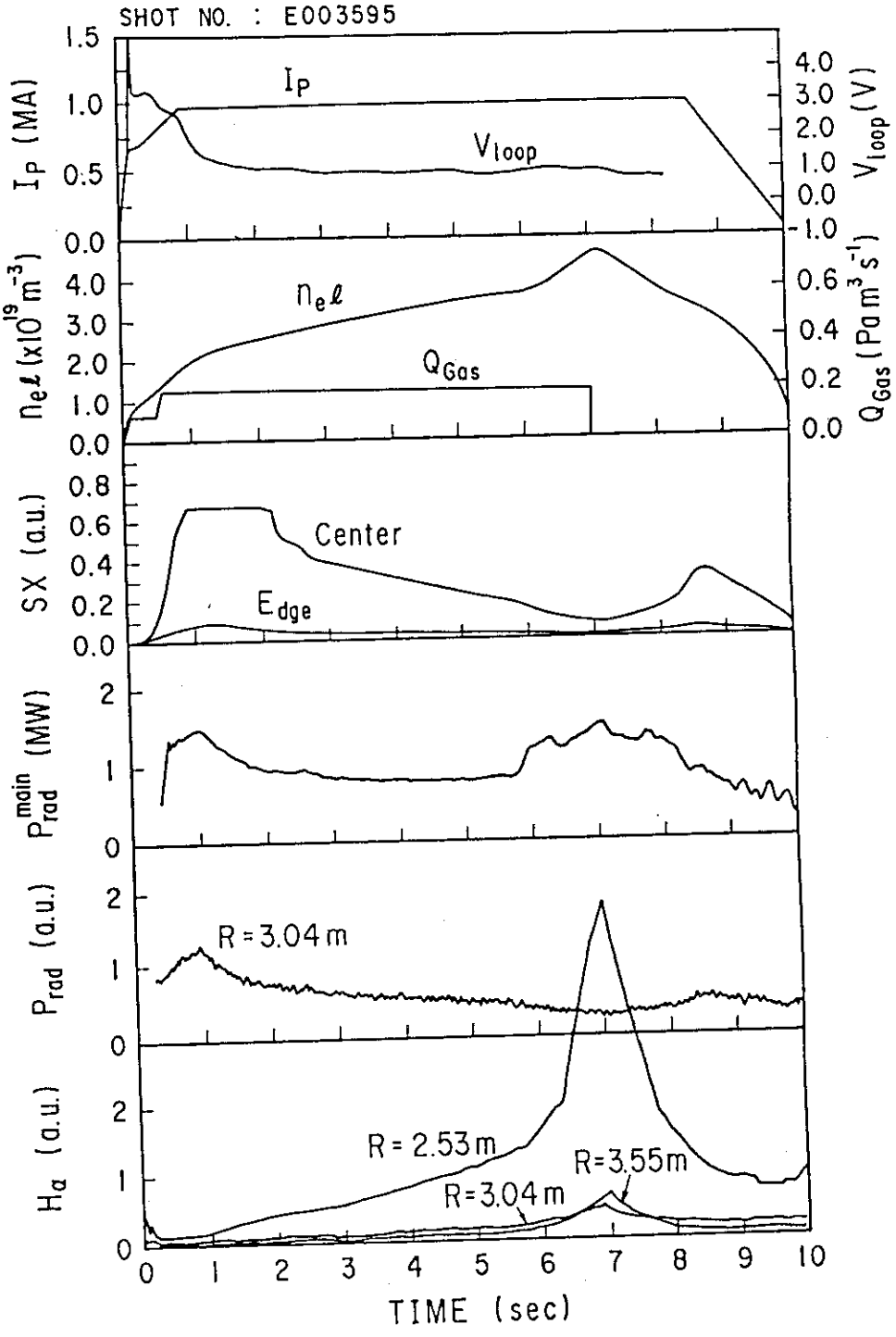

Fig. 7.3 Typical waveforms of the marfe in ohmically heated plasma

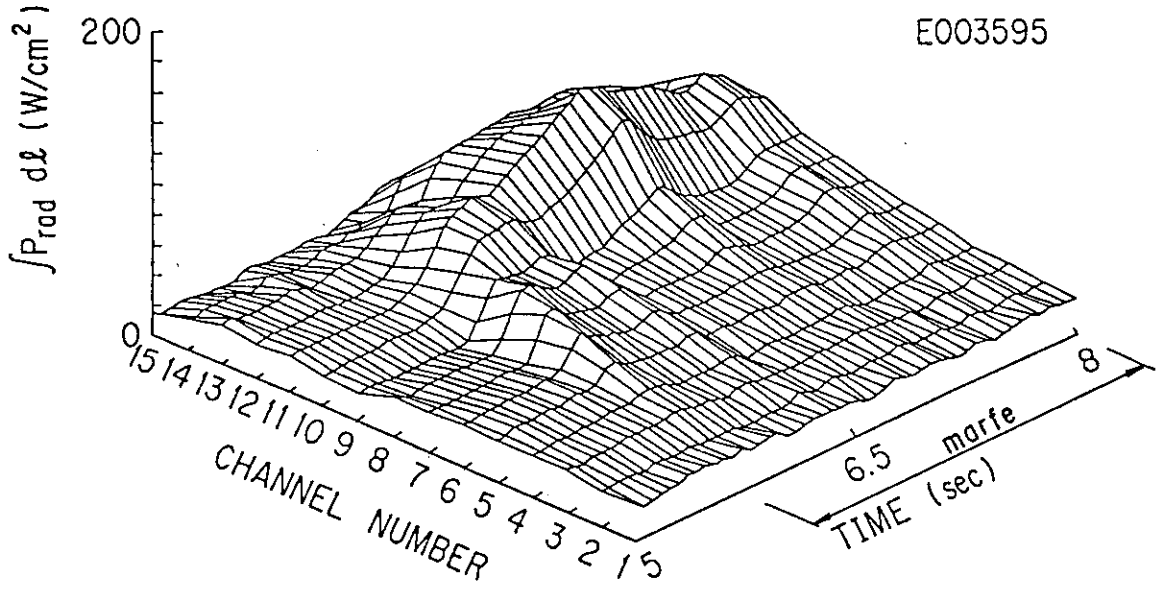

Fig. 7.4 Time evolution of the chord-integrated radiation losses in ohmically heated plasma with marfe.

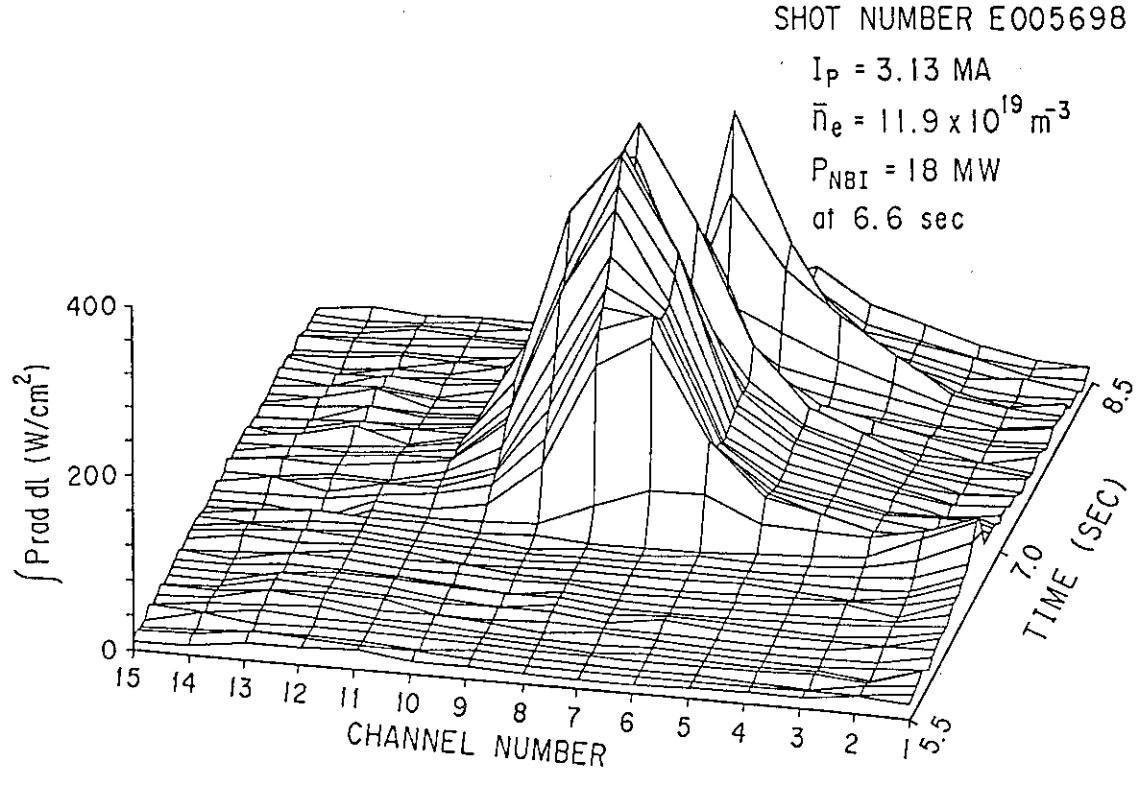

Fig. 7.6 Time evolution of the chord-integrated radiation losses in NB heated plasma with marfe.

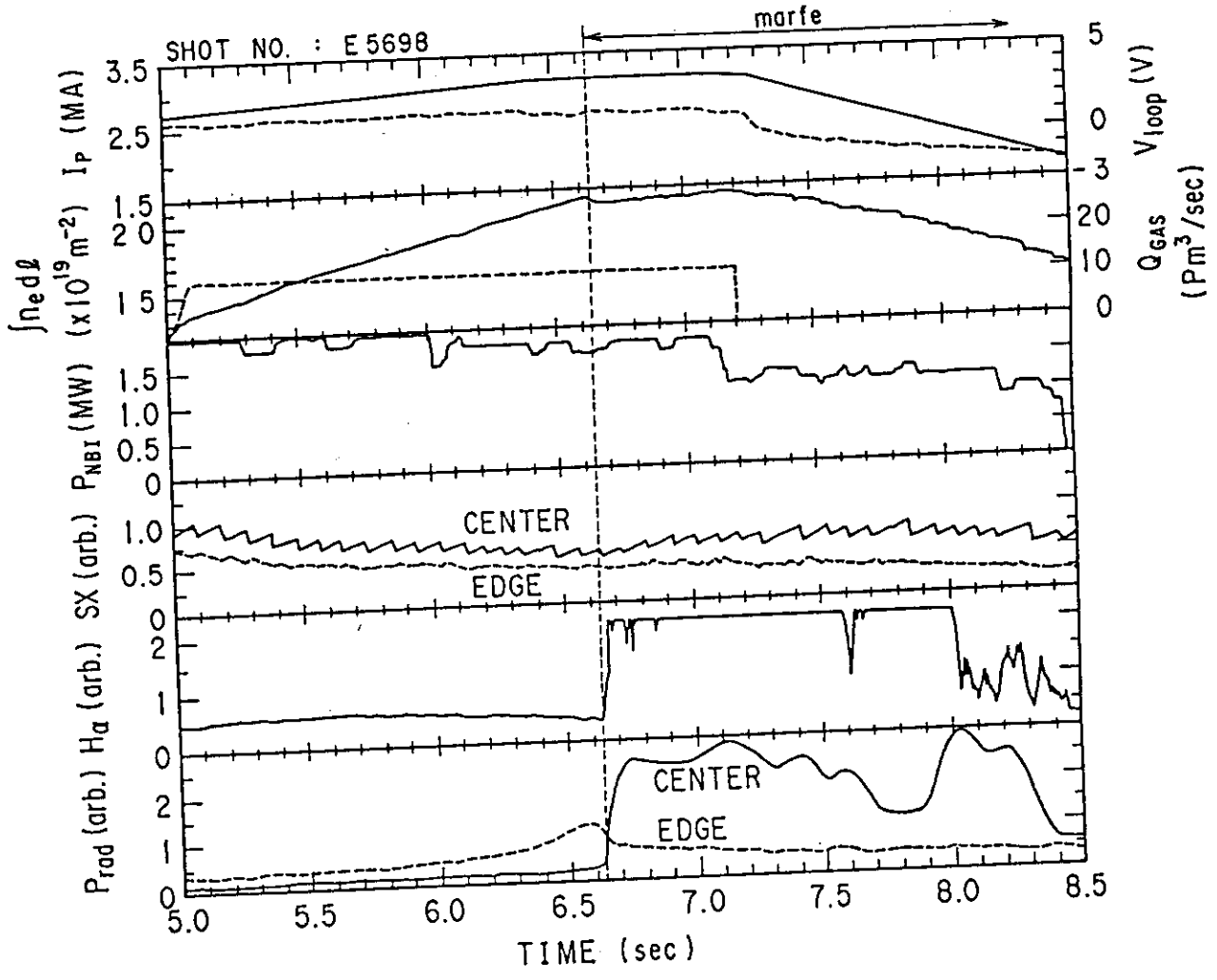

Fig. 7.5 Typical waveforms of the marfe in NB heated plasma.

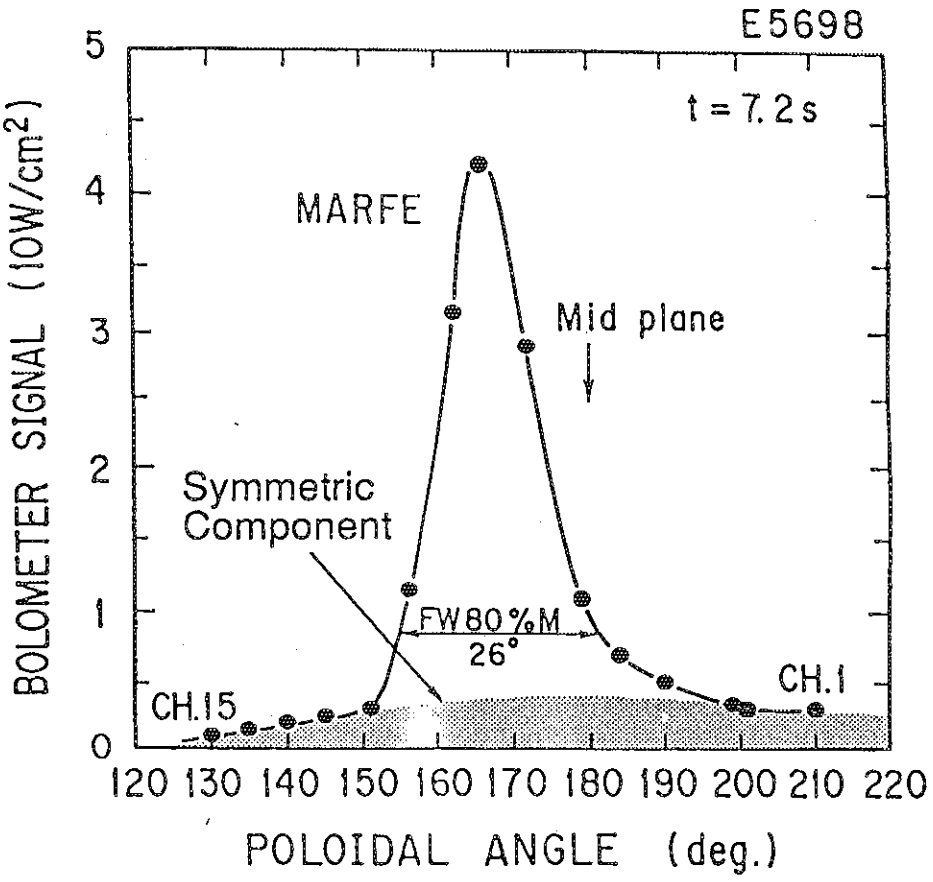

Fig. 7.7 Poloidal extent of the marfe. The center of the marfe is about 10° above the midplane and the FWHM of the radiative band is 15° of poloidal angle.

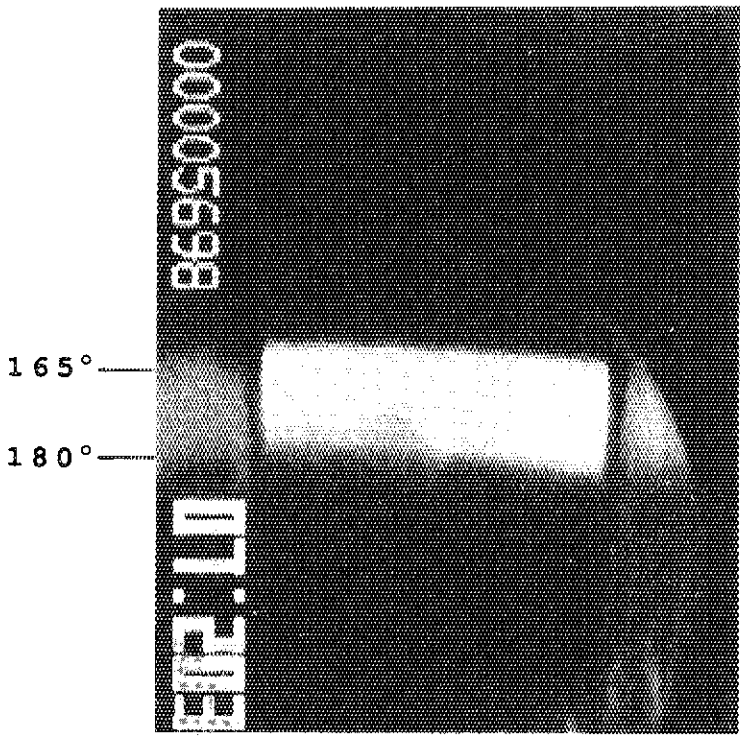

Fig. 7.8 Marfe observed by the visible TV camera. The bright emission band is the marfe.

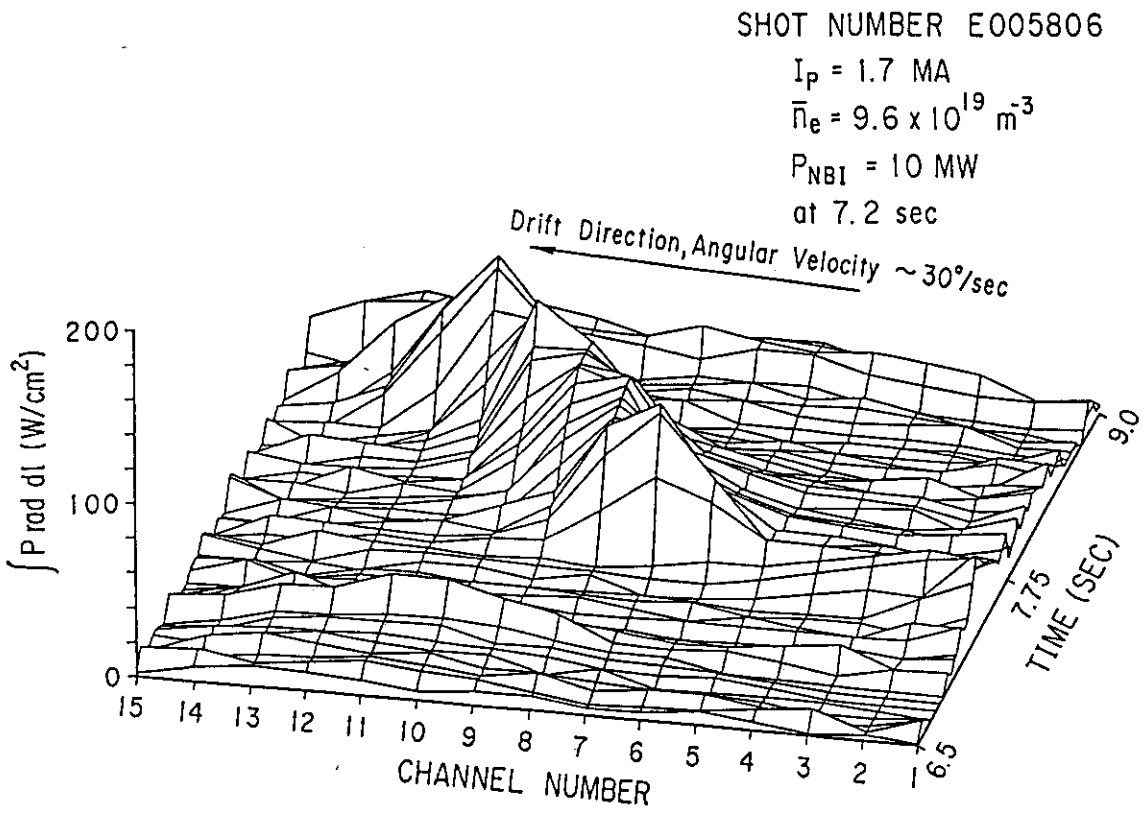

Fig. 7.9 Time evolution of the chord-integrated radiation losses showing drifting marfe.

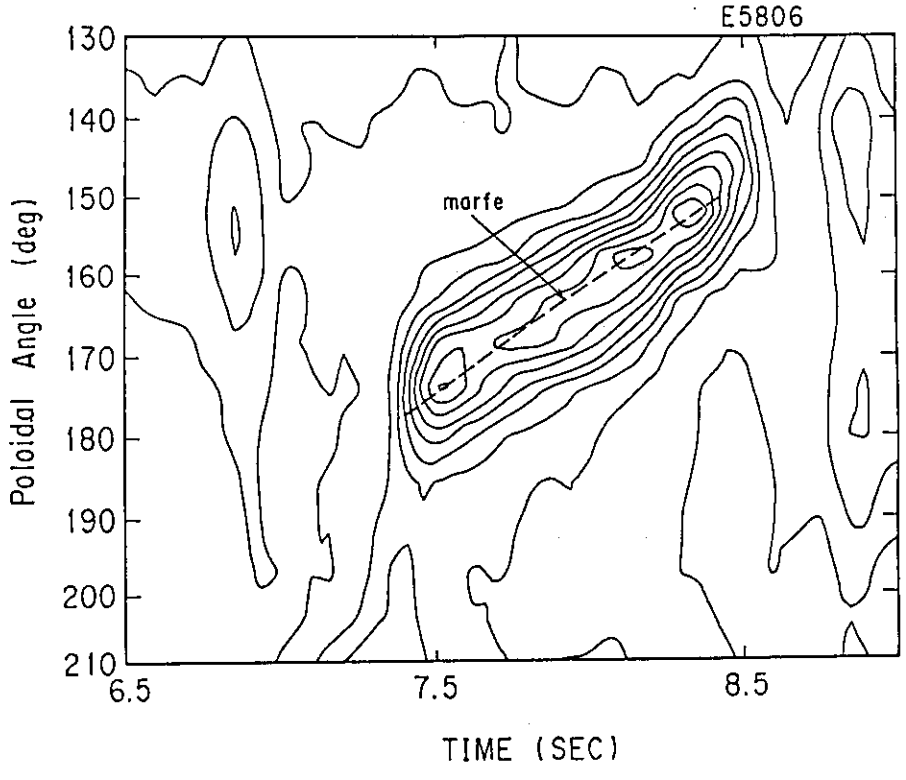

Fig. 7.10 Contour plot of time evolution of the chord-integrated radiation losses showing drifting marfe.

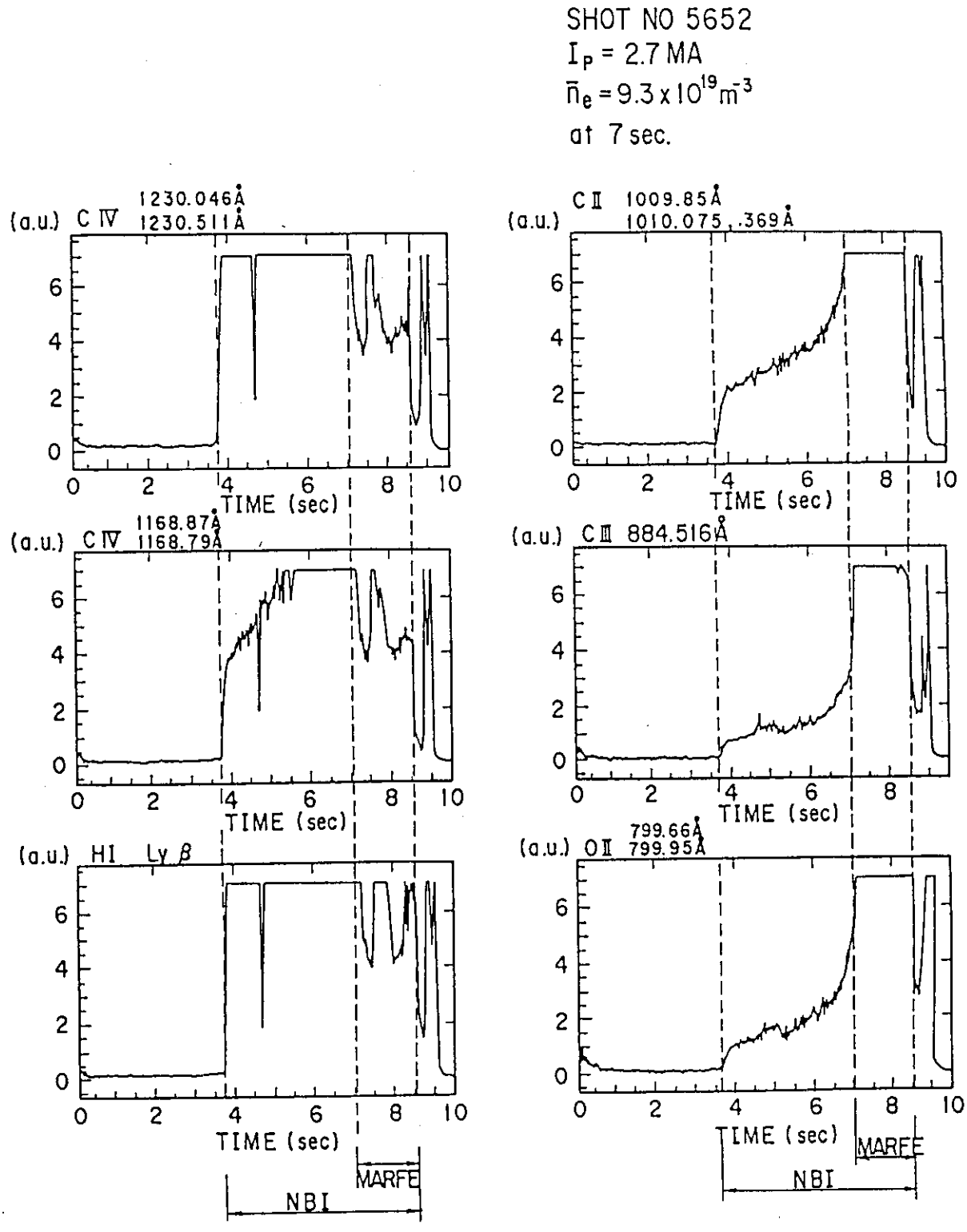

Fig. 7.11 Time evolutions of light impurity brightness in the marfe measured by the normal incidence spectrometer.

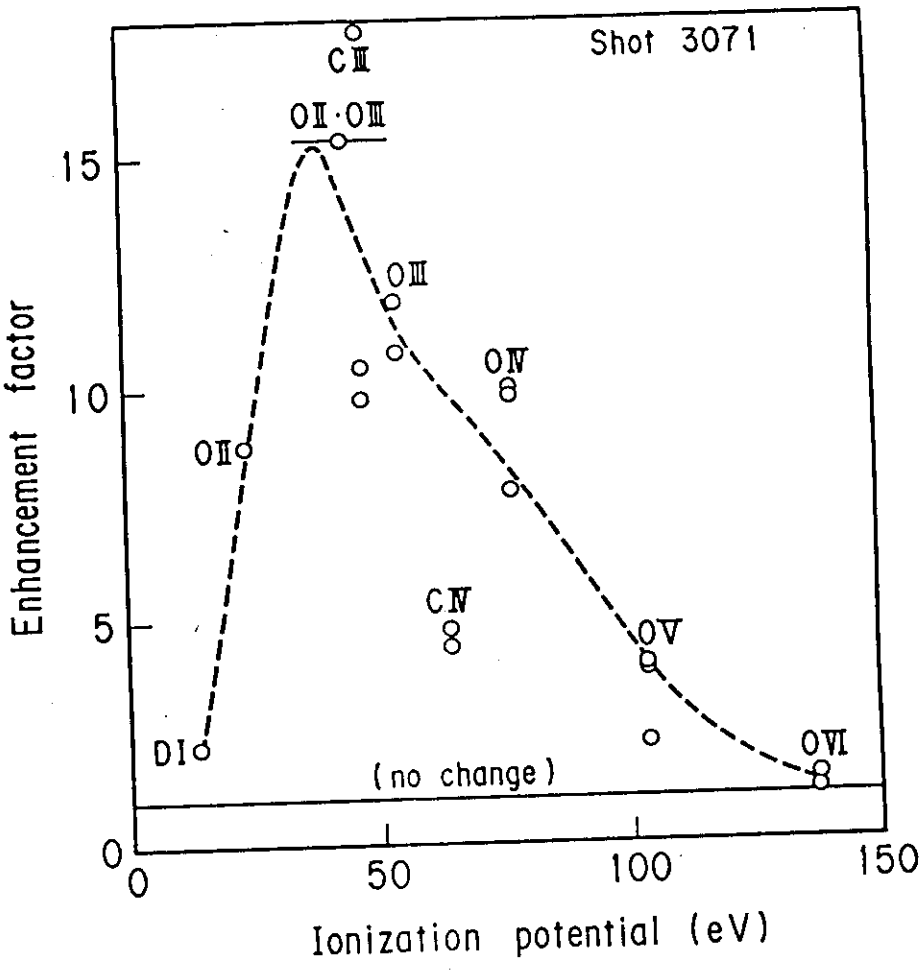

Fig. 7.12 Enhancement factors of low-ionized carbon and oxygen by marfe onset investigated quantitatively in JET.

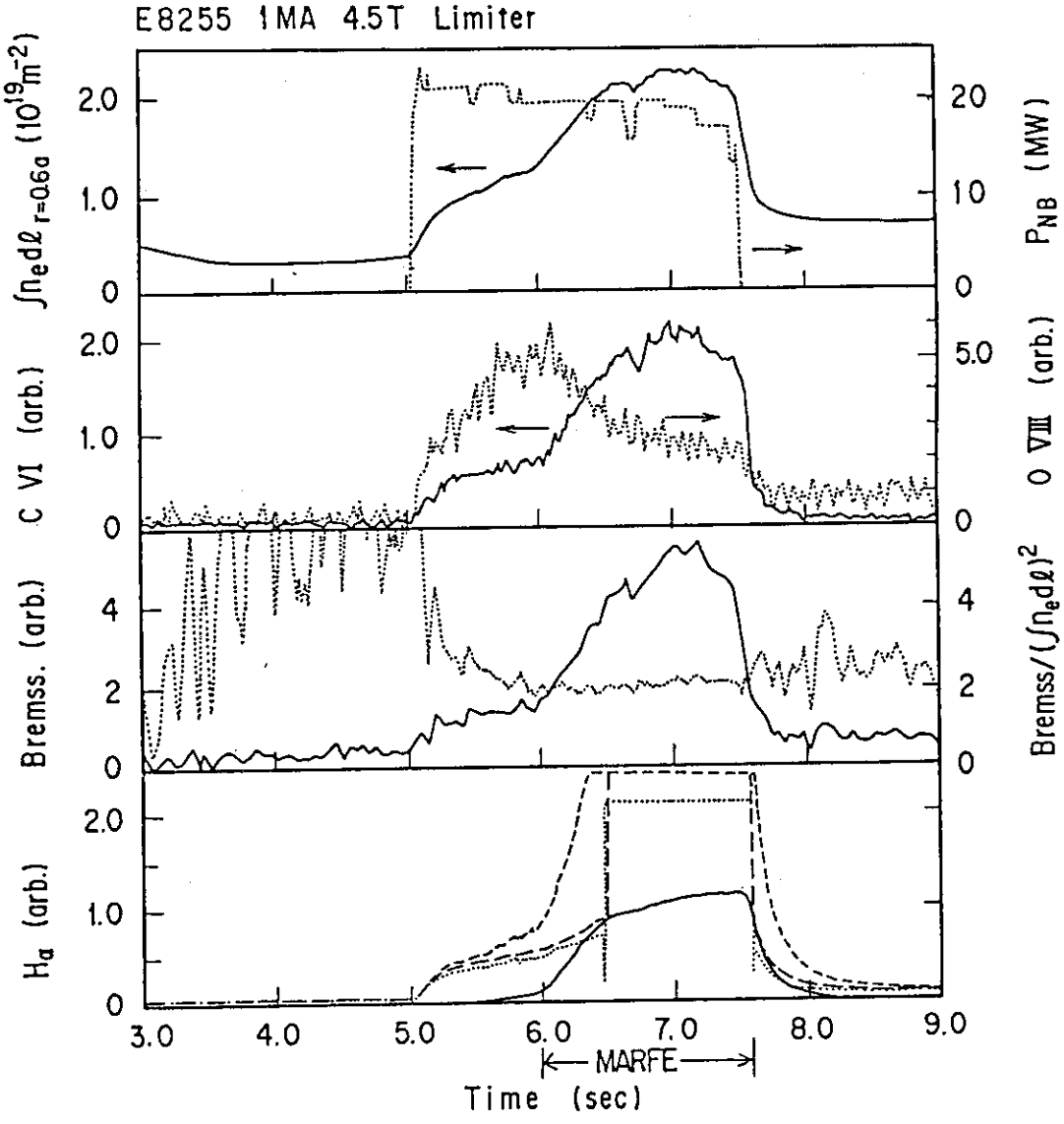

Fig. 7.13 Diagnostics wave forms of the marfe in relatively low density and plasma current plasma with NB heating.

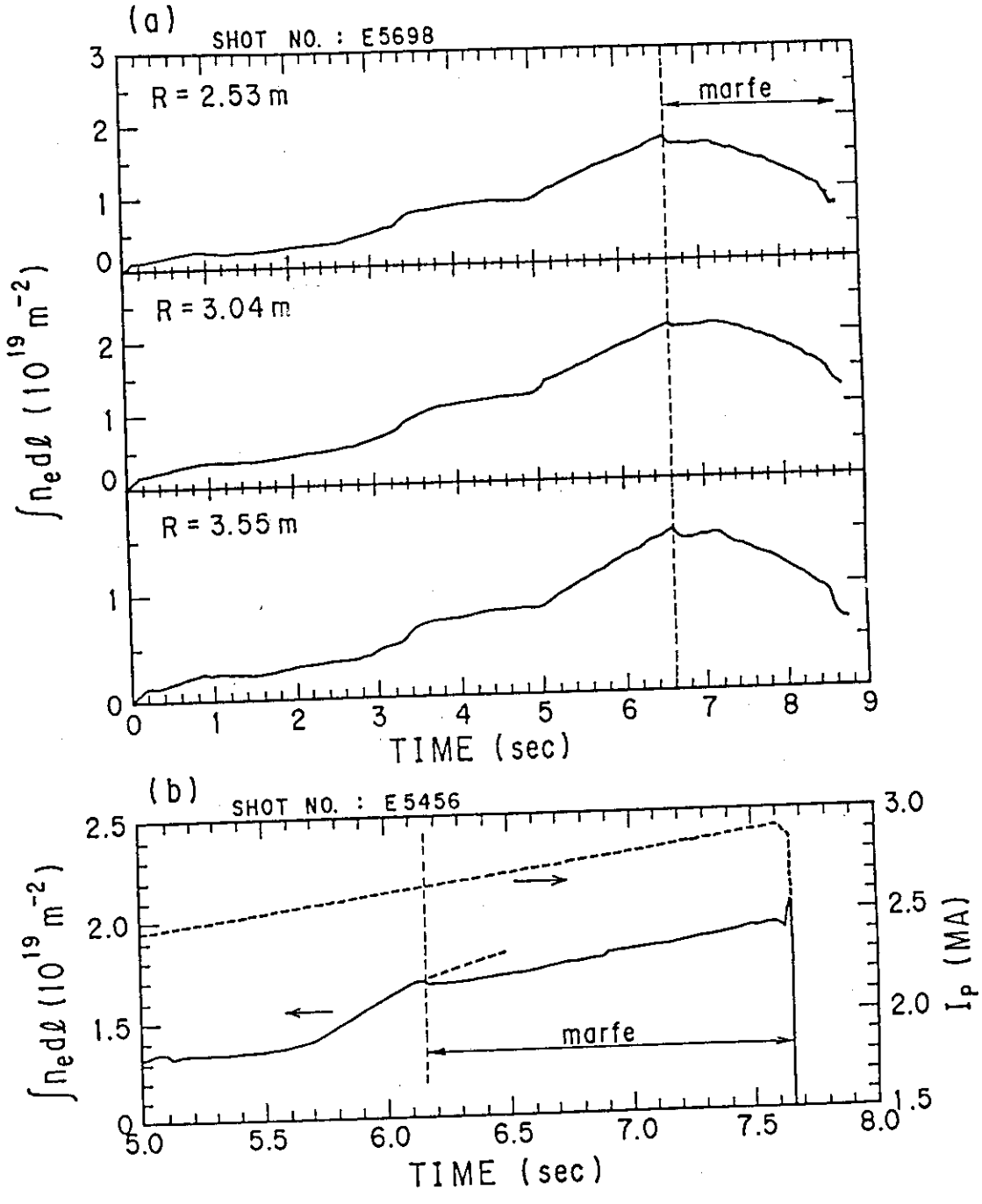

Fig. 7.14 Density behaviors in the marfe. (a) The increases of chord-integrated electron densities along the three vertical chords at R=2.53, 3.04 and 3.55 m are saturated with same manner at the marfe onset in spite of continuous gas puffing. (b) the chord-integrated density decreases ones at the marfe onset and keeps rising within the marfe period resulting in a major disruption at density limit.

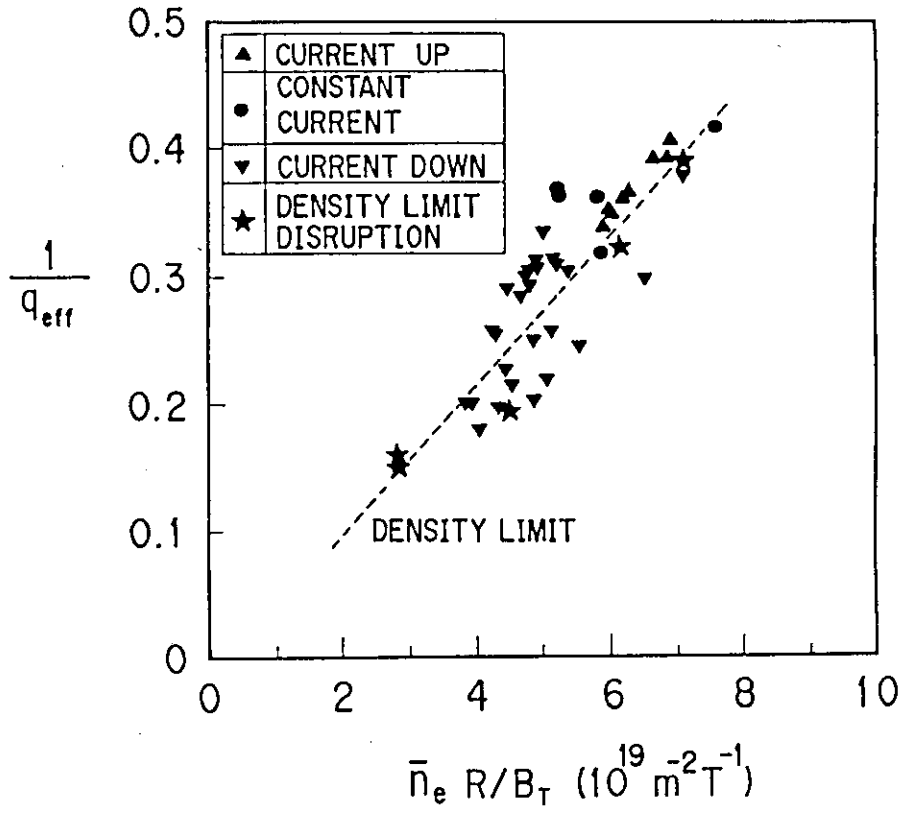

Fig. 7.15 Hugill diagram of the plasma at the marfe onset and the plasma disrupted by density limit.

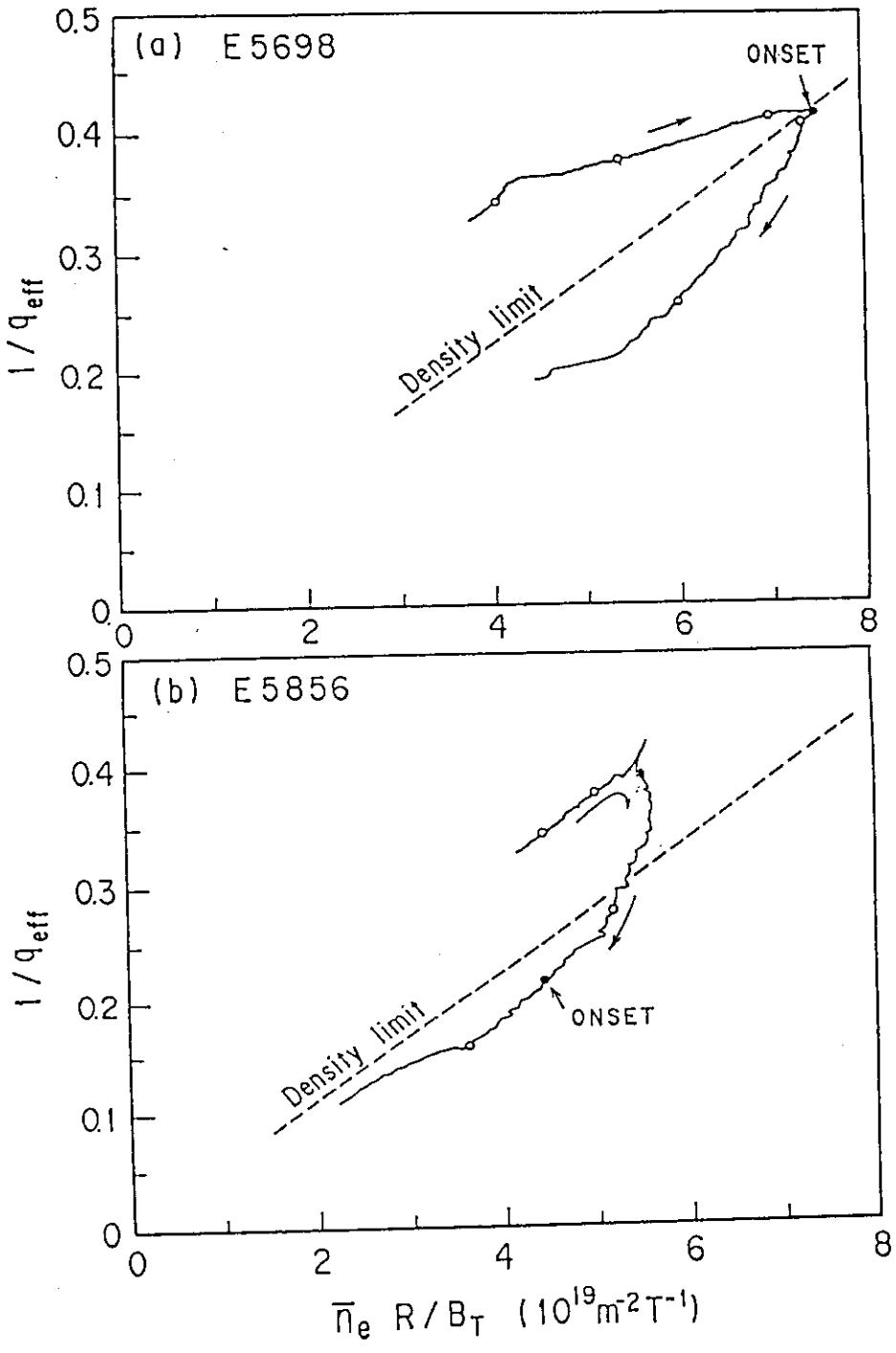

Fig. 7.16 Time trajectories of the plasmas with marfe onset at (a) constant I_P phase and (b) decreasing I_P phase.

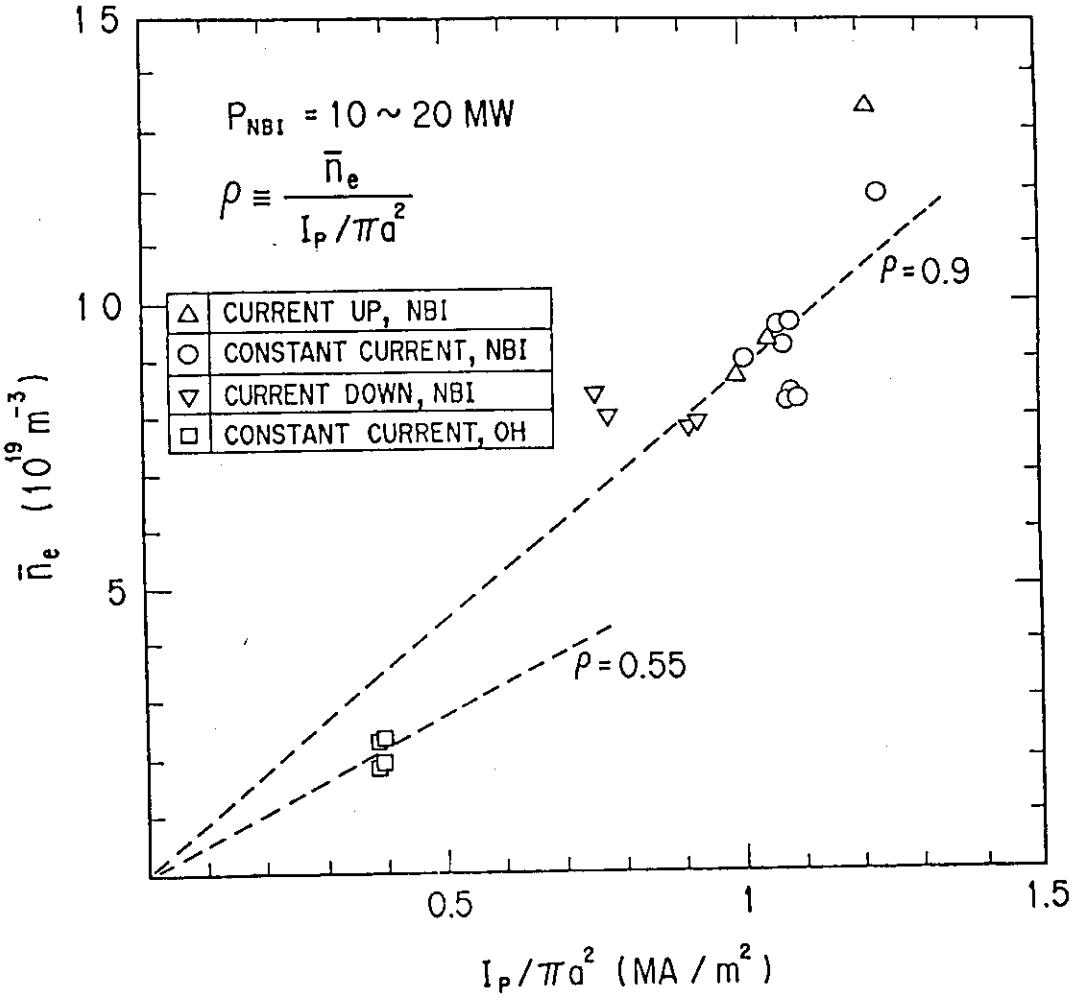

Fig. 7.17 Threshold electron density for the marfe onset plotted against the plasma current normalized by the poloidal cross-section of the plasma.

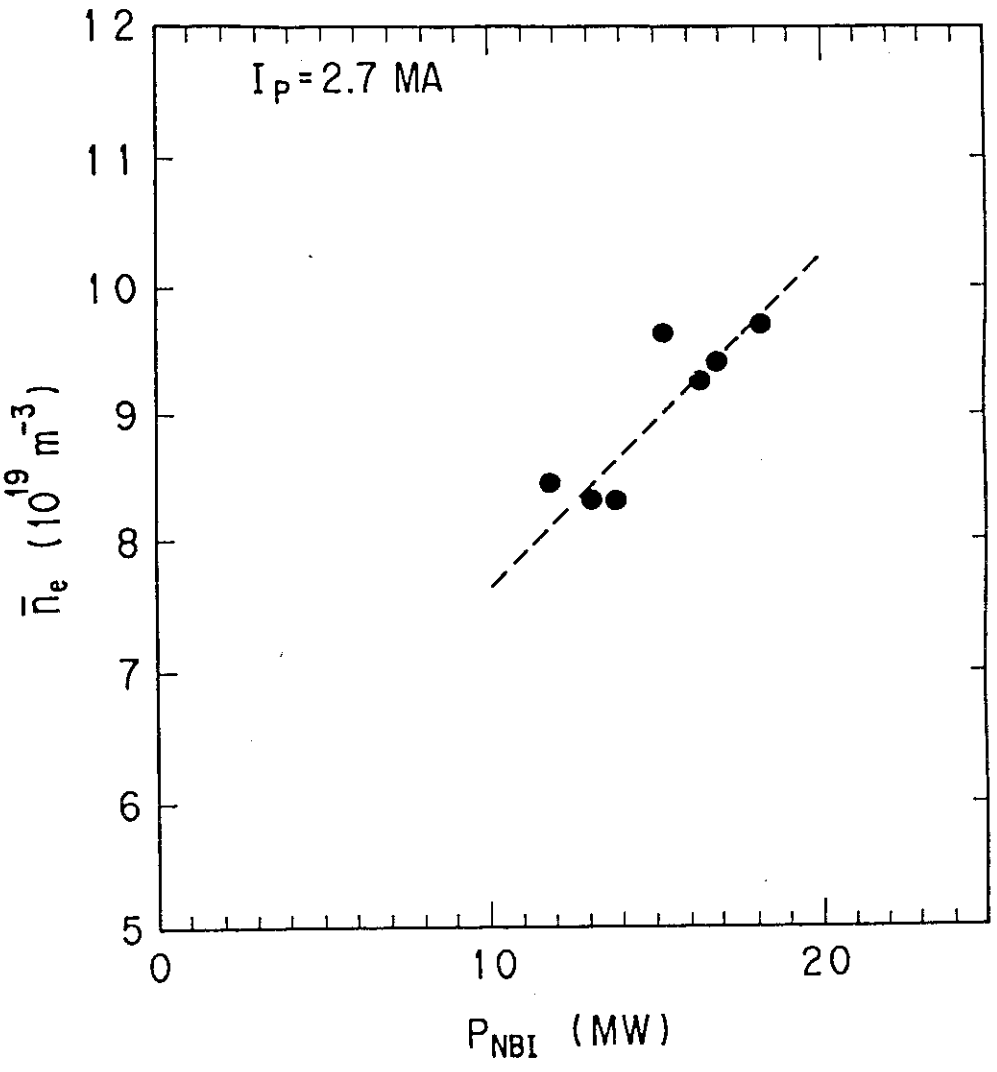

Fig. 7.18 Threshold electron density for the marfe onset plotted against the NB power in the discharges with I_P = 2.7MA.

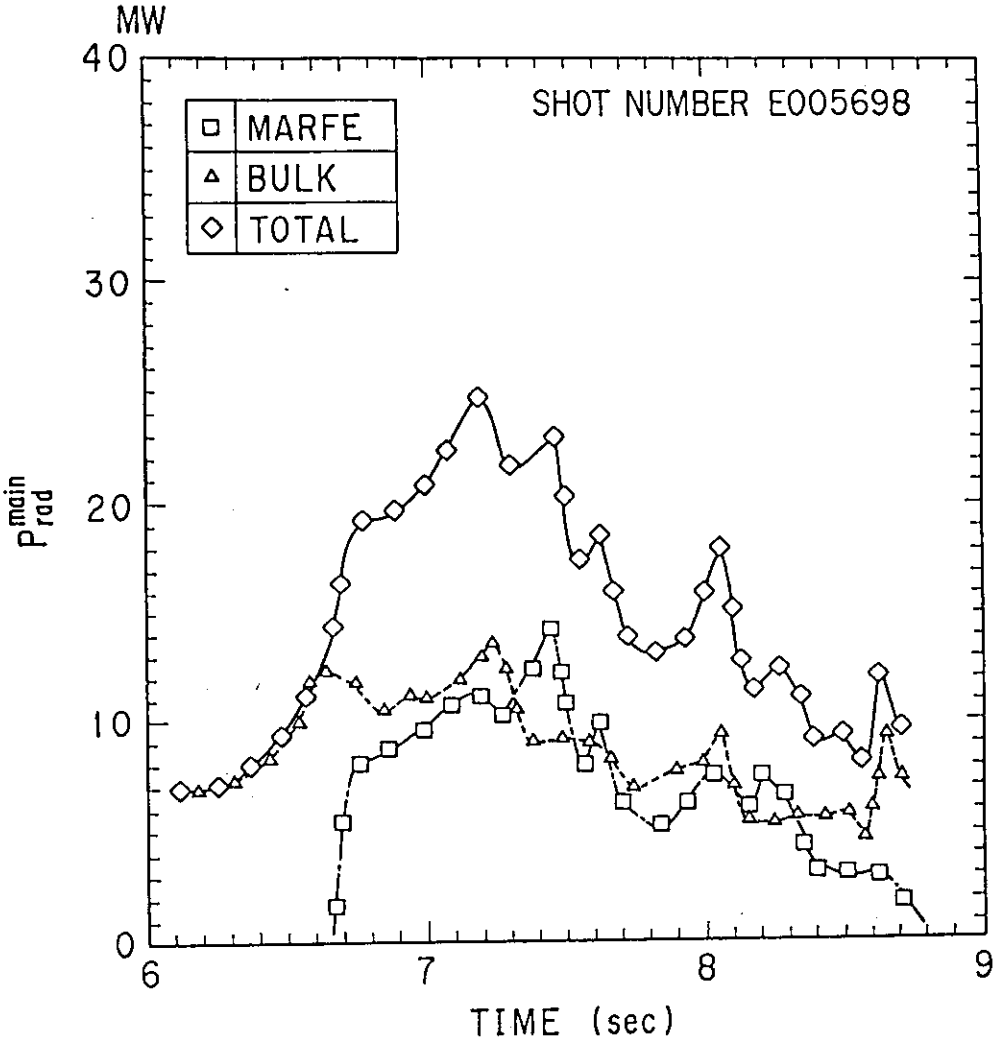

Fig. 7.19 Time evolutions of the symmetric and marfe components of the total radiated power for the plasma as for Fig. 7.5.

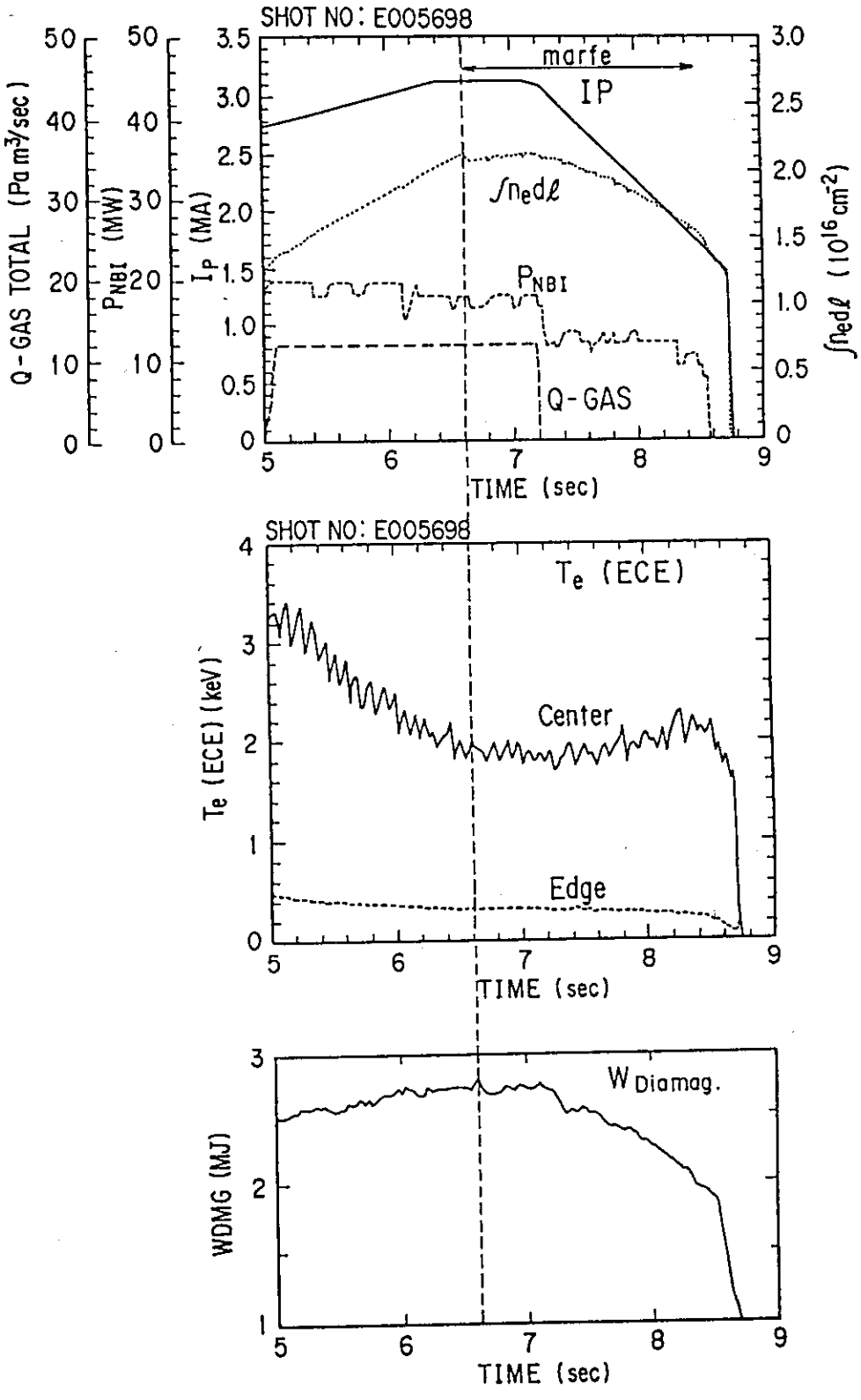

Fig. 7.20 Time evolutions of the stored energy measured by the diamagnetic loop, the electron temperature measured from the ECE emission, and other parameters as for Fig. 7.5.

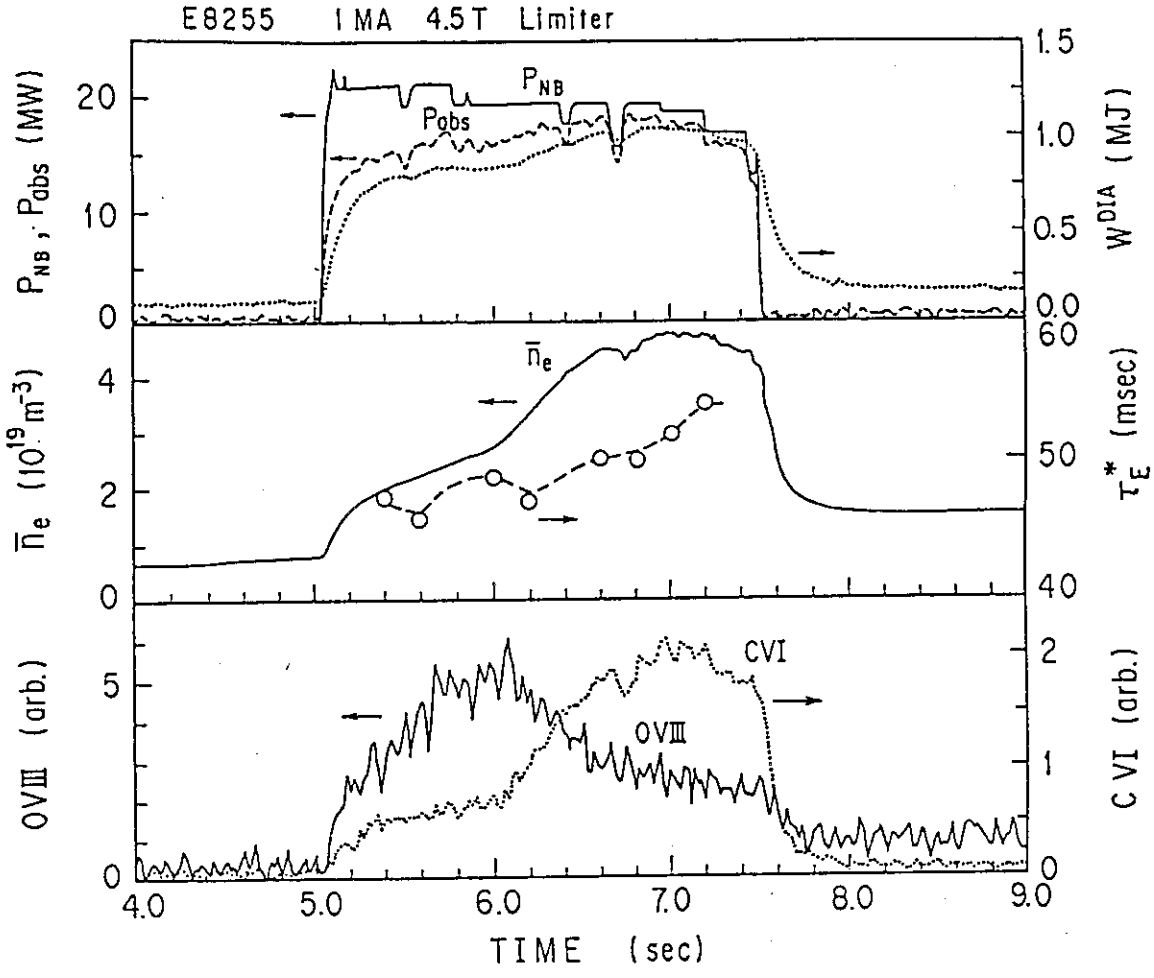

Fig. 7.21 Time evolutions of the stored energy measured by the diamagnetic loop, the energy confinement time and other parameters as for Fig. 7.13.

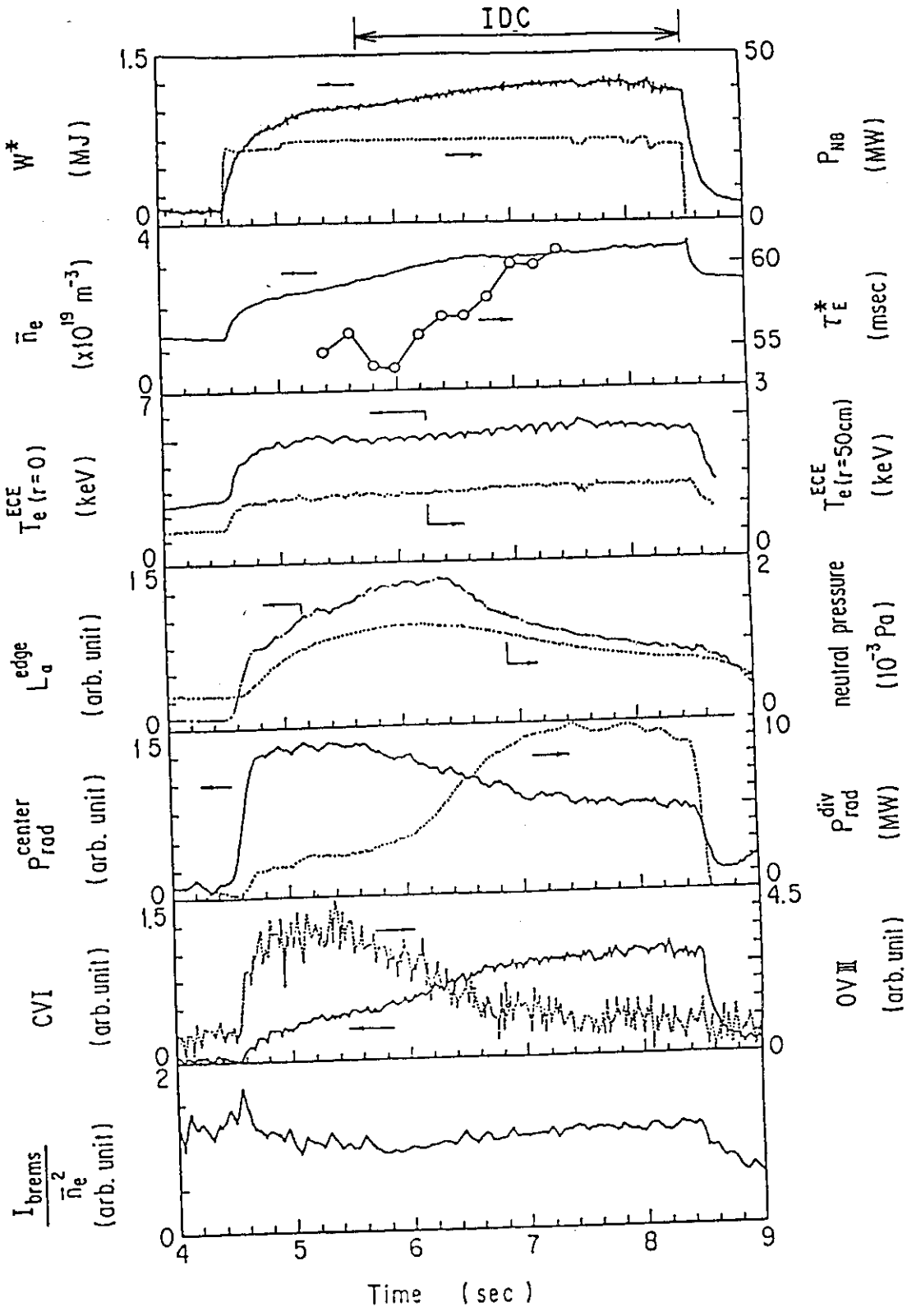

Fig. 7.22 Typical wave forms of the IDC discharge.

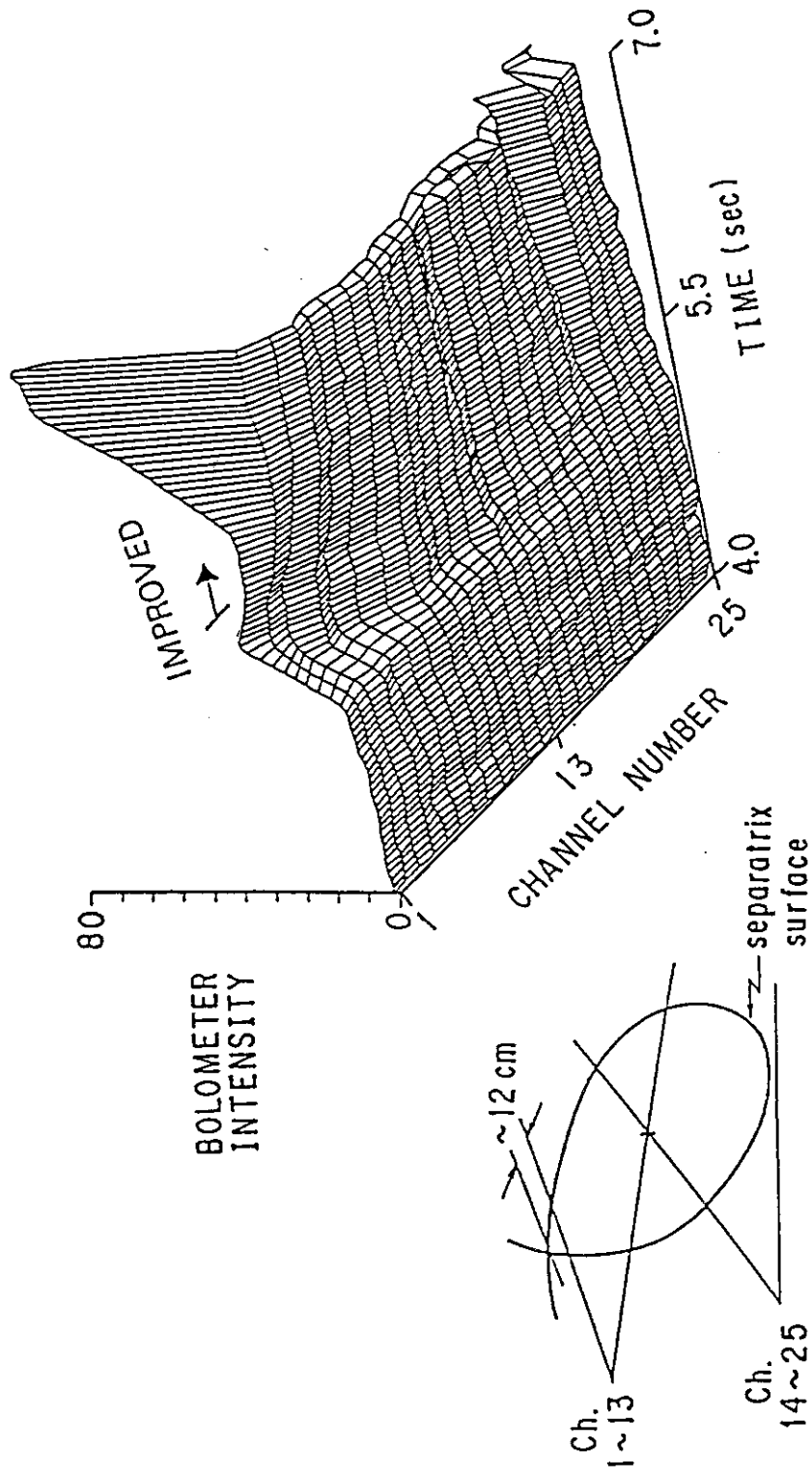

Fig. 7.23 The time evolution of the chord-integral intensities of the bolometers as a function of channel in the IDC.discharge where channel 1-13 and channel 14-25 correspond to the lower and upper arrays, respectively. The intensity of the lowest channel increases steeply in the IDC.

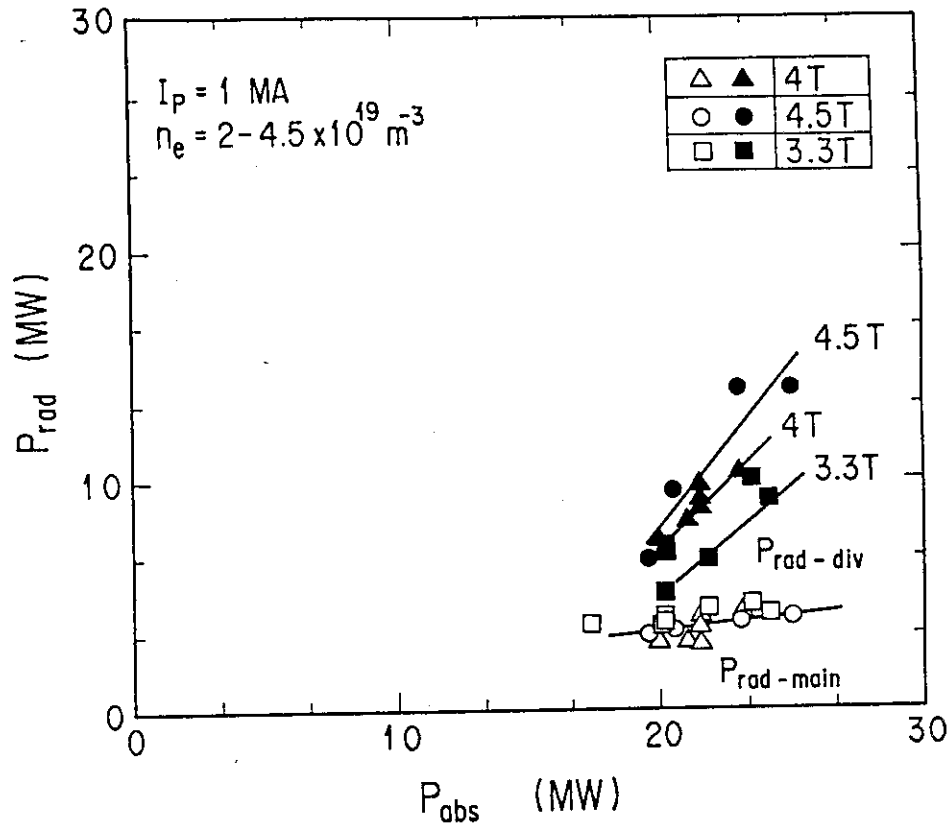

Fig. 7.24 The radiated power from the main and divertor plasmas in IDC discharges as a function of the absorbed power for various B_T.

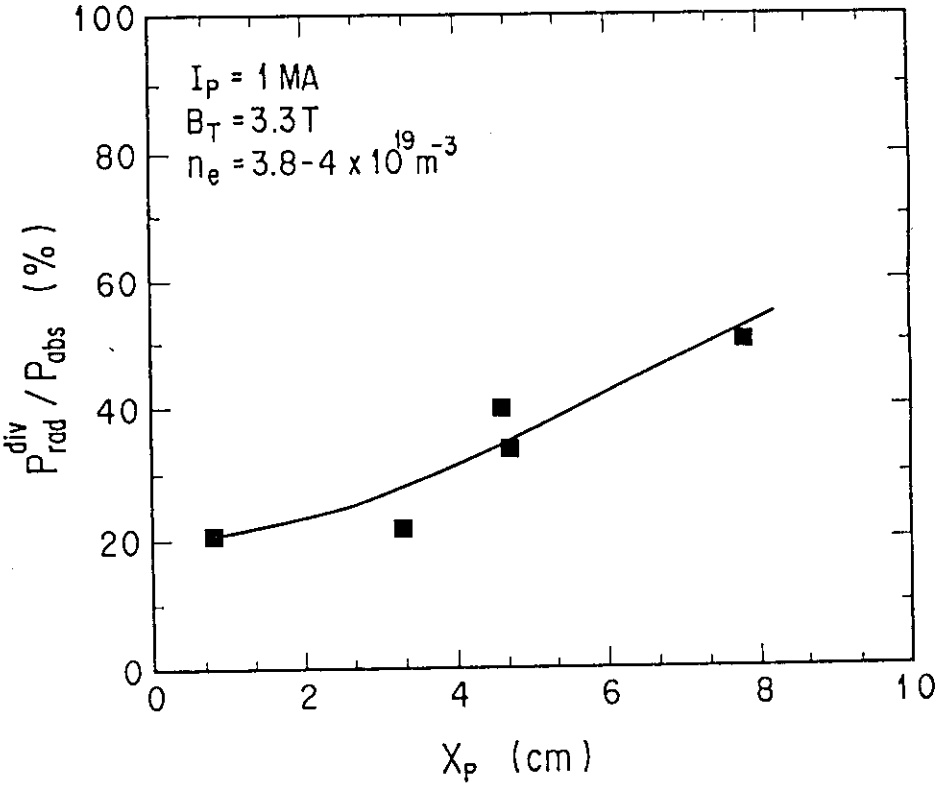

Fig. 7.25 Radiation losses from the divertor region plotted against the distance X_P between the X-point and the divertor plate.

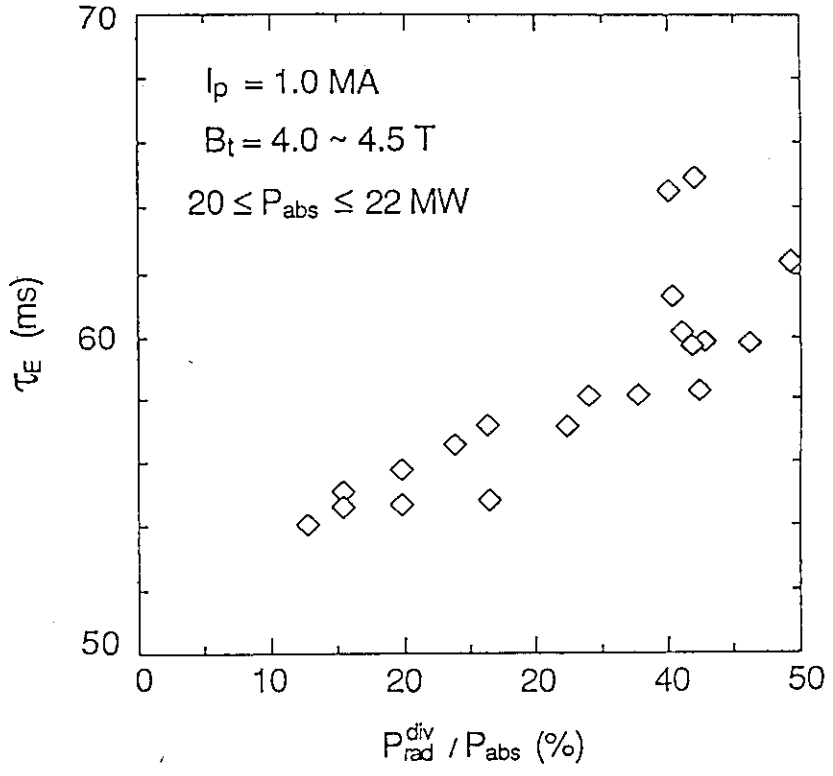

Fig. 7.26 Global energy confinement time of the IDC plasmas plotted against the radiated power from the divertor region.

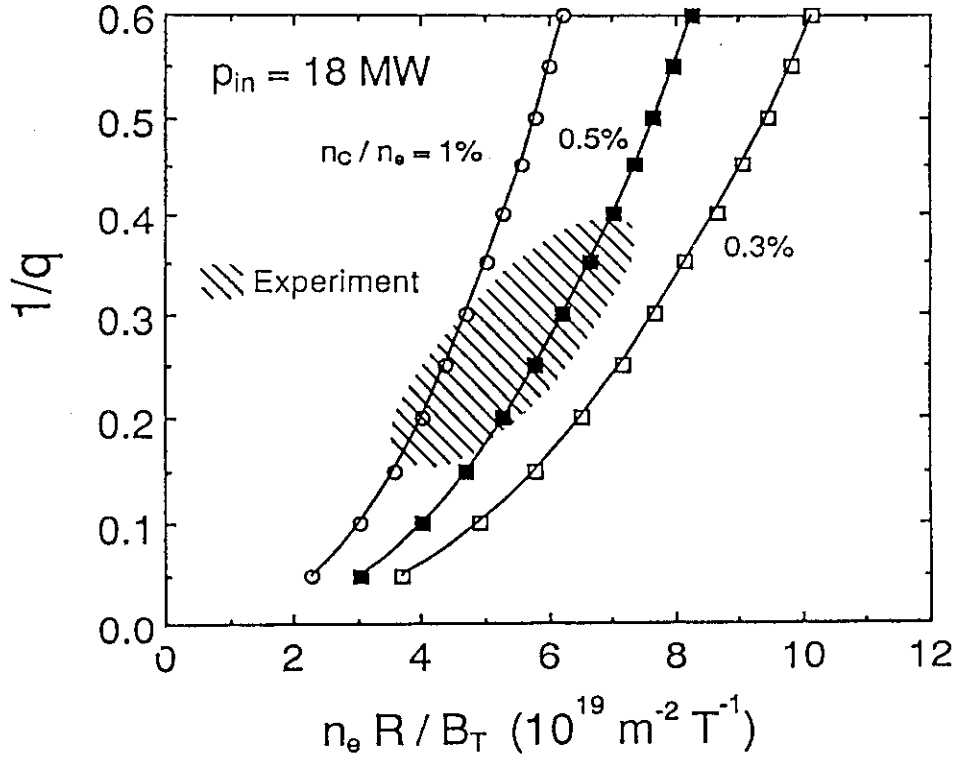

Fig. 7.27 MARFE onset condition on the Hugill diagram calculated by the simple model of the radiative thermal instability for the NB heated plasma in the range of the carbon concentration 0.3-1%.

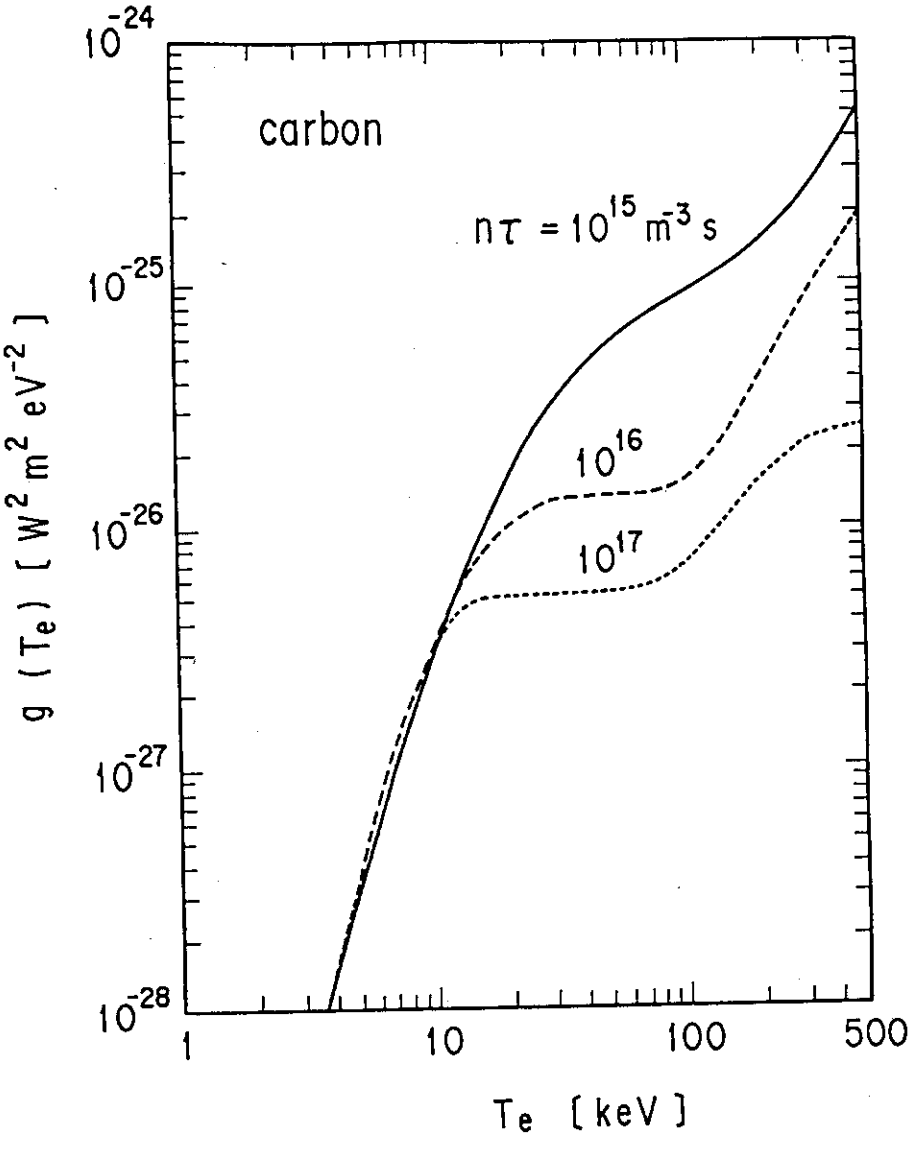

Fig. 7.28 g(T) as a function of T_e for carbon calculated from non-coronal radiative cooling rate. nτ is electron density multiplied by recycling time of the impurity particles.

8. Summary and Conclusion

Chapter.1 reviews the status of the tokamak fusion research and the theoretical background of the radiation-loss processes. The studies of the plasma for the thermonuclear fusion are carried out by tokamaks as a leader. The three large tokamaks in the world, TFTR, JET, and JT-60 are operating now aiming to demonstrate the marginal fusion energy breakeven. The accumulation of impurities and the accompanying radiation losses in a core plasma are serious problem to achieve a reactor grade plasma not only because the radiation losses degrade the energy confinement of the core plasma but also because the impurities dilute the reacting plasma to reduce reaction rate. Whereas, appropriate radiation loss localized in the peripheral plasma is sometimes favorable to reduce the heat load onto the first wall and influx of impurities from the wall by cooling edge plasma namely remote radiative cooling. This thesis describes the developments of radiation-loss-measurement systems and the investigations of the radiation losses and global power balance on the JT-60 tokamak.

Chapter 2 presents the overviews of JT-60 machine and the diagnostics. JT-60 has various features to study physical and technological aspects of reactor-grade plasma. JT-60 has a long discharge duration of 10 seconds, a poloidal divertor for impurity control and confinement improvement, NB and RF heating with high power and long pulse duration, RF current drive and real time plasma control. JT-60 is a unique device having a closed divertor

chamber among the three large tokamaks. JT-60 has three magnetic configurations, outer X-point divertor, lower X-point divert and limiter, and two types first wall, one is a TiC coated molybdenum and another is carbon graphite. Therefore, JT-60 is suitable to investigate the radiation losses and impurity control. JT-60 has 23 different kinds of diagnostics to measure the fundamental parameters of the plasma such as electron density, electron and ion temperatures, impurity contents. The diagnostics data are acquired by CAMAC systems and processed in the computer system.

Development of the bolometric measurement system which is a major diagnostic in the radiation loss study is described in Chapter 3. A new metal resistor bolometer was developed for JT-60. It is composed three layers, 5-μm-thick gold absorber, 7-μm-thick polyimide and 0.1-μm-thick gold resistor. This bolometer with bridge amplifier shows a linear response to the radiation power, including both neutral particle emission and electromagnetic radiation in the range from UV to soft X-ray. Very long cooling time and high sensitivity were performed in this bolometer. Before modification for the lower divertor, single array of 15 channel bolometers measured radiated power from main plasma and two bolometers measured that from outer X-point divertor. After the modification, two arrays of bolometer measured power from main plasma and a bolometer measured that from the lower X-point divertor. Intense poloidal asymmetries of the radiated power localized near the X-point outside the torus were observed in divertor discharges. The profiles of the radiated power were reconstructed by the Abel inversion with an asymmetric term.

Chapter 4 presents the soft x-ray PHA system and its experimental results. The soft x-ray PHA is useful measurement not only for the electron temperature but also the metal impurity radiation in the core plasma. The soft x-ray PHA in the energy range of 3 - 60 keV was performed for JT-60 ohmically heated and NB heated plasma, using a high-purity germanium detector cooled by liquid nitrogen. The time evolution of the electron temperature was derived from the measured spectra with the time resolution of 100 ms. The electron temperature was obtained up to 3.0 keV in the typical divertor ohmically heated discharges with plasma current 2 MA. The dominant metal impurity was titanium. The typical impurity density and the effective ionic charge Z_{eff} were estimated from these measurements, and the titanium density of 10 - 3 % and Z_{eff} of 1.2 were obtained for the typical ohmically heated divertor discharges. And the titanium concentration of NB heating discharges was about factor 2 larger than that of ohmically heating.

Chapter 5 presents the soft x-ray intensity and Balmer α line measurement systems and their principal experimental results. To measure the soft x-ray intensity profiles of JT-60 plasmas, thirty channels of PIN diode detectors were arranged with the changeable multi-absorption filters. The x-ray intensity profile measurement (x-ray imaging) system can operate with the temporal resolution of 20 μs and the spatial resolution of 3.5 cm. Using the x-ray imaging system not only the observation of the MHD behavior was performed, but also the toroidal rotation speed, the inversion radius, the electron conductivity and the electron temperature profile were estimated.

Particle recycling in the edge plasma is important to understand the particle behavior but also the plasma cooling as well as impurity radiations in the edge region. The particle behaviors of the ohmically and NB heated plasmas have been investigated by measuring Hα emissions from the main and divertor plasmas using Hα filtered photodiodes. The fuelling efficiency was almost independent of $\bar{n}_e$. The global particle confinement time of the OH plasma was about 150 ms at low electron density and decreased with $\bar{n}_e$. The τ_p of the NB heated plasma was about 2/3 of that of the OH plasma at same electron density. The τ_p of the NB heated plasmas decreased with the NB power.

The global power balance of OH and NB heated plasmas were described in Chapter 6. The global power balances of the JT-60 plasmas with different inner hardware, and with different plasma configurations were investigated by bolometric measurements, thermocouples and IR TV camera on the JT-60 tokamak. Very low radiation loss of the main plasma (10% of the absorbed power) was realized in NB heated outer X-point discharges with TiC coated molybdenum wall. The radiation loss due to oxygen was dominant in this case. Whereas, the limiter plasma with TiC coated molybdenum limiters were very radiative where the radiated power was more than 60% of the absorbed power in ohmically and NB heated discharges. In the discharges with graphite wall, radiated power from the main plasma was 20 - 25% for both limiter and lower X-point configurations. The radiated power from the divertor region increased from several percent to 40% of the absorbed power with the increase of $\bar{n}_e$. The improved divertor confinement (IDC) regime was obtained in NB heated lower X-point discharges with graphite wall. In IDC discharges the radiation loss from the divertor region increases to be up to 40% (typically 10 MW) of the absorbed power. Whereas, that from the main plasma and the heat load onto divertor plates decreased in IDC.

Characteristics of marfe and IDC phenomena, which are enhanced radiation in the edge plasma and the divertor plasma, respectively, are described in Chapter 7. The marfe is a poloidally asymmetric radiation band localized near the inside midplane and is a common phenomenon among middle and large size tokamaks. In JT-60, the marfe has been observed frequently in high-Ip and high density limited discharges with NB heating after the replacement of the first wall from TiC coated molybdenum tiles to graphite ones. The marfe occurred around the midplane on the inside wall. The poloidal drift motion of the marfe has been observed frequently in the discharges during I_P rump down and/or reducing P_{NB}. The direction of the drift motion was upward independent of the B_T direction. The threshold electron density of the marfe onset was investigated in OH and NB heated plasmas. The threshold electron density increased with the P_{NB}. The empirical scaling of the marfe onset taking account of the NB power was obtained. This scaling was useful to predict the marfe onset condition in NB heated discharges on JT-60. The threshold electron density for marfe onset during I_P rump down was found to be higher than that in constant I_P. The marfe was modelled based on the radiative thermal instability. The simple model can explain the marfe onset condition. The increases of chord-integrated electron densities were saturated in the marfe period in spite of continuous gas puffing. The marfe may degrade the fuelling efficiency of the gas puffing. The radiation power density in the marfe was estimated to be 20 - 30 MW/m^3 typically if the radial extent of the marfe was assumed to be 0.1 m. The major contributors to the large emissively in the marfe were estimated to be carbon and oxygen in low charge states. The power radiated from the marfe reached 20-50% of the total radiated power. The radiated power from the plasma with marfe was about 90% of the absorbed power. Both stored energy and central electron temperatures did not change by the marfe onset in spite of the such intense radiation loss. The marfe onset relatively low Ip improves energy confinement time up to several % accompanied with the increase of electron density.

In the IDC discharges, the strong remote radiative cooling is realized. Radiation losses from the divertor region increased with the toroidal magnetic field and the distance between the X-point and the divertor plates, which suggested that it increased with the connection length of the divertor. The strong radiated power from the divertor region in IDC (typically 10MW) can be explained with a dense and cold carbon plasma in the divertor region by using simple model of the scrape-off layer.

Finally, this study revealed that the most clean plasma was obtained in the metallic first wall with the divertor on JT-60. This fact is suggesting the capability of the metallic material for the first wall of next devices such as ITER and FER. Enhance radiation localized in the peripheral plasma such as marfe and IDC dose not degrade the core plasma confinement or somewhat improves it, so that marfe and IDC are suitable operational regime in the high density region for future devices because they have strong remote-radiative-cooling-effect.

Acknowledgements

The author would like to express his appreciation to Professor M. Nakazawa of University of Tokyo for his continuous guidance and affectionate encouragement. He also wishes to express his gratitude to Professor N. Inoue and Associate Professor T. Iguchi for their encouragement and kind advice.

The author wishes to acknowledge K. Nagashima for useful discussions and collaboration in the experiment. The author wishes to thank M. Hara, T. Sugiyama and T. Kaneko for their technical supports.

The author wishes to acknowledge T. Sugie, H. Kubo and Y. Kawano for providing spectroscopic data and useful discussions about impurity behavior, H. Yoshida for his divertor simulation calculation, T. Ando for providing thermocouples data of the divertor plate, K Itami for providing IR TV data and useful discussions about global power balance, T. Tsuda for his theoretical support about marfe, and S. Tsuji, N. Hosogane, M. Shimada for fruitful discussions about global power balance and IDC. He also wishes to S. Ishida for his support of MHD studies.

The author wishes to thank B. Lipschultz of MIT and J.D. Schievell of Princeton Plasma Physics Laboratory for useful discussions about bolometric measurements and marfe. He also wishes to thank to J. Strachan for his encouragement and support during the author's stay in Princeton Plasma Physics Laboratory.

The author appreciates H. Takeuchi for his enlightening suggestions. This work has been done as a part of the JT-60 project with collaboration and support of the JT-60 Team. All the members of the JT-60 Team are acknowledged. Finally, the author would like to acknowledge M. Funahashi, Y. Suzuki, S. Tamura, and M. Yoshikawa for continuous support and encouragement.

Publication List Concerning This Thesis

Chapter 2

(1) H. Yokomizo, H. Takeuchi, T. Sugie, N. Ogiwara, M. Sato, A. Nagashima, K. Ohasa, Y. Nakamura, T. Nishitani, Y. Neyatani, A. Sakasai, T. Fukuda, H. Kubo, K. Tobita, Y. Yamashita, M. Nemoto, S. Iida, K. Nagashima, Y. Uramoto, O. Yamashita, T. Tsugiyama, M. Shitomi. Y. Tsukahara, T. Ohshima, K. Yamagishi, S. Tahira, S. Konoshima, M. Shiho, H. Maeda and Y. Suzuki, "The JT-60 Diagnostics System", Fusion Eng. Des. 5 (1987) 117.

(2) K. Hayashi, K. Hashimoto, H. Yamato, H. Takeuchi, Y. Miura, T. Nishitani, M. Shiho and H. Maeda, "Charge Exchange Particle Mass and Energy Analyzer for JT-60 Tokamak", Rev. Sci. Instrum. **56** (1985) 359.

(3) T. Nishitai, K. Ohasa, K. Tsukada and Y. Ohgushi, "Optical Serial Highway for CAMAC System Using High-Performance Optical Bus Adapters" , J. Lightwave Technology **LT-3** (1985) 525.

Chapter 3

(1) T. Nishitani, K. Nagashima, T. Sugiyama, M. Hara, H. Takeuchi and JT-60 Team, " Bolometric Measurements in JT-60", Rev. Sci. Instrum. **59** 1988) 1866.

(2) T. Nishitani, K. Nagashima, M. Hara and H. Takeuchi, "Radiation Loss Measurements on JT-60 with Bolometer Array", Kakuyugo Kenkyu **59** Suppl. (1987) 226 (in Japanese).

Chapter 4

(1) T Nishitani, K Nagashima and H Takeuchi, "Soft X-ray Measurements of the JT-60 Tokamak Plasma in The Initial Experiments", Japan Atomic Energy Research Institute Report JAERI-M 87-011 (1987).

(2) K. Nagashima, T. Nishitani and H. Takeuchi, "Soft X-ray Measurement of JT-60 by the Pulse Height Analysis System", Kakuyugo Kenkyu **59** Suppl. (1987) 202 (in Japanese).

Chapter 5

(1) K. Nagashima, T. Nishitani and H. Takeuchi, "Soft X-ray Intensity Profile Measurement by PIN Diode Array System", Kakuyugo Kenkyu **59** Suppl. (1987) 215 (in Japanese).

(2) S. Ishida, T. Nishitani, K. Nagashima, S. Iida, T. Matoba and JT-60 Team, "Internal Mode Oscillations as a Diagnostics for the Plasma Rotation in JT-60", Nucl. Fusion **28** (1988) 2225.

(3) S. Ishida, H. Shirai, K. Nagashima, T. Nishitani, T. Fukuda and JT-60 Team, "Sawtooth Observations in Ohmic Discharges Compared between Hydrogen and Helium Plasmas on JT-60", Plasma Phys. Controlled Fusion **30** (1988) 1069.

(4) T. Nishitani, K. Nagashima, T. Sugiyama, S. Koide and H. Takeuchi, "Particle Recycling Diagnostics with Balmer Line Measurement", Kakuyugo Kenkyu **59** Suppl. (1987) 243 (in Japanese).

(5) K. Yamada, S. Tsuji, K. Shimizu, T. Nishitani, K. Nagashima, "A Study of Particle Confinement Properties in the Ohmically and Neutral Beam Heated Hydrogen Plasmas of the JT-60 Tokamak", Nucl. Fusion **27** (1987) 1203.

(6) Sinji Koide, Katsuhiro Shimizu, Takashi Sugiyama and Takeo Nishitani, "A Study of Particle Confinement Using Skin Radiative Approximation Method in JT-60 Tokamak", Jpn. J. Appl. Phys. **29** (1990) 402.

Chapter 6

(1) T. Nishitani, K. Itami, K. Nagashima, S. Tsuji, N. Hosogane, H. Yoshida, T. Ando, H. Kubo and H. Takeuchi, "Radiation Losses and Global Power Balance of JT-60 Plasmas", to be published in Nucl. Fusion.

Chapter 7

(1) T. Nishitani and S. Ishida, " Study of Marfe Phenomena on JT-60", Japan Atomic Energy Research Institute Report JAERI-M 89-209 (1989).

(2) T. Nishitani and S. Ishida, "Radiative Thermal Instability in Peripheral Plasma (marfe)", Kakuyugo Kenkyu **61** (1989) 137 (in Japanese).